Evanescent wave dynamic light scattering by optically anisotropic Brownian particles

Maciej Krzysztof Lisicki

Institute of Theoretical Physics
Faculty of Physics
University of Warsaw

A dissertation submitted to the University of Warsaw
for the degree of Doctor of Philosophy
under the supervision of Professor Bogdan Cichocki

Warsaw, June 4, 2015

This work was supported by the Foundation for Polish Science within the International PhD Projects Programme MPD co-financed by the EU European Regional Development Fund.

The Author benefited from a Consortium Agreement between Forschungszentrum Jülich in Germany and University of Warsaw in Poland. The Agreement has facilitated extensive collaboration with the group of Prof. Jan K. G. Dhont at Institute of Complex Systems ICS-3, FZ Jülich, where all of the experimental work presented in the Thesis has been completed.

Research on the topic of the Thesis was partly supported by the grant *Dynamics of axisymmetric colloidal particles in the presence of a wall*, financed within the *Preludium* programme by the National Center of Science in Poland under the grant agreement no. 2012/07/N/ST3/03120.

To the memory of Professor Konrad Bajer,
for his friendship, advice and encouragement.

Part of the results contained in the Thesis has been published in three research articles:

1. M. Lisicki, B. Cichocki, J. K. G. Dhont, P. R. Lang,
   One-particle correlation function in evanescent wave dynamic light scattering,
   J. Chem. Phys. **136**, 204704 (2012).

2. S.A. Rogers, M. Lisicki, B. Cichocki, J.K.G. Dhont, P.R. Lang,
   Rotational diffusion of spherical colloids close to a wall,
   Phys. Rev. Lett. **109**, 098305 (2012).

3. M. Lisicki, B. Cichocki, S.A. Rogers, J.K.G. Dhont, P.R. Lang,
   Translational and rotational near-wall diffusion of spherical colloids studied by evanescent wave scattering,
   Soft Matter **10**, 4312 (2014).

Acknowledgements

In 1676, Sir Isaac Newton wrote in a letter to Robert Hooke:

If I have seen further it is by standing on the shoulders of giants.

No progress would be possible without great people behind. I found myself in a fortunate position, surrounded by many wonderful teachers, friends, colleagues, and collaborators, who have fostered my interests and personal development. Only thanks to these relations, I could have completed this work. Below, I would like to mention some of the Giants whom I have encountered on my way.

First and foremost, I would like to express my sincere thanks to my advisor, Professor Bogdan Cichocki, for his support, advice, patience and vigilant assistance during the preparation of this work. I am grateful for the fruitful collaboration, for sharing his deep knowledge and understanding of physics, and also his artistic and musical interests.

The results presented in the Thesis have been obtained thanks to partnership with the group of Prof. Jan K.G. Dhont and Dr. Peter Lang at Forschungszentrum Jülich, whom I sincerely wish to thank for their kind support and collaboration. The opportunity to work as a theorist in an experimentally-oriented group has been exciting, and has contributed greatly to my personal development as a scientist. During my short- and long-term visits to Jülich, I have always encountered an inspiring scientific atmosphere, and a friendly environment, for which I am grateful to all the members of Insitute of Complex Systems ICS-3 at FZJ. I would like to acknowledge particularly Prof. Gerhard Nägele and Dr. Rafael Roa, with whom I discussed, worked, or relaxed during my stays in Germany.

I am indebted to Prof. Eligiusz Wajnryb for his assistance and support. The numerical results of the Thesis would not have been obtained without his numerical routines for precise calculation of hydrodynamic interactions. I benefited greatly from our stimulating discussions and his helpful comments.

I acknowledge friendship and support I received from Prof. Piotr Szymczak. Since our paths crossed at the beginning of my studies in physics 9 years ago, I have benefited largely from his great attitude towards students and colleagues, and his vast scientific expertise.

I bow down to my Parents who supported all my choices and emboldened my curiosity in science. My interests have bloomed in my teenage years thanks to Prof. Stanisław Lipiński, who was a great educator and teacher at XIV Stanisław Staszic High School in Warsaw. Under his supervision, I became involved in the wonderful community gathered around the International Young Physicists Tournament which had had a tremendous influence on my later career choices.

I wish to warmly thank all my Friends, who were always there for me and who brought much colour, passion, and cheerfulness into my everyday life.

Lastly, I owe my utmost gratitude to Marta for her loving support and constant encouragement.

Contents

1 Introduction

The dynamics of microparticles dispersed in a viscous liquid has been an important research topic for more than a century now, and is still attracting the attention of the scientific community. The reason for that is the abundance of technological, industrial, and biological processes, in which such objects are present. Hence, understanding the behaviour of those mesoscopic systems and their macroscopic characteristics is vital for the description of a number of phenomena at the interface between physics, chemistry, and biology.

The so-called *soft matter* systems [1], or *complex fluids*, due to their internal mesoscopic structure, constitute a vast subfield of condensed matter physics, and encompass a wide group of systems, including polymers, colloids, surfactants, liquid crystals, macromolecules, cellular membranes, and even living microscopic organisms, such as bacteria or viruses. In recent decades, the field has witnessed a growing interest, bursting due to potential applications in developing new functional materials, strategies for drug delivery, optimisation of technologies involving flow of mixtures in industrial applications, etc. [2]. Along with rapid development of the applications of soft matter research, extensive progress has been made in theoretical description of such systems. With the advent of experimental techniques allowing to study and manipulate soft matter, the field is still in development with an increasing number of researchers involved.

The history of colloidal physics started in 1827, when Robert Brown, a renowned British botanist, described an irregular, erratic dance of small grains of pollen immersed in a fluid, and seen under a microscope. It took almost a century of researchers' efforts to understand that this motion, later called Brownian, is caused by the thermal fluctuations of the fluid particles and their collisions with suspended bodies, and is the underlying mesoscopic mechanism for diffusion. Starting with the pioneering works of Smoluchowski [3] and Einstein [4, 5], statistical physics of colloidal matter has emerged to be an important subject of research in the 20th century, with a number of notable achievements [6] and numerous practical applications.

Colloidal suspensions are typically composed of small particles, of size varying between 10 and 1000 nm, dispersed in a liquid solvent. Hence, they are much larger than the solvent molecules but small enough for the Brownian motion to play a significant role in their dynamics [7, 8]. Colloidal particles are thus always in motion, setting up a flow in the suspending fluid. The effect of disturbances created by any particle on the motion of the others, called hydrodynamic interactions, may greatly alter the dynamic properties of a suspension, and is an inherent feature of any colloidal system [9]. These dynamic, long-ranged, and many-body interactions have been shown to alter the values of diffusion coefficients in suspensions [10]; influence the characteristics of coil-stretch transition in polymeric solutions [11]; cause polymeric migration in

microfluidic channels [12]; modify the kinetics of phase separation in mixtures [13] and protein adsorption on surfaces [14]; and determine the dynamics of biological macromolecules, such as proteins [15] or DNA [16]. It is important to emphasize that on top of hydrodynamic interactions, colloids are also subject to direct interactions, e.g. electrostatic forces [17], and external fields. Understanding these effects poses a challenge both to theorists, requiring a description of a system with complex interactions, and to experimentalists, since the observations often involve sophisticated and indirect measurements.

The fluid flow on such small length and time scales may be accurately described by the linear Stokes equations [9], and is viscosity-dominated, with no appreciable inertial effects. In this limit, the frictional force $\mathbf{F}$ acting on a spherical particle of radius a moving through the fluid of viscosity η with the velocity $\mathbf{V}$ is given by a linear relation

$$\mathbf{F} = -\zeta_0 \mathbf{V}, \tag{1.1}$$

with the friction coefficient $\zeta_0 = 6\pi\eta a$, as first found by Stokes [18]. Linearity of the Stokes equations will be exploited in the further course of this work. In a reverse situation of a particle moving under the action of force, one introduces the mobility coeffcient $\mu_0 = 1/\zeta_0$. In general, these quantities have a tensorial character. Moreover, in systems involving many interacting particles, the mobility of the particles depends on the configuration of the whole system, which is a manifestation of the long range of hydrodynamic interactions.

In real colloidal systems, Brownian motion often occurs in geometric confinement, or in the presence of a system boundary. Since the boundary reflects the flow incident upon it, interfacial effects may have a significant effect on processes occurring close to walls. Examples are coating processes or any process where particles are deposited onto surfaces [19], membrane filtering, or any other process where dispersed particles migrate in porous media [20]. Boundaries and interfaces also play a vital role in biological processes, like protein adsorption [21], biofilm formation [22], collective motion of sperm cells near planar surfaces [23, 24], sedimentation processes [25], and re-suspension of sediments by shear flow [26–28]. The effects of confinement for macromolecular solutions are most pronounced in the small-scale channel flows, which are omnipresent in micro- [29], nano- [30] and optofluidics [31]. An illustrative example may be given in the rapidly growing "lab-on-a-chip" applications, in which a single colloid might be used as a micropump [32]; confined geometry plays a key role also in e.g. capillary electrophoresis [33] and sorting of white blood cells [34]. The variety and number of presented examples may serve as a strong motivation to investigate the effects of confinement on soft matter dynamics.

In this work, we restrict to the case of an infinite, planar no-slip boundary, and investigate its effect on the hydrodynamic mobility tensor $\boldsymbol{\mu}$ of an anisotropic particle immersed in a viscous liquid. By virtue of the fluctuation–dissipation theorem [35], the mobility tensor $\boldsymbol{\mu}$ is related to the diffusion tensor $\mathbf{D}$ via

$$\mathbf{D} = k_B T \boldsymbol{\mu}, \tag{1.2}$$

where k_B is the Boltzmann constant, and T represents the temperature. For a single spherical particle, this relation becomes $D_0 = k_B T \mu_0 = k_B T/\zeta_0$, as found by Einstein and Smoluchowski. We note here that both diffusivity and mobility are tensorial quantities due to the anisotropy of the wall-bounded fluid, and of the particle itself. Hence, by studying the diffusive properties of a confined suspension, one may infer information about the effect of hydrodynamic interactions on its dynamics, and vice versa.

As a model system, spherical particles in the vicinity of a no-slip hard wall have been considered by many researchers. In such a situation, diffusivity (and mobility) of the particles becomes anisotropic solely due to hydrodynamic effects of the wall, with different coefficients in the direction parallel to the wall, $D_{\parallel}$, and normal to it, $D_{\perp}$. This problem has been studied theoretically for an isolated sphere already by Lorentz [36] and Faxén [37]. Analytic solutions have been found by Brenner *et al.* [38–41], and Dean & O'Neill [42, 43] in the form of infinite series. Finally, efficient multipole techniques by Cichocki and Jones have led to accurate representation of the sphere's mobility close to a wall [44–46]. The available theoretical predictions have then been verified in a number of experiments, employing various techniqes. Applying fluorescence microscopy combined with three dimensional particle tracking, Banerjee and Kihm *et al.* showed that Brenner's predictions for particle mobility parallel to a planar wall are valid for colloids [47, 48]. Using total internal reflection microscopy [49, 50] combined with an optical trapping, Walz and Suresh studied sedimentation of spherical polystyrene latex particles and found very good agreement with theory [51]. Performing a video microscopy experiment with the use of optical tweezers, Lin *et al.* [52] showed that particles of radius 500-1000 nm follow theoretical predictions in both directions, provided they are density-matched with the solvent and electrostatic interactions are sufficiently screened. More recently, Joly *et al.* [53] applied fluorescence correlation spectroscopy to study the influence of surface wetting properties on the dynamics of colloidal particles confined between two flat interfaces, and found excellent agreement of the experimental data with hydrodynamic predictions for wettable surfaces. For larger particles, theoretical predictions have also been verified using optical microscopy of micrometric spheres [54]. In a joint numerical-experimental work, Lele *et al.* [55] traced the trajectories of many spherical particles close to a wall and concluded that to understand their collective behaviour, it is not sufficient to superpose pair interactions. Other experimental studies involving spherical particles of different sizes employed nano-PIV techniques [56, 57], dynamic light scattering (DLS) in the presence of two walls [58], low coherence DLS [59], and resonance enhanced DLS [60–62].

As a first step towards the understanding of complex processes mentioned above, relevant experimental techniques need to be developed, along with a proper theoretical description. In this work, we focus our attention on evanescent wave dynamic light scattering (EWDLS) [63–65] as a method to study the near-wall dynamics of colloidal suspension. For the investigation of Brownian particles close to a boundary, a technique is required which probes the particles' mobility in a distance range smaller than several sphere diameters from the wall. Only with the advent of EWDLS and of powerful modern microscopy techniques this has become possible. In the experiments, only the region of the sample close to the boundary is illuminated, as the electric field strength of an evanescent wave decays with distance z away from the wall as $\exp(-\kappa z/2)$. The characteristic length scale $2/\kappa$, called the penetration depth, is typically of the order of several hundreds of nanometers. Using this feature, one can infer information on the effects of hydrodynamic interactions with the surface on the dynamics of suspended colloids. By changing the scattering vector $\mathbf{q}$, the system is probed on different length scales. In the measurements, the scattered electric field time auto-correlation function (EACF) is recorded. Since its dynamics derives from an interplay between the hydrodynamic effects of near-wall Brownian motion, and the non-uniform illumination profile of the evanescent wave, interpretation of the experimental data requires a thorough analysis.

Starting with the pioneering work by Lan and Ostrowsky [66], EWDLS has been employed in a number of systems to investigate the near-surface dynamics of soft matter. Translational

diffusion of spherical colloids has been studied in dilute solutions [67–71] and in suspensions with volume fractions up to 45 percent, both theoretically [72,73], and experimentally [74,75]. With a set-up which allows independent variation of the components of the scattering vector $q_{\parallel}$, $q_{\perp}$, parallel and perpendicular to the surface, respectively, it was possible to distinguish between the diffusivity of colloidal spheres in these directions experimentally [63,64]. Notably, evanescent waves have also been used for near-wall nanovelocimetry [76,77]. EWDLS has also been employed to study the dynamics of stiff polymers adsorbed to the interface [78], as well as the collective motion of end-grafted polymer brushes [79,80], near-wall diffusion of a spherical particle in a suspension of rod-like depletants [81], and colloidal dumbbells [62]. It is worth stressing that in all the works on systems of non-spherical particles, or in complex environments, very simple models developed for spheres have been used to interpret the data, since so far there were no other theoretical results available for the decay of the measured correlation functions. Our research aims to fill this gap.

In the aforementioned works, only the effect of translational diffusion has been discussed. However, rotational diffusion also plays a crucial role in a number of physical, chemical, and biological processes occurring in a variety of systems. Notable examples include microrheology, in which frequency-dependent viscoelastic shear moduli can be investigated by measuring rotational diffusion of a tracer sphere [82]; random reorientation of biological macromolecules in membranes (like proteins in human erythrocyte membrane [83], or rhodopsin chromophores [84]); rotational-diffusion controlled chemical reactivity [34,85,86]; and gaseous combustion models, where rotational diffusion is of importance for the interpretation of coherent anti-Stokes Raman spectroscopy data [87]. Much attention has been devoted over the last decade to rotational diffusion in bulk systems, particularly in the context of macromolecules. Similar systems in geometrical confinement are, however, much less understood, and are becoming a very active field of research.

In our recent contributions [88–90], which constitute a part of this Thesis, we have presented a study of applicability of EWDLS to trace translational, as well as rotational diffusion in dilute suspensions of spheres, in which single-particle properties completely characterise the system. By means of cumulant expansion based on the Smoluchowski equation, we have developed exact expressions for the initial decay rate of the electric field time autocorrelation function, which is related to the experimentally determined intensity time autocorrelation function by a generalized Siegert relation [64]. In the case of purely translational motion [88], terms up to quadratic order in time have been shown to describe the decay of the correlation function up to moderate times. Comparison with experiments and Brownian Dynamics simulations resulted in fair agreement of the data. Using optically anisotropic spheres [89], we were able to record orientation-dependent signal in the correlation function and extract from the experiments the rotational diffusion coefficients which proved to be consistent with theoretical calculations [46]. Rotational diffusion of spherical particles measured by light scattering has been extensively studied in bulk, both theoretically [91] and experimentally [92–94], using systems of optically anisotropic spherical Brownian particles. It seems, however, that apart from theoretical and numerical calculations for rotational diffusion of spheres confined to diffuse near a wall [39–43,46], or in a parallel-wall channel [95], there has been no experimental investigation of rotational diffusion in such confined systems, and our research aims to fill this gap using a recently developed experimental technique followed by a thorough analysis of its theoretical basis.

The purpose of this Thesis is to provide a suitable theoretical framework for the interpretation of EWDLS measurements involving anisotropic particles. The anisotropy may stem either from

the internal structure and optical properties of the particles, or from their anisotropic shape. The main results presented in this dissertation may be listed as follows

(i) For EWDLS experiments involving dilute suspensions of spherical particles with hard-core interactions, we have developed exact expressions for the first and second cumulant of the scattered field correlation function (EACF). Theoretical findings, supported with Brownian dynamics simulations, have been successfully compared to experimental results, and published in a research article [88]. As we have demonstrated, the penetration-depth averaged diffusion coefficients in the directions parallel and normal to the wall may be theoretically pre-calculated for a given value of κ using the accurate representation of the near-wall mobility of a sphere. Moreover, the approximation by the first two cumulants remains accurate even for intermediate stages of the EACF decay. Thus, the paper outlines practical approximations for experimentalists, allowing to interpret the results of measurements without the need to perform costly simulations. Our findings are summarized in Chapter 7.

(ii) Using optically anisotropic spherical particles in EWDLS experiments, we have demonstrated that it is possible to extract from the measurements the average rotational diffusion coefficients. The use of optical anisotropy allows to study the particle reorientation with the hydrodynamic properties remaining unchanged with respect to the case (i). With the help of two scattering geometries differing in the polarization direction of the scattered light (VH and VV geometry), we were able to separate out the rotational contribution from the first cumulant and discern between the rotational motion about the axes parallel and normal to the wall. For the interpretation of experimental EACFs, a suitable theoretical framework has been developed, basing on the generalised Smoluchowski equation in the configurational (i.e. positional and orientational) space of the particles. The experimental results have been shown to follow the theoretical predictions in two research articles [89, 90], joing the theoretical analysis with the experimental verification of the predictions.

(iii) As the next step towards the interpretation of EWDLS correlation functions, we have developed a systematic theoretical scheme for the calculation of the first cumulant in a dilute suspension of axially symmetric particles. The particles may possess non-uniform optical properties, similarly to the case of spheres in (ii). However, it is superposed with their shape anisotropy which manifests in their hydrodynamic properties becoming tensorial quantities even when considering bulk dynamics. In this work, we derive exact expressions for the first cumulant in EWDLS by axisymmetric particles in the general case of an arbitrary form and optical anisotropy, and study them in detail in Chapter 8 for model rod-like and disc-like particles. We again restrict to the dilute, single-particle case. To this end, we discuss separately the effects of hydrodynamic wall-particle interactions, and scattering effects due to non-uniform illumination of the sample by evanescent waves, and also due to the non-spherical shape of the scatterer. For the description of the effects of hydrodynamic interactions with the wall, we have developed analytical corrections to the bulk mobility tensor of an axisymmetric particle due to the presence of a nearby wall, described also below in (iv), and also employed a precise numerical multipole expansion scheme, HYDROMULTIPOLE [96] for calculations of mobility in the case when the particle is close to the wall. In the course of the work, we point out the regimes in which simplifying approximations for the mobility can be made. The scattering properties of the particles, encoded in the so-called evanescent form factor, are explored and discussed in terms of

the difference to bulk scattering which is measured in standard DLS experiments. We show the relevance of the evanescent penetration depth, κ, with relation to the scattering vector q, for the effects of scattering from a colloidal rod and disc. Our predictions show that in the experimentally accessible range of penetration depths, and scattering vectors, effective approximations may be proposed for the first cumulant. The results of our study are now being prepared for publication.

(iv) A separate question, emerging in the context of near-wall dynamics studied through scattering experiments, concerns the effect of hydrodynamic interactions of an anisotropic object with a wall. In the regime when the particle is moderately distant from the wall, we have developed analytical formulae for the correction, $\Delta\boldsymbol{\mu}_w$, to the bulk mobility tensor $\boldsymbol{\mu}$ of an axially symmetric particle. This allows us to construct an approximate mobility matrix in the presence of the wall as $\boldsymbol{\mu}_w = \boldsymbol{\mu} + \Delta\boldsymbol{\mu}_w$, and study its dependence on the wall-particle distance, and on the orientation of the particle. Previous works involved only numerical considerations [97–99], or slender-body analysis in a number of simple configurations [100]. Here, we provide a full analysis of the dependence of the translational and rotational components of the wall-corrected mobility tensor on the wall-particle distance H in the far-field regime. Interestingly, different components of the correction scale with different powers of the inverse distance, e.g. $1/H$ for translational, and $1/H^3$ for rotational mobility coefficients. Moreover, our analysis allows to find the dependence of the wall-corrected mobility tensor on the orientation of the particle. Comparing with precise numerical results, we assess the range of validity of this approximation.

1.1 Outline of the Thesis

The Thesis is composed of 9 chapters devoted to various aspects of the considered problem. We begin with a basic introduction into light scattering experiments in soft matter physics in Chapter 2. We present a heuristic view of typical bulk scattering experiments, introducing the idea behind DLS measurements and the correlation functions measured in experiments. In the following Chapter 3, we discuss the EWDLS technique, and point out the differences to bulk scattering experiments. This is followed by a description of the details of the experimental set-up, and characterisation of the correlation functions measured in EWDLS experiments.

In order to calculate the experimental correlation functions theoretically, one needs a description of mesoscopic colloidal dynamics. To this end, we present a general introduction into the statistical physics of colloidal suspensions in Chapter 4. We characterise there the relevant time scales for colloidal suspensions, and introduce the probabilistic description. Its central point is the generalised Smoluchowski equation which governs the evolution of the probability densities in diffusive dynamics. Since important quantities in soft matter systems are often encoded in experimentally accessible time correlation functions [7], we express them in the Smoluchowski equation formalism. We also introduce the cumulant expansion as a method of analysis of the short-time dynamics of such correlation functions.

The Smoluchowski equation describes the evolution of a system of colloids affecting each other via the solvent-mediated hydrodynamic interactions, which play a crucial role in soft matter dynamics. Chapter 5 is devoted to these interactions, with a particular focus on wall-particle interactions present in a confined system. After introducing the Stokes governing equations

for the fluid flow, we consider the dynamics of a single particle in a general ambient flow. This leads to the notion of hydrodynamic friction and mobility tensors, and a discussion of their properties. The description is then extended to the case of many spherical colloids immersed in, and interacting through, the viscous solvent. We further show the way to obtain the hydrodynamic mobility tensor of a complex-shaped particle represented by its bead model, i.e. a conglomerate of spheres staying in a fixed relative configuration, from the many-body mobility tensor for many spheres. The technical details have been shifted to Appendix A. The calculation of many-body quantities for this purpose, both in a bulk fluid, and in the presence of a wall, may be performed using the multipole method, which we present and discuss in brief. The multipole method constitutes a powerful tool which will be used in the course of the work to explore hydrodynamic interactions of anisotropic particles. Chapter 5 is concluded by two sections referring explicitly to axisymmetric particles, and devoted to their bulk, and near-wall hydrodynamics, respectively. The results listed in point (iv) of the preceding Section are contained in Sec. 5.5, and in Appendix B.

Having introduced the basic quantities of interest, and a relevant theoretical tools for the analysis of the colloidal dynamics, we explore the initial decay of the electric field autocorrelation function in bulk DLS measurements in Chapter 6. Therein, we provide a detailed description of bulk predictions for axisymmetric rod-like and disc-like particles, which will later serve as reference for the near-wall results.

The main results of the Thesis, related to EWDLS technique, are contained in Chapters 7 and 8. Chapter 7 refers to the near-wall anisotropic diffusion, translational and rotational, of spherical particles, both uniform, and optically anisotropic, viewed in EWDLS experiments. The theoretical findings for the decay of the EACF are exposed there along with their detailed experimental verification. An analysis of the first cumulant in the more complex case of axisymmetric particles is contained in Chapter 8, where we look upon the combined effect of evanescent illumination and hydrodynamic interactions with the boundary on the EWDLS correlation functions. Theoretical developments are supported by numerical procedures which allow for the calculation of the first cumulant for arbitrary experimental conditions. Our results allow for approximations which will facilitate the interpretation of future experiments. Chapter 9 concludes the Thesis and lists in more detail the achieved results and possible future developments.

2 Bulk light scattering experiments

Light scattering experiments are an essential tool to study the dynamics of nanometer-sized particles in dispersions [7, 8]. Although many variations of scattering techniques are available to study soft matter, the basis for all the scattering experiments is essentially the same. Using neutron or X-ray scattering, microscopic details of the particles are probed, such as the crystalline structure. For the dynamics on the mesoscopic scale, described in this work, visible laser light scattering may be employed. In this Chapter, we briefly present the idea behind light scattering techniques, introducing the relevant basic quantities measured in experiments.

Within the molecular theory of scattering a light wave, incident on a suspension of particles, excites the illuminated molecules, inducing creation of dipole moments, which in turn radiate electromagnetic waves recognised as the scattered field. Thermal molecular motion gives rise to fluctuations in the total scattered field due to the motion of scatterers, leading to a random signal recorded by the detector. Encoded in this signal is important structural and dynamical information about the positions and orientations of the particles.

After presenting general principles of light scattering experiments, we discuss the influence of the particle shape and optical properties on the experimentally measured time correlation functions.

The underlying physical principles and more detailed experimental considerations may be found in the books by Dhont [10], Berne & Pecora [101], and van de Hulst [102].

2.1 Theoretical description of scattering experiments

In this Section, no attempt of a rigorous derivation of the scattered electric field dependence on the characteristics of the system has been made. Instead, we prefer to present a heuristic reasoning leading to the understanding of the quantities measured in scattering experiments. For an extensive discussion supported by explicit derivations of the scattered electric field starting form Maxwell equations, see e.g. the excellent textbook by Dhont [10].

2.1.1 Structure of the scattered electric field

In an idealised light-scattering experiment, the incident light is a plane monochromatic wave

$$\mathbf{E}_i(\mathbf{r}, t) = \hat{\mathbf{n}}_0 E_0 \exp[i(\mathbf{k}_i \cdot \mathbf{r} - \omega_0 t)], \tag{2.1}$$

of wavelength λ, frequency ω_0, polarisation $\hat{\mathbf{n}}_0$, and amplitude E_0, propagating in the direction of the wave vector $\mathbf{k}_i$. The incident light excites electric dipoles within the sample, which in turn emit electromagnetic radiation in all directions. The detector collects light scattered in the direction given by the wave vector of the scattered light $\mathbf{k}_s$.

We limit ourselves to elastic light scattering, in which the interaction of the electric field with the material of the particles does not affect the wavelength of light. Therefore the magnitudes of the wave vectors of the incident and the scattered light are equal

$$|\mathbf{k}_i| = |\mathbf{k}_s| = 2\pi/\lambda. \tag{2.2}$$

Typical sizes and optical properties of colloidal particles permit the scattering from such objects to be described in terms of Rayleigh–Gans–Debye theory [10, 101]. Within this framework, the Brownian particles are thought to be composed of a large number of point-like scatterers. The scattered electric field may be then regarded as a sum of contributions from all the scattering centres located within the colloids. For such a treatment, however, three more assumptions need to be made. Firstly, since the incident light might traverse through a portion of colloidal material before it is scattered, we assume that the additional phase difference it might gain with respect to the light traversing through the fluid, is very small (say < 0.1). Denoting the refractive indices of the surrounding fluid by n_f, and the particle material by n_p, considering spherical colloids of radius a, we might express this condition as

$$2\pi|n_p - n_f|\frac{a}{\lambda} < 0.1. \tag{2.3}$$

Secondly, since we assume the direction of the incident field to be the same everywhere within the sample, the refraction of light at the fluid-particle boundary should not be significant. This is the case when the difference of refraction coefficients is small, say

$$|n_p - n_f| < 0.1\ . \tag{2.4}$$

Lastly, we assume that the incident light is not significantly attenuated, neither by scattering nor by absorption. This implies that only a small fraction of the incident light is scattered. Bearing this in mind, we may restrict our considerations only to single scattering events, disregarding higher-order multiple scattering effects. The latter is often referred to as the first-order Born approximation [10].

It should be emphasized that the set of approximations outlined above may be stated in a more rigorous way starting from the Maxwell equations for a fluid containing suspended particles. This is, however, beyond the scope of this work, and we shall outline here only the underlying physical principles.

Under the assumptions mentioned, we may now present a heuristic derivation of the form of the scattered electric field. In Fig. 2.1 we depicted a collection of scattering centres, many of which are incorporated in a single Brownian particle. The phase difference $\Delta\Phi$ of the electric field

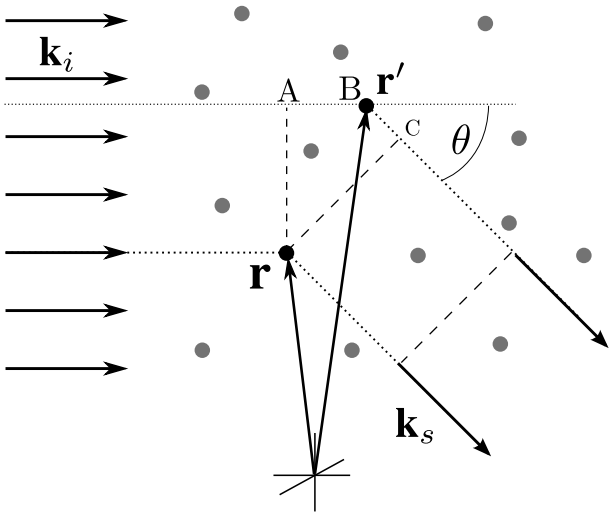

Figure 2.1: Light incident on a collection of independent scatterers. The wave vector of the incident wave is $\mathbf{k}_i$, while the detector is placed at an angle θ to the incident beam, in the direction of the scattered light wave vector $\mathbf{k}_s$. Two scattering centres are indicated for the calculation of the phase difference between the light scattered by them.

scattered by two such centres, located at $\mathbf{r}$ and $\mathbf{r}'$, may be expressed, using simple geometrical relations involving the difference of optical paths, as

$$\Delta\Phi = \mathbf{q} \cdot (\mathbf{r} - \mathbf{r}'), \tag{2.5}$$

where $\mathbf{q} = \mathbf{k}_s - \mathbf{k}_i$ is the scattering vector. Its magnitude may be related to the scattering angle, as

$$q = |\mathbf{q}| = \frac{4\pi}{\lambda} \sin\frac{\theta}{2}, \tag{2.6}$$

with θ being the angle between the incident and the scattered beam. As can be seen from Eq. (2.5), one may assign a phase $\mathbf{q} \cdot \mathbf{r}$ to a volume element at the position $\mathbf{r}$. The scattered electric field will therefore be a sum of exponential terms $\sim f(\mathbf{r}) \exp(i\mathbf{q} \cdot \mathbf{r})$ from all the scattering centres, weighted by the scattering strength of volume elements, $f(\mathbf{r})$. The latter quantity (per unit volume) is proportional to the fraction of light that is scattered at a given point, and is related to the dielectric properties of the particle material at $\mathbf{r}$. We may now express the total electric field scattered from an ensemble of N colloidal particles as an integral over the volume of the particles,

$$\mathbf{E}_s = \sum_{j=1}^{N} \exp(i\mathbf{q} \cdot \mathbf{r}_j) \int_{V_j} \mathrm{d}\mathbf{r}' f(\mathbf{r}') \exp(i\mathbf{q} \cdot \mathbf{r}') \hat{\mathbf{n}}_0 E_0, \tag{2.7}$$

in which we made the distinction between different particles located at $\mathbf{r}_j$ with $j = 1, \ldots, N$. The exponential prefactor describes the interference of light scattered from different particles, while the integrals taken over the volume of the particles describe interference effects from scatterers within single particles. The following shorthand notation will be adopted further on:

$$\mathbf{E}_s = \sum_{j=1}^{N} \exp(i\mathbf{q} \cdot \mathbf{r}_j) \mathcal{B}_j(\hat{\mathbf{u}}; \mathbf{q}) \hat{\mathbf{n}}_0 E_0, \tag{2.8}$$

where $\mathcal{B}_j(\hat{\mathbf{u}}; \mathbf{q}) = \int_{V_j} \mathrm{d}\mathbf{r}' f(\mathbf{r}') \exp(i\mathbf{q} \cdot \mathbf{r}')$ is called the scattering amplitude. In general this amplitude might be a tensorial quantity in case where the dielectric (optical) properties of the

particle material would be anisotropic. It also depends on the orientation $\hat{\mathbf{u}}$ of a non-spherical particle. This fact will be discussed in the next subsection.

The form of the scattered electric field is of importance in light-scattering experiments, since the measured scattered intensity is proportional to

$$I(\mathbf{q}, t) \sim |\mathbf{E}_s \cdot \hat{\mathbf{n}}_s|^2, \tag{2.9}$$

where the unit vector $\hat{\mathbf{n}}_s$ denotes the polarization direction of the scattered light, which is usually imposed by placing polarization filter in front of the detector. It must be stressed that these results hold on the diffusive time scale of colloidal motion which we will discuss thoroughly later.

For illustration, let us consider a simple case of scattering from an ensemble of spherical particles. The instantaneous scattered intensity is proportional to

$$I(\mathbf{q}, t) \sim \sum_{j,k=1}^{N} \exp(i\mathbf{q} \cdot (\mathbf{r}_j(t) - \mathbf{r}_k(t)) = |\hat{\rho}(\mathbf{q}, t)|^2 \tag{2.10}$$

with $\hat{\rho}(\mathbf{q}, t)$ being a component of the Fourier transform of the local microscopic density $\rho(\mathbf{r}, t) = \sum_{j=1}^{N} \delta(\mathbf{r} - \mathbf{r}_j(t))$. The scattering vector $\mathbf{q}$ characterizes the geometrical alignment of the experimental setup and may be changed to probe the density fluctuations on different length scales.

2.1.2 Effects of form and material

The internal optical properties of the scattering particles affect the measured scattered electric field by modifying the scattering amplitude in Eq. (2.8). The strength of the electric field scattered by a small particle is proportional to its induced dipole moments, magnitude of which is quantified in terms of the incident field by the particle polarisability [102]. The latter is in general a tensorial quantity, and follows from the solution of an electrostatic problem of finding the polarization of a particle of a given shape and dielectric constant subjected to an external electric field. Assume the particles to have a tensorial dielectric polarisability $\boldsymbol{\alpha}$, or, equivalently, an anisotropic dielectric constant. Then, a more thorough analysis of the scattered field based on Maxwell equations [10, 101, 102] yields the following form for the scattering amplitude of the particle j

$$\mathcal{B}_j(\hat{\mathbf{u}}; \mathbf{q}) = \int_{V_j} \mathrm{d}\mathbf{r}' \boldsymbol{\alpha}(\mathbf{r}') \exp(i\mathbf{q} \cdot \mathbf{r}'), \tag{2.11}$$

which now depends on the orientation of the particle via the tensorial scattering strength. A case of particular interest in this work is the optical anisotropy of an axisymmetric particle. This anisotropy may stem either from an intrinsic birefringence of the material of the particle, or the so-called form birefringence related to the anisotropic molecular structure of the particle. As a result, the polarisability may be different in the directions of the incident field parallel and perpendicular to the symmetry axis of the particle. Let us denote the two respective polarizabilities by $\alpha_{\parallel}$ and $\epsilon_{\perp}$ and assume they are independent of the position within the particle. If the particle is aligned along the unit vector $\hat{\mathbf{u}}$, its polarisability tensor may be written as

$$\boldsymbol{\alpha} = \alpha \mathbf{1} + \Delta\alpha \left(\hat{\mathbf{u}}\hat{\mathbf{u}} - \frac{1}{3}\mathbf{1} \right), \tag{2.12}$$

with the average polarisability

$$\alpha = \frac{1}{3}\left(2\alpha_\perp + \alpha_\parallel\right), \tag{2.13}$$

and the polarisability anisotropy

$$\Delta\alpha = \alpha_\parallel - \alpha_\perp. \tag{2.14}$$

For a spherical particle, finding the homogeneous polarisability in an external field as a function of the dielectric constants of the particle and the environment is a standard textbook problem [103]. For an ellipsoid, the analytical solution is known [104] for a given aspect ratio. For more complex-shaped objects, the polarizabilities may be calculated either by solving an appropriate integral equation for the scalar potential on the particle surface [105, 106], or by a so-called coupled dipole model (CDM) [107] which allows to calculate polarizabilities of colloids represented as clusters of spherical beads [108–110].

Finally, we may write the scattered electric field signal from optically anisotropic particles measured in the detector as

$$E_S = \mathbf{E}_S \cdot \hat{\mathbf{n}}_s \propto \sum_{j=1}^{N} \exp(i\mathbf{q}\cdot\mathbf{r}_j)\hat{\mathbf{n}}_0 \cdot \boldsymbol{\mathcal{B}}(\hat{\mathbf{u}}_j;\mathbf{q}) \cdot \hat{\mathbf{n}}_s E_0 = \tag{2.15}$$

$$= \sum_{j=1}^{N} V_j \exp(i\mathbf{q}\cdot\mathbf{r}_j)\mathcal{E}(\hat{\mathbf{u}}_j)B(\hat{\mathbf{u}}_j;\mathbf{q})E_0, \tag{2.16}$$

where we introduced the oriented anisotropic dielectric tensor

$$\mathcal{E}_j(\hat{\mathbf{u}}_j) = \hat{\mathbf{n}}_0 \cdot \boldsymbol{\alpha}_j(\hat{\mathbf{u}}_j) \cdot \hat{\mathbf{n}}_s, \tag{2.17}$$

and the scattering amplitude originating purely from the shape of the particle and the effect of interference of light scattered by different parts of it

$$B(\hat{\mathbf{u}}_j;\mathbf{q}) = \frac{1}{V_j}\int_{V_j(\hat{\mathbf{u}}_j)} \mathrm{d}\mathbf{r}' \exp(i\mathbf{q}\cdot\mathbf{r}'), \tag{2.18}$$

normalised by the particle volume V_j for future convenience.

The two quantities, $\mathcal{E}$ and B, will be crucial for the interpretation of light scattering data and the discussion of further results. Remarkably, only the latter one depends on the scattering vector, i.e. the length scale on which the system is probed. In the limit of low scattering vector $\mathbf{q}\cdot\mathbf{r}' \ll 1$, all elements of the particle scatter in phase, and the scattering amplitude becomes equal to unity, and the only dependence of the scattered field enters via the dielectric anisotropy. For brevity, from now on we shall drop the dependence of the scattering amplitude on $\mathbf{q}$, writing simply $B(\hat{\mathbf{u}})$ instead. We introduce the shorthand notation

$$F_j(\hat{\mathbf{u}}_j) = \mathcal{E}(\hat{\mathbf{u}}_j)B(\hat{\mathbf{u}}_j), \tag{2.19}$$

for the combined orientation-dependent factor.

2.2 Static and dynamic light scattering

In essence, one may distinguish two types of light-scattering experiments – static and dynamic measurements. In static light scattering (SLS) experiments, the mean intensity

$$I(\mathbf{q}) = \langle I(\mathbf{q},t)\rangle, \tag{2.20}$$

is measured as a function of the scattering angle, thus probing the structural properties of the system. The ensemble averaging is performed over the positions and orientations of the Brownian particles. In practice, these averages are obtained as time averages, since the intensities are assumed to be collected over time intervals much larger than those needed for the particles to explore the whole configuration space, and ergodicity is assumed. SLS measurements are a fundamental tool for investigation and characterization of structural properties of colloidal suspensions, microgels, polymers, and a variety of soft matter systems.

The second type of experiments, which is more closely related to this work, is the dynamic light scattering (DLS). In such experiments, the actual time dependence of the scattered light intensity is collected in order to investigate the dynamics of the density fluctuations. In a typical DLS experiment, the detector is directly connected to a correlator, and the final measured quantity is the scattered intensity time auto-correlation function (IACF), defined as

$$g_2(\mathbf{q}, t) = \langle I(\mathbf{q}, 0) I(\mathbf{q}, t) \rangle, \tag{2.21}$$

where the average is taken over an equilibrium ensemble. Since the scattered intensity is connected to the scattered electric field by

$$I(\mathbf{q}, t) \sim E(\mathbf{q}, t) E^*(\mathbf{q}, t), \tag{2.22}$$

where for brevity we denoted $E(\mathbf{q}, t) = \mathbf{E}_s \cdot \hat{\mathbf{n}}_s$, it follows that Eq. (2.21) may be written as a four-point correlation function

$$\hat{g}_2(\mathbf{q}, t) \sim \left\langle E(\mathbf{q}, t) E^*(\mathbf{q}, t) E(\mathbf{q}, 0) E^*(\mathbf{q}, 0) \right\rangle. \tag{2.23}$$

Assuming the scattered electric field to be a Gaussian and stationary stochastic process, by virtue of the Wick's theorem we might express this relation by a sum of two-point field correlation functions [10]

$$\begin{aligned} g_2(\mathbf{q}, t) &= \left\langle E(\mathbf{q}, t) E^*(\mathbf{q}, t) \right\rangle \left\langle E(\mathbf{q}, 0) E^*(\mathbf{q}, 0) \right\rangle \\ &+ \left\langle E^*(\mathbf{q}, t) E^*(\mathbf{q}, 0) \right\rangle \left\langle E(\mathbf{q}, t) E(\mathbf{q}, 0) \right\rangle \\ &+ \left\langle E(\mathbf{q}, t) E^*(\mathbf{q}, 0) \right\rangle \left\langle E(\mathbf{q}, 0) E^*(\mathbf{q}, t) \right\rangle. \end{aligned} \tag{2.24}$$

The first term represents the square of the average intensity $I(\mathbf{q}) = \langle I(\mathbf{q}, t) \rangle$ and remains constant in a measurement. The second term can be shown to vanish for $\mathbf{q} \neq 0$ due to the translational invariance of the system. The remaining last term contains the scattered electric field auto-correlation function (EACF)

$$g_1(\mathbf{q}, t) = \langle E(\mathbf{q}, t) E^*(\mathbf{q}, 0) \rangle. \tag{2.25}$$

Normalising both g_1 and g_2 by their initial values according to

$$\hat{g}_2(\mathbf{q}, t) = \frac{g_2(\mathbf{q}, t)}{I^2(\mathbf{q})}, \qquad \hat{g}_1(\mathbf{q}, t) = \frac{g_1(\mathbf{q}, t)}{I(\mathbf{q})}, \tag{2.26}$$

we may rewrite Eq. (2.25) as

$$\hat{g}_2(\mathbf{q}, t) = 1 + |\hat{g}_1(\mathbf{q}, t)|^2, \tag{2.27}$$

which is referred to as the Siegert relation [65]. By definition, $\hat{g}_1(\mathbf{q}, 0) = 1$ and $\hat{g}_2(\mathbf{q}, 0) = 2$. In practical situations, however, it may happen that the scattered light consists of two contributions, light scattered from the sample particles and light scattered from surface roughness or other

small impurities. The latter may be regarded as a purely static contribution, which leads to a mixing of homodyne and heterodyne detection. In this case the more general relation holds [10]

$$\hat{g}_2(\mathbf{q},t) = 1 + 2C_1\mathrm{Re}(\hat{g}_1(\mathbf{q},t)) + C_2^2|\hat{g}_1(\mathbf{q},t)|^2, \tag{2.28}$$

where the coefficients $C_2 = 1 - \sqrt{1-A}$ and $C_1 = C_2 - C_2^2$ are derived from the initial value A of the measured intensity correlation function. It is important to stress that both relations (2.27) and (2.28) hold for a wall-bounded geometry as well, provided that the system remains translationally invariant in the direction parallel to the boundary.

The normalized EACF

$$\hat{g}_1(\mathbf{q},t) = \frac{\left\langle E_S(\mathbf{q},t)E_S^*(\mathbf{q},0)\right\rangle}{\langle|E_S(\mathbf{q},0)|^2\rangle}, \tag{2.29}$$

is often referred to as intermediate scattering function [7, 8] and plays the key role in any scattering experiment. In the course of this work, we shall explore its properties in the short-time regime. To this end, a useful quantity is the initial slope, or the first cumulant, Γ, of the EACF, which is experimentally determined as

$$\Gamma = -\lim_{t\to 0}\frac{\partial \ln g_1(\mathbf{q},t)}{\partial t} = -\lim_{t\to 0}\frac{\partial \hat{g}_1(\mathbf{q},t)}{\partial t}, \tag{2.30}$$

where the limit is taken in the coarse-grained colloidal time scale. The short-time approximation to the EACF reads then $\hat{g}_1(\mathbf{q},t) = \exp(-\Gamma t)$. We now remark, shifting the systematic discussion to Section 4, that for a dilute suspension of spherical particles, characterised by the diffusion coefficient D_0, the first cumulant reads $\Gamma = q^2D_0$. In some situations involving colloidal dynamics, an effective diffusion coefficient $D_{\mathrm{eff}}(\mathbf{q}) = \Gamma/q^2$ is therefore studied instead of the first cumulant [7]. However, since this quantity is intuitively related to translational dynamics, we rather use the more general Γ.

Scattering geometries For experimental reasons, it is often convenient to introduce a specific laboratory coordinate system to define the relative orientations of the directions of polarization of incident and scattered light, and the scattering vector. We shall describe below the two most commonly used configurations [101]. Assume that in the laboratory frame the incident light has the polarization direction $\hat{\mathbf{n}}_0 = \hat{\mathbf{e}}_x$. The polarization direction $\hat{\mathbf{n}}_s$ of the scattered light may be set by installing a polarizer at the detector. One may then align the two directions parallel to each other, $\hat{\mathbf{n}}_0 = \hat{\mathbf{n}}_s$, which is referred to as the VV geometry, or perpendicularly, $\hat{\mathbf{n}}_0 \perp \hat{\mathbf{n}}_s$, which is called VH geometry. Any other configuration may be regarded as having both increments. For optically isotropic particles, when the dielectric tensor in Eq. (2.17) is simply a unit tensor, the signal measured in experiments is proportional to $(\hat{\mathbf{n}}_0 \cdot \hat{\mathbf{n}}_s)^2$, and therefore the EACF can be recorded only in the VV geometry. In the case of optically isotropic particles, or when the optical anisotropy is very small, the scattering signal is also proportional to the product $(\hat{\mathbf{n}}_0 \cdot \hat{\mathbf{n}}_s)^2$, but the correlation function is independent of the optical properties of the particle, i.e. one may take $\boldsymbol{\alpha} = \alpha\mathbf{1}$. This case is referred to as depolarised scattering.

2.3 The single-particle field correlation function

In a bulk DLS experiments, the particles are assumed to be illuminated by the electric field described by Eq. (2.15). Therefore, the normalized scattered electric field correlation function

(2.29) may be written for a suspension of N particles as

$$\hat{g}_1(\mathbf{q},t) = \frac{1}{S(\mathbf{q})}\frac{1}{N}\sum_{j,k=1}^{N}\left\langle \exp\left[i\mathbf{q}\cdot(\mathbf{r}_k(0)-\mathbf{r}_j(t))\right] F_k^*(\hat{\mathbf{u}}_k(0))F_j(\hat{\mathbf{u}}_j(t))\right\rangle, \tag{2.31}$$

with the so-called static structure factor independent of time

$$S(\mathbf{q}) = \frac{1}{N}\sum_{j,k=1}^{N}\left\langle \exp\left[i\mathbf{q}\cdot(\mathbf{r}_k-\mathbf{r}_j)\right] F_k^*(\hat{\mathbf{u}}_k)F_j(\hat{\mathbf{u}}_j)\right\rangle, \tag{2.32}$$

where the orientation-dependent factor $F(\hat{\mathbf{u}})$ is introduced in Eq. (2.19). In a dilute suspension of identical particles, which will be in focus of this work, the system is fully characterized by single-particle properties, and we may neglect non-diagonal (with $j \neq k$) contributions to g_1. In this case, the correlation function simplifies to

$$\hat{g}_1(\mathbf{q},t) = \frac{1}{S(\mathbf{q})}\left\langle \exp\left[i\mathbf{q}\cdot(\mathbf{r}(0)-\mathbf{r}(t))\right] F^*(\hat{\mathbf{u}}(0))F(\hat{\mathbf{u}}(t))\right\rangle, \tag{2.33}$$

with the self-structure factor $S(\mathbf{q}) = \left\langle |F(\hat{\mathbf{u}})|^2\right\rangle$. For a system of optically isotropic particles, the self part of the static structure factor is simply equal to

$$S(\mathbf{q}) = \left\langle B(\mathbf{q})\right\rangle, \tag{2.34}$$

and called the form factor. In the limit $\mathbf{q} \to 0$, we have $S(\mathbf{q}) \to 1$.

In order to explore the behaviour of the measured correlation function $\hat{g}_1(t)$, we now need information on the dynamics of the particles to perform the average in Eq. (2.33), which will be given in Chapter 4. Before that, however, we proceed to the description of EWDLS experiments and the differences brought to the experiments by the presence of an evanescent illumination profile.

3 Evanescent wave light scattering

In this Chapter, we describe the experimental technique which is in focus of this work, and allows for an experimental investigation of the near-wall dynamics of anisotropic colloidal particles. Below, we discuss the differences between standard DLS introduced in the preceding Section and scattering of evanescent waves. We also provide a description of the the experimentally relevant quantities.

3.1 Evanescent wave dynamic light scattering (EWDLS)

In order to probe near-wall dynamics of submicron-sized particles, evanescent wave dynamic light scattering (EWDLS) has been developed in the 1980s, starting with the pioneering works of Lan *et al.* [66]. Since then, EWDLS has been tremendously developed, and employed to investigate the near-wall effects in a variety of systems, as discussed in Chapter 1.

A typical EWDLS setup is presented in Fig. 3.1. The sample cell is placed on top of a lens. The laser light is incident on the glass-fluid boundary at an angle greater than the total internal reflection angle. In consequence, an evanescent wave enters the sample, and its electric field strength decays with distance z away from the wall as $\exp(-\kappa z/2)$. Thus, in EWDLS experiments only the region of the sample close to the boundary is illuminated. Using this feature, one can infer information on the effects of hydrodynamic interactions with the surface on the dynamics of suspended colloids. The characteristic length scale $2/\kappa$, called the penetration depth, is given by

$$\frac{2}{\kappa} = \lambda_0 \Big/ 2\pi\sqrt{(n_1 \sin\alpha_i)^2 - n_2^2}, \tag{3.1}$$

with n_1, n_2 being the refractive indices of glass and solvent, respectively. By varying the incident angle α_i, the penetration depth can be tuned, typically in the range of 100 to 800 nm. The scattering vector $\mathbf{q} = \mathbf{k}_s - \mathbf{k}_i$ is the difference between the evanescent and scattered light wave vectors, $\mathbf{k}_i$ and $\mathbf{k}_s$. For the needs of further analysis, we decompose it into the components $q_\parallel$, $q_\perp$, parallel and perpendicular to the wall, respectively. In the EWDLS setup constructed in Forschungszentrum Jülich (Germany) [63,64], these components can be independently changed by varying the angles α_r and θ_r, where α_r is the angle between the vector $\mathbf{k}_s$ and the wall, and θ_r is the angle between the projection of $\mathbf{k}_s$ on the wall and $\mathbf{k}_i$ (see Fig. 3.1 (a)). The angles and

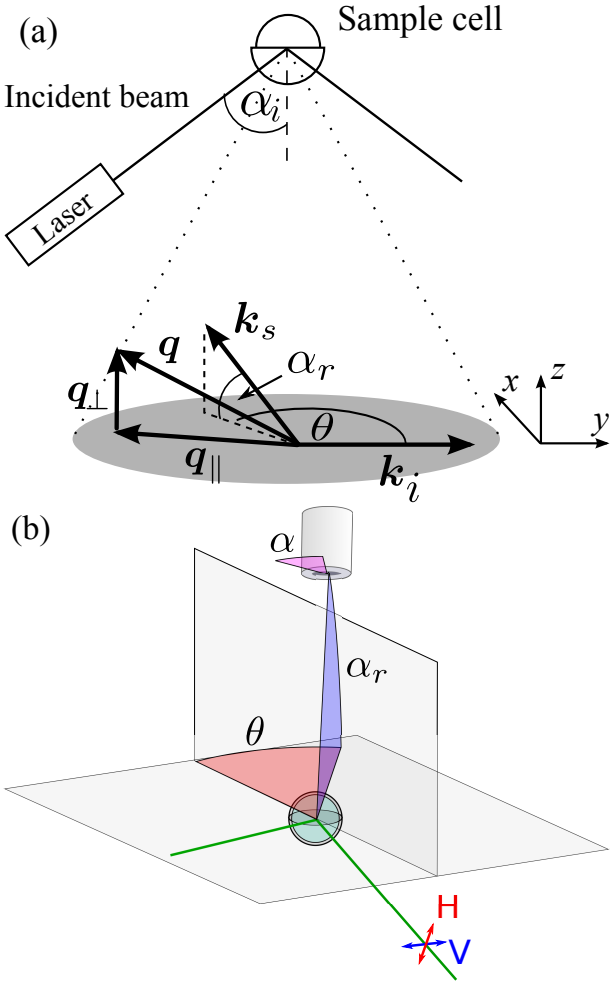

Figure 3.1: Geometry of the EWDLS set-up. (a) The illuminating light is the evanescent wave, which has the wave vector $\mathbf{k}_i$, while the detector records light scattered in the direction of $\mathbf{k}_s$. Note that the x-direction is normal to the plane spanned by the primary and the totally reflected beam, while the z-direction is normal to the reflecting interface. (b) The angles α_r and θ_r define the scattering vector, while α is the angle between the detector transmission direction and the plane, marked in blue, spanned by the wave vector of the scattered light and its projection onto the reflecting surface. The latter angle determines the scattering geometry (VH or VV).

the components of $\mathbf{q}$ are related by

$$q_{\parallel} = 2\pi n_2 \sqrt{1 + \cos^2 \alpha_r - 2 \cos \alpha_r \cos \theta_r}/\lambda_0, \tag{3.2}$$

$$q_{\perp} = 2\pi n_2 \sin \alpha_r / \lambda_0. \tag{3.3}$$

The polarization vector of the scattered light likewise depends on the scattering angles by

$$\hat{\mathbf{n}}_S = \begin{pmatrix} -\sin \alpha_r \sin \theta_r \cos \alpha + \cos \theta_r \sin \alpha \\ -\sin \alpha_r \cos \theta_r \cos \alpha - \sin \theta_r \sin \alpha \\ \cos \alpha_r \cos \alpha \end{pmatrix}, \tag{3.4}$$

with α being the angle between the analyser transmission direction and the plane spanned by the wave vector of the scattered light and its projection onto the reflecting surface, as indicated in Fig. 3.1(b) (see also Ref. [89]).

It is important to stress that there are two essential differences between a bulk DLS experiment and an EWDLS measurement. Firstly, in an evanescent field the illumination intensity varies on the length scales of the penetration depth $2/\kappa$, comparable to the size of particles. Likewise, the strength of the electric field incident on the particle decreases exponentially with its distance from the wall. Hence only the particles staying within distances of the order of the penetration depth from the wall scatter enough light to be detected. Thus the instantaneous electric field scattered from a group of particles has the form

$$\mathbf{E}_S \sim \sum_{j=1}^{N} \exp\left(i\mathbf{q} \cdot \mathbf{r}_j - \frac{\kappa}{2} z_j\right) F(\hat{\mathbf{u}}_j; \mathbf{q}, \kappa) E_0, \tag{3.5}$$

a modified form of Eq. (2.8). Here we have also generalized the scattering strength $F(\hat{\mathbf{u}}_j(t); \mathbf{q}, \kappa)$ to include all possible situations, i.e. optically- and shape-anisotropic particles. Further on, we again omit the dependence of F on its arguments or write simply $F(\hat{\mathbf{u}})$. Remarkably, the scattering strength in this case becomes penetration-depth dependent.

Secondly, since the boundary of the system reflects the flow caused by motion of the particles, affecting their motion in return, the hydrodynamic mobility of particles becomes dependent on their distance from the wall. This fact, which we will discuss in detail in the next section, has a major impact on the dynamics of the system. The interplay between the non-uniform illumination and hydrodynamic effects renders the interpretation of EWDLS measurements much more involved in comparison to standard DLS techniques.

3.2 Correlation functions in EWDLS experiments

In EWDLS experiments, similarly to bulk measurements, one records the time-autocorrelation function of the scattered electric field, defined now by

$$\hat{g}_1(t) \equiv \hat{g}_1(\mathbf{q}, \kappa, t) = \frac{\left\langle E_S^*(\mathbf{q}, \kappa; t = 0) \cdot E_S(\mathbf{q}, \kappa; t) \right\rangle}{\langle |E_S(\mathbf{q}, \kappa; t = 0)|^2 \rangle}. \tag{3.6}$$

We focus on a dilute system and consider an isolated particle, which is optically anisotropic. The scattered electric field now has the form (3.5)

$$E_S(\mathbf{q}, \kappa; t) \sim \exp(i\mathbf{q} \cdot \mathbf{r}(t)) \exp\left(-\frac{\kappa}{2} z(t)\right) F(\hat{\mathbf{u}}(t); \mathbf{q}, \kappa). \tag{3.7}$$

The orientation-dependent factor F includes the oriented dielectric tensor of the particle determined by the scattering geometry. To arrive at the expression (3.7), one needs to repeat the analysis of the bulk case from Chapter 2 including the nonuniform evanescent illumination profile. The explicit form of the scattered field reads now

$$E_S(\mathbf{q}, \kappa; t) \sim \mathcal{E}(\hat{\mathbf{u}}(t)) B(\hat{\mathbf{u}}(t); \mathbf{q}, \kappa) \exp\left(i\mathbf{q} \cdot \mathbf{r}(t) - \frac{\kappa z(t)}{2}\right), \tag{3.8}$$

where the oriented dielectric tensor $\mathcal{E}(\hat{\mathbf{u}})$ is given by Eq. (2.17). The quantity

$$B(\hat{\mathbf{u}}; \mathbf{q}, \kappa) = \frac{1}{V} \int_{V(\hat{\mathbf{u}})} \mathrm{d}\mathbf{r}' \exp(i\mathbf{q} \cdot \mathbf{r}') \exp\left(-\frac{\kappa z'}{2}\right), \tag{3.9}$$

which we will call the evanescent scattering amplitude, describes scattering from different elements within the scattering body in the evanescent field. The integral here is performed over the particle volume, with respect to a chosen centre. For axisymmetric particles, we choose it to be the geometric centre. The evanescent scattering amplitude contains information on the orientation and form of the particle and differs from the standard DLS expression by the exponentially decaying illumination term. For a thin axisymmetric body, the term $\exp(i\mathbf{q} \cdot \mathbf{r}')$ may only depend on the combination $\mathbf{q} \cdot \hat{\mathbf{u}}$ and the illumination term $\exp(-\kappa z'/2)$ may depend on the product $\hat{\mathbf{e}}_z \cdot \hat{\mathbf{u}}$. Thus, $B(\hat{\mathbf{u}}; \mathbf{q}, \kappa)$ depends in fact on the combinations $i\mathbf{q}_\parallel \cdot \hat{\mathbf{u}}$ and $\left(iq_\perp - \frac{\kappa}{2}\right) \hat{\mathbf{e}}_z \cdot \hat{\mathbf{u}}$. In order to assess the relative importance of the scattering vector and the penetration depth, one has to compare the characteristic vertical length scales of the electric field oscillation over the length of the particle, given by $q_\perp L$, and the length scale of the illuminating field decay over the particle size, κL. In the limit of $q_\perp \gg \kappa$, or $q_\perp \kappa^{-1} \gg 1$, the evanescent field does not decay significantly over the particle size, and therefore the scattering amplitude is essentially unchanged with respect to the bulk scattering case. The opposite limit of $q_\perp \kappa^{-1} \ll 1$ corresponds to the case where the spatial oscillations of the illuminating field may be neglected compared to the exponential decay away from the wall. Then, one expects only a part of the particle to be illuminated, giving rise to a scattering signal. In this limit the scattering amplitude is independent of q. It is notable that this limit is recovered experimentally at low scattering angle, when $q \to 0$.

For the next step to be made in evaluation of the EACF $\hat{g}_1(t)$, we need to specify the dynamics of the particles, and then perform the statistical average in Eq. (3.6). To this end, we need to develop a proper statistical description of a suspension dynamics, which we formulate in the next Chapter 5. Before that, we discuss below the effect of the restricted scattering volume on the decay of the EACF.

3.3 Effects of non-uniform illumination

The scattering volume in EWDLS experiments is illuminated by an evanescent wave, thus the regions closer to the wall receive more intensity. This property lies at the root of this scattering technique, as it restricts the scattering volume to a near-wall region where the hydrodynamic interactions with the boundary are most pronounced. The exponential decay of light intensity, with the length scale set by the penetration depth κ, has major consequences for the interpretation of scattering data.

The non-uniform illumination of the scattering volume has a clear manifestation in the structure of the first cumulant. This may be demonstrated in a wall-bounded suspension of spherical particles with the neglect of hydrodynamic interactions, as investigated first by Lan, Ostrowsky and Sornette [111], which we will refer to as LOS solution. Its structure has been discussed in detail in our earlier work [88]. In such a system there is no increase of friction due to the proximity of a wall, and the particles are free to diffuse in the whole wall-bounded half-space. Their diffusion is simply characterized by the Stokes-Einstein coefficient D_0. The full correlation function may then be found analytically by solving the diffusion equation with a reflecting boundary condition at the wall. Its form reads [111]

$$\hat{g}_{\mathrm{LOS}}(\mathbf{q}, \kappa; t) = \exp(-q_{\parallel} D_0 t) g_z(q_{\perp}, \kappa; t) \tag{3.10}$$

with the relaxation function g_z written conveniently in terms of the complex error function $w(z) = e^{-z^2}\mathrm{erfc}(-iz)$ [112] as

$$g_z(q_{\perp}, \kappa; t) = \mathrm{Re}[w(iZ)] - \frac{1}{\eta}\mathrm{Im}[w(iZ)]. \tag{3.11}$$

The variable $Z = \xi(1 + i\eta)$ depends on two dimensionless parameters

$$\xi = \frac{1}{2}\kappa\sqrt{D_0 t}, \qquad \eta = \frac{\kappa}{2q_{\perp}}. \tag{3.12}$$

The variable ξ compares the thickness of the scattering volume with the average distance covered by the diffusing particles, whereas η compares the two mechanisms which lead to the decay of the EACF. The first one is related to diffusion over length scales of $q_{\perp}^{-1}$, as in standard bulk scattering. The second one is due to particles leaving the illuminated near-wall region, that is diffusing over the length scales of κ^{-1}.

The structure of the first cumulant found from Eq. (3.10) using Eq. (2.30) reads then

$$\Gamma = D_0\left(q_{\parallel}^2 + q_{\perp}^2 + \frac{\kappa^2}{4}\right) = D_0\left(q^2 + \frac{\kappa^2}{4}\right). \tag{3.13}$$

The presence of the additional factor $D_0\frac{\kappa^2}{4}$, compared to standard bulk $\Gamma = D_0 q^2$ may be attributed purely to the non-uniform illumination profile within the scattering volume. The restriction of the scattering volume by the evanescent wave leads therefore to an increase in the initial relaxation rates of the EACF. Thus the initial decay is faster than in the bulk case.

It is important to discuss at this point that the validity of the description by the first cumulant, i.e. the time scales at which the description via the initial decay rate is plausible. We estimate that over a time interval t the particles diffuse over length scales $\sqrt{D_0 t}$ which at long times become large compared to the thickness of the illuminated near-wall layer κ^{-1}, and therefore the particles leave the scattering volume. We thus expect the first cumulant to be an adequate description for $\kappa^{-1} \gg \sqrt{D_0 t}$, i.e. for times $t \ll \kappa^2 D_0$. If the penetration depth is too small (large κ), the first cumulant will describe the initial decay of the EACF only for the times so small that its practical value will be limited.

Moreover, from the analysis of the explicit expression for the EACF one concludes that the long-time decay of g_z is algebraic $\sim t^{-1/2}$. We note that the probability for a diffusing particle to be found in a strip of finite thickness above a reflecting wall also decays with the same exponent.

We therefore expect that for long times, the decay of the EACF will be slower than exponential, found in the case of an unbounded fluid.

Remarkably, inclusion of hydrodynamic interaction in this scheme, which is the main aim of Chapters 7 and 8, leads to significant changes in the structure of the first cumulant presented above, which we will discuss in the course of this work.

4 Statistical description of colloidal suspensions

In this Chapter, we outline the physical basis for quantities describing colloidal systems. First, we introduce the basic characteristics of particles in dispersion, which lead to identification of time scales of the processes which govern their dynamics. Next, we focus on the Brownian time scale, on which the suspension dynamics is usually probed in experimental scattering studies, and then proceed to formulation of the proper statistical description of a suspension on that time scale. This is done by means of the generalised Smoluchowski equation. Further, we employ the Smoluchowski equation formalism to derive explicit statistical-mechanical expressions for the colloidal time-correlation functions, quantities measured directly in a variety of experiments, including light scattering. Since in the course of the work we will be particularly interested in short-time dynamics, we introduce the cumulant expansion of the correlation functions and outline how the cumulants may be calculated.

The statistical description of a suspension presented below draws from the books by Dhont [10], Nägele [17], and van Kampen [35], and the review article of Pusey [7] and Jones & Pusey [8], where the topics mentioned here are elaborated in greater detail.

4.1 Time and length scales in colloidal dynamics

Systems of mesoscopic particles immersed in a viscous fluid exhibit rich dynamic behaviour, associated with different time and length scales of interest [7, 8, 10, 113]. Below, we shall briefly discuss the relevant time scales and underlying characteristic physical processes. In an experiment, the time scale is the time interval over which observables are averaged during a measurement. It sets therefore a minimum time resolution of an experiment or theory aimed at calculating these observables.

For the sake of simplicity, we shall now consider a spherical particle of radius a, and density ρ_p, suspended in a solvent of density ρ and viscosity η. The motion of the particle in a viscous liquid is subject to a Stokesian friction force $\mathbf{F} = -\zeta_0 \mathbf{V}$ proportional to its velocity $\mathbf{V}$, where $\zeta_0 = 6\pi\eta a$ is the Stokes friction coefficient.

The finest of the discussed time scales, τ_s, can be attributed to propagation of disturbances in the solvent. These include pressure waves (also called sound waves) and shear waves. The sound

waves are essentially pressure differences propagating through the medium. The time needed for the sound wave to travel a distance of particle radius equals

$$\tau_s = \frac{a}{c}, \tag{4.1}$$

with c being the speed of sound in the solvent. The shear waves are created by the unsteady motion of the particle and involve tangential propagation of sliding layers of fluid. Their characteristic decay time, called the viscous relaxation time, reads

$$\tau_\nu = \frac{a^2\rho}{\eta} = \frac{a^2}{\nu}. \tag{4.2}$$

where the kinematic viscosity $\nu = \eta/\rho$ characterizes molecular diffusion of momentum into the fluid. The time τ_ν can thus be interpreted as the characteristic time needed for the hydrodynamic disturbance to propagate through a distance of the particle radius a.

The motion of the particle through the surrounding viscous fluid is damped by the drag force which causes the particle velocity to decay with a relaxation time equal to

$$\tau_B = \frac{m}{\zeta_0} = \frac{2a^2\rho_p}{9\eta} = \frac{2}{9}\frac{\rho_p}{\rho}\tau_\nu, \tag{4.3}$$

called the momentum relaxation time due to the solvent friction. Here, $m = \frac{4}{3}\pi\rho_p a^3$ is the mass of the particle. Lastly, the diffusion of particle through the medium can also be related to a characteristic time during which it travels a distance equal to its radius. The latter is referred to as the structural relaxation time, and defined as

$$\tau_D = \frac{a^2}{D_0}, \tag{4.4}$$

with D_0 being the free self-diffusion coefficient of the particles. To illustrate the estimates for the mentioned time scales, consider an aqueous suspension of density-matched ($\rho_p \approx \rho$) polystyrene spheres with $a \approx 100$ nm immersed in water at room temperature. Then, the relevant time scales read [7]

$$\tau_c = 6.8 \cdot 10^{-11}\text{s}, \quad \tau_\nu = 2.2 \cdot 10^{-8}\text{s}, \quad \tau_B = 2.2 \cdot 10^{-9}\text{s}, \quad \tau_D = 4.7 \cdot 10^{-3}\text{s}.$$

Hence we conclude that there is a well pronounced separation of time scales

$$\tau_D \gg \tau_B \gg \tau_c, \tag{4.5}$$

which will be further exploited to develop a proper statistical description of the dynamics of colloidal suspensions.

4.2 Generalised Smoluchowski equation

The above-mentioned separation of time scales allows to describe the evolution of the system on time scales $t \sim \tau_D$, large compared to the velocity relaxation time, by means of the spatial configuration of the particles only, with its evolution described as a Markov process [35]. The

statistical properties of a suspension are therefore encoded in the N-particle distribution function $P(\mathbf{X}_N, t)$, where $\mathbf{X}_N = (\mathbf{R}_1, \cdots, \mathbf{R}_N, \hat{\mathbf{u}}_1, \cdots, \hat{\mathbf{u}}_N)$ denotes the positions and orientations of all the particles in the system. For axisymmetric bodies, to which we will confine our attention in this work, $\hat{\mathbf{u}}$ is a unit vector pointing along the particle axis of symmetry. The normalization of the N-particle probability density function (pdf) reads

$$\int \mathrm{d}\mathbf{X}_N \, P(\mathbf{X}_N, t) = 1, \tag{4.6}$$

with $\mathrm{d}\mathbf{X}_N = \mathrm{d}\mathbf{R}_1 \ldots \mathrm{d}\mathbf{R}_N \mathrm{d}\hat{\mathbf{u}}_1 \ldots \mathrm{d}\hat{\mathbf{u}}_N$. The integral is taken here over all the positions of the particles, and over the orientations of the particles on a unit spherical surface. The evolution of the pdf is governed by the N-particle Smoluchowski equation [7, 10]. In the course of this work, we are interested in the dynamics of dilute suspensions, where the system is fully characterized by single-particle properties only. We shall therefore restrict our attention to the single-particle pdf $P(\mathbf{X}, t)$, which satisfies the Smoluchowski equation in the form

$$\frac{\partial P(\mathbf{X}, t)}{\partial t} = \mathcal{L} P(\mathbf{X}, t), \tag{4.7}$$

where the Smoluchowski evolution operator acting on the probability distribution P reads

$$\mathcal{L}(\mathbf{X}) P = \boldsymbol{\nabla}_{\mathbf{X}} \cdot \mathbf{D}(\mathbf{X}) \cdot [\beta P (\boldsymbol{\nabla}_{\mathbf{X}} \Phi) + \boldsymbol{\nabla}_{\mathbf{X}} P] = \boldsymbol{\nabla}_{\mathbf{X}} \cdot \mathbf{D}(\mathbf{X}) P^{\mathrm{eq}} \cdot \boldsymbol{\nabla}_{\mathbf{X}} \frac{P}{P^{\mathrm{eq}}}, \tag{4.8}$$

with the interaction potential $\Phi(\mathbf{X})$ of direct interactions between the particle and the wall, and the equilibrium pdf given by $P^{\mathrm{eq}} \sim \exp(-\beta \Phi(\mathbf{X}))$. Here, $\beta = 1/k_B T$, where k_B is the Boltzmann constant, and T denotes the temperature. The gradient operator is defined as

$$\boldsymbol{\nabla}_{\mathbf{X}} = \left(\frac{\partial}{\partial \mathbf{r}}, \mathbf{L} \right). \tag{4.9}$$

The rotational operator $\mathbf{L}$ may be expressed in terms of the particle orientation[1] as

$$\mathbf{L} = \hat{\mathbf{u}} \times \frac{\partial}{\partial \hat{\mathbf{u}}}. \tag{4.10}$$

Finally, the 6×6 diffusion matrix $\mathbf{D}$ is proportional to the mobility matrix $\boldsymbol{\mu}$ by virtue of the fluctuation-dissipation theorem [35, 114]

$$\mathbf{D} = k_B T \boldsymbol{\mu}. \tag{4.11}$$

The mobility matrix $\boldsymbol{\mu}$ relates the forces and torques acting on the particles to their linear and angular velocities and encodes a specific type of interactions omnipresent in colloidal dynamics, i.e. solvent-mediated hydrodynamic interactions, which we describe in detail in the following Chapter 5. Since the interactions via the viscous fluid are long-ranged, the mobility matrix depends on the configuration of the whole system. In the single-particle case, the symmetry of the particle-wall geometry implies a particular form of $\boldsymbol{\mu}$, depending on the distance from the wall and the particle orientation. The cases of special symmetry, i.e. a spherical particle, and an axially symmetric one, will be treated in detail in further course of this work.

[1] In the general case of an arbitrarily-shaped colloid, $\mathbf{L}$ incorporates derivatives with respect to the Euler angles [101].

4.3 Correlation functions in colloidal systems

In order to characterise the dynamic behaviour of a colloidal system correlation functions are widely employed. A statistical description of the dynamics is feasible on a time scale that is large in comparison to the solvent correlation times. In this framework, the quantities of interest are averaged during measurements over a time interval larger than the solvent relaxation time, and therefore an accompanied coarse graining of phase space coordinates associated to the change of positions and momenta during this time interval is required, and the system may be described using the positional variables on the diffusive time scale $t \sim \tau_D$. We also assume ergodicity of the system, interpreting the time-averages as ensemble statistical averages.

We start the development a general framework for the analysis of correlation functions from a general statistical-mechanical expression for a time correlation function $G(t)$ of two phase space functions, $f(\mathbf{X})$ and $g(\mathbf{X})$, in case of which the only time dependence enters by the changes of the configuration during the evolution of the system. The correlation function is then written as an ensemble average [10]

$$\begin{aligned} G(t) = \langle f(\mathbf{X}(t=0)) g(\mathbf{X}(t)) \rangle &= \int \mathrm{d}\mathbf{X} \int \mathrm{d}\mathbf{X}_0 \, f(\mathbf{X}_0) g(\mathbf{X}) P_2(\mathbf{X}, t; \mathbf{X}_0, 0) = \\ &= \int \mathrm{d}\mathbf{X} \int \mathrm{d}\mathbf{X}_0 \, f(\mathbf{X}_0) g(\mathbf{X}) P_{1|1}(\mathbf{X}, t|\mathbf{X}_0, 0) P(\mathbf{X}_0, 0). \end{aligned} \tag{4.12}$$

Above we have introduced the joint probability distribution $P_2(\mathbf{X}, t; \mathbf{X}_0, 0)$ of the system being in a configuration $\mathbf{X}$ at time t and in a configuration $\mathbf{X}_0$ at $t = 0$. In the second line, we recast P_2 as a product of the conditional probability $P_{1|1}$ and the probability distribution P of the initial configuration of the system. The conditional pdf $P_{1|1}$ likewise obeys the Smoluchowski equation (4.7), and we may formally write its solution as

$$P_{1|1}(\mathbf{X}, t|\mathbf{X}_0, 0) = \exp(\mathcal{L}t)\delta(\mathbf{X} - \mathbf{X}_0). \tag{4.13}$$

Assuming the initial pdf in Eq. (4.12) to be the equilibrium one, $P^{\mathrm{eq}}(\mathbf{X}) \sim e^{-\beta\Phi(\mathbf{X})}$, and using Eq. (4.13), we arrive at

$$G(t) = \int \mathrm{d}\mathbf{X} \int \mathrm{d}\mathbf{X}_0 \, f(\mathbf{X}_0) g(\mathbf{X}) \exp(\mathcal{L}t)\delta(\mathbf{X} - \mathbf{X}_0) P^{\mathrm{eq}}(\mathbf{X}_0). \tag{4.14}$$

Since the Smoluchowski operator is independent of the variable $\mathbf{X}_0$, integration of the Dirac delta function with respect to that variable may be directly performed, resulting in the expression

$$G(t) = \int \mathrm{d}\mathbf{X} \, g(\mathbf{X}) \exp(\mathcal{L}t)[f(\mathbf{X}) P^{\mathrm{eq}}(\mathbf{X})]. \tag{4.15}$$

It is now convenient to introduce the adjoint Smoluchowski operator $\mathcal{L}^\dagger$, defined for two phase-space functions f and g by the scalar product

$$\int \mathrm{d}\mathbf{X} \, f(\mathbf{X}) \mathcal{L} g(\mathbf{X}) = \int \mathrm{d}\mathbf{X} \, g(\mathbf{X}) \mathcal{L}^\dagger f(\mathbf{X}), \tag{4.16}$$

where the adjoint operator acts on the function on its right-hand side. Its explicit form, acting on a pdf P, reads

$$\mathcal{L}^\dagger(\mathbf{X}) P = [\boldsymbol{\nabla}_{\mathbf{X}} - \beta(\boldsymbol{\nabla}_{\mathbf{X}}\Phi)] \cdot \mathbf{D}(\mathbf{X}) \cdot \boldsymbol{\nabla}_{\mathbf{X}} P. \tag{4.17}$$

The adjoint Smoluchowski operator, when acting on the equilibrium pdf, has also the property

$$\mathcal{L}P^{\mathrm{eq}}(\ldots) = P^{\mathrm{eq}}\mathcal{L}^{\dagger}(\ldots). \tag{4.18}$$

With the help of the adjoint operator, it is possible to rewrite Eq. (4.15) as

$$G(t) = \int \mathrm{d}\mathbf{X}\, P^{\mathrm{eq}}(\mathbf{X}) f(\mathbf{X}) \exp(\mathcal{L}^{\dagger}t) g(\mathbf{X}) = \left\langle f(\mathbf{X}) \exp(\mathcal{L}^{\dagger}t) g(\mathbf{X}) \right\rangle_{\mathrm{eq}}, \tag{4.19}$$

where we used the brackets to denote the average with respect to the equilibrium pdf P^{eq},

$$\langle \cdots \rangle_{\mathrm{eq}} = \int \mathrm{d}\mathbf{X}\, P^{\mathrm{eq}}(\mathbf{X})(\cdots). \tag{4.20}$$

Equation (4.19), valid for all times, will serve as a basis for the short-time expansion performed in the next section.

4.4 Short-time Smoluchowski dynamics

One of the methods for the analysis of time-correlation functions is to use either the cumulant expansion, or the moment expansion. Both give an insight into the short-time dynamics, i.e. changes of the correlation function at times shorter than its characteristic decay rate. From now on, we shall consider the normalised correlation function $\widetilde{G}(t) = G(t)/G(0)$, which is normally measured in experiments.

The two expansions (in moments and in cumulants) are related, since the former one is essentially a Taylor expansion of the correlation function

$$\widetilde{G}(t) = \sum_{n=0}^{\infty} \frac{t^n}{n!} m_n, \tag{4.21}$$

with m_n being the moments, while the latter is an expansion of the logarithm of $\widetilde{G}$,

$$\log \widetilde{G}(t) = \sum_{n=0}^{\infty} \frac{t^n}{n!} \Gamma_n, \tag{4.22}$$

where Γ_n are the cumulants. In this study, we will be interested in the short-time decay of the correlation functions, we therefore explicitly analyse the first two terms in both expansions. In the particular case of Eq. (4.19), expanding the exponential operator in Eq. (4.19) in powers of time

$$\exp(\mathcal{L}^{\dagger}t) \approx \mathbf{1} + \mathcal{L}^{\dagger}t + \frac{1}{2}(\mathcal{L}^{\dagger})^2 t^2 + O(t^3), \tag{4.23}$$

leads to the following short-time representation of $\widetilde{G}(t)$

$$\widetilde{G}(t) = 1 + m_1 t + \frac{1}{2} m_2 t^2 + O(t^3), \tag{4.24}$$

with the two first moments equal to

$$m_1 = \frac{\left\langle f(\mathbf{X})\mathcal{L}^\dagger g(\mathbf{X})\right\rangle}{\langle f(\mathbf{X})g(\mathbf{X})\rangle}, \tag{4.25}$$

$$m_2 = \frac{\left\langle f(\mathbf{X})\mathcal{L}^\dagger\mathcal{L}^\dagger g(\mathbf{X})\right\rangle}{\langle f(\mathbf{X})g(\mathbf{X})\rangle}, \tag{4.26}$$

where we omitted the subscript 'eq' in the equilibrium ensemble averages. On the other hand, the first terms of the cumulant expansion read

$$\widetilde{G}(t) = \exp\left(-\Gamma_1 t + \frac{1}{2}\Gamma_2 t^2 + O(t^3)\right). \tag{4.27}$$

Comparison of Eqns. (4.27) and (4.24) yields the relations between the cumulants and moments

$$\Gamma_1 = -m_1, \tag{4.28}$$

$$\Gamma_2 = m_2 - m_1^2. \tag{4.29}$$

These explicit expressions may now be evaluated for any configuration-dependent functions $f(\mathbf{X})$ and $g(\mathbf{X})$ to yield a short-time approximation of their correlation function. In principle, one could build an approximation of any correlation function valid for longer times by simply calculating the higher-order terms in the expansions above. It turns out, however, that this might not be possible due to the divergence of the higher cumulants/moments. We shall discuss the existence of cumulants in evanescent scattering correlation function in the further course of this work.

In most cases, we will restrict our attention to the first cumulant $\Gamma \equiv \Gamma_1$, characterising the initial decay of the measured correlation function. For practical calculations, it is convenient to recast the expression (4.25) by means of partial integration as

$$\Gamma = \frac{\langle[\boldsymbol{\nabla}_\mathbf{X} f(\mathbf{X})]\cdot\mathbf{D}(\mathbf{X})\cdot[\boldsymbol{\nabla}_\mathbf{X} g(\mathbf{X})]\rangle}{\langle f(\mathbf{X})g(\mathbf{X})\rangle}, \tag{4.30}$$

where the action of gradient operators is restricted to square brackets. The boundary terms vanish here, which follows from the Gauss' theorem combined with (a) vanishing of the translational diffusion matrix at contact with the wall, and (b) asymptotic exponential decay of the integrand for large distances. For details, see e.g. Ref. [88, 90]. We will make extensive use of the expression above to derive the first cumulant for both bulk and wall-bounded systems.

5 Hydrodynamic interactions

The solvent-mediated hydrodynamic interactions play a crucial role in the dynamics of soft matter. In mesoscopic systems, such as suspensions, the fluid flow caused by the presence of dispersed particles is known to alter their dynamic behaviour to a large extent. Below, we provide a brief description of hydrodynamic interactions of colloids both in a quiescent fluid, and in the presence of a no-slip boundary.

To begin with, we introduce the notion of hydrodynamic friction and mobility tensors, discuss their general properties and dependence on the particle shape. Next, we outline a method to calculate these quantities for conglomerates of spherical particles, used to model complex-shaped particles. To this end, we present and discuss the multipole formalism, developed by Cichocki, Schmitz, Felderhof and collaborators [115–118], which can be used to calculate the many-body hydrodynamic tensors for suspended spheres. We then proceed to analyse the special case of axisymmetric particles, exploiting the symmetry to devise the specific form of their mobility tensors in a bulk fluid. We conclude the Chapter discussing the effect of the presence of a no-slip wall on the mobility of axially symmetric particles. Using the multipole formalism, we derive analytical asymptotic expressions for correction to the bulk mobility tensor due to the wall. In a detailed analysis, we discuss its dependence on the wall-particle distance and orientation, and assess the range of distances at which it may be successfully applied.

In most of the general introduction we follow the excellent monographs of Kim & Karrila [9] and Happel & Brenner [38].

5.1 The Stokes equations

We shall analyse the motion of mesoscopic particles immersed in a viscous fluid medium of shear viscosity η and uniform density ρ. For a particle of characteristic size a, moving through the fluid with a characteristic velocity U, the relative importance of the non-linear inertial term compared to the viscous term in the Navier–Stokes equations, is given by the dimensionless Reynolds number [119]

$$\mathrm{Re} = \frac{\rho U a}{\eta}. \tag{5.1}$$

For a nanometer-sized particle in water, the Reynolds number is typically of order of $10^{-4} - 10^{-5}$ [7], and thus the inertial terms may be neglected. Moreover, since we consider motion on time scales much larger than the solvent relaxation time, we may neglect the time derivative in the

already linearised Navier-Stokes equations. In this case, the motion of the fluid is governed by the stationary Stokes equations [9]

$$\eta\nabla^2\mathbf{v}(\mathbf{r}) - \nabla p(\mathbf{r}) = -\mathbf{f}(\mathbf{r}), \qquad \nabla\cdot\mathbf{v}(\mathbf{r}) = 0, \tag{5.2}$$

where $\mathbf{v}(\mathbf{r})$ is the velocity field, $\mathbf{f}(\mathbf{r})$ is the force density acting on the fluid, and $p(\mathbf{r})$ stands for modified pressure field which includes the effect of gravity. Physically, Eq. (5.2) in the absence of external forces expresses the balance of pressure and viscous forces at any instant of time. Accordingly, the instantaneous values of velocity, pressure, and consequently, the stress field, are independent of the earlier flow history. They depend solely on the current configuration of particles, and on the boundary conditions on the surfaces of particles, and the confining walls. Thus, microparticles of colloidal size experience the mechanics of Aristotle, with their velocity proportional to a driving force. In the absence of driving, the flow ceases rapidly. In the biologically important case of motile microorganisms, once the swimming motion is suppressed, the velocity field relaxes to zero within a very small time interval of the order of τ_B, as first remarked by Purcell [120]. It is worth emphasizing that this framework holds sway on the Brownian time scale τ_D, and an analysis of processes occurring on a finer time scale would involve a time-dependent version of Stokes equations.

5.2 Dynamics of particles in flow

We now focus our attention on microparticles suspended in the fluid. In the following, we provide a suitable theoretical description for the motion of such objects and relate it to the forces acting on them. Our ultimate goal is a method to describe hydrodynamic interactions of a non-spherical particle with a no-slip wall. Since interactions with a wall may be intuitively understood as interactions with a system of image particles, in analogy to electrostatics, we will need to calculate hydrodynamic interactions between many particles. We therefore begin with introducing the notion of hydrodynamic resistance and mobility for spherical particles in Stokes flow and outline a way to calculate the hydrodynamic tensors for colloids in the presence of a wall. As we will show, the knowledge of these tensors allows for calculation of the friction (mobility) tensor of a single particle represented by a conglomerate of spheres moving collectively.

5.2.1 Many-particle resistance and mobility relations

Consider an ensemble of N spherical colloidal particles immersed in an incompressible Newtonian solvent. The configuration of the system is described only by positions of all the particles abbreviated in a $3N$-dimensional vector $\mathbf{X} = (\mathbf{R}_1, \dots \mathbf{R}_N)$. The particles are immersed in the flow field $\mathbf{v}(\mathbf{r})$ described by the linear Stokes equations (5.2) with $\mathbf{f}(\mathbf{r}) = \sum_i \mathbf{f}_i(\mathbf{r})$ being the force density the particles exert on the fluid. This flow field may be superposed with an ambient linear flow $\mathbf{v}_0(\mathbf{r})$ satisfying the homogeneous Stokes equations

$$\eta\nabla^2\mathbf{v}_0(\mathbf{r}) = \nabla p_0(\mathbf{r}), \qquad \nabla\cdot\mathbf{v}_0(\mathbf{r}) = 0, \tag{5.3}$$

with the vorticity and rate of strain defined at a point $\mathbf{r}$ as

$$\boldsymbol{\omega}_0(\mathbf{r}) = \tfrac{1}{2}\nabla\times\mathbf{v}_0(\mathbf{r}), \qquad \mathbf{E}_0(\mathbf{r}) = \overline{\nabla\mathbf{v}_0(\mathbf{r})}, \tag{5.4}$$

where the bar denotes the symmetric and traceless part.

Given the force density, one can calculate the force, torque, and symmetric dipole moment (stresslet) for each particle $i \in \{1, \ldots, N\}$, according to

$$\mathbf{F}_i = \int_{\Sigma_i} \mathrm{d}\mathbf{r}\, \mathbf{f}_i(\mathbf{r}), \tag{5.5}$$

$$\mathbf{T}_i = \int_{\Sigma_i} \mathrm{d}\mathbf{r}\, (\mathbf{r} - \mathbf{R}_i) \times \mathbf{f}_i(\mathbf{r}), \tag{5.6}$$

$$\mathbf{S}_i = \int_{\Sigma_i} \mathrm{d}\mathbf{r}\, \overline{(\mathbf{r} - \mathbf{R}_i)\mathbf{f}_i(\mathbf{r})}, \tag{5.7}$$

where the integrals are performed over the particle surface Σ_i. Higher-order moments are defined in an analogous way.

In result of the external flow, motion is induced, and the particles gain linear and angular velocities, written as $\widetilde{\mathbf{V}} = (\mathbf{V}_1, \ldots, \mathbf{V}_N)$, and $\widetilde{\boldsymbol{\Omega}} = (\boldsymbol{\Omega}_1, \ldots, \boldsymbol{\Omega}_N)$. In an similar way, we write the forces $\boldsymbol{\mathcal{F}} = (\mathbf{F}_1, \ldots, \mathbf{F}_N)$, torques $\boldsymbol{\mathcal{T}} = (\mathbf{T}_1, \ldots, \mathbf{T}_N)$, and stresslets $\boldsymbol{\mathcal{S}} = (\mathbf{S}_1, \ldots, \mathbf{S}_N)$. The ambient flow velocities and their gradients, taken at the centre of each particle, may also be denoted as $\widetilde{\mathbf{v}}_0 = (\mathbf{v}_0(\mathbf{R}_1), \ldots, \mathbf{v}_0(\mathbf{R}_N))$, $\widetilde{\boldsymbol{\omega}}_0 = (\boldsymbol{\omega}_0(\mathbf{R}_1), \ldots, \boldsymbol{\omega}_0(\mathbf{R}_N))$, and $\widetilde{\mathbf{E}}_0 = (\mathbf{E}_0(\mathbf{R}_1), \ldots, \mathbf{E}_0(\mathbf{R}_N))$.

Owing to linearity of the Stokes equations, the force moments $\boldsymbol{\mathcal{F}}$, $\boldsymbol{\mathcal{T}}$, and $\boldsymbol{\mathcal{S}}$, are linearly related to the velocity moments via the many-particle generalised friction (or grand resistance) tensor $\boldsymbol{\zeta}_N$ [9, 96]

$$\begin{pmatrix} \boldsymbol{\mathcal{F}} \\ \boldsymbol{\mathcal{T}} \\ \boldsymbol{\mathcal{S}} \end{pmatrix} = -\boldsymbol{\zeta}_N \cdot \begin{pmatrix} \widetilde{\mathbf{v}}_0 - \widetilde{\mathbf{V}} \\ \widetilde{\boldsymbol{\omega}}_0 - \widetilde{\boldsymbol{\Omega}} \\ \widetilde{\mathbf{E}}_0 \end{pmatrix}, \tag{5.8}$$

which depends on the configuration of the whole system. We will discuss its structure in detail later. Knowledge of the generalised friction tensor is essential to determine the hydrodynamic friction forces and torques, given the particle motion and ambient flow.

On the other hand, if the forces and torques are known, as well as the ambient flow, the particle motion may be resolved by determining the generalised (grand) mobility tensor

$$\begin{pmatrix} \widetilde{\mathbf{v}}_0 - \widetilde{\mathbf{V}} \\ \widetilde{\boldsymbol{\omega}}_0 - \widetilde{\boldsymbol{\Omega}} \\ \boldsymbol{\mathcal{S}} \end{pmatrix} = -\boldsymbol{\mu}_N \cdot \begin{pmatrix} \boldsymbol{\mathcal{F}} \\ \boldsymbol{\mathcal{T}} \\ \widetilde{\mathbf{E}}_0 \end{pmatrix}. \tag{5.9}$$

Knowledge of the dependence of $\boldsymbol{\mu}_N$ or $\boldsymbol{\zeta}_N$ on the configuration opens a way to explore the suspension dynamics without the need to evaluate the accompanying fluid flow. In the regime where the particles are large enough for the Brownian motion to be negligible, the equations of motion of the particles may be integrated to yield their individual trajectories [121]. On the other hand, in the Brownian regime, the mobility matrix is needed both to account for the viscous friction and for the random displacements which the particles experience as a result of the fluctuations of the solvent, leading to the so-called Brownian dynamics numerical scheme [122, 123].

5.2.2 Mobility of a single particle in a viscous fluid

We consider now in more detail the special case of a single colloidal particle of an axially symmetric shape. Its configuration $\mathbf{X}$ is specified by the position of its centre $\mathbf{R}$ and its orientation along the unit vector $\hat{\mathbf{u}}$.[1]

The single-particle generalised friction tensor ζ follows from the general Eq. (5.8) as

$$\begin{pmatrix} \mathbf{F} \\ \mathbf{T} \\ \mathbf{S} \end{pmatrix} = -\begin{pmatrix} \zeta^{tt} & \zeta^{tr} & \zeta^{td} \\ \zeta^{rt} & \zeta^{rr} & \zeta^{rd} \\ \zeta^{dt} & \zeta^{dr} & \zeta^{dd} \end{pmatrix} \begin{pmatrix} \mathbf{v}_0(\mathbf{R}) - \mathbf{V} \\ \boldsymbol{\omega}_0(\mathbf{R}) - \boldsymbol{\Omega} \\ \mathbf{E}_0(\mathbf{R}) \end{pmatrix}, \tag{5.10}$$

and is now decomposed into 9 submatrices. The indices tt and rr denote the translational and rotational parts, respectively. The tensors $\mathbf{z}^{tr}$ and $\mathbf{z}^{rt}$ describe the translation-rotation coupling, for a force acting on a particle may cause rotational motion apart from translational one, and a torque may cause translation. The tensors with superscript d describe the response of the particle to an external elongational flow. In most cases, it is sufficient to consider only the 6×6 friction matrix relating the force and torque to linear and angular velocities. Here, however, we extend the friction matrix to the symmetric dipole moment subspace, since these elements turn out to be essential for the calculation of the correction to the friction matrix of a general particle due to the presence of a nearby wall, as we will discuss in detail in Sec. 5.5.3.

The inverse problem of finding the velocities due to given force distributions is written in terms of the mobility matrix $\boldsymbol{\mu}$ which is a partial inverse of the friction matrix, and follows from Eq. (5.9) as

$$\begin{pmatrix} \mathbf{v}_0(\mathbf{R}) - \mathbf{V} \\ \boldsymbol{\omega}_0(\mathbf{R}) - \boldsymbol{\Omega} \\ \mathbf{S} \end{pmatrix} = -\begin{pmatrix} \boldsymbol{\mu}^{tt} & \boldsymbol{\mu}^{tr} & \boldsymbol{\mu}^{td} \\ \boldsymbol{\mu}^{rt} & \boldsymbol{\mu}^{rr} & \boldsymbol{\mu}^{rd} \\ \boldsymbol{\mu}^{dt} & \boldsymbol{\mu}^{dr} & \boldsymbol{\mu}^{dd} \end{pmatrix} \begin{pmatrix} \mathbf{F} \\ \mathbf{T} \\ \mathbf{E}_0 \end{pmatrix}, \tag{5.11}$$

from which we find

$$\begin{pmatrix} \zeta^{tt} & \zeta^{tr} \\ \zeta^{rt} & \zeta^{rr} \end{pmatrix}^{-1} = \begin{pmatrix} \boldsymbol{\mu}^{tt} & \boldsymbol{\mu}^{tr} \\ \boldsymbol{\mu}^{rt} & \boldsymbol{\mu}^{rr} \end{pmatrix}. \tag{5.12}$$

Moreover, the following relations hold

$$\begin{aligned} \boldsymbol{\mu}^{td} &= \boldsymbol{\mu}^{tt}\zeta^{td} + \boldsymbol{\mu}^{tr}\zeta^{rd}, \\ \boldsymbol{\mu}^{rd} &= \boldsymbol{\mu}^{rt}\zeta^{td} + \boldsymbol{\mu}^{rr}\zeta^{rd}, \\ \boldsymbol{\mu}^{dt} &= -\zeta^{dt}\boldsymbol{\mu}^{tt} - \zeta^{dr}\boldsymbol{\mu}^{rt}, \\ \boldsymbol{\mu}^{dr} &= -\zeta^{dt}\boldsymbol{\mu}^{tr} - \zeta^{dr}\boldsymbol{\mu}^{rr}, \\ \boldsymbol{\mu}^{dd} &= \zeta^{dd} - \zeta^{dt}\boldsymbol{\mu}^{td} - \zeta^{dr}\boldsymbol{\mu}^{rd} \\ &= \zeta^{dd} + \boldsymbol{\mu}^{dt}\zeta^{td} + \boldsymbol{\mu}^{dr}\zeta^{rd}. \end{aligned} \tag{5.13}$$

Using the Lorentz reciprocal theorem [9], one may prove the symmetry properties of the mobility tensors:

$$\mu^{tt}_{\alpha\beta} = \mu^{tt}_{\beta\alpha}, \qquad \mu^{tr}_{\alpha\beta} = \mu^{rt}_{\beta\alpha}, \qquad \mu^{td}_{\alpha\beta\gamma} = -\mu^{dt}_{\beta\gamma\alpha} \tag{5.14}$$

$$\mu^{rr}_{\alpha\beta} = \mu^{rr}_{\beta\alpha}, \qquad \mu^{rd}_{\alpha\beta\gamma} = -\mu^{dr}_{\beta\alpha\gamma}, \qquad \mu^{dd}_{\alpha\beta\gamma\delta} = \mu^{dd}_{\gamma\delta\alpha\beta}, \tag{5.15}$$

[1] In the general case of a particle of arbitrary shape, the orientation is given by a set of three Euler angles [101,124].

where the Greek letters denote the Cartesian components. Moreover, from the properties of $\mathbf{S}$ and $\mathbf{E}_0$ we find that $\mu^{td}_{\alpha\beta\gamma}$, $\mu^{rd}_{\alpha\beta\gamma}$ are symmetric and traceless in (β, γ), $\mu^{dt}_{\alpha\beta\gamma}$, $\mu^{dr}_{\alpha\beta\gamma}$ are symmetric and traceless in (α, β), and $\mu^{dd}_{\alpha\beta\gamma\delta}$ is symmetric and traceless in (α, β) and (γ, δ).

In a bulk system, the mobility tensor does not depend on the position of the particle due to translational invariance, and the dependence on the orientation follows purely from the rotation of the particle; that means that $\boldsymbol{\mu}$ rotates with the particle and its components with respect to body-fixed axes are constant. It is important, to stress, however, that the mobility tensor depends on the choice of the body-fixed reference point inside the particle, which we discuss below.

For a spherical particle, the tt and rr parts reduce to 3×3 unit tensors

$$\boldsymbol{\mu}^{tt} = \mu^t_0 \mathbf{1}, \qquad \boldsymbol{\mu}^{rr} = \mu^r_0 \mathbf{1}, \tag{5.16}$$

where the single-particle mobility coefficients are given for stick boundary conditions at the spheres' surfaces by

$$\mu^t_0 = \frac{1}{6\pi\eta a}, \qquad \mu^r_0 = \frac{1}{8\pi\eta a^3}. \tag{5.17}$$

5.2.3 Hydrodynamic centre of mobility

The hydrodynamic mobility tensors depend on the shape and orientation of the particle, and can be calculated by solving the Stokes equations. However, it is important to stress that e.g. existence of non-zero components of $\boldsymbol{\mu}^{rt}$ does not imply the skewness of the particle, and does not allow any conclusions on the shape of the particle. In fact, since $\boldsymbol{\mu}$ depends on the choice of the reference point $\mathbf{R}$, $\boldsymbol{\mu}^{rt}$ and $\boldsymbol{\mu}^{tr}$ have non-zero components even in the case of a spherical particle, provided that a point outside the centre is chosen as reference. In the centre of the sphere, the coupling tensors vanish. The translational theorems for mobility [9] relate the mobility $\boldsymbol{\mu}_1$ calculated at a centre $\mathbf{r}_1$ and the mobility $\boldsymbol{\mu}_2$ at a centre $\mathbf{r}_2$

$$\boldsymbol{\mu}^{rr}_2 = \boldsymbol{\mu}^{rr}_1 = \boldsymbol{\mu}^{rr}, \tag{5.18}$$

$$\boldsymbol{\mu}^{rt}_2 = \boldsymbol{\mu}^{rt}_1 + \boldsymbol{\mu}^{rr} \times (\mathbf{r}_2 - \mathbf{r}_1), \tag{5.19}$$

$$\boldsymbol{\mu}^{tt}_2 = \boldsymbol{\mu}^{tt}_1 - (\mathbf{r}_2 - \mathbf{r}_1) \times \boldsymbol{\mu}^{rr} \times (\mathbf{r}_2 - \mathbf{r}_1) - (\mathbf{r}_2 - \mathbf{r}_1) \times \boldsymbol{\mu}^{rt}_1 + \boldsymbol{\mu}^{tr}_1 \times (\mathbf{r}_2 - \mathbf{r}_1) \tag{5.20}$$

with the notation that for a second-rank tensor $\mathbf{A}$ and a vector $\mathbf{v}$, one has $[\mathbf{A} \times \mathbf{v}]_{ij} = A_{ik}\epsilon_{jkl}v_l$ and $[\mathbf{v} \times \mathbf{A}]_{ij} = \epsilon_{ilk}v_l A_{kj}$. These relations may be used to show that for a given shape of the particle there is a unique point, called the centre of mobility, at which the coupling tensor $\boldsymbol{\mu}^{rt}$ becomes symmetric. Calculation of the mobility matrix at the unique centre of mobility allows for determination if the particle is skewed or not by examining if the coupling tensor $\boldsymbol{\mu}^{tr}$ has a non-zero component at this point. A similar reasoning may be applied for the friction tensor $\boldsymbol{\zeta}$, leading to the determination of the hydrodynamic centre of friction, where the friction coupling tensors $\boldsymbol{\zeta}^{rt}$ and $\boldsymbol{\zeta}^{tr}$ become symmetric, which in general is different from the centre of mobility [9, 125, 126].

For highly symmetric particles, like spheres or rods, the centre of mobility coincides with the centre of mass (and the geometric centre). This is no longer true, however, if the symmetry is lost, e.g. by the presence of a nearby boundary.

5.2.4 Friction and mobility of a conglomerate of spheres

The problem of determining the friction (or mobility) tensor of a particle of given shape requires solution of the Stokes equations for the flow around the particle. The problem, very difficult in general, may be solved differently.

In the following, we will present a general method used for determination of the N-particle grand resistance and mobility tensors for spherical particles. Suppose now we construct a bead model of a complex-shaped particle by gluing together a handful of spherical particles, thus restricting their relative motion. The single-particle friction matrix for such a conglomerate may then be obtained from the many-particle friction matrix by projecting it onto the subspace of rigid-body motion by including the constraints on the forces and velocities of the constituting spheres due to their fixed configuration. The details of this procedure are outlined in Appendix A.

In result, we find that the friction matrix $\boldsymbol{\zeta}$ for the conglomerate moving like a rigid-body is given in terms of the many-particle friction tensor $\boldsymbol{\zeta}_N$ by

$$\boldsymbol{\zeta} = \mathbf{K} \cdot \boldsymbol{\zeta}_N \cdot \mathbf{K}^{\mathrm{T}}, \tag{5.21}$$

where the detailed form of the $6N \times 6$ matrix $\mathbf{K}$ is given in Appendix A. The mobility tensor $\boldsymbol{\mu}$ of the conglomerate is then calculated by inverting the friction tensor $\boldsymbol{\zeta}$ in the FT subspace.

5.3 The multipole method

Having introduced a way of finding the mobility of complex-shaped particles, we proceed to the description of a numerical method which allows for the calculation of the N-particle friction and mobility tensors, needed as the input for the procedure described above. To this end, we use the multipole method [127] which relies on the projection of a set of boundary integral equations for the unknown force density distributions onto a set of irreducible multipole solutions of the Stokes equations. The set of algebraic equations obtained in this way may be truncated in a controlled way and solved numerically. Moreover, the method allows to determine analytically the asymptotic behaviour of the particle mobilities when the interacting objects are well separated.

Below, we shall first introduce the so-called induced forces picture which leads to construction of the boundary integral equations relating the force densities and velocities on the surfaces of the particles. It is followed by the discussion of the Green's tensors for the Stokes equations in three simple cases of an infinite fluid, fluid bounded by a planar free surface, and a hard no-slip wall. Then we will present in brief the infinite set of solutions of the Stokes equations suited for the problem and sketch the multipole expansion procedure. Next, we outline the idea of numerical solutions of the multipole equations.

5.3.1 Boundary integral equation formulation

Consider an ensemble of N spheres of radii a_i, $i = 1, \ldots, N$ in an incompressible Newtonian fluid. The fluid flow in this case satisfies the Stokes equations (5.2) outside the particles,

supplemented with appropriate boundary conditions on the surface of each sphere, which for stick boundary conditions on the sphere surfaces take the form

$$\mathbf{v}(\mathbf{r}) = \mathbf{v}_i(\mathbf{r}) = \mathbf{V}_i + \boldsymbol{\Omega}_i \times (\mathbf{r} - \mathbf{R}_i) \qquad \text{for} \quad |\mathbf{r} - \mathbf{R}_i| = a_i, \tag{5.22}$$

where $\mathbf{V}_i$ and $\boldsymbol{\Omega}_i$ are translational and rotational velocities of sphere i located at $\mathbf{R}_i$. The field $\mathbf{v}_i(\mathbf{r})$ hence follows the rigid motion of the particle i.

With the use of the concept of induced forces due to Bedeaux and Mazur [128], the validity of the Stokes equations (5.2) may be formally extended inside the particles, by taking $\mathbf{v}(\mathbf{r}) = \mathbf{v}_i(\mathbf{r})$ for $|\mathbf{r} - \mathbf{R}_i| \leq a_i$, with the force density $\mathbf{f}(\mathbf{r}) = \sum_i \mathbf{f}_i(\mathbf{r})$ acting on the fluid localized on the surfaces of the spheres, so that the force density arising from the sphere i, $\mathbf{f}_i(\mathbf{r})$, is non-zero only if $|\mathbf{r} - \mathbf{R}_i| = a_i$. Here, we assumed that the particles are impenetrable to the flow, but this assumption may be relaxed and a generalization to permeable particles is possible [96].

Using the concept of induced forces, it is possible to write the solution of the Stokes equations in the form of a boundary integral equation [117]

$$\mathbf{v}(\mathbf{r}) = \mathbf{v}_0(\mathbf{r}) + \int \mathrm{d}\mathbf{r}' \, \mathbf{T}(\mathbf{r}, \mathbf{r}') \cdot \mathbf{f}(\mathbf{r}'), \tag{5.23}$$

where $\mathbf{v}_0(\mathbf{r})$ is a regular solution to the Stokes equations in given geometry, representing an ambient flow which may be present in the absence of the spheres, and $\mathbf{T}(\mathbf{r}, \mathbf{r}_0)$ is the Green's tensor for the Stokes equations in given geometry. Its explicit form for the most important cases of a quiescent and a wall-bounded fluid is discussed in the following Sec. 5.3.2.

In order to establish a relation between the force densities and the velocities of the particles, we first consider a single particle i undergoing a rigid-body motion $\mathbf{v}_i(\mathbf{r})$, and immersed in an incident flow $\mathbf{v}_i^{\text{in}}$. The force density $\mathbf{f}_i$ it exerts on the fluid is linearly related to the relative velocity at the surface, viz.

$$\mathbf{f}_i = -\mathbf{Z}_0(i)(\mathbf{v}_i^{\text{in}} - \mathbf{v}_i), \tag{5.24}$$

where $\mathbf{Z}_0(i)$ is an integral operator, called the single-particle resistance operator, or friction kernel. Its explicit form is obtained by solving the Stokes equations for an isolated particle subject to an external flow [129], and therefore depends solely on the internal composition (e.g. porosity) and surface properties of the considered particle [116].

The flow incident on the surface Σ_i of particle i may now be regarded as sum of contributions from the external flow and from all the other particles

$$\mathbf{v}_i^{\text{in}}(\mathbf{r}) = \mathbf{v}_0(\mathbf{r}) + \sum_{j \neq i}^{N} \int \mathrm{d}\mathbf{r}' \, \mathbf{T}(\mathbf{r}, \mathbf{r}') \cdot \mathbf{f}_j(\mathbf{r}'), \qquad \mathbf{r} \in \Sigma_i, \tag{5.25}$$

where we assumed stick boundary conditions on the particle surfaces. Introducing the Green's integral operator (propagator), defined as

$$[\mathbf{G}(ij)\mathbf{f}_j](\mathbf{r}) \equiv \int \mathrm{d}\mathbf{r}' \, \mathbf{T}(\mathbf{r}, \mathbf{r}') \cdot \mathbf{f}_j(\mathbf{r}'), \qquad i \neq j, \qquad \mathbf{r} \in \Sigma_i, \tag{5.26}$$

we recast Eq. (5.25) in a compact form for each particle

$$\mathbf{f}_i = \mathbf{Z}_0(i) \left[\mathbf{v}_i - \mathbf{v}_0 - \sum_{j \neq i}^{N} \mathbf{G}(ij)\mathbf{f}_j \right], \qquad i = 1, \ldots, N. \tag{5.27}$$

Applying the inverse operator $\mathbf{Z}_0^{-1}(i)$ to both sides of the above equation, we finally arrive at a set of integral equations for the force densities on the surfaces S_i, $i = 1, \ldots N$, of the spheres

$$\mathbf{v}_i - \mathbf{v}_0 = \mathbf{Z}_0^{-1}(i)\mathbf{f}_i + \sum_{j\neq i}^{N} \mathbf{G}(ij)\mathbf{f}_j. \tag{5.28}$$

On the right-hand side of Eq. (5.28), the first term accounts for the contribution to the velocity of particle i from the induced forces located on its own surface, while the second term describes the sum of velocity increments of particle i due to induced forces located on the surface of particle j. Remarkably, the latter term is independent of the hydrodynamic model of the particles.

In the following, we shall outline a method of solving Eq. (5.28) using the multipole expansion of Stokes equations, and remark how this method can be used to construct the friction and mobility tensors with a well-controlled accuracy.

5.3.2 The Green's tensor for Stokes flows

Linearity of the Stokes equations allows to introduce the Green's tensor, called also the fundamental solution of the Stokes equations. The form of the Green's tensor $\mathbf{T}(\mathbf{r}, \mathbf{r}')$, together with the associated pressure vector $\mathbf{Q}(\mathbf{r}, \mathbf{r}')$ follows from the solution of the Stokes equations with a Dirac delta force density (point-force density) at $\mathbf{r}'$,

$$\eta\nabla^2\mathbf{T}(\mathbf{r}, \mathbf{r}') - \nabla\mathbf{Q}(\mathbf{r}, \mathbf{r}') = -\mathbf{1}\delta(\mathbf{r} - \mathbf{r}'), \qquad \nabla \cdot \mathbf{T}(\mathbf{r}, \mathbf{r}') = 0, \tag{5.29}$$

where $\mathbf{1}$ is the unit tensor, the gradients are taken with respect to $\mathbf{r}$, and the solution satisfies appropriate boundary conditions at infinity and at the boundaries of the system. For an unbounded fluid, $\mathbf{T}(\mathbf{r}, \mathbf{r}') = \mathbf{T}(\mathbf{r} - \mathbf{r}')$ is the Oseen tensor [9, 130]

$$\mathbf{T}_0(\mathbf{r}) = \frac{1}{8\pi\eta r}\left(\mathbf{1} + \hat{\mathbf{r}}\hat{\mathbf{r}}\right), \tag{5.30}$$

with $r = |\mathbf{r}|$ and $\hat{\mathbf{r}} = \mathbf{r}/r$, and the pressure field $\mathbf{Q}(\mathbf{r} - \mathbf{r}')$ reads

$$\mathbf{Q}_0(\mathbf{r}) = \frac{1}{4\pi}\frac{\hat{\mathbf{r}}}{r^2}. \tag{5.31}$$

In the presence of system boundaries, it is convenient to decompose the full Green's tensor into the Oseen tensor $\mathbf{T}_0$ and the part describing the flow reflected from interfaces

$$\mathbf{T}(\mathbf{r}, \mathbf{r}') = \mathbf{T}_0(\mathbf{r} - \mathbf{r}') + \tilde{\mathbf{T}}(\mathbf{r}, \mathbf{r}'). \tag{5.32}$$

For a fluid bounded by a planar hard wall, or a free surface, a closed form of the Green's tensor $\mathbf{T}$ is known. To present it, we assume the geometry of the system as sketched in Fig. 5.1 with the fluid occupying the upper half-space $z > 0$ above a boundary at $z = 0$. To give explicit expressions for $\mathbf{T}$, we introduce a reflection operator

$$\mathbf{P} = \mathbf{1} - \hat{\mathbf{e}}_z\hat{\mathbf{e}}_z, \tag{5.33}$$

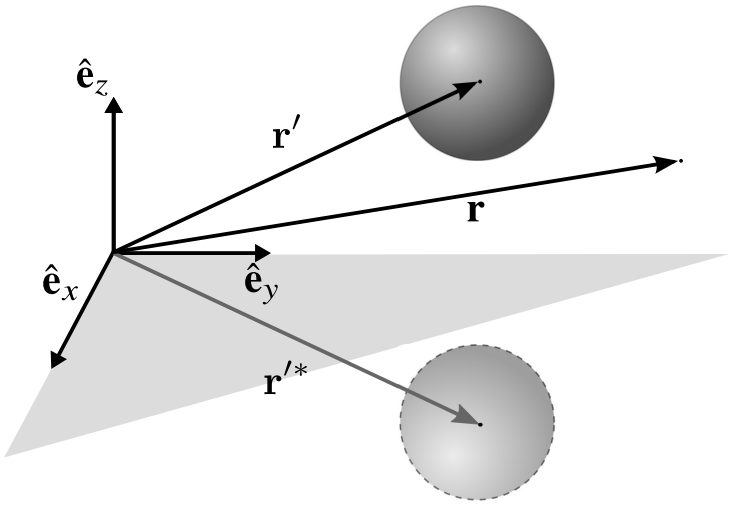

Figure 5.1: The image sphere for a spherical particle in the presence of a boundary which may be either a free slip surface, or a hard no-slip wall.

which transforms a point $\mathbf{r} = (x, y, z)$ into $\mathbf{r}^* = P \cdot \mathbf{r} = (x, y, -z)$. In the following, the asterisk will always refer to a mirror image point. For a free surface, at which the normal velocity and tangential stress vanish, the Green's tensor reads [44]

$$\mathbf{T}_\mathrm{f}(\mathbf{r}, \mathbf{r}') = \mathbf{T}_0(\mathbf{r} - \mathbf{r}') + \tilde{\mathbf{T}}_f(\mathbf{r}, \mathbf{r}') = \mathbf{R}_0(\mathbf{r} - \mathbf{r}') + \mathbf{T}_0(\mathbf{r} - \mathbf{r}'^*) \cdot \mathbf{P}. \tag{5.34}$$

In particular we see that for a point force (a Stokeslet) $\mathbf{f}_0\delta(\mathbf{r} - \mathbf{r}')$, the velocity field $\mathbf{v}(\mathbf{r}) = \mathbf{T}_\mathrm{F}(\mathbf{r}, \mathbf{r}') \cdot \mathbf{f}_0$ in the presence of a free surface is equivalent to that of a Stokeslet with its mirror image at $\mathbf{P} \cdot \mathbf{r}'$.

For a hard no-slip wall, the Green tensor has been found by Lorentz in 1907 [36] as

$$\begin{aligned}\mathbf{T}_\mathrm{w}(\mathbf{r}, \mathbf{r}') = \mathbf{T}_0(\mathbf{r} - \mathbf{r}') + \tilde{\mathbf{T}}_w(\mathbf{r}, \mathbf{r}') = \mathbf{T}_0(\mathbf{r} - \mathbf{r}') - \mathbf{T}_0(\mathbf{r} - \mathbf{r}'^*) \cdot \mathbf{P} \\ - 2z_0\hat{\mathbf{e}}_z \cdot \mathbf{T}_0(\mathbf{r} - \mathbf{r}'^*)\overleftarrow{\boldsymbol{\nabla}}_\mathbf{r} \cdot \mathbf{P} \\ + z_0^2\nabla_\mathbf{r}^2\mathbf{T}_0(\mathbf{r} - \mathbf{r}'^*) \cdot \mathbf{P},\end{aligned} \tag{5.35}$$

where $[\mathbf{a}\overleftarrow{\boldsymbol{\nabla}}_\mathbf{r}]_{\alpha\beta} = \frac{\partial}{\partial \mathbf{r}_\beta}\mathbf{a}_\alpha$. Other forms of this expression are available e.g. in Refs. [118,131,132]. We note that in this case the image system for a Stokeslet involves faster decaying additional terms, the so-called Stokeslet doublet and source doublet, which are discussed in detail in Blake's work [131]. However, since their amplitude is proportional to the wall-particle distance h, asymptotically they die out with distance r as $1/r$.

5.3.3 Spherical solutions of the Stokes equations

To describe the motion of the fluid in the presence of spherical boundaries (particles), Felderhof and co-workers [91, 133] derived a set of solutions of the homogeneous Stokes equations which form a complete orthogonal basis on a spherical surface. Their set comprises of linear combinations of solutions due to Lamb [9, 38, 134] and is better suited to the solution of the inhomogeneous equations which appear in the presence of colloidal spheres.

The spherical solutions may be divided into two sets $\{\mathbf{v}^+_{lm\sigma}(\mathbf{r})\}$ and $\{\mathbf{v}^-_{lm\sigma}(\mathbf{r})\}$, characterized by a set of three quantum numbers: the angular momentum number $l = 1, 2, \ldots$, the azimuthal number m taking the values $-l, \ldots, l$ and the subscript $\sigma \in \{0, 1, 2\}$. Explicit expressions for these solutions are given in Refs. [116, 118, 127]. The solutions $\{\mathbf{v}^+_{lm\sigma}(\mathbf{r})\}$ grow at infinity and are regular at $\mathbf{r} = 0$, while $\{\mathbf{v}^-_{lm\sigma}(\mathbf{r})\}$ are singular at $\mathbf{r} = 0$ and vanish at infinity.

We also define the adjoint sets of functions $\{\mathbf{w}^\pm_{lm\sigma}(\mathbf{r})\}$, which are orthonormal with respect to $\{\mathbf{v}^\pm_{lm\sigma}(\mathbf{r})\}$ on a sphere of arbitrary radius b

$$\left\langle \mathbf{w}^\pm_{lm\sigma}(\mathbf{r})\delta_b | \mathbf{v}^\pm_{l'm'\sigma'}(\mathbf{r}) \right\rangle = \delta_{ll'}\delta_{mm'}\delta_{\sigma\sigma'}, \tag{5.36}$$

where we introduced a scalar product of two complex-valued vector fields $\mathbf{f}(\mathbf{r})$ and $\mathbf{g}(\mathbf{r})$

$$\langle \mathbf{f} | \mathbf{g} \rangle = \int \mathrm{d}\mathbf{r}\, \mathbf{f}^*(\mathbf{r}) \cdot \mathbf{g}(\mathbf{r}), \tag{5.37}$$

and δ_b is a shorthand for $\delta_b(\mathbf{r}) = \frac{1}{b}\delta(|\mathbf{r}| - b)$.

5.3.4 The multipole expansion method

The general procedure of the multipole expansion applies in both an infinite fluid, and in the presence of boundaries, provided that the form of the Green function $\mathbf{T}$ is known [127]. The forces, torques, and velocities are projected on (or expanded in) a basic set of irreducible multipole functions [116,117,133,135,136] described above. The coefficients of this expansion, called force and velocity multipoles, form an infinite set of algebraic equations which then may be solved at a desired precision. Without loss of generality, we consider the wall-bounded fluid below.

We begin with expanding the velocity on the surface of particle i in terms of regular solutions $\{\mathbf{v}^+_{lm\sigma}\}$ centred at $\mathbf{R}_i$, viz.

$$\mathbf{v}_i(\mathbf{r}) - \mathbf{v}_0(\mathbf{r}) = \sum_{lm\sigma} c(ilm\sigma)\mathbf{v}^+_{lm\sigma}(\mathbf{r} - \mathbf{R}_i), \tag{5.38}$$

where the velocity multipoles are defined using the adjoint functions as

$$c(ilm\sigma) = \left\langle \mathbf{w}^+_{lm\sigma}(i)\delta_a(i) | \mathbf{v}_i - \mathbf{v}_0 \right\rangle, \tag{5.39}$$

with $\mathbf{w}^+_{lm\sigma}(i)$ being short for $\mathbf{w}^+_{lm\sigma}(\mathbf{r} - \mathbf{R}_i)$ and $\delta_a(i) = \delta_a(\mathbf{r} - \mathbf{R}_i)$. In a similar manner, one defines the force multipole moments on the sphere j, viz.

$$f(jlm\sigma) = \int \mathrm{d}\mathbf{r}'\, \mathbf{v}^{+*}_{lm\sigma}(\mathbf{r}' - \mathbf{R}_j)\mathbf{f}_j(\mathbf{r}') = \left\langle \mathbf{v}^+_{lm\sigma} | \mathbf{f}_j \right\rangle. \tag{5.40}$$

By the use of the so-called antenna theorems [135], the Oseen tensor may be expanded in terms of the flow solutions about an arbitrary point [44]. In Eq. (5.35), the Green's tensor $\mathbf{T}_w$ in the presence of a hard wall is decomposed into two parts, as in Eq. (5.32), the former describing the flow in an unbounded space (Oseen tensor $\mathbf{T}_0$) and the latter accounting for that reflected from

the wall (Blake's images $\tilde{\mathbf{T}}_w$). Accordingly, the associated propagator $\mathbf{G}$, defined in Eq. (5.26), admits the following decomposition

$$\mathbf{G} = \mathbf{G}_0 + \mathbf{G}_w, \tag{5.41}$$

where the former part $\mathbf{G}_0$ consists of the multipole elements of the Oseen tensor and accounts for interactions between the particles in flow, and the latter, $\mathbf{G}_w = \mathbf{G}' \cdot \mathcal{R}$, encompasses interactions with image particles. The multipole matrix elements of $\mathbf{G}_0$, $\mathbf{G}'$, and $\mathcal{R}$ may be found in Ref. [118]. In this case, the propagator between particles, say, i and j, has two parts: $\mathbf{G}_0(ij)$ describing direct interaction alike to that in an infinite fluid, and $[\mathbf{G}' \cdot \mathcal{R}](ij)$ accounting for interaction between the particle i and the mirror image of particle j with respect to the boundary (usually denoted by j^*). In the latter, $\mathbf{G}'$ denotes the propagator of interaction between an actual particle (i) and the image of the second particle (j^*), while the tensor $\mathcal{R}$, depending on the distance of the particle j from the wall, accounts for the change of the multipolar character of the flow due to a reflection off the wall. Differently to the free-space propagator $\mathbf{G}_0$, the wall propagator $\mathbf{G}_w$ is non-zero for self-interaction, that is for a particle i interacting with its own image i^*.

It is important to note that the multipole matrix elements of the propagator $\mathbf{G}(ij)$ depend on the distance between the particles as

$$(lm\sigma|\, \mathbf{G}(ij)\, |l'm'\sigma') \sim \left(\frac{1}{R_{ij}}\right)^{l+l'+\sigma+\sigma'-1}. \tag{5.42}$$

Moreover, we note here that the matrix elements of $\mathbf{G}_w$ follow the same distance-dependence. Although the image system in Eq. (5.35) contains higher-order multipoles already in response to a point force, they are multiplied by the wall-particle distance (encoded in $\mathcal{R}$), and in result the matrix elements of $\mathbf{G}_w$ decay according to their multipole indices in the same way as in Eq. (5.42) above.

Inserting the expansion of $\mathbf{T}$, together with Eq. (5.38) for $\mathbf{v}_i - \mathbf{v}_0$, and Eq. (5.40) for $\mathbf{f}_j$, into Eq. (5.28), we arrive at the following infinite system of algebraic equations

$$c(ilm\sigma) = \sum_{jl'm'\sigma'} (lm\sigma|\, \mathbf{M}(ij)\, |l'm'\sigma')\, f(jl'm'\sigma'), \tag{5.43}$$

where $(lm\sigma|\, \mathbf{M}(ij)\, |l'm'\sigma')$ denotes the multipole matrix elements of the operator

$$\mathbf{M}(ij) = \mathbf{Z}_0^{-1}(i)\delta_{ij} + \mathbf{G}(ij)(1 - \delta_{ij}), \tag{5.44}$$

and may be derived from the multipole representation of the operators $\mathbf{Z}_0^{-1}(i)$ and $\mathbf{G}(ij)$.

Introducing inifnite-dimensional vectors $\mathbf{c}$ and $\mathbf{f}$ with components $c(ilm\sigma)$ and $f(jlm\sigma)$, respectively, we may write Eq. (5.43) in a compact form

$$\mathbf{c} = \mathbf{M} \cdot \mathbf{f} = (\mathbf{Z}_0^{-1} + \mathbf{G}) \cdot \mathbf{f}. \tag{5.45}$$

Upon inverting this relation, one may define the grand resistance matrix $\mathbf{Z}$ via

$$\mathbf{f} = \mathbf{Z} \cdot \mathbf{c}, \qquad \mathbf{Z} = \mathbf{M}^{-1}. \tag{5.46}$$

The forms of the infinite-dimensional tensors $\mathbf{Z}$ and $\mathbf{M}$ for unbounded fluid, fluid bounded by a free surface and fluid bounded by a hard wall, are given explicitly in Ref. [46]. It is worth

noting that the matrix $\mathbf{Z}_0$ is diagonal in particle indices, since it comprises of single-particle friction operators. These are obtained by solving the Stokes equations for an isolated particle in an external flow and fully determined by the particle internal structure and boundary conditions on its surface. Moreover, due to spherical symmetry, the matrix $\mathbf{Z}_0(i)$ is diagonal in indices l, m. The explicit form of the coefficients of this matrix for specific boundary conditions are given in Refs. [91, 116].

5.3.5 Physical meaning of the lowest-order multipoles

In the course of this work, we will be interested in extracting from the multipole expansion coefficients the relation between forces and torques acting on the particles and their translational and angular velocities. It is therefore important to interpret these quantities in the language of velocity and force multipoles, defined in Eqs. (5.38) and (5.40), respectively. For simplicity, we consider here a quiescent fluid with no external flow.

In the multipole description, components of the total force $\mathbf{F}_i$ in spherical basis [137] are given by the elements of $f(ilm\sigma)$ with indices $l = 1$, $\sigma = 0$, and $m = -1, 0, 1$. The terms with $l = 1$, $\sigma = 1$ and $m = -1, 0, 1$ encode the components of the total torque $\mathbf{T}_i$. Similarly, the components of $c(ilm\sigma)$ with $l = 1$, $\sigma = 0$, and $m = -1, 0, 1$ correspond to the total velocity $\mathbf{V}_i$, while those with $\sigma = 1$ describe the angular velocity $\mathbf{\Omega}_i$. The terms with $l = 2$ and $\sigma = 0$ refer to dipolar components: symmetric dipole moment for the force, and rate of strain for velocity. The Cartesian form of these quantities may be recovered from the complex multipole representation by a simple change of basis. In the same manner, the higher order moments of the force and velocity distributions are encoded in the multipole coefficients. For a broader discussion, see Ref. [127].

In the following, we shall use the following shorthand notation for the lowest-order multipole matrix elements

$$\begin{aligned} (lm\sigma) = (1m0) &\to t, \\ (1m1) &\to r, \\ (2m0) &\to d, \end{aligned} \tag{5.47}$$

with indices referring to translational (t), rotational (r) and dipolar (d) type of motion. For example, in this notation the matrix element $(1m0|\,\mathbf{M}(ij)\,|1m'1)$ appearing in Eq. (5.43) may be written as $[\mathbf{M}^{tr}(ij)]_{m,m'}$.

5.3.6 Numerical calculation of friction and mobility

In numerical computations, the infinite matrices $\mathbf{Z}_0$ and $\mathbf{G}$ (and therefore also $\mathbf{M}$) in Eq. (5.45) are truncated at the multipole order ℓ, so that only the elements with $l \leq \ell$ are considered [117]. After such a truncation, the matrix $\mathbf{M}$ is inverted, and the force multipoles are determined. To improve numerical convergence of this scheme, the obtained grand friction matrix $\mathbf{Z}$ in Eq. (5.46) is additionally corrected for lubrication effects which play a dominant role when the particles come close together [121, 127, 138, 139]. Remarkably, the matrix $\mathbf{Z}$ constructed in the multipole method is not pairwise additive, and accounts fully for many-body hydrodynamic

interactions. The approximation is introduced at the level of truncation of the multipoles, and its error may be controlled.

The forces and torques may now be found by projecting the grand friction matrix on the subspaces $l = 1$, $\sigma = 0$ (t), and $l = 1$, $\sigma = 1$ (r), respectively. This procedure leads to the solution of the friction problem in which the forces and torques are searched for, given the velocities. The mobility problem of finding the translational and rotational velocities once the forces and torques are given requires the inversion of the matrix $\mathbf{Z}$, but only in the space spanned by the multipole functions with $l = 1$ and $\sigma = \{0, 1\}$. According to this procedure, the mobility matrix $\boldsymbol{\mu}$ is found [115]. One may also proceed differently to avoid direct inversion of a large matrix, and use the method described in Ref. [117].

The procedures outlined above have been implemented in a Fortran code HYDROMULTIPOLE [117, 138] by Wajnryb and collaborators. We will make use of these codes for the calculation of friction and mobility of non-spherical particles represented by bead-models.

It is worth adding that over the years, many simpler methods have been devised in order to account for hydrodynamic interactions between particles close to a planar boundary. Early numerical studies used simply the point-particle approximation, with additional Blake-type images [131] to mimic the flow reflected off the boundary. Other attempts were based on adaptation of the unbounded fluid approximate schemes, like the Rotne-Prager [140] model, with the wall taken into account by a multipole expansion of the Stokeslet reflection off the wall [141], or by a reflection of the Rotne-Prager tensor [142]. More accurate techniques, being a generalisation of Stokesian Dynamics method, were developed by J. Brady and co-workers [139, 143]. Here, we have decided to use the most precise technique available to explore near-wall hydrodynamics of axisymmetric colloids.

5.4 Bulk dynamics of axisymmetric particles

We will now confine our attention to the case of an axisymmetric particle and see how the symmetry influences the general form of the single-particle mobility matrix $\boldsymbol{\mu}$. For the description of the particle configuration, it suffices then to specify a body-fixed centre $\mathbf{R}$, which we choose to be the geometric centre, and a unit orientation vector $\hat{\mathbf{u}}$ pointing along the axis of symmetry.

First, we employ arguments of translational and rotational invariance to express the Cartesian

components of the mobility matrix in terms of a set of scalar functions [116]

$$
\begin{aligned}
\mu^{tt}_{\alpha\beta} &= \mu^{t}_{\parallel} u_\alpha u_\beta + \mu^{t}_{\perp}(\delta_{\alpha\beta} - u_\alpha u_\beta), \\
\mu^{rr}_{\alpha\beta} &= \mu^{r}_{\parallel} u_\alpha u_\beta + \mu^{r}_{\perp}(\delta_{\alpha\beta} - u_\alpha u_\beta), \\
\mu^{tr}_{\alpha\beta} &= \mu^{tr} \epsilon_{\alpha\beta\sigma} u_\sigma, \\
\mu^{rt}_{\alpha\beta} &= \mu^{rt} \epsilon_{\alpha\beta\sigma} u_\sigma, \\
\mu^{td}_{\alpha\beta\gamma} &= \mu^{td}_1 u_\alpha \overline{u_\beta u_\gamma}^{(\beta\gamma)} + \mu^{td}_2 \overline{(\delta_{\alpha\beta} - u_\alpha u_\beta) u_\gamma}^{(\beta\gamma)}, \\
\mu^{rd}_{\alpha\beta\gamma} &= \mu^{rd} u_\sigma \overline{\epsilon_{\sigma\alpha\beta} u_\gamma}^{(\beta\gamma)}, \\
\mu^{dt}_{\alpha\beta\gamma} &= \mu^{dt}_1 \overline{u_\alpha u_\beta}^{(\alpha\beta)} u_\gamma + \mu^{td}_2 \overline{u_\alpha (\delta_{\beta\gamma} - u_\beta u_\gamma)}^{(\alpha\beta)}, \\
\mu^{dr}_{\alpha\beta\gamma} &= \mu^{dr} \overline{u_\alpha \epsilon_{\beta\gamma\sigma}}^{(\alpha\beta)} u_\sigma, \\
\mu^{dd}_{\alpha\beta\gamma\nu} &= \mu^{dd}_1 \overline{u_\alpha u_\beta}^{(\alpha\beta)} \overline{u_\gamma u_\nu}^{(\gamma\nu)} + \mu^{dd}_2 \left[\overline{\delta_{\alpha\gamma} u_\beta u_\nu}^{(\alpha\beta)(\gamma\nu)} - \overline{u_\alpha u_\beta}^{(\alpha\beta)} \overline{u_\gamma u_\nu}^{(\gamma\nu)} \right] \\
&\quad + \mu^{dd}_3 \left[\overline{\delta_{\alpha\gamma}\delta_{\beta\nu}}^{(\alpha\beta)(\gamma\nu)} - 2\overline{\delta_{\alpha\gamma} u_\beta u_\nu}^{(\alpha\beta)(\gamma\nu)} + \frac{1}{2} \overline{u_\alpha u_\beta}^{(\alpha\beta)} \overline{u_\gamma u_\nu}^{(\gamma\nu)} \right].
\end{aligned}
\tag{5.48}
$$

where the Greek letters denote the Cartesian components. The symbol $\overline{}^{(\alpha\beta)}$ indicates the symmetric and traceless part in the index pair (α, β). The appropriate reductions read

$$
\begin{aligned}
&\overline{u_\alpha u_\beta}^{(\alpha\beta)} && = u_\alpha u_\beta - \tfrac{1}{3}\delta_{\alpha\beta}, \\
&\overline{u_\alpha(\delta_{\beta\gamma} - u_\beta u_\gamma)}^{(\alpha\beta)} && = \tfrac{1}{2}(u_\alpha \delta_{\beta\gamma} + u_\beta \delta_{\alpha\gamma}) - u_\alpha u_\beta u_\gamma, \\
&\overline{\delta_{\alpha\gamma}\delta_{\beta\nu}}^{(\alpha\beta)(\gamma\nu)} && = \tfrac{1}{2}(\delta_{\alpha\gamma}\delta_{\beta\nu} + \delta_{\alpha\nu}\delta_{\beta\gamma}) - \tfrac{1}{3}\delta_{\alpha\beta}\delta_{\gamma\nu}, \\
&\overline{u_\alpha \epsilon_{\beta\gamma\sigma}}^{(\alpha\beta)} u_\sigma && = \tfrac{1}{2}(u_\alpha \epsilon_{\beta\gamma\sigma} u_\sigma + u_\beta \epsilon_{\alpha\gamma\sigma} u_\sigma), \\
&\overline{\delta_{\alpha\gamma} u_\beta u_\nu}^{(\alpha\beta)(\gamma\nu)} && = \tfrac{1}{4}(\delta_{\alpha\gamma} u_\beta u_\nu + \delta_{\alpha\nu} u_\beta u_\gamma + \delta_{\beta\gamma} u_\alpha u_\nu + \delta_{\beta\nu} u_\alpha u_\gamma) \\
&&& \quad - \tfrac{1}{3}(\delta_{\alpha\beta} u_\gamma u_\nu + u_\alpha u_\beta \delta_{\gamma\nu}) + \tfrac{1}{9}\delta_{\alpha\beta}\delta_{\gamma\nu}.
\end{aligned}
\tag{5.49}
$$

In addition, it follows from the Lorentz theorem that

$$
\mu^{tr} = -\mu^{rt}, \qquad \mu^{td}_1 = -\mu^{dt}_1, \qquad \mu^{td}_2 = -\mu^{dt}_2, \qquad \mu^{rd} = \mu^{dr}. \tag{5.50}
$$

It is important to mention here that the components of the friction matrix have the same form as in Eq. (5.48) with the symbol μ simply replaced by ζ, but the scalar friction coefficient behave differently to those of mobility, and read

$$
\zeta^{tr} = -\zeta^{rt}, \qquad \zeta^{td}_1 = \zeta^{dt}_1, \qquad \zeta^{td}_2 = \zeta^{dt}_2, \qquad \zeta^{rd} = -\zeta^{dr}. \tag{5.51}
$$

For the specific choice of the geometric centre as the reference point, it follows from symmetry arguments that the mobility matrix has the form [144]

$$
\boldsymbol{\mu} = \begin{pmatrix} \boldsymbol{\mu}^{tt} & \mathbf{0} & \boldsymbol{\mu}^{td} \\ \mathbf{0} & \boldsymbol{\mu}^{rr} & \boldsymbol{\mu}^{rd} \\ \boldsymbol{\mu}^{dt} & \boldsymbol{\mu}^{dr} & \boldsymbol{\mu}^{dd} \end{pmatrix}, \tag{5.52}
$$

with no tr components present. Importantly, this form is valid for arbitrary solids of revolution (pear-shaped objects). With an additional assumption of inversional symmetry (i.e. invariance under the change $\hat{\mathbf{u}} \to -\hat{\mathbf{u}}$), such as rod-shaped particles, we additionally have $\boldsymbol{\mu}^{dt} = \boldsymbol{\mu}^{td} = \mathbf{0}$.

For axisymmetric bodies modelled as spheroids, both oblate and prolate, the scalar mobility coefficients in Eq. (5.48) may be calculated from the corresponding scalar friction functions which are given in the monograph by Kim & Karrila [9] in terms of their eccentricity. The mobility functions may then be calculated using the results from Sec. 5.2.2.

5.4.1 Slender body theory

The slender body theory allows to determine the friction and mobility of an elongated, needle-like body moving in a viscous fluid. Typically, the far-field flow due to the motion of a particle is obtained by a multipole expansion of the surface distribution of Stokeslets about the particle centre. Here, taking advantage of the slenderness of the particle, the original idea due to Batchelor [145] was that the disturbance flow such a rigid body produces may be accurately represented by a line distribution of Stokeslets along the body centre line. In this way, one may find the velocity field by integrating this distribution over the body length L. An asymptotic expansion of these integrals is made in the limit of large particle aspect ratio $p = L/a$, where a is the particle diameter. The small parameter in the expansion reads

$$\epsilon = \left[\log\left(\frac{L}{a}\right)\right]^{-1}. \tag{5.53}$$

This procedure yields the translational friction coefficients for an elongated rod as

$$\begin{aligned} \zeta^t_{\parallel} &= \pi\eta L\epsilon(2 - 0.614\epsilon + O(\epsilon^2)), \\ \zeta^t_{\perp} &= 2\pi\eta L\epsilon(2 - 1.386\epsilon + O(\epsilon^2)). \end{aligned} \tag{5.54}$$

Such a calculation disregards any end-effects that come into play for particles of non-negligible thickness. To correctly reproduce them, one needs to adopt a more refined model, such as the bead model described in the following. Over the years, slender body theory has been improved [146] and applied to curved filaments [147]. It is worth noting that the slender body theory has later been generalised to particles moving close to walls [100] where analytical results have been obtained for near-wall friction in special cases of the rod parallel and normal to the wall. Numerical integration of the resulting equations of motion has led to an analysis of trajectories of rods sedimenting next to a vertical wall [99, 148].

5.4.2 Bead and shell models

Since the slender body theory is applicable only to very elongated bodies, it is of limited value for the determination of bulk mobility of particles with a moderate aspect ratio. Moreover, since many problems involve asymmetric particles, it is important to be able to calculate their hydrodynamic properties accurately. To this end, a different approach may be used which relies on modelling particles as collections of subunits staying at a fixed configuration. This idea dates back to pioneering works of Riseman and Kirkwood [149], who modelled a rod as a string

of beads. It has later been developed and extensively used to model e.g. macromolecules in solutions [150], like small proteins [151], particle aggregates [152], or to trace the hydrodynamic effect of particle shape reconfiguration, like in the case of fibrinogen [153].

These hydrodynamic models have evolved into two main classes: bead models, where a particle is represented by an array of a moderate number of spherical beads of different radii, and shell models in which the contour of a particle is represented by a shell composed of a large number of minibeads. While the former may be treated e.g. using the above described multipole method, the latter have the advantage of being capable of accurately reproducing fine details of the particle structure which is especially interesting from the point of view of biological macromolecules.

Using such models, bulk hydrodynamic coefficients may be very accurately determined by the use of the HYDROSUB numerical routines [154], which rely on modelling a complex-shaped particle as a collection of spherical minibeads constituting a shell model of the particle. Then its hydrodynamic properties are retrieved using the HYDRO codes [155] which employ the approximate Rotne-Prager-Yamakawa tensor [140,156] to account for hydrodynamic interactions between the minibeads. By repeating this procedure for several values of the minibead radius r_m, and results are extrapolated to the shell model limit of $r_m \to 0$. For the particularly interesting in the scope of this work case of rod-like and disk-like particles, the results of this procedure have been summarized by Ortega and García de la Torre [157]. For a cylindrical particle of aspect ratio p and length L in a solvent of viscosity η, the mean translational mobility

$$\bar{\mu}^t = \frac{1}{3}\left(\mu^t_{\parallel} + 2\mu^t_{\perp}\right) = \frac{1}{3\pi\eta L}(\ln p + C^t), \tag{5.55}$$

and the rotational mobility

$$\mu^r_{\perp} = \frac{3}{\pi\eta L^3}(\ln p + C^r_{\perp}), \tag{5.56}$$

differ from their slender body values by the end-effect terms, C^t and $C^r_{\perp}$, which have been shown [158, 159] to be well approximated by the following interpolation functions

$$C^t = \quad 0.312 + 0.565/p - 0.100/p^2, \tag{5.57}$$

$$C^r_{\perp} = -0.662 + 0.917/p - 0.050/p^2, \tag{5.58}$$

in the range of aspect ratios p between 2 and 20. Analogous results for the sidewise and lengthwise translational mobility coefficients, $\mu^t_{\parallel}$ and $\mu^t_{\perp}$, are summarized and extended in Refs. [157–159]. Importantly, since the mobility coefficients are related to diffision coefficients by $\mathbf{D} = k_B T \boldsymbol{\mu}$, using these results one can accurately predict bulk diffusion coefficients for rod- and disk-shaped particles, which can be used as reference values, provided that the shape is known, or, conversely, determine the aspect ratio of particles if the experimental values for $D^{t,r}$ are available.

5.5 Mobility of an axisymmetric particle close to a wall

Axially symmetric particles moving close to a boundary experience an additional anisotropic drag force on top of their own friction anisotropy stemming from their non-spherical shape. This coupling leads to a complicated behaviour, observed e.g. in simulations of such particles

sedimenting next to a vertical wall [99, 148], with the mobility of the particle depending on its inclination and distance to the wall. The available predictions for the near-wall mobility of an axisymmetric particle feature either a slender-body approach, applied only in several special alignments [100], or numerical predictions [97,98] from which empirical relations are extracted. Below, we find the analytical form of the leading order terms of the correction to bulk mobility due to the presence of a wall, and assess its validity in terms of distance and orientation of the particle. Our analysis leads to a convenient representation of the mobility tensor in situations when the particle is moderately far from the wall.

For the particle staying very close to the wall, lubrication theory has to be used to describe the asymptotic behaviour of the mobility matrix components when approaching the wall [160]. We discuss this motion in more detail in Chapter 7, focusing now on the far-field effects.

5.5.1 Geometry of the system

For a convenient description of the near-wall dynamics of an axisymmetric particle, we introduce three coordinate systems exploiting the symmetries of the considered situation, and sketched in Fig. 5.2.

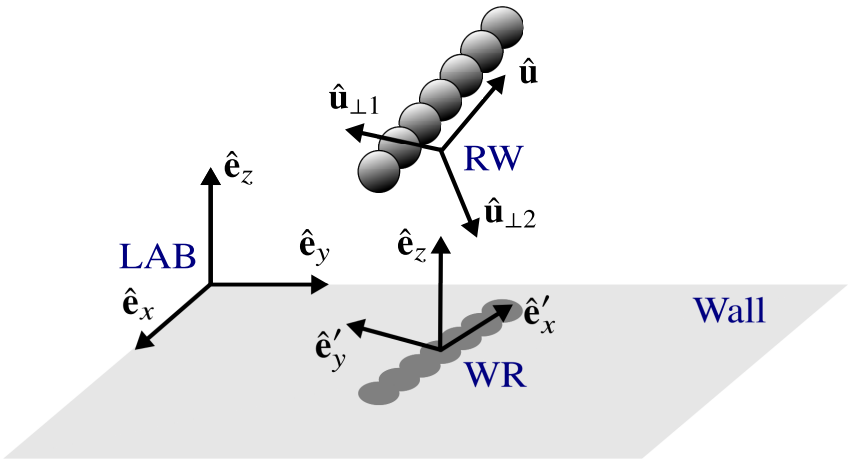

Figure 5.2: Three orthogonal coordinate systems used to describe the dynamics of an axisymmetric particle. Laboratory frame (LAB), body-fixed frame (RW), and the so-called wall-rod (WR) frame following the particle's projection on the wall.

The laboratory coordinate system (**LAB**) consists of three basis vectors $\left\{\hat{\mathbf{e}}_x, \hat{\mathbf{e}}_y, \hat{\mathbf{e}}_z\right\}$, with the z-axis normal to the wall, as described before. We also introduce the normal vector $\hat{\mathbf{n}} = \hat{\mathbf{e}}_z$.

The rod-wall (**RW**) system is a body-fixed set of basis vectors $\{\hat{\mathbf{u}}, \hat{\mathbf{u}}_{\perp 1}, \hat{\mathbf{u}}_{\perp 2}\}$, where $\hat{\mathbf{u}}$ is the unit vector along the long axis of the particle, $\hat{\mathbf{u}}_{\perp 1}$ is parallel to the wall and perpendicular to the particle axis, and $\hat{\mathbf{u}}_{\perp 2}$ completes the orthonormal basis. The basis vectors are thus given by

$$\hat{\mathbf{u}}_{\perp 1} = \frac{\hat{\mathbf{n}} \times \hat{\mathbf{u}}}{|\hat{\mathbf{n}} \times \hat{\mathbf{u}}|}, \qquad \hat{\mathbf{u}}_{\perp 2} = \hat{\mathbf{u}}_{\perp 1} \times \hat{\mathbf{u}}. \tag{5.59}$$

Hence their components in the LAB system read

$$\hat{\mathbf{u}} = (\sin\theta\cos\varphi, \sin\theta\sin\varphi, \cos\theta), \tag{5.60}$$
$$\hat{\mathbf{u}}_{\perp 1} = (-\sin\varphi, \cos\varphi, 0), \tag{5.61}$$
$$\hat{\mathbf{u}}_{\perp 2} = (\cos\theta\cos\varphi, \cos\theta\sin\varphi, -\sin\theta), \tag{5.62}$$

where θ and φ are the spherical angles of $\hat{\mathbf{u}}$ in the LAB frame, with $\cos\theta = \hat{\mathbf{n}} \cdot \hat{\mathbf{u}}$. Additionally, we have the relation $\hat{\mathbf{u}}_{\perp 1} = \hat{\mathbf{u}} \times \hat{\mathbf{u}}_{\perp 2}$.

The wall-rod (**WR**) system is constructed as a mixture of the two aforementioned systems to facilitate the form of the mobility matrix. Its basis vectors $\left\{\hat{\mathbf{e}}'_x, \hat{\mathbf{e}}'_y, \hat{\mathbf{e}}'_z\right\}$ are defined as

$$\hat{\mathbf{e}}'_y = \hat{\mathbf{u}}_{\perp 1}, \qquad \hat{\mathbf{e}}'_z = \hat{\mathbf{e}}_z, \qquad \hat{\mathbf{e}}'_x = \hat{\mathbf{u}}_{\perp 1} \times \hat{\mathbf{e}}_z, \tag{5.63}$$

i.e. the z'-axis is normal to the wall, the y'-axis is parallel to the wall and normal to the particle axis, and finally the x'-axis is parallel to the wall and lies in the plane $(\hat{\mathbf{u}}, \hat{\mathbf{n}})$. The WR basis vectors may be obtained from the LAB basis by rotating it by the angle φ about the axis $\hat{\mathbf{e}}_z$.

5.5.2 General form of the mobility tensors

For an axially symmetric particle, it is convenient to use the representation of the mobility matrix in the RW frame. Taking into account the invariant properties of the rod-wall system and the Lorentz symmetry one can write the translational-translational part as

$$\boldsymbol{\mu}^{tt}_w(z, \hat{\mathbf{u}}; \hat{\mathbf{n}}) = \begin{pmatrix} a_t(z,w) & 0 & c_t(z,w) \\ 0 & b_t(z,w) & 0 \\ c_t(z,w) & 0 & d_t(z,w) \end{pmatrix}_{RW} \tag{5.64}$$

where $w = \cos\theta$.

The matrix $\boldsymbol{\mu}^{rr}(z, \hat{\mathbf{u}}; \hat{\mathbf{n}})$ has a similar structure with elements a_r, b_r, c_r, and d_r, respectively. In both cases, the elements a, b and d are even functions of w and the elements c are odd ones. For the (tr) part one has

$$\boldsymbol{\mu}^{tr}_w(z, \hat{\mathbf{u}}; \hat{\mathbf{n}}) = \begin{pmatrix} 0 & a_{tr}(z,w) & 0 \\ b_{tr}(z,w) & 0 & c_{tr}(z,w) \\ 0 & d_{tr}(z,w) & 0 \end{pmatrix}_{RW} \tag{5.65}$$

The elements a_{tr} and b_{tr} are even functions of w, while c_{tr} and d_{tr} are odd ones. By taking the transposition of the above matrix we get the (rt) part. Remarkably, if we choose the hydrodynamic centre of mobility as the reference point inside the particle, the $\boldsymbol{\mu}^{tr}_w$ matrix becomes symmetric, implying $c_{tr} = d_{tr}$ and $a_{tr} = b_{tr}$. For large particle-wall distances, we expect the centre of mobility to coincide with the geometric centre of the rod.

For practical calculations and further analysis, it is also useful to explore the explicit form of the mobility matrix in the WR wall frame. Using the appropriate basis transformation (a simple rotation by θ about the axis $\hat{\mathbf{e}}'_y \equiv \hat{\mathbf{u}}_{1\perp}$), one can write the RW mobility matrices in the WR frame. The WR matrices share the same symmetries as their corresponding WR parts with different coefficients being combinations of those from the RW system. These elementary relations are omitted here.

5.5.3 Correction to bulk mobility due to the wall

In many systems bounded by a wall it is of importance to assess the effect of hydrodynamic interactions between the boundary and relatively distant suspended bodies. The content of this Section provides an answer to this question by deriving asymptotic correction to the bulk mobility matrix of a particle of general shape due to the presence of the wall. For the characteristic length scale of the body L, the relative correction scales as $(L/H)^{\alpha}$, where H is the wall-particle distance, and the exponent $\alpha = 1, 2, 3$ depends on the component of the mobility matrix. Below, we provide explicit analytical expressions for the first term correction to bulk mobility tensors $\boldsymbol{\mu}^{pq}$ with $p, q \in \{t, r\}$.

The expressions are further evaluated for a rod-like particle to determine the dependence of the components of $\boldsymbol{\mu}$ on the inclination angle of the rod θ. By comparing to numerical simulations using the multipole method, we examine the quality of approximation by first-term corrections only, which proves to be useful even for close distances $L/H \sim 2$, or even less in the case of rotational motion.

In the following, we rather quote the final results, shifting the technical part of the calculations to Appendix B.

Scattering series in the presence of a wall

In order to find the asymptotic correction to the bulk mobility of a particle moving close to a wall, we employ the scattering expansion [115] to identify the dominant contribution from the wall to the friction matrix of the particle. Having determined these corrections, we invert the friction matrix and obtain the correction to mobility.

We start from rewriting the grand resistance matrix in Eq. (5.46) in the following form

$$\mathbf{Z} = \mathbf{Z}_0(\mathbf{1} + \mathbf{G}_0\mathbf{Z}_0 + \mathbf{G}_w\mathbf{Z}_0)^{-1}, \tag{5.66}$$

for the wall-bounded case, where we explicitly decomposed the propagator $\mathbf{G}$ into the 'self' part $\mathbf{G}_0$ encompassing the effect of force density distribution within the particle, and the wall contribution $\mathbf{G}_w = \mathbf{G}' \cdot \mathcal{R}$, as described below Eq. (5.41). In the absence of the boundary, the term $\mathbf{G}_w$ vanishes, and the remaining scattering series describes the solution for a bead-modelled particle in an unbounded space. Our aim is to find a correction to this behaviour due to the presence of the wall. As we show in Appendix B, expanding Eq. (5.66) in $\mathbf{G}_w$ for large wall-particle distances yields the asymptotic near-wall grand resistance matrix in the form

$$\mathbf{Z} = \mathbf{Z}_b - \mathbf{Z}_b\mathbf{G}_w\mathbf{Z}_b + \mathbf{Z}_b\mathbf{G}_w\mathbf{Z}_b\mathbf{G}_w\mathbf{Z}_b + \ldots, \tag{5.67}$$

where $\mathbf{Z}_b = \mathbf{Z}_0(\mathbf{1} + \mathbf{G}_0\mathbf{Z}_0)^{-1}$ is the bulk grand resistance matrix of the particle. Thus we see that the leading order correction has the multipolar form $-\mathbf{Z}_b\mathbf{G}_w\mathbf{Z}_b$.

The propagator $\mathbf{G}_w$ connects the beads building up the particles with the beads of the image particle. Consider two interacting particles p and q^* from the conglomerate and its image, respectively, as illustrated in Fig. 5.3. Introducing coordinates relative to the centre of each conglomerate, we have $\mathbf{R}_p = \mathbf{R}_0 + \mathbf{r}_p$ and $\mathbf{R}^*_q = \mathbf{R}^*_0 + \mathbf{r}^*_q$. Hence the distance between the particles

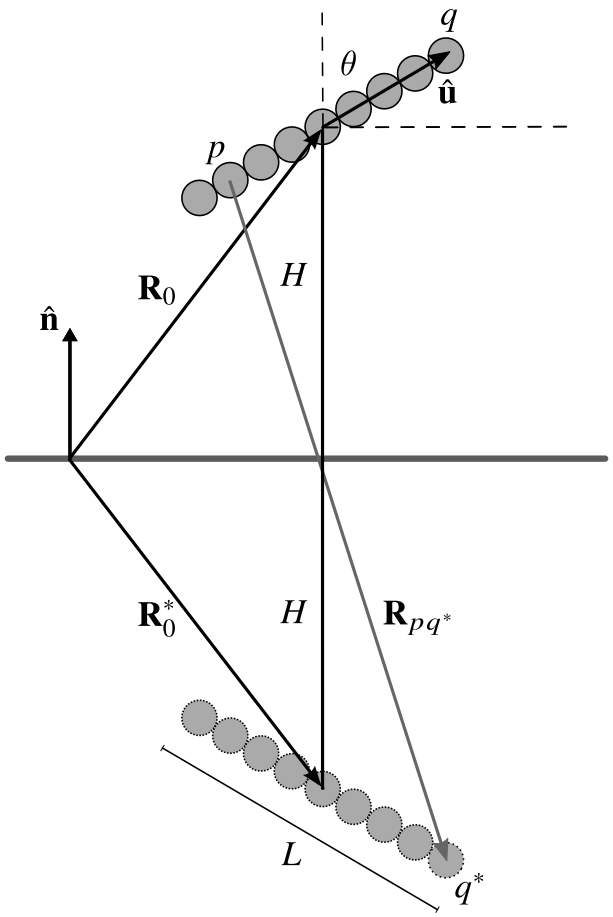

Figure 5.3: Schematic illustration of the idea of expansion of the distance between interacting beads from the particle and its image. Here we depict the interaction between the particle p with the image q^* of particle q. For large wall-particle distances, it may be expanded around the vertical line connecting the particles' centres lying at a distance $2H$ apart, so that $\mathbf{R}_{pq^*} \approx \mathbf{R}_0 - \mathbf{R}_0^* = 2H\hat{\mathbf{n}}$.

may be written as

$$\mathbf{R}_{pq^*} = \mathbf{R}_p - \mathbf{R}_q^* = 2H\hat{\mathbf{n}} + (\mathbf{r}_p - \mathbf{r}_q^*), \tag{5.68}$$

where we have used the fact that $\mathbf{R}_0 - \mathbf{R}_0^* = 2H\hat{\mathbf{n}}$. For the wall-particle distance H large compared to the particle size L, and thus for $|\mathbf{r}_p - \mathbf{r}_q^*| \ll H$, we may expand the distance between each pair of spherical beads around the direction normal to the wall, connecting the centres of the original particle and its image.

In leading order, the propagator takes the form $\mathbf{G}_w(\mathbf{R} = 2H\hat{\mathbf{n}})$. Due to this fact, its multipole elements have the axial symmetry around the normal direction $\hat{\mathbf{n}}$. Thus, the form of the matrix elements of $\mathbf{G}_w$ is the same as of the mobility matrix in Eq. (5.48), with the unit vector $\hat{\mathbf{u}}$ replaced by $\hat{\mathbf{n}}$. In this case, the bulk grand resistance matrix $\mathbf{Z}_b$ reduces to the single-particle bulk friction matrix $\boldsymbol{\zeta}$ as in Eq. (5.10).

The dominant correction may thus be looked upon as interaction of a particle of a given bulk friction matrix $\boldsymbol{\zeta}$ with an image particle via a propagator $\mathbf{G}_w$, which accounts for the flow reflected by the wall. It is different to the free space propagator $\mathbf{G}_0$, since the reflection of the flow off the wall induces other velocity multipoles. The distance-dependence of the propagator

elements follows from their multipolar character. The matrix elements of $\mathbf{G}_w$ decay according to their multipole indices as

$$\mathbf{G}_w^{ab}(\mathbf{R} = 2H\hat{\mathbf{n}}) = \frac{1}{8\pi\eta}\left(\frac{1}{2H}\right)^{l+l'+\sigma+\sigma'-1}\mathbf{g}^{ab}(\hat{\mathbf{n}}), \tag{5.69}$$

with the multipolar indices denoted by $a, b \in \{t, r, d\}$ and introduced in Eq. (5.47). The indices l, σ refer to the superscript a, while $l'\sigma'$ refer to b. The tensors $\mathbf{g}(\hat{\mathbf{n}})$ depend only on the direction of the normal vector $\hat{\mathbf{n}}$ and are listed in Appendix B. The exact form of these matrix elements can be found from the multipole representation of $\mathbf{G}_w$, described in Refs. [46, 118]. Importantly, all the multipolar contributions corresponding to the image system in Eq. (5.35) and incorporated in $\mathbf{G}_w$ decay with the same distance dependence, determined by the indices a, b. Further details of the calculations may be found in Appendix B.

The form of the correction obtained in this way is valid for any particle of a given bulk friction matrix, since it involves only interaction between the centre of the particle and its image. For the evaluation of the next terms of the correction, decaying with higher powers of $1/H$, one has to consider the next term in expansion of $\mathbf{R}_{pq*}$ around the particle-image centre line. The expansion in distance from the centre of the particle, as in Eq. (5.68), will introduce the next correction terms, which will depend on the shape of the particle.

Correction to mobility for an axisymmetric particle

The general framework outlined above allows us to derive explicit expressions for the wall-corrected friction tensor, which has then to be inverted as discussed in Sec. 5.2.2 to yield the leading-order expressions for mobility. We will specify to the case of a general axisymmetric particle for which the bulk mobility matrix contains no tr, rt elements.

The wall-corrected mobility tensor $\boldsymbol{\mu}_w$ has then the form

$$\boldsymbol{\mu}_w = \boldsymbol{\mu} + \boldsymbol{\Delta\mu}_w, \tag{5.70}$$

with the leading order terms given by

$$\boldsymbol{\Delta\mu}_w^{tt} = \frac{1}{8\pi\eta}\frac{1}{2H}\mathbf{g}^{tt} + \ldots, \tag{5.71}$$

$$\boldsymbol{\Delta\mu}_w^{tr} = -\frac{1}{8\pi\eta}\frac{1}{(2H)^2}\mathbf{g}^{td}\boldsymbol{\mu}^{dr} + \ldots, \tag{5.72}$$

$$\boldsymbol{\Delta\mu}_w^{rt} = \frac{1}{8\pi\eta}\frac{1}{(2H)^2}\boldsymbol{\mu}^{rd}\mathbf{g}^{dt} + \ldots, \tag{5.73}$$

$$\boldsymbol{\Delta\mu}_w^{rr} = \frac{1}{8\pi\eta}\frac{1}{(2H)^3}\left[\mathbf{g}^{rr} - \mathbf{g}^{rd}\boldsymbol{\mu}^{dr} + \boldsymbol{\mu}^{rd}\mathbf{g}^{dr} - \boldsymbol{\mu}^{rd}\mathbf{g}^{dd}\boldsymbol{\mu}^{dr}\right] + \ldots. \tag{5.74}$$

where the tensors $\mathbf{g}^{ab}$, with $a, b \in \{t, r, d\}$ are functions of particle orientation. The dots incorporate terms higher in powers of $1/H$.

Several remarks are in place here. Firstly, we see that different parts of the mobility correction decay with different powers of the wall-particle distance H. Rescaling the correction terms by the bulk mobility coefficients, we conclude that the dimensionless correction may be regarded

as an expansion in powers of $L/2H$. The effect of the wall is most pronounced in translational motion, since this term scales as H^{-1}. The next term in Eq. (5.71) scales as H^{-2}, however, it is proportional to the bulk mobility matrix $\boldsymbol{\mu}^{td}$ and $\boldsymbol{\mu}^{tr}$, which vanish for particles with axial (tr) and inversional (td) symmetry ($\hat{\mathbf{u}} \to -\hat{\mathbf{u}}$), such as rods. For such particles, the next term in Eq. (5.71) scales as H^{-3}, so we expect the asymptotic behaviour of the translational mobility coefficients to be well represented by the first term only. The coupling tensors in Eqs. (5.72)-(5.73) scale as H^{-2}, while the rotational motion is even less affected by the presence of the wall, with the correction scaling as H^{-3}. Secondly, we note that for the derivation of the tr, rt, and rr correction terms it is necessary to include the dipolar (rd) elements of the bulk mobility tensor. Finally, we note that the wall-corrected mobility matrix constructed as $\boldsymbol{\mu} + \boldsymbol{\Delta\mu}$ possesses all the requires symmetries outlined in Sec. 5.2.2.

Magnitude and applicability of the correction

In order to estimate the magnitude of the correction terms, we compare them to their respective bulk values, defined in Eq. (5.48). We use the following normalisation of the tt mobility matrix elements

$$\tilde{a}_t = \frac{a_t}{\mu^t_{\parallel}}, \qquad \tilde{b}_t = \frac{b_t}{\mu^t_{\perp}}, \qquad \tilde{d}_t = \frac{d_t}{\mu^t_{\perp}}, \qquad \tilde{c}_t = \frac{c_t}{\sqrt{\mu^t_{\parallel}\mu^t_{\perp}}}, \tag{5.75}$$

and analogously for the rr part, so that the non-diagonal elements, which vanish for $H \to \infty$ are normalised by appropriate combinations of bulk scalar mobility functions defined in Eq. (5.48). We do accordingly for the tr and rt part, e.g. $\tilde{a}_{tr} = a_{tr}/\sqrt{\mu^t_{\parallel}\mu^r_{\perp}}$. After rescaling, we are able to assess (a) the relative magnitude of the correction to bulk values, (b) the range of distances L/H over which the correction accurately reproduces the full-HI result obtained numerically using the multipole method.

It turns out that the corrections to the tr and rt part, both those calculated from simulations, and predicted by theory, typically do not exceed 5% at $L/H = 1$. We therefore may neglect this contribution to the full mobility matrix, and focus on the tt and rr parts.

We now take on an illustrative example of a colloidal rod of aspect ratio $p = 10$, modelled using 10 aligned spherical beads. The mobility corrections, defined as excess over their bulk values $-\boldsymbol{\mu}^{-1}\boldsymbol{\Delta\mu} = \mathbf{1} - \boldsymbol{\mu}^{-1}\boldsymbol{\mu}_w$, and for brevity denoted $1 - \mu/\mu_0$ are plotted as functions of dimensionless inverse distance to the image source, $L/2H$, in Fig. 5.5 for translational part, and in Fig. 5.6 for rotational part. The points are results of HYDROMULTIPOLE simulations, while the solid lines represent the correction terms from Eqs. (5.71)–(5.74). In each graph, the simulation data point for the largest value of L/H corresponds to a nearly touching configuration. For different inclination angles, this correspond to different values of H. It is clear that the dominant terms included in the correction represent the behaviour of bulk coefficients even for relatively large values of L/H for all the angles of rod inclination studied, being an accurate representation up to L/H of order of 1.

Correction for slender bodies

It is a vital question to assess the importance of hydrodynamic interactions with the wall for a given shape of the axisymmetric particle. In other words: is the particle mobility more affected if it has a spherical, or a needle-like shape? Let us first consider the translational mobility. The correction term is inversely proportional to the wall-particle distance H, so neglecting the tensorial character of the correction, for each component we may write symbolically $\Delta\mu^{tt} \sim 1/H$. To find the relative correction to bulk mobility, we divide by the bulk coefficients, which scale as $\mu^{tt} \sim 1/(\epsilon L)$, where L is the particle length, and ϵ is the slenderness parameter, defined in Eq. (5.53), which is small for elongated particles. In result,

$$\frac{\Delta\mu^{tt}}{\mu^{tt}} \sim \epsilon\frac{L}{H}. \tag{5.76}$$

For the rr part, $\Delta\mu^{rr}/\mu^{rr}$ has contributions proportional to $1/\mu^{rr}$, μ^{dr}/μ^{rr} and $(\mu^{dr})^2/\mu^{rr}$, but since from Eq. (5.13) $\mu^{rd} \sim \mu^{rr}\zeta^{rd}$, with $\mu^{rr} \sim 1/(\epsilon L^3)$ and $\zeta^{rd} \sim (\epsilon L)^3$, we finally conclude that the same result as above holds true but with the factor $(L/H)^3$ instead[2].

The magnitude of the relative correction is thus proportional to the parameter ϵ which decays logarithmically with increasing the particle aspect ratio p. Therefore we conclude that for fixed particle length and particle-wall distance, in the limit of very thin particles, there will be no effect of hydrodynamic interactions with the wall. For very slender particles we expect their bulk hydrodynamic properties to describe their dynamics properly even in the vicinity of the wall.

Angular structure of the correction

Apart from the distance dependence of the wall correction, which we have derived in the preceding section, our method enables us to determine the angular structure of $\boldsymbol{\mu}_w$. In previous studies using the slender body theory, de Mestre & Russel [100] were able to determine the correction in two limiting cases of $\theta = 0$ and $\pi/2$. Our results correctly reproduce their friction coefficients a for rod-like slender particle translating sideways or lengthways close to a wall. Moreover, using our method we find the components of correction to the mobility matrix for an arbitrary inclination angle θ. For the presentation of the results we choose the RW (particle) frame of reference in which the bulk mobility tensors are diagonal. The detailed angular form follows from the transformation of the propagator, which has an axial structure about $\hat{\mathbf{n}} = \hat{\mathbf{e}}_z$ in the wall frame WR, to the RW frame, and tensor contraction with the friction tensors which have an axial structure about $\hat{\mathbf{u}}$. The calculations are elementary but rather tedious, so we quote only the final results below. In the following, we refer to the components of the mobility matrix as defined in Sec. 5.5.2. More details can again be found in Appendix B.

For the translational part (5.71), we find the correction's angular dependence in the body-fixed

[2]The ratio $B = \zeta^{rd}/\zeta_{\perp}^{rr}$, called the Bretherton constant, is sometimes used as a hydrodynamic measure of particle nonsphericity [9], ranging from $B = 0$ for spheres, to $B \to 1$ for thin needles.

frame of reference RW explicitly as

$$\mathbf{g}^{tt} = -\frac{3}{2}\begin{pmatrix} 1+\cos^2\theta & 0 & -\cos\theta\sin\theta \\ 0 & 1 & 0 \\ -\cos\theta\sin\theta & 0 & 1+\sin^2\theta \end{pmatrix}_{RW} . \tag{5.77}$$

We note here that since the axis perpendicular to the rod and parallel to the wall (in the direction of $\hat{\mathbf{e}}'_y$ and $\hat{\mathbf{u}}_{1\perp}$) is invariant with respect to the WR to RW frame transformation, the element b_t of the matrix above is angle-independent. The rotational part follows from Eq. (5.74) as a sum of three contributions

$$\mathbf{g}^{rr} = -\frac{1}{2}\begin{pmatrix} 5-3\cos^2\theta & 0 & 3\sin\theta\cos\theta \\ 0 & 5 & 0 \\ 3\sin\theta\cos\theta & 0 & 5-3\sin^2\theta \end{pmatrix}_{RW} , \tag{5.78}$$

$$\boldsymbol{\mu}^{rd}\mathbf{g}^{dr} - \mathbf{g}^{rd}\boldsymbol{\mu}^{dr} = -\frac{3\mu^{dr}}{2}\begin{pmatrix} 0 & 0 & \sin\theta\cos\theta \\ 0 & 2(\cos^2\theta-1) & 0 \\ \sin\theta\cos\theta & 0 & 2\cos^2\theta \end{pmatrix}_{RW} ,$$

$$-\boldsymbol{\mu}^{rd}\mathbf{g}^{dd}\boldsymbol{\mu}^{dr} = \frac{3(\mu^{dr})^2}{2}\begin{pmatrix} 0 & 0 & 0 \\ 0 & \cos^4\theta-\cos^2\theta-3 & 0 \\ 0 & 0 & -(2\cos^2\theta+1) \end{pmatrix}_{RW} .$$

These results indicate a very simple angular relations for the components – low-order polynomials in $\sin\theta$ and $\cos\theta$. We again disregard here the non-diagonal components and the tr parts, since they are small. As an illustration, consider the diagonal components of the tt and rr parts of the mobility matrix. The correction factor for each of the normalised components may be written as

$$tt \text{ part :} \qquad \tilde{f}_t = 1 - C_t^f(\theta)\frac{L}{H}, \tag{5.79}$$

$$rr \text{ part :} \qquad \tilde{f}_r = 1 - C_r^f(\theta)\left(\frac{L}{H}\right)^3, \tag{5.80}$$

where $\tilde{f} \in \{\tilde{a}, \tilde{b}, \tilde{d}\}$. In Fig. 5.4, we present the results of a comparison between the values of the function C for the diagonal components of the tt and rr mobility matrix theoretically predicted using our calculations vs. numerically computed using the HYDROMULTIPOLE[3] algorithm for a bead-modelled rod of aspect ratio $p = 10$. The numerical results are linear fits to the large-distance behaviour of the calculated mobility using Eq. (5.79). We emphasize that no fitting is involved in the comparison, and the agreement is very good in all three cases.

In their recent work, Padding & Briels [98] stated empirically, basing on numerical calculations of friction on a rod close to a wall, that the wall effect on all the components of the particle friction matrix dies out as $1/d$, with d being the distance from the wall to the closest point of the particle (usually the tip), and its angular dependence may be well represented by fourth-order polynomials in $\cos\theta$. Our exact result presented above differs from their findings. However, in accord with their work, we confirm that the mobility (or friction) components may be well approximated by simple polynomials.

[3]It is important to mention that the normalization of the mobility functions given in Eq. (5.48) differs from that in the numerical codes, which follows Ref. [96]. For a successful comparison, an appropriate transformation has to be performed.

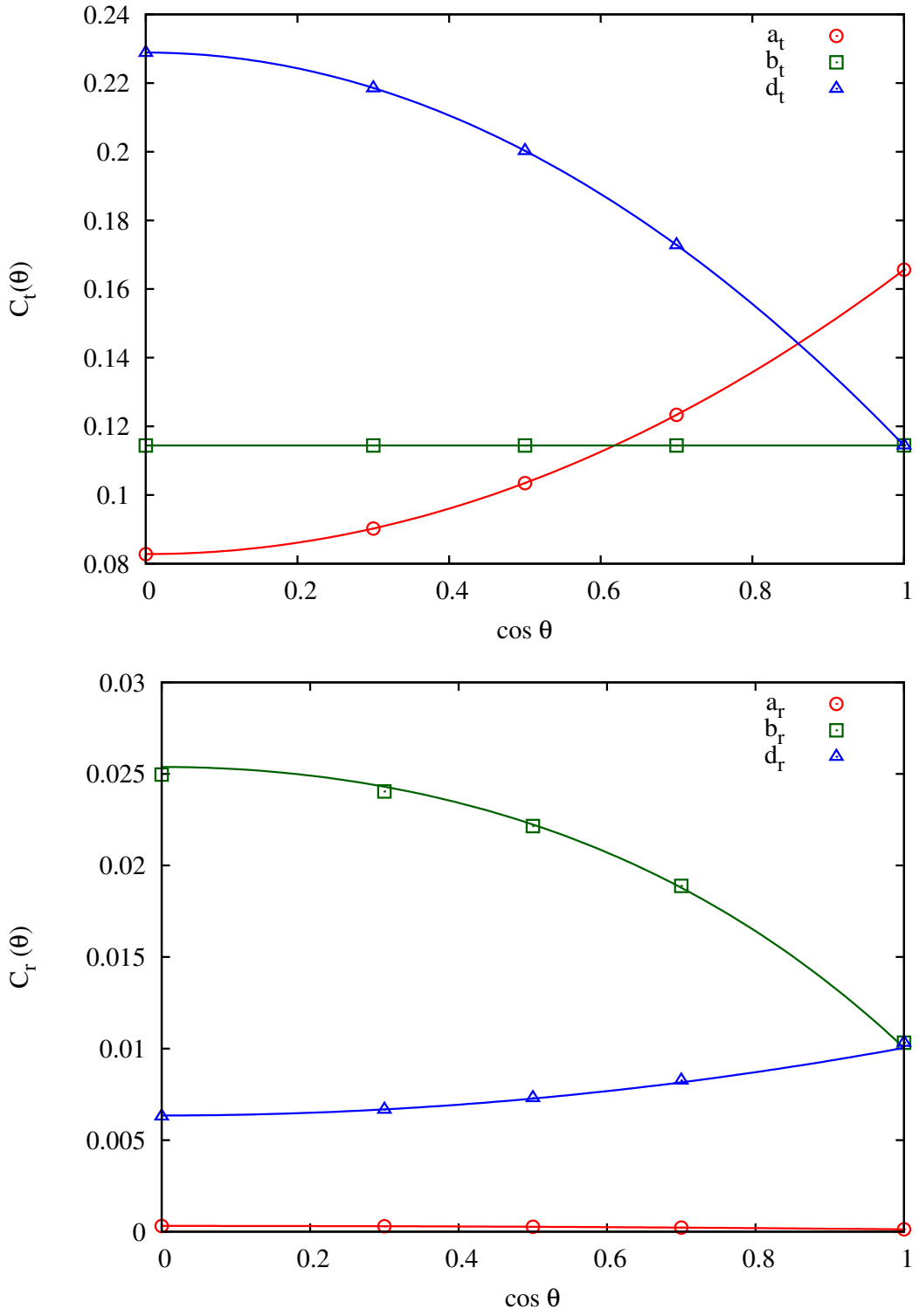

Figure 5.4: Comparison of the angular dependence of the tt and rr mobility tensor correction for a rod of aspect ratio $p = 10$, using the functions $C^i_{t,r}(\theta)$ defined in Eq. (5.79), obtained using the multipole method (points), and the predictions from our theoretical results - simple polynomials in $\cos\theta$ (solid lines). The agreement for all the three diagonal components of $\mathbf{\Delta\mu}^{tt}$ and $\mathbf{\Delta\mu}^{rr}$ is quite clear. The coefficients $b_{t,r}$ and $d_{t,r}$ attain the same value for the rod oriented along $\hat{\mathbf{e}}_z$, i.e. for $\theta = 0$, as they should from symmetry.

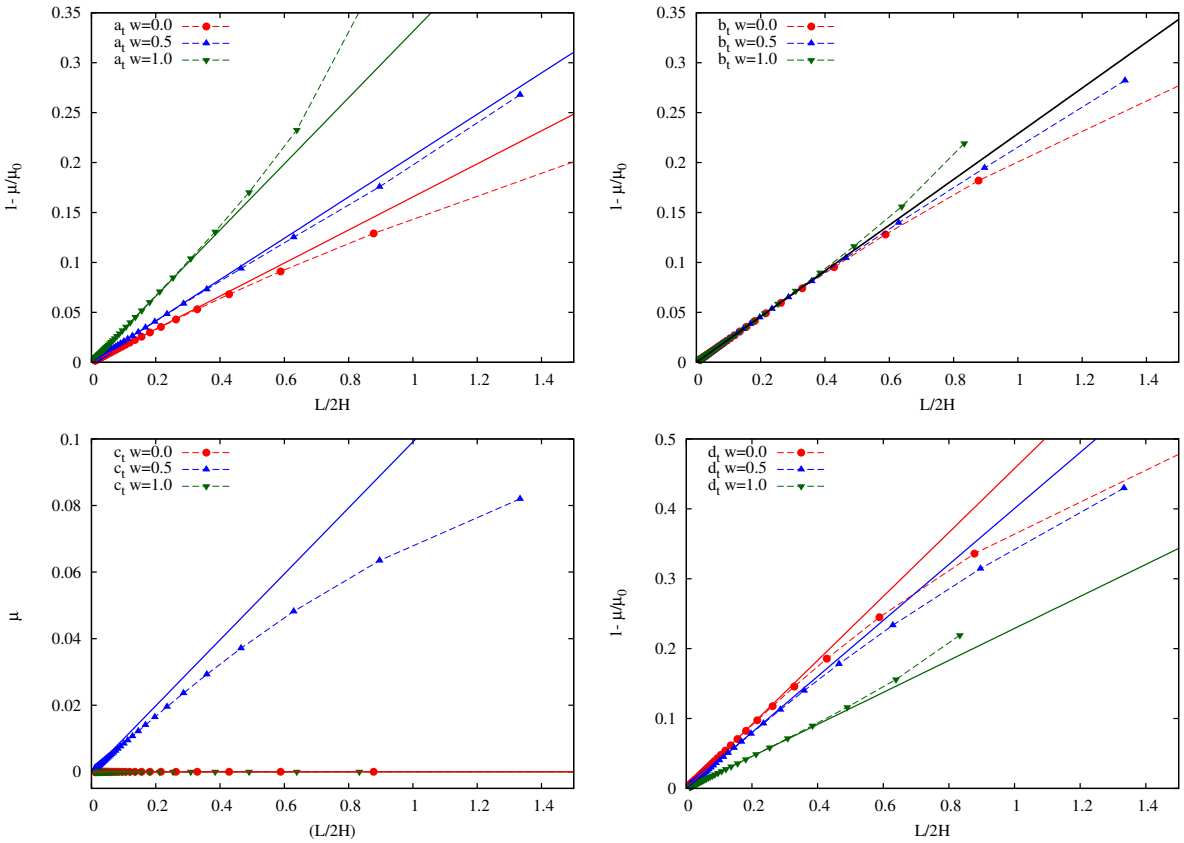

Figure 5.5: Normalised corrections for the elements of the translational mobility matrix $\boldsymbol{\mu}^{tt}$ with respect to their bulk values obtained by precise numerical simulations (points) and from the asymptotic predictions (solid lines) for a selection of rod inclination angles $w = \cos\theta$. The last point in each series corresponds to the rod nearly touching the wall. Translational mobility is strongly altered by the presence of the wall, with the correction arising up to ca. 40% at $L/2H \sim 1$, but the asymptotic result holds quite well even up to this distance from the wall. Results are plotted for the rod's aspect ratio $p = 10$.

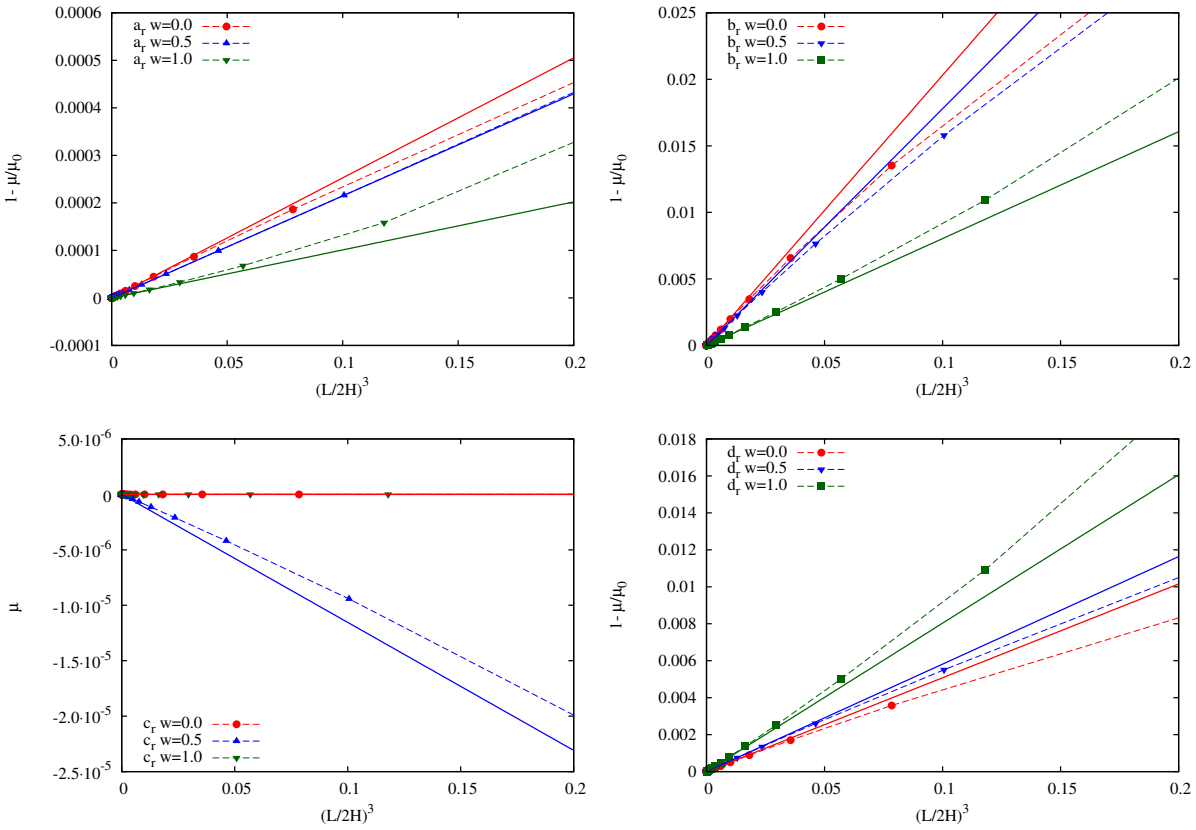

Figure 5.6: Normalised corrections for the elements of the rotational mobility matrix $\boldsymbol{\mu}^{rr}$ with respect to their bulk values obtained by precise numerical simulations (points) and from the asymptotic predictions (solid lines) for a selection of rod inclination angles $w = \cos\theta$. Rotational mobility is much less altered by the hydrodynamic interactions with the wall, with the correction being of order of 2% at $L/2H \sim 0.6$ (or $(L/2H)^3 \sim 0.2$). At this point we see the analytical correction to deviate from numerical predictions. Results are plotted for the rod's aspect ratio $p = 10$.

6 The first cumulant in bulk DLS

In the following, we examine the effect of anisotropy of an axially symmetric particle on the dynamics of the DLS correlation functions, focusing on the first cumulant. The anisotropy may stem either from the shape effects, encoded in the form factor, or from the intrinsic optical properties of the material, which we discuss in detail below. The bulk results will serve as reference for the EWDLS predictions obtained in the further course of the work.

6.1 Derivation of the first cumulant

We may now use the general expression (4.30) derived using the Smoluchowski equation formalism to find the first cumulant for the scattered electric field auto-correlation function, which in this case reads

$$\Gamma = \frac{\left\langle [\boldsymbol{\nabla}_{\mathbf{X}} E_S] \cdot \mathbf{D}(\mathbf{X}) \cdot \left[\boldsymbol{\nabla}_{\mathbf{X}} E_S^*\right] \right\rangle}{\langle |E_S|^2 \rangle}, \tag{6.1}$$

with $\mathbf{X} = (\mathbf{r}, \hat{\mathbf{u}})$ specifying the configuration of the particle. The scattered electric field has the form

$$E_S = F(\hat{\mathbf{u}}) \exp(i\mathbf{q} \cdot \mathbf{r}), \tag{6.2}$$

with the scattering properties of the particle encoded in the function F, defined in Eq. (2.19). Since the diffusion tensor $\mathbf{D}$ in Eq. (6.1) is related to the mobility matrix $\boldsymbol{\mu}$ by $\mathbf{D} = k_B T \boldsymbol{\mu}$, and using the general structure of the single-particle mobility matrix, discussed in Sec. 5.2.2, we immediately see that the first cumulant may be split into four distinct parts

$$\Gamma = \Gamma^t + \Gamma^r + \Gamma^{tr} + \Gamma^{rt}, \tag{6.3}$$

corresponding to the four submatrices of the mobility matrix (5.11). Their explicit form reads

$$\Gamma^t = \frac{1}{S(\mathbf{q})} \left\langle \boldsymbol{\nabla} E_S \cdot \mathbf{D}^{tt} \cdot \boldsymbol{\nabla} E_S^* \right\rangle, \tag{6.4}$$

$$\Gamma^r = \frac{1}{S(\mathbf{q})} \left\langle \mathbf{L} E_S \cdot \mathbf{D}^{rr} \cdot \mathbf{L} E_S^* \right\rangle, \tag{6.5}$$

$$\Gamma^{tr} = \frac{1}{S(\mathbf{q})} \left\langle \boldsymbol{\nabla} E_S \cdot \mathbf{D}^{tr} \cdot \mathbf{L} E_S^* \right\rangle, \tag{6.6}$$

$$\Gamma^{rt} = \frac{1}{S(\mathbf{q})} \left\langle \mathbf{L} E_S \cdot \mathbf{D}^{rt} \cdot \boldsymbol{\nabla} E_S^* \right\rangle, \tag{6.7}$$

with the gradient operators, $\boldsymbol{\nabla} = \frac{\partial}{\partial \mathbf{r}}$ and $\mathbf{L} = \hat{\mathbf{u}} \times \frac{\partial}{\partial \hat{\mathbf{u}}}$, defined in Eqs. (4.9) and (4.10). The static structure factor $S(\mathbf{q})$ reads

$$S(\mathbf{q}) = \left\langle |E_S|^2 \right\rangle. \tag{6.8}$$

Using the specific form of E_S from Eq. (6.2), we rewrite the first cumulant as

$$\Gamma^t = \frac{\left\langle |F|^2 (\mathbf{q} \cdot \mathbf{D}^{tt} \cdot \mathbf{q}) \right\rangle_{\hat{\mathbf{u}}}}{\langle |F|^2 \rangle_{\hat{\mathbf{u}}}}, \tag{6.9}$$

$$\Gamma^r = \frac{\langle [\mathbf{L}F] \cdot \mathbf{D}^{rr} \cdot [\mathbf{L}F^*] \rangle_{\hat{\mathbf{u}}}}{\langle |F|^2 \rangle_{\hat{\mathbf{u}}}}, \tag{6.10}$$

$$\Gamma^{tr} = i \frac{\langle \mathbf{q} \cdot \mathbf{D}^{tr} \cdot [F \mathbf{L} F^*] \rangle_{\hat{\mathbf{u}}}}{\langle |F|^2 \rangle_{\hat{\mathbf{u}}}}, \tag{6.11}$$

$$\Gamma^{rt} = -i \frac{\langle [F^* \mathbf{L} F] \cdot \mathbf{D}^{rt} \cdot \mathbf{q} \rangle_{\hat{\mathbf{u}}}}{\langle |F|^2 \rangle_{\hat{\mathbf{u}}}}, \tag{6.12}$$

omitting the arguments for brevity. We have replaced here the full configurational average by the orientational average over a unit sphere

$$\langle (\ldots) \rangle_{\hat{\mathbf{u}}} = \frac{1}{4\pi} \oint \mathrm{d}\hat{\mathbf{u}} (\ldots), \tag{6.13}$$

since in the above expressions there is no dependence on the position of the particle. A remark is in order here: as we described in Chapter 5, the diffusion (mobility) tensor depends on the choice of the reference point of the particle. However, so does the scattering amplitude defined in Eq. (2.18) as an integral over the volume of the particle with respect to a chosen centre. It is now easy to show, using the translational theorems for the mobility tensors introduced in Section 5.2.3, and the definition of the scattering amplitude, that the total first cumulant is indeed independent of the choice of the reference point of the particle.

The structure of the first cumulant shown in Eqs (6.9) - (6.12) stems purely from the form of the scattered electric field. Notably, the function $F(\hat{\mathbf{u}})$ encoding the particle properties also depends on the scattering vector $\mathbf{q}$.

Choosing the particle centre as reference, we now insert into these equations the specific form of the mobility tensor for an axisymmetric particle, as given in Eqs. (5.48), which we may conveniently rewrite for the diffusion tensors using the fluctuation-dissipation relation $\mathbf{D} = k_B T \boldsymbol{\mu}$ as

$$\mathbf{D}^{tt} = \bar{D}^t \mathbf{1} + \Delta D^t \left(\hat{\mathbf{u}}\hat{\mathbf{u}} - \frac{1}{3}\mathbf{1} \right), \tag{6.14}$$

$$\mathbf{D}^{rr} = D^r_\perp \mathbf{1} + (D^r_\parallel - D^r_\perp) \hat{\mathbf{u}}\hat{\mathbf{u}}, \tag{6.15}$$

$$\mathbf{D}^{tr} = \mathbf{D}^{rt} = \mathbf{0}, \tag{6.16}$$

introducing the mean translational diffusion coefficient

$$\bar{D}^t = \frac{1}{3} \left(D^t_\parallel + 2 D^t_\perp \right), \tag{6.17}$$

and the translational diffusivity anisotropy

$$\Delta D^t = D^t_\parallel - D^t_\perp. \tag{6.18}$$

Before quoting the final result we note that from the definition of the rotational operator $\mathbf{L} = \hat{\mathbf{u}} \times \frac{\partial}{\partial \hat{\mathbf{u}}}$, it follows that $\mathbf{L}(...) \perp \hat{\mathbf{u}}$, and therefore the rotational contribution to the first cumulant only contains the rotational diffusion coefficient $D^r_\perp$. Moreover, since the coupling tensors vanish for the considered particles, $\Gamma^{tr} = \Gamma^{rt} = 0$. The translational and rotational parts read then

$$\Gamma^t = q^2 \bar{D}^t + q^2 \Delta D^t \frac{\left\langle |F|^2 \left[\hat{\mathbf{q}} \cdot \left(\hat{\mathbf{u}}\hat{\mathbf{u}} - \frac{1}{3}\mathbf{1} \right) \cdot \hat{\mathbf{q}} \right] \right\rangle_{\hat{\mathbf{u}}}}{\langle |F|^2 \rangle_{\hat{\mathbf{u}}}}, \tag{6.19}$$

$$\Gamma^r = D^r_\perp \frac{\left\langle |\mathbf{L}F|^2 \right\rangle_{\hat{\mathbf{u}}}}{\langle |F|^2 \rangle_{\hat{\mathbf{u}}}}, \tag{6.20}$$

with $\hat{\mathbf{q}} = \mathbf{q}/q$ and $q = |\mathbf{q}|$. Interestingly, the behaviour of the translational part is quadratic in the scattering vector q, whereas the rotational contribution depends on $\mathbf{q}$ only via the orientation-dependent factor F incorporating the optical effects of shape and material anisotropy.

6.2 Results for model systems

We shall now discuss the first cumulant in four interesting model cases, namely, a sphere (both optically isotropic and anisotropic); a long and thin rod; and a thin circular disc (platelet). All the results in this Chapter have been obtained using Fortran codes relying on the numerical integration of the expressions given above, and written by us. These results will serve as reference for EWDLS correlation functions in wall-bounded geometry.

Isotropic spherical particles The most trivial case is that of a suspension of optically isotropic spherical particles of radius a. For identical spherical particles, the factor F is constant, and the scattering amplitudes B drop out due to normalisation. It follows that $\Gamma^r = 0$, since $\mathbf{L}$ is a differential operator. Moreover, the diffusion tensors are now constant and isotropic, and given by $D^t_0 = k_B T/6\pi\eta a$ and $D^r_0 = k_B T/8\pi\eta a^3$, in accordance with Eq. (5.17). Direct evaluation of the angular average (6.19) leads to the simple expression

$$\Gamma = \Gamma^t = q^2 D^t_0, \tag{6.21}$$

using which the diffusion coefficient may be extracted experimentally as the slope of the curve Γ vs. q^2, enabling to further calculate the hydrodynamic radius a of suspended microparticles. This result may also be reproduced by calculating the full correlation function, since in this case an analytical solution for the EACF is available and reads $\hat{g}_1(\mathbf{q}, t) = \exp(-q^2 D^t_0)$ [10].

Optically anisotropic spheres Model systems of spherical particles exhibiting optical anisotropy have been characterized and studied with bulk scattering over the recent decades, both in the dilute [92, 93, 161–164] and concentrated regime [94, 165], by the group of Degiorgio and Piazza. In the studies, spherical particles made of PTFE (polytetrafluoroethylene) copolymer have been shown to have a crystalline structure and an intrinsic optical anisotropy $\Delta\alpha$ which may be used to explore their rotational relaxation. The advantage of using such a system is that the particles have isotropic hydrodynamic properties, and therefore their optical properties are more pronounced in experiments.

For a dilute suspension, the full EACF can likewise be found due to the high level of symmetry. The first cumulant contains now both rotational and translational contributions $\Gamma = \Gamma^t + \Gamma^r$, which may be calculated by taking derivatives at $t = 0$ of the explicit correlation functions given in the book of Berne & Pecora [101]. The translational part reads $\Gamma^t = q^2 D_0^t$ as before, and for the rotational part we find, depending on the scattering geometry,

$$\text{VH}: \qquad \Gamma^r_{\text{VH}} = 6D^r_0, \tag{6.22}$$

$$\text{VV}: \qquad \Gamma^r_{\text{VV}} = \frac{24|\Delta\alpha|^2}{45|\alpha|^2 + 4|\Delta\alpha|^2} D^r_0, \tag{6.23}$$

where α and $\Delta\alpha$ are, respectively, the mean polarisability and polarisability anisotropy. Interestingly, in the VH case the first cumulant is independent of the optical properties of the particle due to the normalisation of the EACF. On the other hand, the VV term is negligibly small if the optical anisotropy is not too large. The latter may be assessed by measuring the intensity ratio in an SLS experiment in both geometries [101], as

$$\frac{I_{\text{VH}}}{I_{\text{VV}}} = \frac{3|\Delta\alpha|^2}{45|\alpha|^2 + 4|\Delta\alpha|^2}. \tag{6.24}$$

The relations above suggest a simple way to extract the rotational diffusion coefficient of spherical particles from DLS measurements. Since the VV contribution (similar to depolarised scattering) may be approximated to have only the translational component, the rotational diffusion coefficient may be obtained as

$$D^r_0 \approx \frac{1}{6}(\Gamma_{\text{VH}} - \Gamma_{\text{VV}}). \tag{6.25}$$

Thin rod-like particles The dynamics of dilute suspensions of axisymmetric particles in DLS experiments have been addressed in a number of works [10, 101, 166, 167], both in the presence of optical anisotropy, and for isotropic particles. We briefly review the results of DLS analysis below as a reference to the later presented EWDLS results. The full analysis of the EACF for long and rigid rods may be found in Dhont's book [10]. Here, we rather outline the main points of the calculation and focus on the first cumulant.

The object under consideration is a thin rod of length L, thus the relevant dimensionless parameter for the analysis is qL. The shape of the particle manifests itself in the scattered electric field via the non-trivial form factor. The scattering strength of a thin rod oriented along a director $\hat{\mathbf{u}}$ may be easily calculated from Eq. (2.18) as

$$B(\hat{\mathbf{u}}) = \frac{1}{L}\int_{-L/2}^{L/2} \mathrm{d}x\, \exp(ix\mathbf{q}\cdot\hat{\mathbf{u}}) = j_0(x), \tag{6.26}$$

where $x = \frac{1}{2}qL\hat{\mathbf{q}}\cdot\hat{\mathbf{u}}$, and $\hat{\mathbf{q}} = \mathbf{q}/q$ is the unit vector in the direction of $\mathbf{q}$. The function $j_0(x)$ is defined as $\sin x/x$. As expected, for $x \to 0$, the scattering strength reduces to unity. This result is also recovered as a limiting case of a general expression for the scattering strength of a cylinder of thickness (length) L and radius R [10] as

$$B(\hat{\mathbf{u}}) = \frac{2J_1\left(qR\sqrt{1-(\mathbf{q}\cdot\hat{\mathbf{u}}/q)^2}\right)}{qR\sqrt{1-(\mathbf{q}\cdot\hat{\mathbf{u}}/q)^2}} \frac{\sin(\frac{h}{2}\mathbf{q}\cdot\hat{\mathbf{u}})}{\frac{h}{2}\mathbf{q}\cdot\hat{\mathbf{u}}}, \tag{6.27}$$

in the limit of $R \to 0$. Notably, the other limit ($L \to 0$ at fixed R) corresponds to the case of a flat circular disc, discussed further. Here, J_1 is the Bessel function of the first kind [112].

Two cases here are of particular interest: **(a)** the case of small optical anisotropy, $|\Delta\alpha| \ll |\alpha|$, where the orientational dependence enters only through the shape of the particle (form factor), and **(b)** VH geometry measurements for larger polarisability anisotropy where the orientational relaxation stems from both shape and polarisability effects.

(a) For small optical anisotropy, which is the case for many systems of practical importance, the orientation of the particle enters the correlation function only through the form of B. This case is recovered in depolarised scattering measurements. The EACF for a dilute suspension of rigid rods may be written as

$$\hat{g}_1(\mathbf{q}, t) = \frac{1}{S(\mathbf{q})}\Big\langle j_0(x(t)) j_0(x(0)) \exp(i\mathbf{q} \cdot (\mathbf{r}(0) - \mathbf{r}(t))\Big\rangle, \tag{6.28}$$

in accordance with Eq. (2.33), where the equilibrium averaging is performed with respect to the position and the orientation of the particle, and with the form factor which may be analytically found in this case as

$$S(\mathbf{q}) = \left\langle j_0^2(x)\right\rangle = \frac{1}{4\pi}\oint \mathrm{d}\hat{\mathbf{u}}\, j_0^2(x) = \frac{2}{qL}\int_0^{qL/2} \mathrm{d}z\, \left(\frac{\sin z}{z}\right)^2. \tag{6.29}$$

The calculation of the first cumulant is now straightforward using Eqs. (6.19)-(6.20). We may write it as

$$\Gamma = q^2\left[\bar{D}^t + \Delta D^t C_1(qL)\right] + L^2 D_\perp^r C^r(qL), \tag{6.30}$$

where the functions C_1 and C^r are defined as

$$C_1(qL) = \frac{1}{q^2}\frac{\left\langle |B|^2\left(w^2 - \frac{1}{3}\right)\right\rangle_{\hat{\mathbf{u}}}}{\left\langle |B|^2\right\rangle_{\hat{\mathbf{u}}}}, \qquad C^r(qL) = \frac{1}{L^2}\frac{\left\langle |\mathbf{L}B|^2\right\rangle_{\hat{\mathbf{u}}}}{\left\langle |B|^2\right\rangle_{\hat{\mathbf{u}}}}, \tag{6.31}$$

with $w = \hat{\mathbf{q}} \cdot \hat{\mathbf{u}} = \cos\theta$. We have decided here for such a notation for future convenience and easy comparison with EWDLS results. For a slender rod-like particle, these integrals can be computed analytically for the form of B given in Eq. (6.26). Since the resulting expressions are complicated, we rather plot them in Fig. 6.1. In the limit of low scattering vector, the first cumulant may be approximated by

$$\Gamma = q^2 \bar{D}^t. \tag{6.32}$$

For large values of $qL \gg 1$, the limiting values are $C_1(\infty) = -1/3$ and $C^r(q \to \infty) \sim q^2/12$, and the first cumulant becomes

$$\Gamma = q^2\left(\bar{D}^t - \frac{1}{3}\Delta D^t + \frac{L^2}{12} D_\perp^r\right), \tag{6.33}$$

in accordance with results obtained from the analysis of the full EACF [166, 167]. Notably, in the limit of an infinitely thin rod, a slender-body type of analysis yields the following relations between the diffusion coefficients, $D_\parallel = 2D_\perp$ and $D_\perp^r = 12D_\parallel/L^2$, so that for the effective diffusion coefficient $D_{\mathrm{eff}} = \Gamma/q^2$ we have $D_{\mathrm{eff}}(q = \infty) > D_{\mathrm{eff}}(q = 0)$. From the point of view of DLS experiments it is, however, practical to consider only the scattering vectors in the physical range $qL \in (0, 10)$, with the upper bound in most experimental situations not exceeding $qL \approx 5$.

(b) For optically anisotropic particles, the modification to the previous case is that in Eq. (6.28), the oriented dielectric tensor $\mathcal{E}(\hat{\mathbf{u}})$ appears together with the scattering amplitude j_0, and both depend on the orientation. An important difference to the case (a) is that now the first cumulant attains a non-zero value at $q = 0$. With the form of the first cumulant unchanged, the functions C_1 and C^r are obtained by replacing B in Eq. (6.31) by $F = \mathcal{E}B$. We plot the results in Fig. 6.1. In the low-q regime the scattering amplitude simplifies to unity, and only the anisotropic polarisability influences the measured correlation function. In consequence, we arrive at the result for spherical particles (6.22)-(6.23), since there is no dependence on the shape of the scatterers.

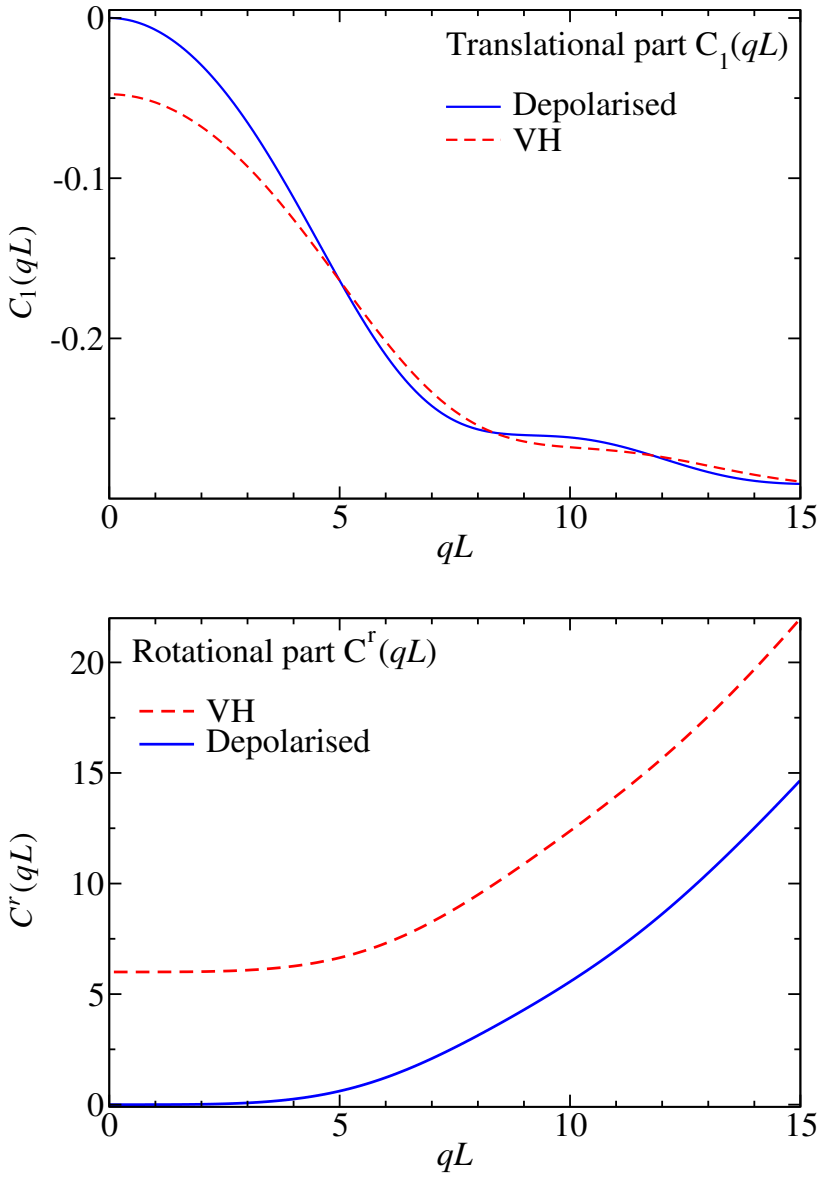

Figure 6.1: Components of the first cumulant for rod-like particles, defined in Eq. (6.31), in depolarized scattering (case (a) of optically isotropic particles), and in VH scattering (case (b)). The function C_1 describes the contribution to the first cumulant proportional to the diffusivity anisotropy, while C^r is related to the rotational contribution. The differences in the depolarized vs. VH scattering are most pronounced in the low-q experimental regime.

It is also common to analyse the rotational relaxation of the EACF in a different way by decomposing the orientation-dependent part of Eq. (6.28) into spherical harmonics and exploiting the fact that they are eigenfunctions of the squared rotational operator $\mathbf{L}^2$ present in the Smoluchowski equation. In this work, however, we confine our attention to the first cumulant only, where an analytic calculation of the rotational contribution may be performed, and for other approaches we refer to the textbooks by Dhont [10] and Berne & Pecora [101].

Thin disc-like particles and platelets For a thin platelet, the scattering amplitude can again be found by direct integration or as a limiting form of Eq. (6.27), and reads

$$B = \frac{2J_1(qR\sqrt{1-(\hat{\mathbf{q}}\cdot\hat{\mathbf{u}})^2})}{qR\sqrt{1-(\hat{\mathbf{q}}\cdot\hat{\mathbf{u}})^2}}, \tag{6.34}$$

and the general theoretical framework outlined before holds sway. We again restrict our attention to depolarized and VH scattering geometries.

(a) In the case of optically isotropic platelets, an analogous procedure to the one outlined for rods leads to the correction functions C_1 and C^r as shown in Fig. 6.2, the difference lying now in the fact that these were obtained by numerical integration, since there seem to be no analytic expressions for the integrals involved, contrary to the previous case. The general form of the first cumulant valid for arbitrary q is the same as in Eq. (6.30) for rod-shaped particles, with L interchanged with R. Again, in the low-q regime, the first cumulant reads

$$\Gamma = q^2 \bar{D}^t. \tag{6.35}$$

For large values of $qL \gg 1$, the limiting values are $C_1(\infty) = 2/3$ and $C^r(q \to \infty) \sim q^2/2$, and the first cumulant becomes

$$\Gamma = q^2 \left(\bar{D}^t + \frac{2}{3}\Delta D^t + \frac{R^2}{2} D^r_\perp \right), \tag{6.36}$$

in agreement with the result of Fujime and Kubota [167].

(b) The presence of optical anisotropy slightly changes the behaviour of the functions C_1 and C^r. The main and most pronounced difference is a finite intercept of the rotational contribution to the first cumulant, which is presented in Fig. 6.2, and which may be exploited in the experiments to extract the rotational diffusion coefficient of platelet-shaped particles [168].

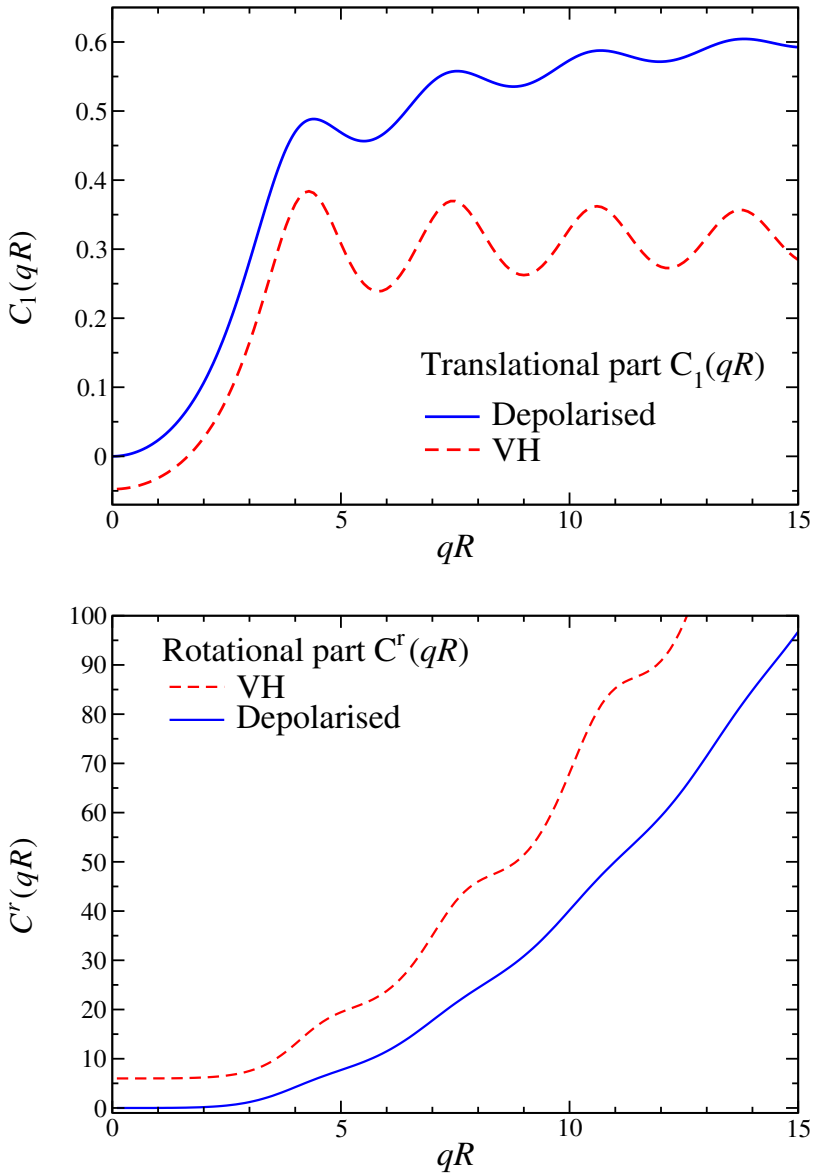

Figure 6.2: Components of the first cumulant for disc-like particles in the depolarized case and in VH scattering. In this case, compared to rod-shaped colloids, the oscillatory character of the functions C_1 and C^r from Eq. (6.31) is more pronounced. Their general behaviour, however, is similar to the slender rod case. From the experimental point of view, the most interesting region is $qR < 5$ where the rotational contribution in the VH mode is much pronounced.

7 Evanescent wave scattering from spherical colloids

In this Chapter, we will apply the previously outlined general procedure to derive and analyse exact expressions for the short-time dynamics on the field correlation function in the case of a dilute suspension of spherical colloids possessing an optical anisotropy. The latter feature allows for the detection of rotational diffusion in EWDLS experiments. To our knowledge, EWDLS is the first technique available to probe spatially resolved rotational diffusion of nanoparticles in the vicinity of a wall.

First, we shall discuss the hydrodynamic mobility of a spherical particle interacting hydrodynamically with the nearby wall. Next, we describe the derivation of the first cumulant, and analyse its structure in detail. Considering an optically homogeneous sphere, we derive the first and the second cumulant, and present a discussion of validity of such an approximation to the full EACF for the intermediate stages of its decay, supported by Brownian Dynamics simulations. We then proceed to the analysis of rotational motion observed in scattering experiment involving birefringent colloidal spheres, and derive the expression for the rotational contribution to the first cumulant.

The effect of translational motion on the structure of the first cumulant in EWDLS for spherical particles has recently been explored both in the dilute case [63, 64, 88], and for concentrated hard-sphere suspensions [73, 75, 169, 170], both experimentally and theoretically. Rotational relaxation has been observed in the last years, starting from 2012, [89,90] for optically anisotropic spherical colloids.

Results presented in this chapter have been published in three research articles [88–90].

7.1 Near-wall translational and rotational motion of a sphere

The hydrodynamic problem of motion of a spherical particle in a viscous liquid bounded by a planar no-slip wall is important from the point of view of model systems for colloidal dynamics in confinement, and has therefore been investigated in great detail, theoretically and experimentally, as stated in the introductory Chapter 1. Below, we discuss the anisotropic translational and rotational motion of a sphere close to a wall. Later on, we will demonstrate how this anisotropy may be traced in EWDLS measurements.

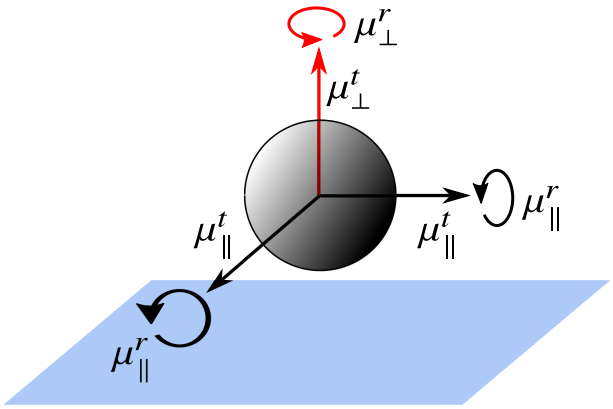

Figure 7.1: Schematic drawing of the motion corresponding to the independent components of the mobility matrix of a spherical particle above a planar wall. The component μ^{tr}, describing to the translation-rotation coupling, is not pictured.

In the case of a spherical particle, the 6×6 mobility matrix characterising the translational and rotational motion of the sphere near the wall is anisotropic, with the components (mobility coefficients) depending on the distance z of the sphere centre to the wall. Five independent mobility coefficients are required to characterise the sphere motion, as sketched in Fig. 7.1. The four coefficients $\mu^t_\parallel$, $\mu^t_\perp$, $\mu^r_\parallel$, $\mu^r_\perp$ characterise the translational and rotational motion in the directions parallel and perpendicular to the wall, while the additional coefficient μ^{tr} describes the wall-induced coupling of translational and rotational motion. Its presence might be intuitively argued by the following example: imagine a sphere acted upon by a force parallel to the wall. As a result, the sphere translates in the direction of the force but the frictional force acting on its bottom part (i.e. the one closer to the boundary) is higher than on the upper part, and the resulting torque induces rotation of the particle, in order to satisfy the torque-free condition. At large distances from the wall this effect is absent, and two bulk coefficients μ^t_0 and μ^r_0 suffice to characterise the dynamics. As discussed in Chapter 5, due to the symmetry of the system, the elements of the mobility matrix depend only on the wall-particle distance z, and we find that the mobility matrix

$$\boldsymbol{\mu}(z) = \begin{pmatrix} \boldsymbol{\mu}^{tt}(z) & \boldsymbol{\mu}^{tr}(z) \\ \boldsymbol{\mu}^{rt}(z) & \boldsymbol{\mu}^{rr}(z) \end{pmatrix} \tag{7.1}$$

has the following invariant structure

$$\begin{aligned} \boldsymbol{\mu}^{tt}(z) &= \mu^t_\perp(z)\hat{\mathbf{e}}_z\hat{\mathbf{e}}_z + \mu^t_\parallel(z)(\mathbf{1} - \hat{\mathbf{e}}_z\hat{\mathbf{e}}_z) && (7.2)\\ \boldsymbol{\mu}^{rr}(z) &= \mu^r_\perp(z)\hat{\mathbf{e}}_z\hat{\mathbf{e}}_z + \mu^r_\parallel(z)(\mathbf{1} - \hat{\mathbf{e}}_z\hat{\mathbf{e}}_z) && (7.3)\\ \boldsymbol{\mu}^{tr}(z) &= \mu^{tr}(z)\boldsymbol{\epsilon}\cdot\hat{\mathbf{e}}_z, && (7.4)\\ \boldsymbol{\mu}^{rt}(z) &= \mu^{rt}(z)\boldsymbol{\epsilon}\cdot\hat{\mathbf{e}}_z && (7.5) \end{aligned}$$

with $\hat{\mathbf{e}}_z$ being normal to the wall, and $\boldsymbol{\epsilon}$ denoting the Levi-Civita tensor. From the Lorentz reciprocal theorem [9], it follows that the symmetry of mobility matrix requires that $\boldsymbol{\mu}^{rt} = (\boldsymbol{\mu}^{tr})^\mathsf{T}$, where T is the transposition operation. Hence we conclude that $\mu^{tr}(z) = -\mu^{rt}(z)$. For later convenience, we introduce now the dimensionless mobility coefficients

$$\tilde{\mu}^t_{\parallel,\perp} = \frac{\mu^t_{\parallel,\perp}}{\mu^t_0}, \qquad \tilde{\mu}^r_{\parallel,\perp} = \frac{\mu^r_{\parallel,\perp}}{\mu^r_0}, \qquad \tilde{\mu}^{tr} = \frac{\mu^{tr}}{a\mu^r_0}, \tag{7.6}$$

normalising by the corresponding bulk values for the tt and rr parts, and choosing to normalise the tr part by $a\mu^r_0$, with a being the particle radius.

For over a century, the problem of finding the mobility of a spherical particle moving close to a no-slip planar wall, has attracted attention of the scientific community due to its fundamental importance. The earliest works of Lorentz [36] and Faxén [37] using the method of reflections [38] have led to approximate expressions for the two translational coefficients in terms of the reciprocal sphere-wall distance $b = a/z$, given by

$$\tilde{\mu}^t_\perp(b) \approx 1 - \frac{9}{8}b, \tag{7.7}$$

$$\tilde{\mu}^t_\parallel(b) \approx 1 - \frac{9}{16}b + \frac{1}{8}b^3 - \frac{45}{256}b^4 - \frac{1}{16}b^5. \tag{7.8}$$

Notably, the inverse-distance parameter was usually denoted by t in earlier works [44–46]. The approximation by these two expressions is rather crude, and may be effectively used only for a particle moderately distant from the wall, i.e. $z/a \geq 2$. Notably, the dominant terms are in agreement with the correction to bulk mobility, which we have derived in Chapter 5.

More refined calculations by Brenner *et al.* [38–41] and Dean and O'Neill [42, 43] including solutions in the lubrication zone for a nearly touching sphere have led to formally exact expressions for some of the the mobility coefficients in terms of infinite series. These are, however, of limited practical value due to their slow convergence with the gap size. More recently, practical inverse-distance power series results for all five mobility coefficients have been obtained using a high-precision numerical scheme based on the force multipoles method by Cichocki and Jones [46] combined with a Padé approximation used to account for near-contact lubrication effects. It is an improved version of results obtained for a sphere in the presence of a free surface (e.g. an air-water interface) and for a hard wall by Perkins and Jones [44,45]. This representation will serve us as the basis for further numerical computations. The mobility functions calculated according to Ref. [46] are plotted in Fig. 7.2 as functions of inverse distance from the wall.

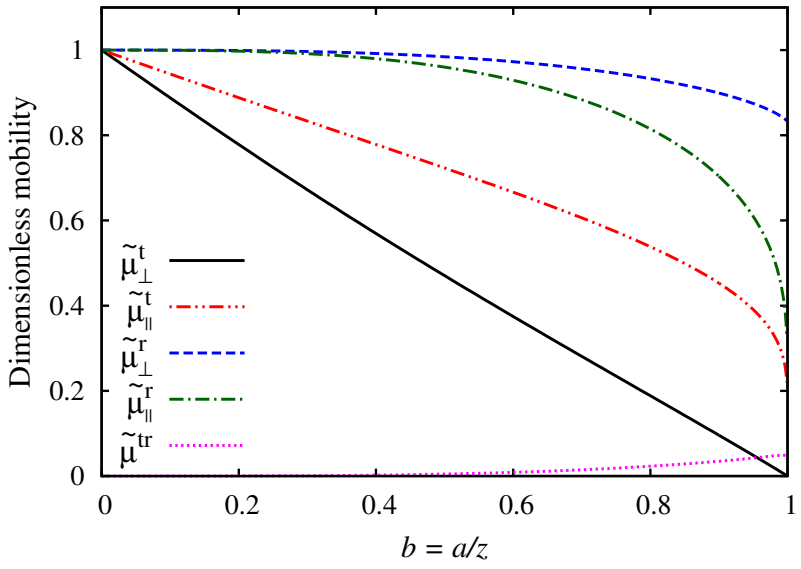

Figure 7.2: Dimensionless mobility functions of a wall-bounded spherical particle plotted against the inverse distance to the wall $b = a/z$, normalised according to Eq. (7.6). The hindrance of translational mobility is visibly stronger than of the rotational one.

Significant deviations from the bulk mobility values are observed for distances $z/a < 5$, and are in general more pronounced in the case of translational than rotational motion. Interestingly,

this difference may be of importance in physical processes such as cellular adhesion [171, 172], or channel flows where translational mobility is hindered but rotational effects are strong enough to allow for reorientation of particles in external fields [95].

Hydrodynamic lubrication has a strong effect on the near-wall behaviour of the mobility coefficients. As the contact is approached for $b = 1$, all mobility coefficients but $\tilde{\mu}^r_\perp$ tend to 0 in a non-analytical manner. It follows from lubrication theory that the asymptotic behaviour of the mobility coefficients close to the wall can be expressed in terms of the dimensionless gap width $\varepsilon = (z - a)/a$ [46]. For small gaps, one finds the following asymptotic behaviour

$$\begin{aligned} \tilde{\mu}^t_\perp &\sim \varepsilon + \frac{1}{5}\varepsilon^2 \log \varepsilon, \qquad \tilde{\mu}^t_\parallel \sim -2(\log \varepsilon)^{-1}, \\ \tilde{\mu}^r_\parallel &\sim -\tfrac{8}{3}(\log \varepsilon)^{-1}, \qquad \tilde{\mu}^r_\perp \sim \frac{1}{\zeta(3)}, \end{aligned} \tag{7.9}$$

with the Riemann zeta function $\zeta(3) \approx 1.202$. While $\tilde{\mu}^r_\parallel(b \to 1) = 0$, lubrication still allows the sphere to rotate with the angular velocity normal to the wall even at contact, with the mobility coefficient $\tilde{\mu}^r_\perp$ reduced by about 18 % below the bulk value. The coefficient $\tilde{\mu}^{tr}$ relating translational motion to applied torque tends to zero at sphere-wall contact, and vanishes for a far-distant particle, attaining its maximal value of ca. 0.05 very close to the wall.

7.2 The cumulants in EWDLS from spherical particles

In this Section, we consider scattering from spherical particles possessing an intrinsic optical anisotropy. The particular symmetry of the shape implies that the scattering amplitude is independent of the particle orientation. Therefore, the only dependence on $\hat{\mathbf{u}}$ enters through the anisotropic dielectric properties of the particle encoded in the oriented dielectric tensor $\mathcal{E}(\hat{\mathbf{u}})$, and discussed in Chapter 2. Assuming the particle to have axially symmetric dielectric properties, its general form reads

$$\mathcal{E}(\hat{\mathbf{u}}) = \hat{\mathbf{n}}_0 \cdot \left[\alpha \mathbf{1} + \Delta\alpha \left(\hat{\mathbf{u}}\hat{\mathbf{u}} - \frac{1}{3}\mathbf{1}\right)\right] \cdot \hat{\mathbf{n}}_s, \tag{7.10}$$

with the mean polarisability α and polarisability anisotropy $\Delta\alpha$. Similarly to the bulk case, the first cumulant may be written as in Eq. (6.1),

$$\Gamma = \frac{\left\langle [\boldsymbol{\nabla}_\mathbf{X} E_S] \cdot \mathbf{D}(\mathbf{X}) \cdot \left[\boldsymbol{\nabla}_\mathbf{X} E_S^*\right]\right\rangle}{\langle |E_S|^2 \rangle}, \tag{7.11}$$

and all the formulae (6.4)-(6.7) are valid, provided that one uses a different form of the scattered field, which in this case is given by

$$E_S = \exp\left(-\frac{\kappa}{2}\hat{\mathbf{e}}_z \cdot \mathbf{r}\right) \mathcal{E}(\hat{\mathbf{u}}) \exp(i\mathbf{q} \cdot \mathbf{r}). \tag{7.12}$$

We shall shift the discussion of the first cumulant in the general case of axisymmetric particles to the next Chapter. With the electric field as in Eq. (7.12), we write the first cumulant as

$$\Gamma = \Gamma^t + \Gamma^r. \tag{7.13}$$

As we will show later, due to the symmetry of the diffusion tensor, the *tr* and *rt* contributions to the first cumulant vanish in this case, i.e. $\Gamma^{tr} + \Gamma^{rt} = 0$. Basing on the general expressions (6.4) and (6.5) one may write the translational and rotational part as

$$\Gamma^t = -\left(i\mathbf{q} - \frac{\kappa}{2}\hat{\mathbf{e}}_z\right) \cdot \left\langle \mathbf{D}^{tt} \right\rangle_\kappa \cdot \left(i\mathbf{q} + \frac{\kappa}{2}\hat{\mathbf{e}}_z\right), \tag{7.14}$$

$$\Gamma^r = \frac{\langle [\mathbf{L}\mathcal{E}(\hat{\mathbf{u}})] \cdot \langle \mathbf{D}^{rr} \rangle_\kappa \cdot [\mathbf{L}\mathcal{E}^*(\hat{\mathbf{u}})] \rangle_{\hat{\mathbf{u}}}}{\left\langle |\mathcal{E}(\hat{\mathbf{u}})|^2 \right\rangle_{\hat{\mathbf{u}}}}, \tag{7.15}$$

where the exponentially weighted 'κ-average' is defined as

$$\langle A \rangle_\kappa = \frac{\displaystyle\int_a^\infty \mathrm{d}z\, e^{-\kappa(z-a)} e^{-\beta\Phi(z)} A(z)}{\displaystyle\int_a^\infty \mathrm{d}z\, e^{-\kappa(z-a)} e^{-\beta\Phi(z)}}, \tag{7.16}$$

and the angular average over a unit sphere defined by Eq. (6.13). The diffusion coefficients follow from the mobility coefficients by virtue of the fluctuation-dissipation relation (4.11).

The translational contribution (7.14) contains no effect of dielectric anisotropy, as one would expect for spherical particles, and bears only the information concerning the particle displacement. The dielectric properties cancel out in this expression, so that the translational component contains only the averaged translational diffusion matrix. The polarisability effects imply a non-zero rotational contribution which additionally depends on the scattering geometry.

Introducing the decomposition of the scattering vector $\mathbf{q}$ into its components parallel and perpendicular to the wall, $\mathbf{q} = q_\perp \hat{\mathbf{e}}_z + \mathbf{q}_\parallel$, we evaluate Eqns. (7.14) and (7.15) to find the well-known expression for the translational contribution [63, 64, 88]

$$\Gamma^t = \left\langle D^t_\parallel \right\rangle_\kappa q_\parallel^2 + \left\langle D^t_\perp \right\rangle_\kappa \left(q_\perp^2 + \frac{\kappa^2}{4}\right), \tag{7.17}$$

which is independent of the scattering geometry. As we argued in Chapter 3, the presence of an additional factor $\frac{\kappa^2}{4}$ stems from the restriction of scattering volume by the evanescent wave. The expressions for the rotational contribution, depending on the VV or VH alignment of the experimental setup read [89]

$$\Gamma^r_{VH} = \left\langle D^r_\parallel \right\rangle_\kappa \left(2 + 3n_z^2\right) + \langle D^r_\perp \rangle_\kappa \left(1 + 3n_y^2\right), \tag{7.18}$$

$$\Gamma^r_{VV} = \frac{12|\Delta\alpha|^2}{45|\alpha|^2 + 4|\Delta\alpha|^2} \left(\left\langle D^r_\parallel \right\rangle_\kappa + \langle D^r_\perp \rangle_\kappa\right). \tag{7.19}$$

Here, we have chosen the coordinate system such that $\hat{\mathbf{n}}_0 = (1, 0, 0)$, and $\hat{\mathbf{n}}_s = (0, n_y, n_z)$. Interestingly, in the VH geometry, due to the normalisation of $\hat{g}_1$ so that $\hat{g}_1(0) = 1$, the rotational component is independent of the optical properties of the particle, as in the bulk case. In the VV geometry, the prefactor depends on the characteristic polarisability properties of the material. In the calculation below, we have used the fact that the rotational operator acting on the oriented dielectric tensor may be explicitly written as

$$\mathbf{L}\mathcal{E}(\hat{\mathbf{u}}) = \mathbf{L}(\hat{\mathbf{n}}_s \cdot \boldsymbol{\epsilon}(\hat{\mathbf{u}}) \cdot \hat{\mathbf{n}}_0) = \Delta\alpha \left[(\hat{\mathbf{n}}_s \cdot \hat{\mathbf{u}})\hat{\mathbf{u}} \times \hat{\mathbf{n}}_0 + (\hat{\mathbf{n}}_0 \cdot \hat{\mathbf{u}})\hat{\mathbf{u}} \times \hat{\mathbf{n}}_s\right]. \tag{7.20}$$

The expressions (7.17) - (7.19) are valid for an arbitrary potential of direct sphere-wall interactions. We will now restrict to hard-core interactions, so that $\Phi = +\infty$ when there is overlap between the sphere and the wall, and $\Phi = 0$ otherwise. Then, the average (7.16) reduces to

$$\langle A \rangle_\kappa = \kappa \int_a^\infty \mathrm{d}z\, e^{-\kappa(z-a)} A(z). \tag{7.21}$$

This framework allows for construction of convenient predictive tools, since the values of the averaged diffusion coefficients may be pre-calculated for a given experimental value of κ. To reconstruct the slope of the curve Γ vs. q^2 in Eq. (7.17), one only needs to know the values of those coefficients, which we give in Table I. It is worth noticing, that for small penetration depths (corresponding to large values of κa), the averaged diffusion coefficients tend to their contact values at $z = 0$. It can be understood, since in this regime only the near-wall region is illuminated and only particles in the proximity of the boundary contribute to the measured correlation function, and in consequence the hindrance effects of the wall are more pronounced. In general, the scaled values of averaged rotational diffusion coefficients are larger than the translational ones due to a much weaker dependence of $\mathbf{D}^{rr}$ on the distance from the wall, compared to the *tt* part, as presented in Fig. 7.2.

Contributions from the coupling tensors We shall now prove that for a spherical particle, it follows from the symmetry of the diffusion tensors and the fact they depend solely on the distance to the particle from the wall that

$$\Gamma^{tr} + \Gamma^{rt} = 0, \tag{7.22}$$

independent of the scattering geometry [90], provided that the dielectric tensor of the particle has the axisymmetric form (7.10). To this end, we note first that in the general expression (8.14) one encounters angular averages involving the term

$$\mathcal{E}(\hat{\mathbf{u}})\mathbf{L}\mathcal{E}^*(\hat{\mathbf{u}}), \tag{7.23}$$

and its complex conjugate. Now, according to Eq. (7.10), $\mathcal{E}(\hat{\mathbf{u}})$ contains an isotropic part proportional to α, and an orientation-dependent contribution proportional to $\Delta\alpha$. Since $\mathbf{L}$ can be regarded as differentiation with respect to the angles describing the orientation, we have

$$\oint \mathrm{d}\hat{\mathbf{u}}\, \mathbf{L}(\ldots) = 0, \tag{7.24}$$

for an arbitrary function of orientation. Using this property, we conclude that the isotropic part of $\mathcal{E}(\hat{\mathbf{u}})$, which produces in (7.23) a term proportional to $\mathbf{L}\mathcal{E}^*(\hat{\mathbf{u}})$, averages out to zero. Therefore only the anisotropic part may contribute, resulting in an expression $\Delta\alpha(\hat{\mathbf{n}}_s \cdot \hat{\mathbf{u}}\hat{\mathbf{u}} \cdot \hat{\mathbf{n}}_0)\mathbf{L}\mathcal{E}^*(\hat{\mathbf{u}})$. The rotational operator acting on $\mathcal{E}(\hat{\mathbf{u}})$ acts also only on the non-isotropic part, as the isotropic term vanishes under the action of the derivative. The result of this operation is proportional to the complex polarisability anisotropy $\Delta\alpha$. Due to the structure of Eq. (8.14) we arrive at real-valued integrands

$$|\Delta\alpha|^2(\hat{\mathbf{n}}_s \cdot \hat{\mathbf{u}}\hat{\mathbf{u}} \cdot \hat{\mathbf{n}}_0)\mathbf{L}(\hat{\mathbf{n}}_s \cdot \hat{\mathbf{u}}\hat{\mathbf{u}} \cdot \hat{\mathbf{n}}_0) = \tfrac{1}{2}|\Delta\alpha|^2\mathbf{L}(\hat{\mathbf{n}}_s \cdot \hat{\mathbf{u}}\hat{\mathbf{u}} \cdot \hat{\mathbf{n}}_0)^2, \tag{7.25}$$

which again average out to zero.

κa	Translational coefficients		Rotational coefficients	
	$\left\langle \tilde{D}^t_{\parallel} \right\rangle_\kappa$	$\left\langle \tilde{D}^t_{\perp} \right\rangle_\kappa$	$\left\langle \tilde{D}^r_{\parallel} \right\rangle_\kappa$	$\left\langle \tilde{D}^r_{\perp} \right\rangle_\kappa$
0.1	0.884	0.781	0.983	0.994
0.2	0.831	0.682	0.968	0.989
0.3	0.791	0.612	0.954	0.983
0.4	0.761	0.559	0.942	0.979
0.5	0.736	0.516	0.931	0.976
0.6	0.715	0.481	0.920	0.971
0.7	0.697	0.451	0.910	0.968
0.8	0.681	0.425	0.901	0.965
0.9	0.667	0.403	0.892	0.962
1	0.654	0.383	0.884	0.960
1.1	0.643	0.365	0.876	0.957
1.2	0.632	0.349	0.868	0.955
1.3	0.622	0.335	0.861	0.952
1.4	0.614	0.322	0.854	0.949
1.5	0.605	0.310	0.848	0.947
1.7	0.591	0.288	0.836	0.944
1.9	0.578	0.270	0.825	0.940
2	0.572	0.262	0.820	0.939
5	0.473	0.140	0.716	0.907
7	0.442	0.108	0.677	0.896
9	0.420	0.088	0.647	0.888

Table I: Translational and rotational components of first cumulant approximation to $\hat{g}_1(\mathbf{q}, t)$ for hard-core interactions between the wall and the particle obtained by numerical integration of distance-dependent translational and rotational diffusivities of the particle near a wall. The coefficients are given here in the dimensionless form, according to (7.6). Compiled from [88,90].

The second cumulant for translational motion and the existence of higher terms The general formalism developed for the cumulant and moment expansion in Chapter 4 allows for the derivation of higher-order terms in the time series, in principle extending the applicability of the approximation to longer times. Below, we shall calculate the second cumulant for purely translational motion, and discuss the existence of higher cumulants.

Using Eq. (4.25) and (4.28), and the specific form of the *tt* mobility matrix (7.2) one may repeat the procedure outlined above and derive the second moment m_2 as

$$\begin{aligned} m_2 &= q_\parallel^4 \left\langle (D^t_\parallel)^2 \right\rangle_\kappa + \left(q_\perp^2 + \frac{\kappa^2}{4} \right)^2 \left\langle (D^t_\perp)^2 \right\rangle_\kappa - 2q_\parallel^2 \left(\frac{\kappa^2}{4} - q_\perp^2 \right) \left\langle D^t_\parallel D^t_\perp \right\rangle_\kappa \\ &+ \kappa q_\parallel^2 \left\langle D^t_\parallel \left(\frac{\mathrm{d}D^t_\perp}{\mathrm{d}z} - D^t_\perp \beta \frac{\mathrm{d}\Phi}{\mathrm{d}z} \right) \right\rangle_\kappa - \kappa \left(q_\perp^2 + \frac{\kappa^2}{4} \right) \left\langle D^t_\perp \left(\frac{\mathrm{d}D^t_\perp}{\mathrm{d}z} - D^t_\perp \beta \frac{\mathrm{d}\Phi}{\mathrm{d}z} \right) \right\rangle_\kappa \\ &+ \left(q_\perp^2 + \frac{\kappa^2}{4} \right) \left\langle \left(\frac{\mathrm{d}D^t_\perp}{\mathrm{d}z} - D^t_\perp \beta \frac{\mathrm{d}\Phi}{\mathrm{d}z} \right)^2 \right\rangle_\kappa . \end{aligned} \tag{7.26}$$

from which the second cumulant is calculated using Γ^t, as in Eq. (7.17). The above expression,

valid for an arbitrary interaction potential, corrects the one given in the appendix to Ref. [64], which contains an erroneous sign in the fourth and fifth term on the right-hand side.

Restricting now to the hard-core interaction potential

$$\Phi(z) = \begin{cases} 0 & z > a, \\ +\infty & z \leq a. \end{cases} \tag{7.27}$$

we evaluate Eq.(7.26). Special care has to be taken while calculating the derivatives of the interaction potential in this limit. The expression

$$-D_\perp^t(z)\beta\frac{\mathrm{d}\Phi}{\mathrm{d}z}e^{-\beta\Phi} = D_\perp^t(z)\frac{\mathrm{d}}{\mathrm{d}z}\left(e^{-\beta\Phi}\right), \tag{7.28}$$

within the averages, reduces then to $D_\perp(a)\delta(z-a)$. With the neglect of hydrodynamic interactions, we would have $D_\perp^t(z=a) \neq 0$, and the last term on the right-hand side of Eq. (7.26) diverges, and therefore the second cumulant does not exist. The short-time expansion of the exact solution due to Lan *et al.* [66] in this (unphysical) case, which is discussed in Ref. [88], shows that the first term in the series is of order t, which guarantees the existence of the first cumulant, while the next term is of order $t^{3/2}$. Due to hydrodynamic interactions, however, $\mathbf{D}^t(z) \to 0$ when $z \to a$. This assures that the right-hand side of Eq. (7.26) exists and has a finite hard-core limit.

In this case the derivation, as shown in the Appendix to Ref. [88], leads to the second moment in the form

$$\begin{aligned} m_2 &= q_\parallel^4\left\langle (D_\parallel^t)^2\right\rangle_\kappa + \left(q_\perp^4 - \frac{\kappa^4}{16}\right)\left\langle (D_\perp^t)^2\right\rangle_\kappa - 2q_\parallel^2\left(\frac{\kappa^2}{4} - q_\perp^2\right)\left\langle D_\parallel^t D_\perp^t\right\rangle_\kappa \\ &+ \kappa q_\parallel^2\left\langle (\partial_z D_\perp^t) D_\parallel^t\right\rangle_\kappa + \left(q_\perp^2 + \frac{\kappa^2}{4}\right)\left\langle \left(\partial_z D_\perp^t\right)^2\right\rangle_\kappa, \end{aligned} \tag{7.29}$$

where $\partial_z \equiv \frac{\mathrm{d}}{\mathrm{d}z}$ denotes a derivative with respect to z. In addition, the penetration-depth average for the hard-core potential is given by Eq. (7.21). The second cumulant reads then

$$\Gamma_2^t = m_2 - (\Gamma^t)^2. \tag{7.30}$$

It may also be proved that Γ_2, constructed using Γ^t and m_2, is non-negative [88].

We have calculated the values of the coefficients appearing in the second moment in Table II using the method given by Cichocki and Jones [46]. For convenience, in the Table we rescaled the diffusion coefficients by the single particle bulk diffusion coefficient in accordance with Eq. (7.6). Once the experimental parameters κ, $q_\parallel$, $q_\perp$, are known, the table allows for a fast and straightforward calculation of two approximations to the EACF (3.6) for purely translational motion: by means of the first cumulant

$$\hat{g}_1^{(1)}(t) = \exp(-\Gamma^t t), \tag{7.31}$$

and the second cumulant approximation

$$\hat{g}_1^{(2)}(t) = \exp(-\Gamma^t t + \tfrac{1}{2}\Gamma_2^t t^2). \tag{7.32}$$

For hard-core interactions, the cumulant expansion can be performed only up to the third order for the following reason. The diffusion coefficients are non-analytical at $z = a$, as argued in Sec.

κa	Second moment for translational relaxation				
	$\left\langle (\tilde{D}^t_{\parallel})^2 \right\rangle_\kappa$	$\left\langle (\tilde{D}^t_{\perp})^2 \right\rangle_\kappa$	$\left\langle \tilde{D}^t_{\parallel} \tilde{D}^t_{\perp} \right\rangle_\kappa$	$a \left\langle (\partial_z \tilde{D}^t_{\perp}) \tilde{D}^t_{\parallel} \right\rangle_\kappa$	$a^2 \left\langle (\partial_z \tilde{D}^t_{\perp})^2 \right\rangle_\kappa$
0.1	0.796	0.652	0.715	0.053	0.029
0.2	0.708	0.516	0.597	0.088	0.055
0.3	0.647	0.429	0.517	0.115	0.079
0.4	0.600	0.367	0.459	0.137	0.101
0.5	0.563	0.321	0.414	0.155	0.121
0.6	0.533	0.284	0.377	0.171	0.141
0.7	0.507	0.254	0.347	0.184	0.159
0.8	0.485	0.230	0.322	0.195	0.176
0.9	0.466	0.209	0.300	0.206	0.192
1	0.449	0.191	0.281	0.214	0.208
1.1	0.434	0.176	0.264	0.222	0.222
1.2	0.420	0.163	0.249	0.230	0.236
1.3	0.408	0.151	0.236	0.236	0.249
1.4	0.396	0.141	0.224	0.242	0.262
1.5	0.386	0.131	0.213	0.247	0.274
1.7	0.368	0.116	0.194	0.256	0.297
1.9	0.352	0.103	0.179	0.264	0.318
2	0.345	0.097	0.172	0.268	0.328
5	0.236	0.031	0.078	0.311	0.518
7	0.206	0.019	0.056	0.317	0.587
9	0.186	0.013	0.043	0.319	0.636

Table II: Components of second cumulant of the EACF for hard-core interaction between the wall and the particle. The values of the cumulants can be reproduced from eq. (7.17) and (7.29) using the above averaged values of the diffusion coefficients. The derivative with respect to z is denoted by ∂_z, and the tilde denotes the diffusion coefficients rescaled by the single-particle bulk diffusion coefficient D_0, $\tilde{D}^t_{\perp,\parallel} = D^t_{\perp,\parallel}/D^t_0$. Partially reproduced from [88].

7.1. The adjoint Smoluchowski operator $\mathcal{L}^\dagger$ contains two derivatives with respect to z, so that consecutive terms in the cumulant expansion contain averages of higher order derivatives of $D^t_\perp$ and $D^t_\parallel$. Careful analysis of the integrals in these averages, taking into account the nonanalytic behaviour of the diffusion coefficients in the proximity the wall, given by Eq. (7.9), leads to a conclusion that the third cumulant exists, while the fourth cumulant and all higher ones do not exist.

It is worth noticing that when the penetration depth is small (which corresponds to large values of κa), the penetration-depth averages of the diffusion coefficients in Table II become small as well. The reason for such behaviour is that in this case only the particles that are very close to the wall contribute to the average. Moreover, for those particles, their diffusion coefficients decrease due to hydrodynamic interactions with the wall.

7.3 Beyond the cumulants: Brownian Dynamics simulations

The decay of $\hat{g}_1(\mathbf{q}, t)$ for longer times, beyond the approximation by the first cumulant, is less understood, and there seems to be no exact expressions for the decay of the EACF. The relaxation of the correlation functions may be studied by means of higher cumulants but this may not always be possible due to their divergent character. To infer knowledge about the longer-time decay of g_1, and to assess the validity of an approximation of the EACF by means of the first cumulant (or two cumulants for purely translational motion), we have employed a numerical Brownian Dynamics simulations scheme.

In our simulations, the electric field correlation function $\hat{g}_1(\mathbf{q}, t)$ is calculated by averaging the expression $\langle E_s^*(\mathbf{q}, t = 0) E_s(\mathbf{q}, t)\rangle$ over many trajectories of a Brownian particle in its configuration space $\mathbf{X} = (\mathbf{r}, \hat{\mathbf{u}})$. We typically generated $N = 10^5$ trajectories to obtain a statistical error of order of 1%. The starting points are distributed initially with an exponential weight $e^{-\kappa z/2}$. The statistics is then improved by exploiting the Markov property of diffusion processes, which allows multiple use of the same trajectories with different moments of time taken as starting points [173].

The Brownian Dynamics technique [122, 123] relies on numerical integration of the Langevin equation, corresponding to the relevant Smoluchowski equation [35, 174]. Explicit expressions for the Brownian Dynamics increments to position and orientation, given in general by Dickinson *et al.* [175], are discussed for a sphere in the presence of a wall in the work of Jones and Alavi [176]. The length scale is set by the particle radius a, while the time scale is related to the structural relaxation time $\tau = a^2/D_0^t$, i.e. the time needed by the particle to diffuse over a distance of its own radius.

Below we discuss two numerical schemes used in our calculations. The first one includes full hydrodynamic interactions of a sphere with a no-slip planar wall to resolve its translational and rotational motion. The second one poses a simplification by neglecting the translation-rotation coupling in the particle motion. Then, the routines may be simplified to greatly reduce the time of computations.

Inclusion of hydrodynamic interactions The Langevin equation which lies at the root of Brownian Dynamics simulations, is obtained from the corresponding Smoluchowski equation (4.7). In the case of a single hard-core particle in a wall-bounded fluid, we may use the structure of the diffusion matrix $\mathbf{D}$, given in Eqs. (7.2) - (7.5) to rewrite the Smoluchowski equation in a more explicit form

$$\begin{aligned}\frac{\partial P}{\partial t} = &\frac{\partial}{\partial z}\left(D_\perp^t(z)\frac{\partial P}{\partial z}\right) + D_\parallel^t(z)\left(\frac{\partial^2}{\partial x^2} + \frac{\partial^2}{\partial y^2}\right)P \\ &+ D_\parallel^r(z) L_z^2 P + D_\perp^r(z)[\mathbf{L}^2 - L_z^2]P \\ &+ 2D^{tr}(z)\cdot(\nabla\times\mathbf{L})_z P,\end{aligned} \tag{7.33}$$

where the unit vector $\hat{\mathbf{e}}_z$ indicates again the direction normal to the wall, and we have denoted $A_z = \hat{\mathbf{e}}_z \cdot \boldsymbol{A}$ for any vector $\boldsymbol{A}$. The Euler integration scheme basing on a corresponding Langevin equation was given earlier by Jones and Alavi [176]. Below, we briefly describe the update rules

for the configuration $\mathbf{X} = (\mathbf{r}, \hat{\mathbf{u}})$ of the particle in a short period of time Δt. In the following, we rescaled the diffusivities by their bulk values, as defined in Eq. (7.6).

Suppose the initial coordinates at the beginning of the step to be $(\mathbf{r}_0, \hat{\mathbf{u}}_0)$ at time t_0. In a time step of Δt the coordinates attain their new values $(\mathbf{r}, \hat{\mathbf{u}})$ in accordance with the following update rules

$$\mathbf{r} = \mathbf{r}_0 + \frac{\mathrm{d}\tilde{D}^t_\perp}{\mathrm{d}z}\hat{\mathbf{e}}_z\Delta t + \mathbf{s}^t, \tag{7.34}$$

$$\hat{\mathbf{u}} = \frac{\mathbf{u}'}{|\mathbf{u}'|}, \tag{7.35}$$

where

$$\mathbf{u}' = \hat{\mathbf{u}}_0 - \frac{3}{4}\left(\tilde{D}^r_\perp - \tilde{D}^r_\parallel\right)(u^2_{z,0}\hat{\mathbf{u}}_0 - u_{z,0}\hat{\mathbf{e}}_z)\Delta t + \mathbf{s}^r \times \hat{\mathbf{u}}_0, \tag{7.36}$$

with $u_{z,0} = \hat{\mathbf{e}}_z \cdot \hat{\mathbf{u}}_0$. All the diffusivities on the right-hand side are evaluated at the initial position z_0. The random displacement vector $\mathbf{S} = (a\mathbf{s}^t, \mathbf{s}^r)$ has to satisfy the conditions

$$\langle \mathbf{S} \rangle = 0, \quad \langle \mathbf{SS} \rangle = 2\Delta t \mathbf{D}, \tag{7.37}$$

where $\mathbf{D}$ is the diffusion tensor for a sphere at $(\mathbf{r}_0, \hat{\mathbf{u}}_0)$. The explicit expressions for the noise term may be obtained by performing the standard [122] Cholesky decomposition of the diffusion tensor $D_{ij} = B_{ik}B_{jk}$ and generating six independent Gaussian random variables f_i having the stochastic properties

$$\langle f_i \rangle = 0, \quad \left\langle f_i f_j \right\rangle = 2\delta_{ij}\Delta t. \tag{7.38}$$

The indices $i = 1, 2, 3$ refer to translational components along x, y, z, respectively, while $i = 4, 5, 6$ describe the rotations along these axes. We may now write the required noise terms as

$$s_i = \sum_{j=1}^{6} B_{ij} f_j, \tag{7.39}$$

where the components of $\mathbf{B}$ are given by [172, 176]

$$\begin{aligned}
B_{11} &= B_{22} = \sqrt{\tilde{D}^t_\parallel}, \qquad B_{33} = \sqrt{\tilde{D}^t_\perp}, \\
B_{42} &= -B_{51} = -\frac{3}{4}\frac{\tilde{D}^{tr}}{\sqrt{\tilde{D}^t_\parallel}}, \\
B_{44} &= B_{55} = \frac{3}{4}\frac{1}{\sqrt{\tilde{D}^t_\parallel}}\left(\frac{4}{3}\tilde{D}^t_\parallel\tilde{D}^r_\parallel - (\tilde{D}^{tr})^2\right)^{1/2}, \\
B_{66} &= \frac{1}{2}\sqrt{3\tilde{D}^r_\perp}.
\end{aligned} \tag{7.40}$$

Simplified scheme It is important to emphasize that the routine presented above can be simplified by reducing the number of degrees of freedom, provided that we disregard the translational-rotational motion coupling. Indeed, letting $D^{tr} = 0$ in Eq. (7.33), we arrive at an equation describing rotational and translational diffusion with only coupling encoded in the z-dependence of the diffusion matrix. This simplification is particularly useful when one is

interested in purely translational effects, and has been used in our earlier work [88], to which we refer for details. This scheme can be easily generalised to include (independent) rotations. The simplified routine relies on performing the Fourier transformation in the xy-plane, which leads to the equation for the transformed pdf $\widetilde{P} \equiv \widetilde{P}(q_{\|}, z, z_0, t)$ being the transformed conditional pdf for a particle to be at the distance z from the wall, provided that it was at z_0 at $t = 0$. Its form reads

$$\frac{\partial \widetilde{P}}{\partial t} = \frac{\partial}{\partial z}\left(D_{\perp}^{t}(z) \frac{\partial \widetilde{P}}{\partial z} \right) - q_{\|} D_{\|}^{t}(z) \widetilde{P}, \tag{7.41}$$

which can be looked upon as a one-dimensional diffusion-reaction equation, or a diffusion equation with a probability sink. The reduction from the three-dimensional Smoluchowski equation to one dimension allows for significant acceleration of the simulation. We now recast Eq. (7.41) as

$$\widetilde{P}(q_{\|}, z, z_0, t) = e^{\mathcal{L}t} \widetilde{P}(q_{\|}, z, z_0, t = 0), \tag{7.42}$$

and decompose the evolution operator $\mathcal{L}$ into two distinct parts: the diffusion operator $\mathcal{L}_1 = \partial_z[D_{\perp}(z)\partial_z(\cdot)]$, and the probability-sink operator $\mathcal{L}_2 = -q_{\|}^2 D_{\|}(z)$. To obtain a suitable numerical scheme, we use the Trotter identity [173] and treat each part in a different way. The evolution according to $\mathcal{L}_1$ can be obtained from a Brownian dynamics numerical scheme. We generate trajectories of Brownian particles in the z-direction. Obtained trajectories build the corresponding probability distribution and are then used as an ensemble for calculating the averages. Every Brownian dynamics step is followed by application of $\mathcal{L}_2$. We account for this type of evolution by introducing a decay of $\widetilde{P}$, according to

$$\widetilde{P}(q_{\|}, z, z_0, t + \Delta t) = e^{\mathcal{L}_2 \Delta t} \widetilde{P}(q_{\|}, z, z_0, t) = \widetilde{P}(q_{\|}, z, z_0, t) e^{-q_{\|}^2 D_{\|}(z) \Delta t}. \tag{7.43}$$

Thus, the weight a particle contributes to the probability distribution is dependent on its trajectory.

Numerical results - translational diffusion The case of optically isotropic hard-sphere suspensions can be treated using the simplified algorithm. In Fig. 7.3, a comparison of EACF's is made as obtained from our simulations, which account for hydrodynamic interactions, and the analytical LOS (Lan-Ostrowsky-Sornette) solution [111] where hydrodynamic interactions are completely neglected. The figures 7.3(a) and (b) are plotted for two different penetration depths at fixed $q_{\perp}a = 0.97$ and $q_{\|}a = 1.25$. The square data points are the simulation results and the lowest curve are the results for a constant diffusion coefficient where hydrodynamic interactions are neglected. As can be seen, there is a large deviation between the results with and without hydrodynamic interactions, also for the initial slope, which implies that hydrodynamic interactions are of essential importance to describe the dynamics of spherical colloids near walls. Also included in Fig. 7.3 are the results from the first and second order cumulant approximation. The the second cumulant approximation is almost exact for sufficiently large penetration depths, typically of order $\kappa a \sim 1$, and becomes less accurate for small penetration depth (large κa). Then the cumulant values calculated for large κa with the help of Tables I and II can be used to predict the initial decay rate of the EACF. These results are quantified in our work [88] in terms of deviation form the numerically calculated values.

Numerical results - rotational and translational diffusion For optically anisotropic spheres, numerical codes involving the full mobility matrix have to be used for the calculation of EACF.

Comparison of the approximation by the first cumulant and BD simulation is presented in Fig. 7.4. Due to the presence of additional relaxation mode, Γ^{rr}, the decay of $\hat{g}_1$ is generally faster than compared to isotropic spherical particles exhibiting only translational motion. This effect is, however, much more pronounced for VH-scattering, since the rotational contribution is independent of dielectric properties of the particle. The validity of the first cumulant approximation can be extensively tested using the aforementioned simulation schemes.

7.4 Experimental details

All the EWDLS experiments have been conducted in Forschungszentrum Jülich (Germany) with a home-built instrument based on a triple axis diffractometer, which has been described in detail elsewhere [64]. Its alignment has also been discussed in Chapter 3. As a light source, a frequency doubled Nd/Yag Laser (Excelsior; Spectra Physics) was used, with a vacuum wavelength of $\lambda = 532$ nm and a nominal power output of 150 mW. Two samples (A and B) have been used, both involving a dilute suspension of spherical particles. We describe them in detail below:

Isotropic spherical particles (A) EWDLS experiments involving optically isotropic particles [88] were performed on poly-(methyl methacrylate) (PMMA) particles, which were sterically stabilized by a thin poly-12-hydrohystearic acid layer (purchased from Andrew Schoffield, University of Edinburgh), in a refracting index matching solvent mixture ($n_2 = 1.498$) consisting of cis-decaline and tetraline (20/80 w/w). The solvent was chosen to minimize suspension turbidity and thereby multiple scattering, as well as van der Waals interactions. The particle concentration was determined by drying a small aliquot of the suspension and weighing the remaining polymer. We employed standard DLS measurements to determine the particles hydrodynamic radius, where we used three different methods to analyse the IACF, namely cumulant analysis, stretched exponential fitting and inverse Laplace transformation. The three methods gave a hydrodynamic radius of $a = 98$ nm varying less than 1 nm and indicated a size polydispersity of less than 5 %. The latter finding is confirmed by the observation that the suspensions crystallize at sufficiently large particle volume fractions, which is usually regarded as indication, that polydispersity effects can be excluded. As the particles are not charged, and suspended in a non-polar solvent with matching dielectric properties, DLVO interactions between the particles as well as between the wall and the particles can be neglected to a good approximation and the system may be regarded as a suspension of hard spheres [177].

Optically anisotropic spherical colloids (B) For the measurements involving rotational diffusion [89, 90] optically anisotropic spheres (produced by Ausimont) made of a copolymer of tetrafluoroethylene (TFE) suspended in an aqueous NaCl-solution were used, with a salt concentration of 10 mMol/l, corresponding to a Debye screening length of 3 nm. This is sufficiently small to allow approximation of the interactions between the colloids and the wall by a hard core potential. The particles were dialysed extensively against 10^{-2} mMol/l NaCl solution to ensure that all surfactants from the emulsion polymerisation were removed and therefore no steric stabilisation layers are present. The refractive index and the viscosity of the solvent were approximated by the values for water, that is $n_2 = 1.33$ and $\eta = 1$ mPas at T=293 K . The

radius of the particles was determined by bulk depolarised dynamic light scattering (DDLS) measurements to be $a = 110$ nm with a polydispersity of less than 10%, as indicated in Fig. 7.5. The fact that the rotational and translational diffusion coefficients yield the same hydrodynamic radius when calculated from D_0^r and D_0^t proves that the particles are of spherical shape.

Data analysis Compared to conventional DLS experiments, the analysis of correlation functions measured in EWDLS is usually hampered by two problems. Firstly, there is always a static contribution to the scattered intensity, which originates from surface roughness and small impurities. This leads to a mixing of homodyne and heterodyne detection. To account for this, a general formulation of the Siegert relation has to be used to relate the field correlation function $g_1(t)$ to the measured intensity correlation function $g_2(t)$

$$g_2(t) = 1 + 2C_1 g_1(t) + (C_2 g_1(t))^2 \tag{7.44}$$

where $C_2 = 1 - \sqrt{1 - A}$ and $C_1 = C_2 - C_2^2$, with A being the intercept of $g_2(t)$ [64]. Secondly, EWDLS correlation functions often exhibit a very slow decay at large times. Although the physical origin of this slow relaxation has not been clarified yet, it was conjectured that the slow decay is due to inevitable stray-light originating from surface corrugations which is scattered into the detector by solute particles. The scattering vector of this contribution, q_{add} would be roughly two orders of magnitude smaller than the regular scattering vectors for the given setup [88]. Accordingly, the scattered field which is detected contains an additional contribution with the phase $\mathbf{q}_{\text{add}} \cdot \mathbf{r}(t)$, and the corresponding correlation function will exhibit an additional exponential relaxation at long times. Therefore we fit the long time part of the experimental TCF, typically at $t > 10$ ms, by an exponential and subtract this contribution from the experimental data, which results a TCF which decays to $g_2(t) - 1 = 0$ for large times. Subsequently the initial part ($t < 0.2$ ms) of the resulting TCF is fitted with

$$g_2(t) = 1 + 2C_1 \exp\{-\Gamma t\} + (C_2 \exp\{-\Gamma t\})^2 \tag{7.45}$$

to determine the first cumulant, Γ.

7.5 Results

The predictions by means of the cumulants and Brownian dynamics simulations may be directly compared to experimental results. We present here two types of experiments involving samples A and B. In the first case, only translational diffusion is resolved, whereas the latter case allows us to measure rotational diffusion in addition. By a careful analysis of collected data, we were able to discern between the two processes, and also extract the anisotropic diffusion coefficients of a near-wall spherical particle from experiments.

7.5.1 Translational diffusion

The first cumulant for purely translational motion is given by Eq. (7.17). This relation may be straightforwardly tested in experiments. In particular, it gives an experimental access to

averaged near-wall diffusion coefficients, which may be measured using the EWDLS setup as slopes of the curves Γ vs. $q_{\parallel}^2$ with the $q_{\perp}$ kept fixed, and vice versa.

It turns out that there are huge fluctuations in the scattered intensity when the volume fraction of colloids is less than about 0.1. This is probably due to a too small number of colloids within the scattering volume. These large fluctuations render accurate measurements at very low concentrations not feasible. We therefore have to restrict the experiments to a volume fraction of 0.1. At this concentration the effects of inter-colloidal interactions cannot be fully neglected, so that only a semi-quantitative comparison to the theory is feasible.

Experimental results are given in Fig. 7.6, as empty triangles, for a concentration corresponding to a volume fraction of 0.106. The left panel of plots is for a small penetration depth ($\kappa a = 1.3$), and the right panel is for a large penetration depth ($\kappa a = 0.77$). From top to bottom, the parallel component of the scattered wave vector increases (from $q_{\parallel} a = 1.06$, 1.49, to 1.92). For all plots, the perpendicular component of the scattered wave vector is fixed at $q_{\perp} a = 1.49$. The filled squares are the simulation results, the solid lines correspond to the second cumulant approximation, and the dotted lines to the LOS predictions, where hydrodynamic interactions are neglected. As can be seen, the simulation results for infinite dilution are in reasonable agreement with the experiments. There are deviations at later times, which can have two reasons. First of all the concentration is not low enough to be able to completely neglect inter-colloidal interactions. Bulk DLS measurements actually show that in the relevant q-range the IACF decay rates measured at $\phi = 0.106$ are about 30% smaller than those obtained at infinite dilution. Secondly, in many EWDLS experiments a long time decay of the IACF, as shown in Fig. 7.7, is observed, which so far is not yet well understood. A possible reason is the unavoidable heterodyne stray-light originating from surface defects which is scattered by colloids in the bulk of the suspension into the detector [178]. Due to the scattering optics, only the light scattered from particles which are located in the solid angle defined by the position of the defect and the detector aperture will be detected. This corresponds to scattering vectors in the range smaller than approximately 10^{-4} nm^{-1} for the given set up. Taking into account the particles bulk diffusion constant this will lead to relaxation times around 10 seconds and above. This might partly explain the slower decay of the experimental data as compared to the simulations at longer times. In view of the good agreement between simulation data and the second cumulant expansion, it is no surprise that the second cumulant approximation also describes the experimental data quite accurately. Again, the correlation functions without hydrodynamics (the dotted lines) are far off from both experiments and simulations.

Due to the complicated hydrodynamic interactions of colloids and a wall, it is not possible to derive a closed analytical expression for EWDLS correlation functions. At infinite dilution, where inter-colloidal interactions can be neglected, the EACF for spherical colloids in bulk is simply equal to $\exp(-q^2 D_0 t)$, where D_0 is the Stokes-Einstein diffusion coefficient. A similar expression for the full time dependence of the EWDLS-correlation, also at infinite dilution, has so far not been reported. It seems that the full time dependence of EWDLS-correlation functions, even for very dilute suspensions of spherical colloids, requires cumulant approximations and/or simulations. We made a comparison between first- and first-two-cumulant approximations and results obtained from a new simulation algorithm (with numerical errors that do not exceed the size of points). These results are also compared to experiments on hard-sphere like colloids, where the penetration depth and scattering wave vectors are varied. The first-two-cumulants approximation is surprisingly accurate, especially for somewhat larger penetration depths. This is important, since one can rely on an analytic form for the correlation function based on the

known forms of the first two cumulants. Furthermore, there is reasonable agreement between the simulations and experiments. For future experiments, it would be desirable to use sample cells where the path length of stray light through the bulk of the sample is minimized.

7.5.2 Rotational diffusion

Examples for the initial part of typical time correlation functions (TCFs) are shown in Fig. 7.8. There we compare experimental data obtained at different scattering geometries to theoretical first cumulant predictions, and to Brownian Dynamics simulations including full hydrodynamic interactions. The measured intensity TCFs were non-linear least-squares fitted using the procedure described above, and the obtained parameter values were used to calculate the normalised field correlations functions, $g_1(t)$, shown in the plots. The simulation data, which were calculated free of adjustable parameters match the experimental data almost perfectly down to a correlation level of 10%. Somewhat surprisingly, the first cumulant predictions agree very well with the experimental and the simulated data up to long times, which we demonstrate for a chosen set of data in Fig. 7.9. It is expected that the variation of the particle diffusion coefficients along the z-direction, in combination with the evanescent illumination profile, causes a deviation of the TCF from a single exponential, similar to the deviation observed for TCFs obtained from samples with a large size polydispersity in bulk. However, if the penetration depth in an EWDLS experiment is small, as in the present case, the distribution of diffusion coefficients within the illuminated volume is small and consequently the correlation functions will deviate significantly from a single exponential only at large times.

In EWDLS experiments, the components of the scattering vector may be changed independently, as we discussed in Section 3. Since, however, also the polarisation vector of the scattered light depends on the scattering angles by Eq. (3.4), it is rather cumbersome to maintain VV- or VH-geometry, while scanning only one of the scattering vector components. In this study, we rather choose to keep $\theta_r = 0$ and scan only α_r from 30 to 130 degrees, which results in variation of both $q_{\parallel}$ and $q_{\perp}$ viz.

$$q_{\perp} = q_0 \sin \alpha_r, \tag{7.46}$$

$$q_{\parallel} = q_0(1 - \cos \alpha_r), \tag{7.47}$$

with $q_0 = 2\pi n_2/\lambda_0$. Then we have $q^2_{\text{total}} = 2q_0^2(1 - \cos \alpha_r)$.

The first cumulant values obtained from the data fitting, are shown in Fig. 7.10. In the top part we plot Γ in dependence of the total scattering vector magnitude squared, while in the bottom part the cumulants are plotted versus n_z^2. From both representations it is obvious that the parameter free predictions for the first cumulant describe the experimental data correctly. Although the experimental data are scattered, it is obvious, that they follow the non-linear variation with q^2_{total}, which is predicted by theory. This non-linearity is due to the fact that $q_{\text{total}} \approx q_{\perp}$ for low scattering angles, while at high angles $q_{\parallel}$ is the dominating component. Accordingly, values of Γ are dominated by the diffusion normal to the interface at low q_{total} while at high q_{total} the diffusion parallel to the interface is prominent.

The expressions for the first cumulant in EWDLS, given by Eqs. (7.17) - (7.19), and DDLS reflect an important distinguishing property – even for large optical anisotropy, the amplitude of the rotational contribution in the VV case, is much smaller than in the VH case. From bulk SLS

measurement we determine the ratio of averaged scattered intensities to be $I_{VH}/I_{VV} \approx 1/20$. Since this ratio is given by [101]

$$\frac{I_{VH}}{I_{VV}} = \frac{|\Delta\alpha|^2}{15|\alpha|^2 + \frac{4}{3}|\Delta\alpha|^2}, \tag{7.48}$$

we may use it, together with Eqns. (7.18) and (7.19), to estimate the rotational contribution to Γ in the VV case to be of the order of 5% at $(qa)^2 \approx 2$ and decreasing with increasing qa. Therefore, as this ratio is not very large, we might approximate the first cumulant in VV-geometry not to have any rotational contribution. One can then measure the sole rotational component in the VH case, described by Eq. (7.18), by measuring the full initial decay rate in VH and VV and subtracting one from the other

$$\Gamma^r_{VH} \approx \Gamma_{VH} - \Gamma_{VV}. \tag{7.49}$$

In this way, at the level of the first cumulant, translations and rotations may be decoupled and therefore purely rotational properties become experimentally accessible [89].

The rotational contribution to the TCF relaxation, Γ^r_{VH} is plotted vs. n_z^2 in Fig. 7.11. As these data represent the difference of two sets of experimental results, which each have a relative error of 5 to 10 %, the Γ^r_{VH} are rather scattered. Nevertheless, they show the linear trend predicted by Eq. (7.18), which is added as a solid line to the graph. Since $n_z^2 + n_y^2 = 1$, Eq. (7.18) may be reformulated as

$$\Gamma^r_{VH} = 2\left\langle D^r_{\parallel}\right\rangle_\kappa + 4\left\langle D^r_{\perp}\right\rangle_\kappa + 3\left(\left\langle D^r_{\parallel}\right\rangle_\kappa - \left\langle D^r_{\perp}\right\rangle_\kappa\right) n_z^2 \tag{7.50}$$

indicating that the averaged rotational diffusion constants can be determined from the intercept and the slope of a linear regression of Γ^r_{VH} vs. n_z^2. In Fig. 7.11, a linear fit to data results in a fair agreement with theoretical predictions, with both diffusivities differing by less than 8% from the theoretical predictions.

Performing the experiments for different penetration depths, we were able to extract from the data the average rotational diffusion coefficients of a sphere close to a wall which we compare with theoretical predictions in Fig. 7.12. The experimental data falls on top of the theoretical predictions with reasonable agreement.

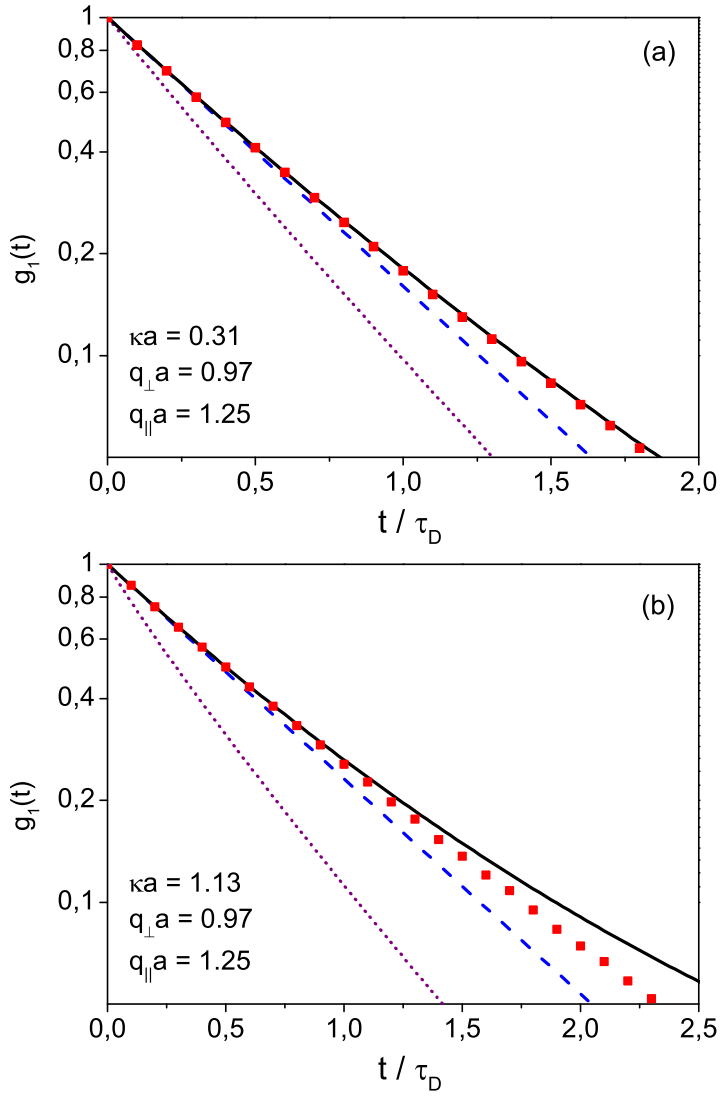

Figure 7.3: Numerical values for the EACF for two penetration depths at fixed values of the wave-vector components parallel and perpendicular to the wall, typical for experiments. The data points (red squares) are simulation results. The dotted curve is the EACF obtained by neglecting the hydrodynamic interactions (LOS solution). The dashed curve is an approximation by means of the first cumulant, while the solid line is the two-cumulant approximation, given by Eqs. (7.31) and (7.32), respectively. Reprinted from [88].

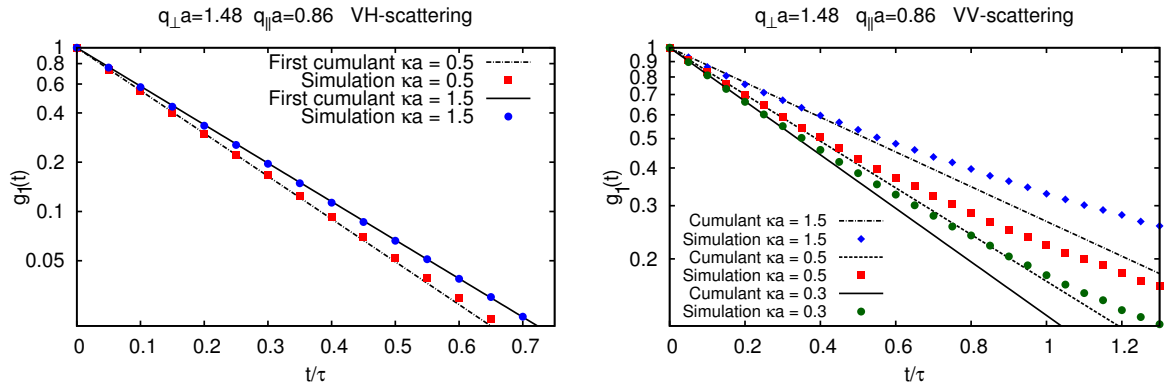

Figure 7.4: Comparison of approximation by the first cumulant (7.13) and the BD simulation for optically anisotropic particles. Here, we assumed $|\alpha| = |\Delta\alpha| = 1$ and $n_y = n_z = 1/\sqrt{2}$ in VH mode. In both cases the decay can be accurately described by the first cumulant even for moderate times – up to 0.5 of the initial value of g_1 for VV, and even for longer times for VH-geometry. The decay is generally faster in the VH case, as the additional rotational relaxation mode is more pronounced then. The statistical error of simulation data is of the order of point size. Reprinted from [90].

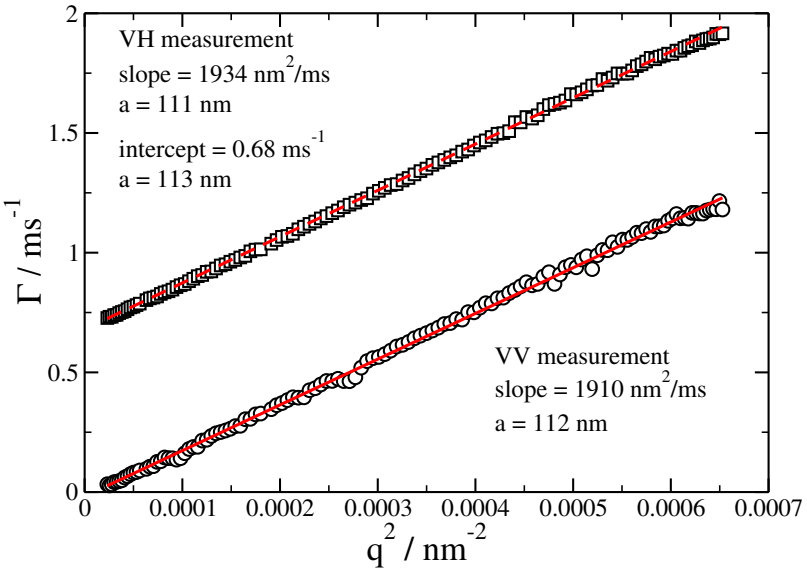

Figure 7.5: The first cumulant Γ measured as a function of q^2 in bulk DDLS experiments with sample B in VV and VH geometry. From the slopes of the dependencies, and the intercept of the VH curve, in accordance with Eqs. (6.21)-(6.23), one may calculate the hydrodynamic radius of particles from the relevant diffusion coefficients, which confirms the spherical shape of the particles.

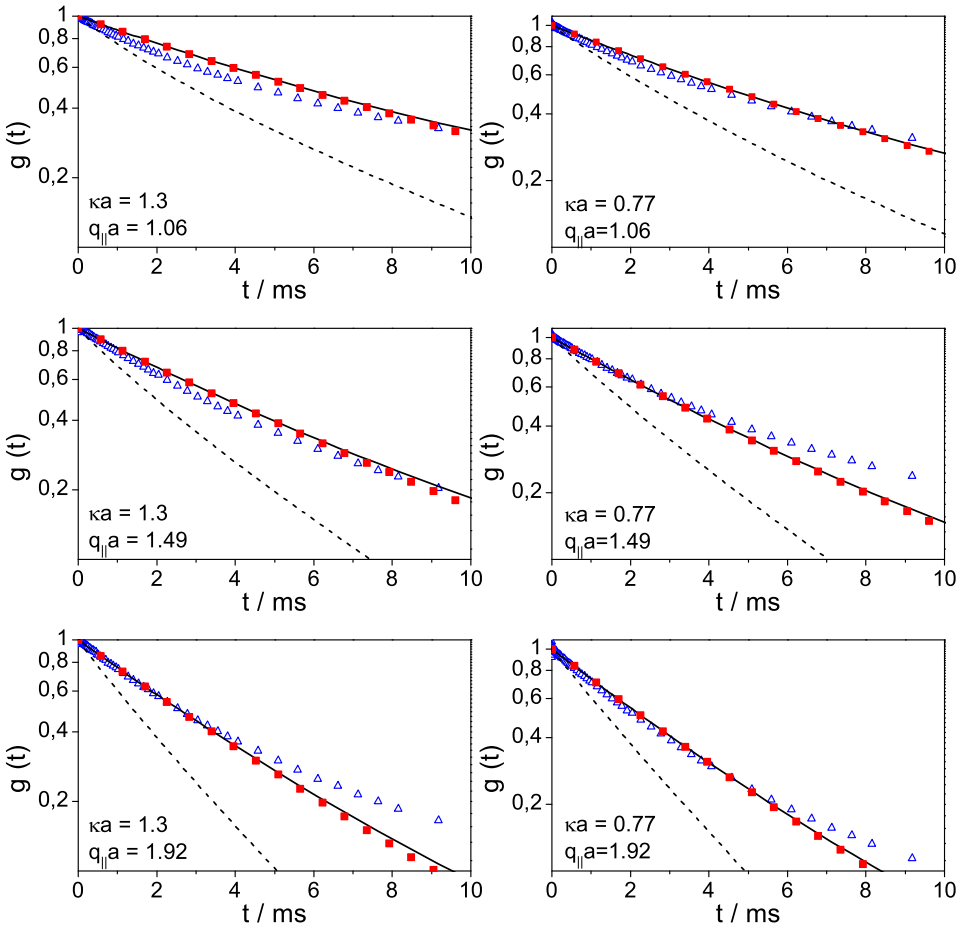

Figure 7.6: Experimental correlation functions for translational relaxation at a volume fraction of 0.106, for two penetration depths $\kappa a = 1.30$ and 0.77. Here $q_\perp a = 1.49$ is the same for all experiments while $q_\parallel a$ varies from 1.06 to 1.92, as indicated in the figures. The square symbols refer to simulation predictions, while the empty triangles are the experimental results. The solid lines refer to the two-cumulants approximation, and the dashed lines are the LOS predictions where hydrodynamic interactions are neglected.

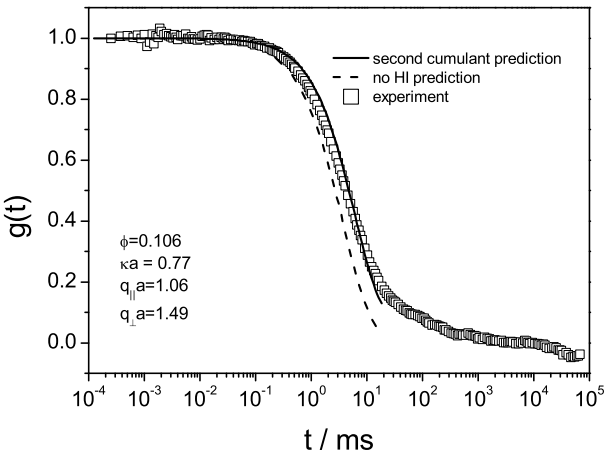

Figure 7.7: Experimental EACF showing a long time decay as described in the text (symbols) together with the second cumulant (full line) and the LOS (dashed line) predictions.

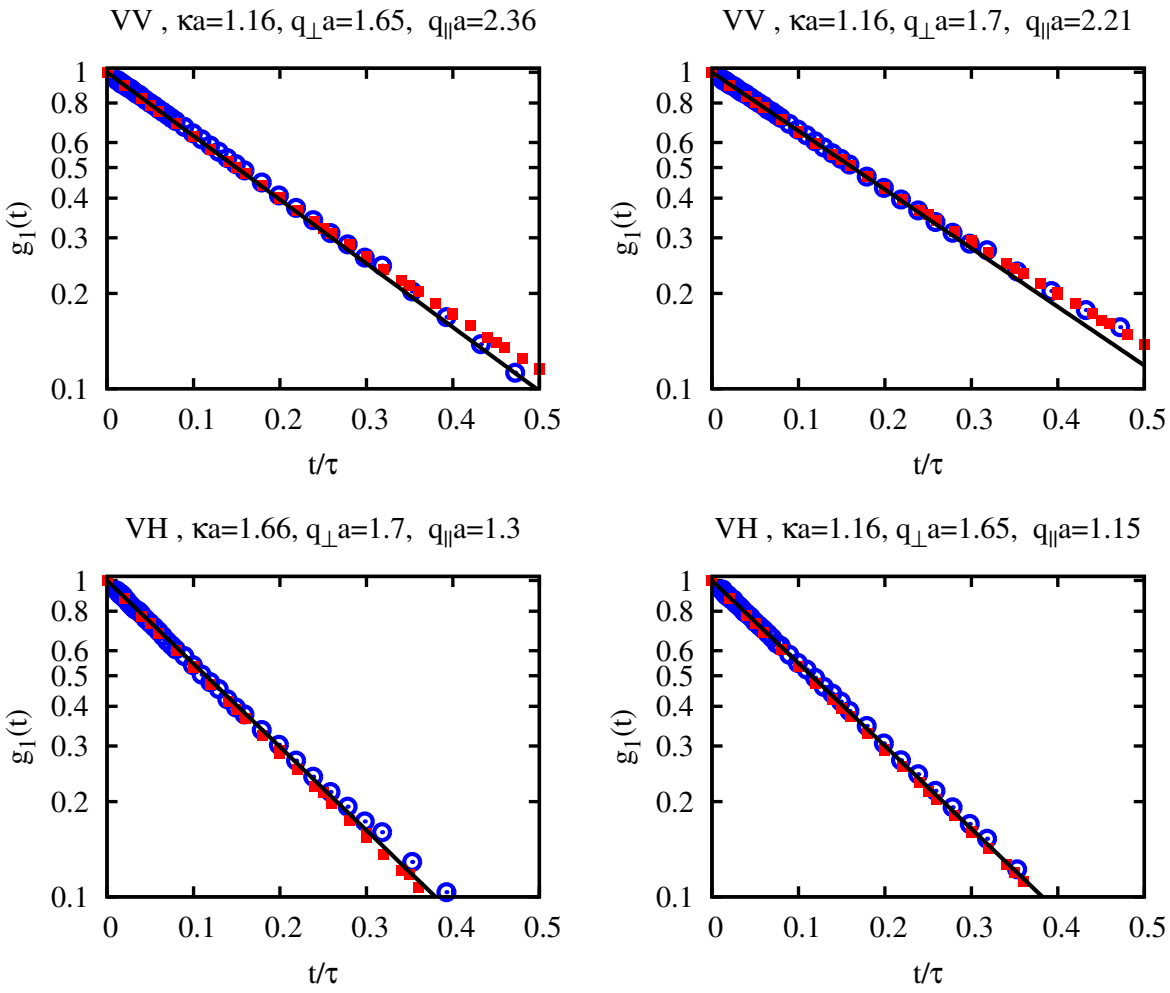

Figure 7.8: Normalised electric field correlation functions $g_1(t)$ recorded from optically anisotropic particles with different scattering geometries, as indicated in individual headlines. Blue circles are experimental data, red squares are simulation results and the full lines are theoretical first cumulant predictions, *i.e.* $\exp(-\Gamma t)$.

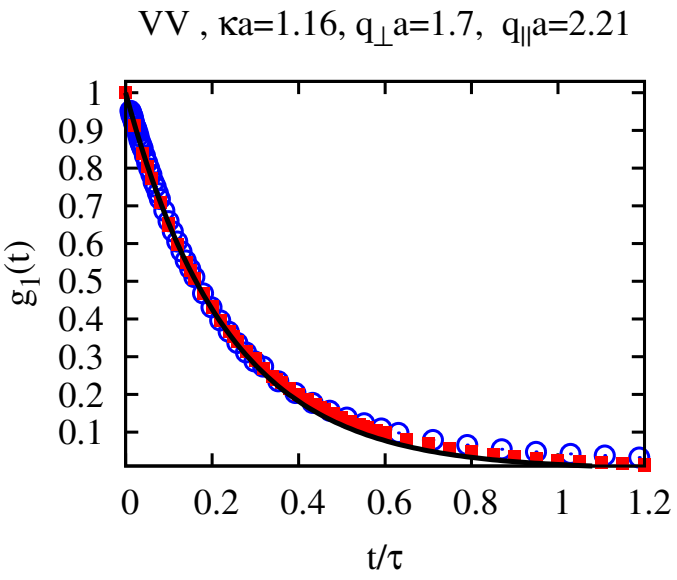

Figure 7.9: Longer time decay of g_1 - comparison of experimental data (blue circles), results of the BD simulations (red squares) and predictions by means of the first cumulant. Results are presented for a chosen set of parameters. The agreement is good even for moderate times.

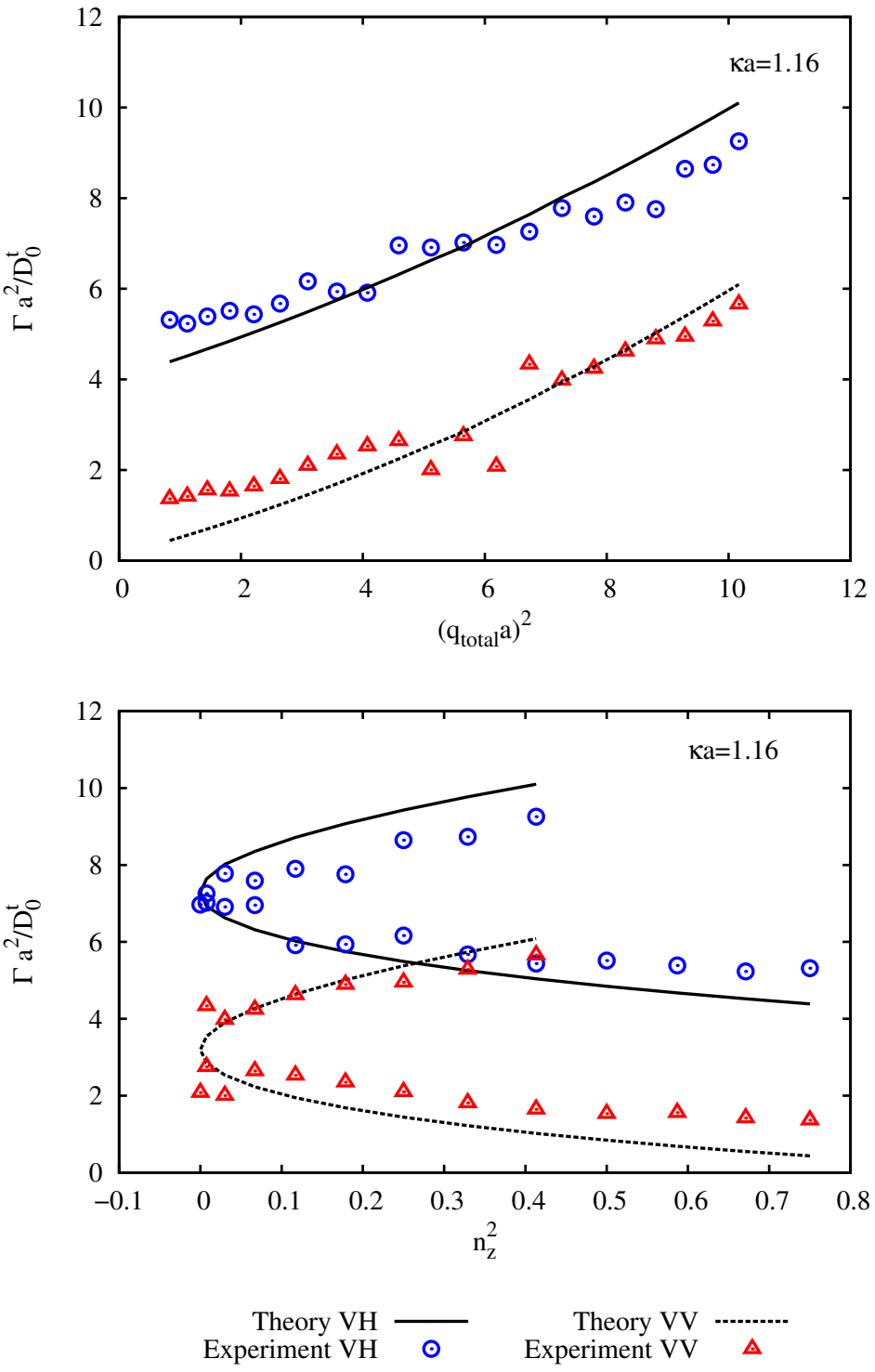

Figure 7.10: First cumulants vs. the total scattering vector squared (left) and vs. the z-component of the scattered light polarisation vector squared (right). Symbols are experimental data obtained in VV (red triangles) and VH (blue circles) while the lines represent theoretical predictions for the first cumulant. Redrawn from [90].

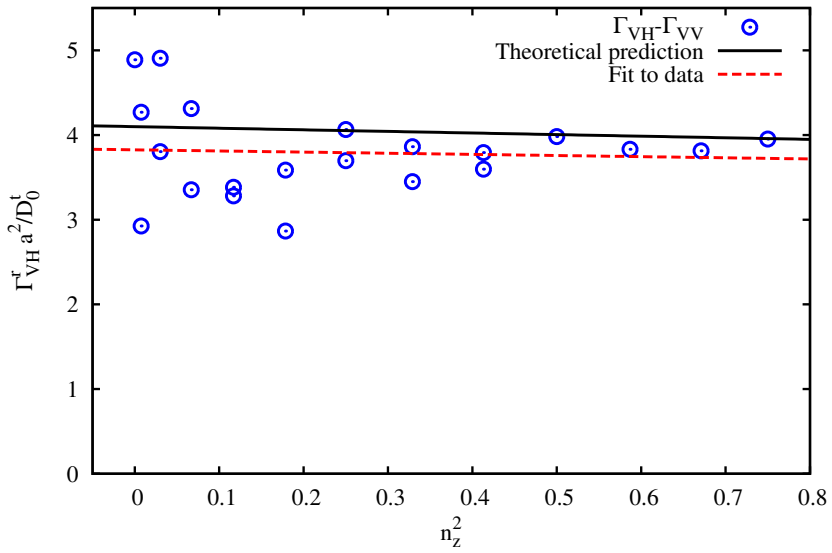

Figure 7.11: Rotational relaxation rate vs. the z-component of the scattered light polarisation vector squared. The points represent the experimental data, as given by Eq. (7.49), while the theoretical prediction linear in n_z^2, marked with the solid line, follows from Eq. (7.50). A linear fit to data results in diffusion coefficients differing from theoretically predicted $\langle D_{\parallel} \rangle_{\kappa}$ and $\langle D^r_{\perp} \rangle_{\kappa}$ by 5% and 7.5%, respectively. Redrawn from [90].

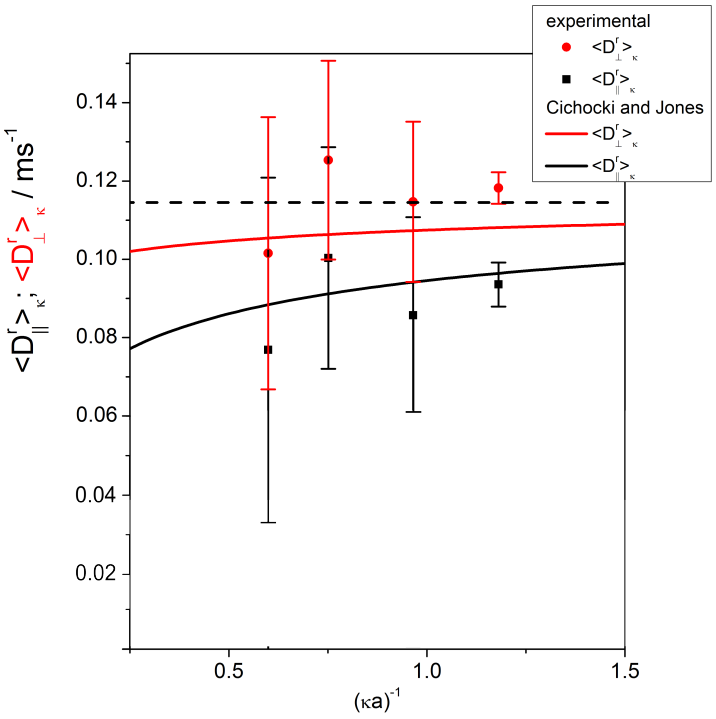

Figure 7.12: Rotational diffusion coefficients extracted from experimental data recorded at different penetration depths, plotted together with theoretically predicted $\left\langle D^r_{\parallel} \right\rangle_{\kappa}$ and $\langle D^r_{\perp} \rangle_{\kappa}$ based on numerical calculations of Cichocki and Jones [46]. Redrawn after [89].

8 EWDLS from axisymmetric particles: the first cumulant analysis

In this Chapter, we apply the general theoretical framework for the description and interpretation of EWDLS measurements to a dilute suspension of axially symmetric colloids bounded by a planar no-slip wall. After identifying and characterizing typical soft matter systems to which the model can be applied, we present exact expressions for the first cumulant of the EACF measured in scattering experiments involving optically anisotropic axisymmetric scatterers. We then describe a general numerical method which we have developed for the calculation of the first cumulant in an arbitrary experimental configuration. For the analysis of the structure of the cumulant, we restrict our attention to a particular experimental arrangement. We then discuss the differences between bulk DLS and EWDLS by model particles, i.e. colloidal rods and platelets. By separating out the effects of hydrodynamic interactions with the wall and form anisotropy, we were able to identify the influence of the shape and internal composition of the particles on the field correlation function. This allows us to propose approximations to the first cumulant in certain ranges of experimental parameters.

8.1 Characteristics of typical colloidal rods and disks

Axisymmetric particles constitute model systems for studying the effects of shape anisotropy on soft matter dynamics. Hence, a number of experimental realisations of such colloids have been developed and studied extensively. Table I contains a selection of typical particles, together with their characteristic sizes, that is length L, diameter d, and aspect ratio $p = L/d$. Together with the evanescent wave penetration depth, $2/\kappa$, which may be varied in the range between 100 nm and 1μm [63], and the characteristic magnitude of the scattering vector $5 \cdot 10^{-3}$ nm$^{-1} \leq q \leq$

Material	Length L (nm)	Diameter d (nm)	Aspect ratio $p = L/d$
fd-viruses [179]	880	7	125
Boehmite rods [180]	100-200	20	5-10
Boehmite rods [181]	100-500	10-20	5-50
Gold rods [182]	20-100	20	1-5
Gibbsite platelets [168]	10 (thickness)	$2R = 240$	0.04

Table I: Typical model experimental systems involving axisymmetric particles, mostly rod-like or disk-like. Their characteristic size is of order of 100 nm.

$2.5 \cdot 10^{-2}$ nm^{-1}, these quantities determine the dimensionless parameters which characterise the dynamics observed in EWDLS experiments. We therefore find, for a typical rod of diameter $d = 20$ nm, and aspect ratio $p = 5$, the typical values of governing parameters to be

$$\kappa d \in \{0.04, 0.4\}, \qquad qd \in \{0.01, 0.5\}, \tag{8.1}$$

or, equivalently,

$$\kappa L \in \{0.2, 2\}, \qquad qL \in \{0.05, 2.5\}. \tag{8.2}$$

For a typical platelet (disk), we find

$$\kappa d \in \{0.02, 0.2\}, \qquad qd \in \{0.05, 0.25\}, \tag{8.3}$$

which translates to

$$\kappa R \in \{0.2, 2\}, \qquad qR \in \{0.6, 3\}. \tag{8.4}$$

We note that these values are all relatively small, and for practical use one should focus the analysis on the region of $qL < 5$, $\kappa L < 5$, L being the characteristic size of the particle. Since our approach allows for the investigation of broader range of the values of parameters, in the following we analyse the range $qL < 15$ and $\kappa L < 5$.

8.2 The first cumulant in EWDLS experiments

Below, we formulate general expressions for the first cumulant in EWDLS involving axially symmetric colloids, and study its structure in detail. Both shape and optical anisotropy of the particles are taken into account and discussed. The exact expressions derived in this Section are evaluated in further course of the Chapter. After presenting the general structure of the first cumulant, we proceed to the evaluation of the resulting expressions numerically for a particular geometric arrangement of the set-up. We wish to stress, however, that the numerical procedures for calculations outlined below may be easily applied to an arbitrary experimental configuration.

For the derivation of the first cumulant of the EWDLS field correlation function, the starting point is again the general expression (6.1), used already in the previous Chapter, which we repeat here for clarity

$$\Gamma = \frac{\left\langle [\boldsymbol{\nabla}_{\mathbf{X}} E_S] \cdot \mathbf{D}(\mathbf{X}) \cdot \left[\boldsymbol{\nabla}_{\mathbf{X}} E_S^*\right] \right\rangle}{\langle |E_S|^2 \rangle}. \tag{8.5}$$

Similarly to the case of EWDLS from spherical particles, the form of the scattered field contains the exponential damping due to the evanescent illumination, and reads

$$E_S = \exp\left(-\frac{\kappa}{2}\hat{\mathbf{e}}_z \cdot \mathbf{r}\right) F(\hat{\mathbf{u}}) \exp(i\mathbf{q} \cdot \mathbf{r}). \tag{8.6}$$

The difference is now the factor $F(\hat{\mathbf{u}}) = \mathcal{E}(\hat{\mathbf{u}})B(\hat{\mathbf{u}})$, which incorporates both the particle intrinsic optical anisotropy and the effects of particle shape. The anisotropic polarisability is encoded in $\mathcal{E}$, while the latter is accounted for by the evanescent scattering amplitude B, absent in the case of spherical particles discussed before.

The general structure of the first cumulant given for bulk DLS in Eqs. (6.4)-(6.7) also remains unchanged, owing to the form of the mobility tensor (5.11),

$$\Gamma = \Gamma^t + \Gamma^r + \Gamma^{tr} + \Gamma^{rt}, \tag{8.7}$$

the difference lying only in the form of E_S. The first cumulant in this case may thus be explicitly written as in Eqs (6.9)-(6.12), with an additional factor $e^{-\kappa z}$ inside the averages, and with the evanescent static structure factor

$$S(\kappa, \mathbf{q}) = \left\langle e^{-\kappa z} |F|^2 \right\rangle \tag{8.8}$$

in the denominator of the expressions. The single-particle equilibrium average in a wall-bounded system is defined as

$$\langle ... \rangle = \oint \mathrm{d}\hat{\mathbf{u}} \int_{z_0} \mathrm{d}\mathbf{r}\, P^{\mathrm{eq}}(\mathbf{r}, \hat{\mathbf{u}}) ... \tag{8.9}$$

where the equilibrium probability distribution P^{eq} is given by the wall-particle interaction potential $\Phi(\mathbf{r}, \hat{\mathbf{u}})$ as $P^{\mathrm{eq}} \sim e^{-\beta\Phi(z,\theta)}$. We note that the interaction potential depends only on the distance from the wall z and the inclination angle θ due to symmetry. Using the explicit form of the electric field, we arrive at

$$\Gamma^t = -\frac{1}{S(\kappa, \mathbf{q})} \left(i\mathbf{q} - \frac{\kappa}{2}\hat{\mathbf{e}}_z \right) \cdot \left\langle e^{-\kappa z} |F|^2 \mathbf{D}^{tt} \right\rangle \cdot \left(i\mathbf{q} + \frac{\kappa}{2}\hat{\mathbf{e}}_z \right), \tag{8.10}$$

$$\Gamma^r = \frac{1}{S(\kappa, \mathbf{q})} \langle e^{-\kappa z} [\mathbf{L}F] \cdot \mathbf{D}^{rr} \cdot [\mathbf{L}F^*] \rangle, \tag{8.11}$$

$$\Gamma^{tr} = \frac{1}{S(\kappa, \mathbf{q})} \left(i\mathbf{q} - \frac{\kappa}{2}\hat{\mathbf{e}}_z \right) \cdot \left\langle e^{-\kappa z} F \mathbf{D}^{tr} \cdot [\mathbf{L}F^*] \right\rangle, \tag{8.12}$$

$$\Gamma^{rt} = -\frac{1}{S(\kappa, \mathbf{q})} \left\langle e^{-\kappa z} F^* [\mathbf{L}F] \cdot \mathbf{D}^{rt} \right\rangle \cdot \left(i\mathbf{q} + \frac{\kappa}{2}\hat{\mathbf{e}}_z \right). \tag{8.13}$$

We may also combine Eqs. (8.12) and (8.13) using the symmetry properties of $\mathbf{D}^{tr}$ and $\mathbf{D}^{rt}$ into

$$\Gamma^{tr} + \Gamma^{rt} = \frac{1}{S(\kappa, \mathbf{q})} \left[-\frac{\kappa}{2}\hat{\mathbf{e}}_z \cdot \left\langle e^{-\kappa z} \mathbf{D}^{tr} \cdot \mathbf{L}|F|^2] \right\rangle + 2\mathbf{q} \cdot \left\langle e^{-\kappa z} \mathbf{D}^{tr} \cdot \mathrm{Im}[F\mathbf{L}F^*] \right\rangle \right]. \tag{8.14}$$

We shall introduce a notation to order the resulting formulae. The first step here is the structure introduced by the dependence on the scattering vector $\mathbf{q} = \mathbf{q}_\parallel + q_\perp \hat{\mathbf{e}}_z$ and the penetration depth κ^{-1} that appears due to the presence of gradients in the general expressions, Eqs. (8.10)-(8.13). We may then write the first cumulant as

$$\Gamma^t = \left(q_\perp^2 + \frac{\kappa^2}{4} \right) A_\perp^t(\kappa, \mathbf{q}) + q_\parallel^2 A_\parallel^t(\kappa, \mathbf{q}) + q_\parallel q_\perp A_{\parallel\perp}^t(\kappa, \mathbf{q}) \tag{8.15}$$

$$\Gamma^r = A^r(\kappa, \mathbf{q}) \tag{8.16}$$

$$(\Gamma^{tr} + \Gamma^{rt}) = -\frac{\kappa}{2} A^{tr}(\kappa, \mathbf{q}) + 2q_\perp A_\perp^{tr}(\kappa, \mathbf{q}) + 2q_\parallel A_\parallel^{tr}(\kappa, \mathbf{q}). \tag{8.17}$$

Using the previously introduced coordinates, and taking into account the form of the mobility matrix (5.64), we may arrive at explicit expressions including the matrix elements of $\boldsymbol{\mu}^{tt}$, $\boldsymbol{\mu}^{rr}$,

and $\boldsymbol{\mu}^{tr}$. We explicitly write the coefficients $\bar{A}(\kappa,\mathbf{q}) = A(\kappa,\mathbf{q})S(\kappa,\mathbf{q})$ below as

$$\begin{aligned}
S(\kappa,\mathbf{q}) &= \left\langle e^{-\kappa z}|F|^2\right\rangle, \\
\bar{A}^t_{\perp}(\kappa,\mathbf{q}) &= \left\langle e^{-\kappa z}\,|F|^2\,\hat{\mathbf{e}}_z\cdot\mathbf{D}^{tt}\cdot\hat{\mathbf{e}}_z\right\rangle, \\
\bar{A}^t_{\parallel}(\kappa,\mathbf{q}) &= \left\langle e^{-\kappa z}\,|F|^2\,\hat{\mathbf{q}}_{\parallel}\cdot\mathbf{D}^{tt}\cdot\hat{\mathbf{q}}_{\parallel}\right\rangle, \\
\bar{A}^t_{\parallel\perp}(\kappa,\mathbf{q}) &= 2\left\langle e^{-\kappa z}\,|F|^2\,\hat{\mathbf{q}}_{\parallel}\cdot\mathbf{D}^{tt}\cdot\hat{\mathbf{e}}_z\right\rangle, \\
\bar{A}^r(\kappa,\mathbf{q}) &= \langle e^{-\kappa z}[\mathbf{L}F]\cdot\mathbf{D}^{rr}\cdot[\mathbf{L}F^*]\rangle, \\
\bar{A}^{tr}_{\kappa}(\kappa,\mathbf{q}) &= \left\langle e^{-\kappa z}\hat{\mathbf{e}}_z\cdot\mathbf{D}^{tr}\cdot\mathbf{L}|F|^2\right\rangle, \\
\bar{A}^{tr}_{\perp}(\kappa,\mathbf{q}) &= \left\langle e^{-\kappa z}\hat{\mathbf{e}}_z\cdot\mathbf{D}^{tr}\cdot\mathrm{Im}[F\mathbf{L}F^*]\right\rangle, \\
\bar{A}^{tr}_{\parallel}(\kappa,\mathbf{q}) &= \left\langle e^{-\kappa z}\hat{\mathbf{q}}_{\parallel}\cdot\mathbf{D}^{tr}\cdot\mathrm{Im}[F\mathbf{L}F^*]\right\rangle,
\end{aligned} \tag{8.18}$$

where $\hat{\mathbf{q}}_{\parallel}$ is a unit vector in the direction of $\mathbf{q}_{\parallel}$. Introducing the following shorthand notation for the components of the diffusion matrix in the LAB frame:

$$D^{tt}_{zz} = \hat{\mathbf{e}}_z\cdot\mathbf{D}^{tt}\cdot\hat{\mathbf{e}}_z, \quad D^{tt}_{qq} = \hat{\mathbf{q}}_{\parallel}\cdot\mathbf{D}^{tt}\cdot\hat{\mathbf{q}}_{\parallel}, \quad D^{tt}_{qz} = \hat{\mathbf{q}}_{\parallel}\cdot\mathbf{D}^{tt}\cdot\hat{\mathbf{e}}_z, \tag{8.19}$$

we may write the above relations with the explicit form of $F = \mathcal{E}B$ as

$$S = \left\langle e^{-\kappa z}|\mathcal{E}|^2|B|^2\right\rangle, \tag{8.20}$$

$$\bar{A}^t_{\perp} = \left\langle e^{-\kappa z}|\mathcal{E}|^2|B|^2 D^{tt}_{zz}\right\rangle, \tag{8.21}$$

$$\bar{A}^t_{\parallel} = \left\langle e^{-\kappa z}|\mathcal{E}|^2|B|^2 D^{tt}_{qq}\right\rangle, \tag{8.22}$$

$$\bar{A}^t_{\parallel\perp} = 2\left\langle e^{-\kappa z}|\mathcal{E}|^2|B|^2 D^{tt}_{qz}\right\rangle, \tag{8.23}$$

$$\begin{aligned}
\bar{A}^r = \Big\langle e^{-\kappa z}\Big\{&|\mathcal{E}|^2[\mathbf{L}B]\cdot\mathbf{D}^{rr}\cdot[\mathbf{L}B^*] + |B|^2[\mathbf{L}\mathcal{E}]\cdot\mathbf{D}^{rr}\cdot[\mathbf{L}\mathcal{E}^*] \\
&+2\mathrm{Re}\left[(B^*\mathbf{L}B)\cdot\mathbf{D}^{rr}\cdot(\mathcal{E}\mathbf{L}\mathcal{E}^*)\right]\Big\}\Big\rangle,
\end{aligned} \tag{8.24}$$

$$\bar{A}^{tr}_{\kappa} = \left\langle e^{-\kappa z}\hat{\mathbf{e}}_z\cdot\left\{|\mathcal{E}|^2\mathbf{D}^{tr}\cdot\mathbf{L}|B|^2 + |B|^2\mathbf{D}^{tr}\cdot\mathbf{L}|\mathcal{E}|^2\right\}\right\rangle, \tag{8.25}$$

$$\bar{A}^{tr}_{\perp} = \left\langle e^{-\kappa z}\hat{\mathbf{e}}_z\cdot\left\{|\mathcal{E}|^2\mathbf{D}^{tr}\cdot\mathrm{Im}[B\mathbf{L}B^*] + |B|^2\mathbf{D}^{tr}\cdot\mathrm{Im}[\mathcal{E}\mathbf{L}\mathcal{E}^*]\right\}\right\rangle, \tag{8.26}$$

$$\bar{A}^{tr}_{\parallel} = \left\langle e^{-\kappa z}\hat{\mathbf{q}}_{\parallel}\cdot\left\{|\mathcal{E}|^2\mathbf{D}^{tr}\cdot\mathrm{Im}[B\mathbf{L}B^*] + |B|^2\mathbf{D}^{tr}\cdot\mathrm{Im}[\mathcal{E}\mathbf{L}\mathcal{E}^*]\right\}\right\rangle. \tag{8.27}$$

We emphasize here that $B = B(\hat{\mathbf{u}};\mathbf{q},\kappa)$ depends on κ and $\mathbf{q}$, while $\mathcal{E}(\hat{\mathbf{u}})$ depends on the particle polarisability and the experimental alignment. From now on, for brevity we shall skip the dependence of A on the arguments $(\kappa,\mathbf{q})$. We note here that the first cumulant depends on the polarisability tensor and on the scattering strength through the combinations $|\mathcal{E}|^2$, $\mathcal{E}\mathbf{L}\mathcal{E}^*$ and $|B|^2$, $B\mathbf{L}B^*$ in the tt and tr parts. In the rr part, only the coefficients of mobility in the directions of $\mathbf{L}\mathcal{E}$ and $\mathbf{L}B$ enter the final expression. It is worthwhile stressing here that upon the action of the rotational operator $\mathbf{L}$, only the components perpendicular to $\hat{\mathbf{u}}$ are generated, and therefore only a subspace of $\mathbf{D}^{rr}$ contributes to the first cumulant. This submatrix is given by $(\mathbf{1}-\hat{\mathbf{u}}\hat{\mathbf{u}})\cdot\mathbf{D}^{rr}\cdot(\mathbf{1}-\hat{\mathbf{u}}\hat{\mathbf{u}})$, and has only two non-zero components in the RW frame:

$$D^{rr}_{11} = \hat{\mathbf{u}}_{1\perp}\cdot D^{rr}\cdot\hat{\mathbf{u}}_{1\perp} = k_BTb_r, \qquad D^{rr}_{22} = \hat{\mathbf{u}}_{2\perp}\cdot D^{rr}\cdot\hat{\mathbf{u}}_{2\perp} = k_BTd_r, \tag{8.28}$$

where k_B is the Boltzmann constant, T is the temperature, and the mobility coefficients b_r and d_r in the RW frame of reference are defined in Sec. 5.5.1.

The level of complexity of the above presented expressions is considerably higher than in the case of a spherical particle discussed in Chapter 7. In particular, there is no clear distinction between the effects of hydrodynamic interactions and the scattering properties of the particle. Importantly, the latter depend on the scattering vector $\mathbf{q}$ in a manner we will explore in the course of this Chapter. For further analysis, we confine our attention to the case of hard-core interaction between the wall and the particle. It is important to stress, however, that the method of analysis we follow is general enough to include the effects of an arbitrary interaction potential in the numerical calculations.

Hard-core interaction potential In the particular case of hard-core interactions with the wall, the averages over spatial and orientational degrees of freedom may be split. The resulting expressions contain the angular averages:

$$\langle(\ldots)\rangle_{\hat{\mathbf{u}}} = \frac{1}{4\pi}\oint \mathrm{d}\hat{\mathbf{u}}\,(\ldots) = \frac{1}{4\pi}\int_{-1}^{1}\mathrm{d}w\int_{0}^{2\pi}\mathrm{d}\varphi\,(\ldots) \tag{8.29}$$

with $w = \cos\theta$, and the full equilibrium average may be written as

$$\langle(\ldots)\rangle \;\propto\; \langle\langle(\ldots)\rangle_{\kappa}\rangle_{\hat{\mathbf{u}}}\,, \tag{8.30}$$

where the κ-average reads, defined in Eq. (7.16), reads explicitly

$$\langle(\ldots)\rangle_{\kappa} = \kappa e^{\kappa z_0}\int_{z_0}^{\infty}\mathrm{d}z\, e^{-\kappa z}(\ldots). \tag{8.31}$$

in analogy to Eq. (7.21). Here, $z_0 = z_0(\theta)$ is the minimum wall-particle distance at a given inclination angle. For example, for a slender rod of length L and negligible thickness, it is given by $z_0 = \frac{L}{2}\cos\theta = wL/2$.

In the expressions for the first cumulant, the elements of the diffusion tensors appear again in the form of κ-averages. For example, in $A^t_\perp$ we arrive at

$$A^t_\perp = \frac{1}{S}\left\langle e^{-\kappa z_0}|\mathcal{E}|^2|B|^2\left\langle D^{tt}_{zz}\right\rangle_{\kappa}\right\rangle_{\hat{\mathbf{u}}}, \tag{8.32}$$

with $D^{tt}_{zz} = \hat{\mathbf{e}}_z\cdot\mathbf{D}^{tt}\cdot\hat{\mathbf{e}}_z$, and the spatially-integrated structure factor

$$S = \left\langle e^{-\kappa z_0}|\mathcal{E}|^2|B|^2\right\rangle_{\hat{\mathbf{u}}}. \tag{8.33}$$

The κ-average now depends on the particle orientation via the angles (θ,φ), since (a) the minimal distance z_0 depends on θ, and (b) the oriented matrix element D^{tt}_{zz} is evaluated in the LAB frame. The key information is, however, that the structure of the first cumulant involves the κ-averages of the matrix elements of $\mathbf{D}$, namely $\langle a_t\rangle_\kappa$, $\langle b_t\rangle_\kappa$, $\langle b_r\rangle_\kappa$, $\langle d_r\rangle_\kappa$, etc. These depend on purely hydrodynamic properties of the particles and may be evaluated conveniently using the HYDROMULTIPOLE codes [118]. We discuss this matter in detail in the forthcoming section.

8.3 Hydrodynamic effects

Hydrodynamic mobility coefficients of an axisymmetric particle enter the first cumulant in an averaged form stemming from the non-uniform illumination of the sample, as we have shown

above. Since the primary aim of EWDLS experiments is to explore the near-wall hydrodynamic interactions, it is important to investigate how the enhancement of friction for particles close to the boundary affects the coefficients A in the first cumulant. Below we discuss in detail the dependence of the averaged mobility (diffusion) coefficients on the penetration depth of the evanescent wave.

8.3.1 Averaged mobility coefficients

In this Section, we focus on the hydrodynamic properties of particles viewed in EWDLS experiments. To this end, we analyse the penetration-depth averaged mobility coefficients, defined in Eq. (8.31). It is clear that the averages are normalised, i.e. $\langle 1 \rangle_\kappa = 1$. However, even for constant hydrodynamic properties, the full ensemble averages in the first cumulant retain the factor $e^{-\kappa z_0}$, stemming from the restricted configurational space of the particle close to the wall.

Below we present the effect of hydrodynamic interactions on the quantities entering the first cumulant by analysing the κ-averages of the normalised mobility functions for different inclination angles of the particle. We examine the components of the mobility matrix in the body-fixed frame RW, since the bulk mobility matrix is diagonal in this frame. It is worth noting that in the first cumulant, the components of $\boldsymbol{\mu}$ (or $\mathbf{D}$) are evaluated in the LAB frame, with the two representations linked by a simple transformation of basis.

For numerical results contained in this Section, and obtained using the HYDRODMULTIPOLE routines, we take an example of a rod modelled as a string of spherical beads, although such an analysis may easily be performed for an arbitrary bead model of an axially symmetric body. For practical reasons, we restrict here one aspect ratio $p = 5$, and to the set of penetration depths

$$\kappa L \in \{0.01,\ 0.1,\ 0.5,\ 1,\ 2,\ 5\}, \tag{8.34}$$

which cover the experimentally accessible range.

The length scales relevant for the analysis of the averages are the penetration depth $1/\kappa$ and the rod length L, from which a dimensionless parameter κL may be constructed. The limit $\kappa L \ll 1$ corresponds to the uniform bulk illumination where we expect to see no effects of walls, and the diffusion tensor to have the bulk structure, as analysed in Chapter 6. In the opposite limit, $\kappa L \gg 1$, the non-uniform rapidly decaying electric field confines the area over which the averaging is performed to the region closest to the wall. Hence, we expect for large values of κL the averaged diffusion coefficients to attain their contact values, since in this limit asymptotically we have

$$\kappa e^{\kappa z_0} \int_{z_0}^{\infty} \mathrm{d}z\, e^{-\kappa z} f(z) \sim f(z_0) \quad \text{for} \quad \kappa L \to \infty. \tag{8.35}$$

We normalise the diagonal mobility matrix elements by their bulk values, and the off-diagonal elements which decay to zero with distance from the wall we divide by the geometric average of the diagonal bulk values, as indicated in the captions of Figures 8.1 - 8.3.

The translational coefficients are plotted in Fig. 8.1. The averages decrease with increasing κ because of the increased friction in the near-wall region. In addition, the angular dependence of the averages is present, with the strongest hindrance effect mostly for $\theta = \pi/2$ (that is $w = 0$), as

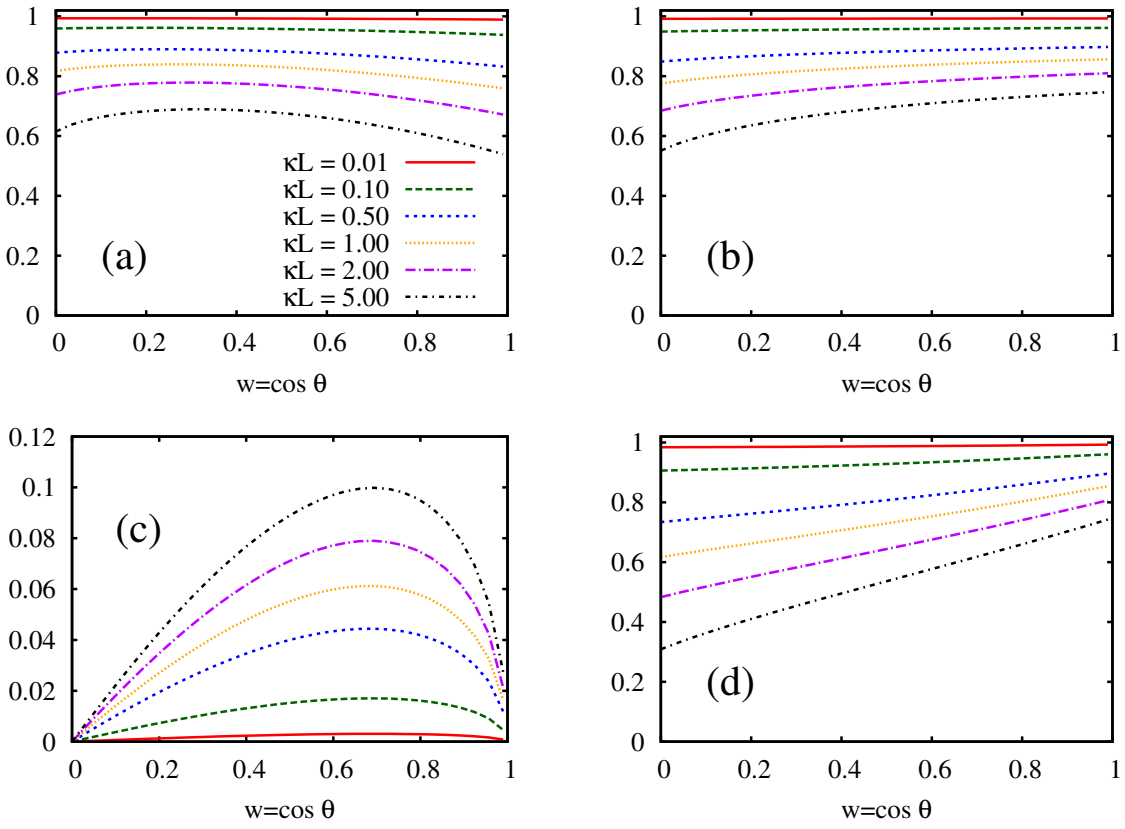

Figure 8.1: The κ-averaged translational (tt) mobility coefficients normalised by their bulk values (or $\sqrt{\mu^t_\parallel \mu^t_\perp}$ in the case of c_t) plotted as functions of the tilt angle $w = \cos\theta$ for relevant values of the penetration depth κL. (a) a_t, (b) b_t, (c) c_t, (d) d_t. Plots for a rod of aspect ratio $p = 5$.

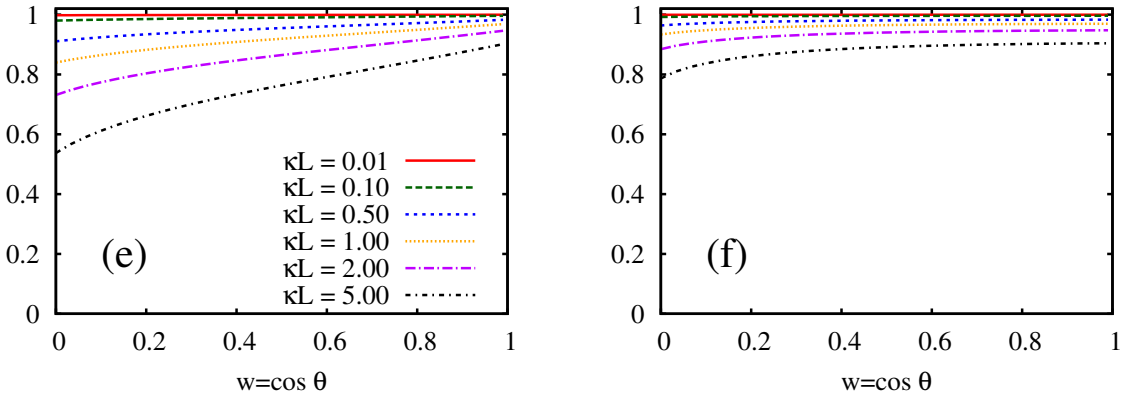

Figure 8.2: The κ-averaged rotational (rr) mobility coefficients normalised by their bulk values plotted as functions of the tilt angle $w = \cos\theta$ for relevant values of the penetration depth κL. (e) b_r, (f) d_r. Plots for a rod of aspect ratio $p = 5$.

then the rod is aligned with the wall, and the interaction between the constituting beads between the rod and its image is similar for all beads. The non-diagonal term c^{tt} is small even for large values of κL, which suggests it might be neglected when seeking for approximations.

The rotational coefficients in Fig. 8.2 are less affected by the presence of the wall, in accord with our results for the mobility correction in Chapter 5, and similarly to the previously discussed case of a spherical particle. Again, the effect of the wall on rotations is most pronounced for $\theta = \pi/2$, since then we expect the strongest differences in friction acting on different parts of the rod.

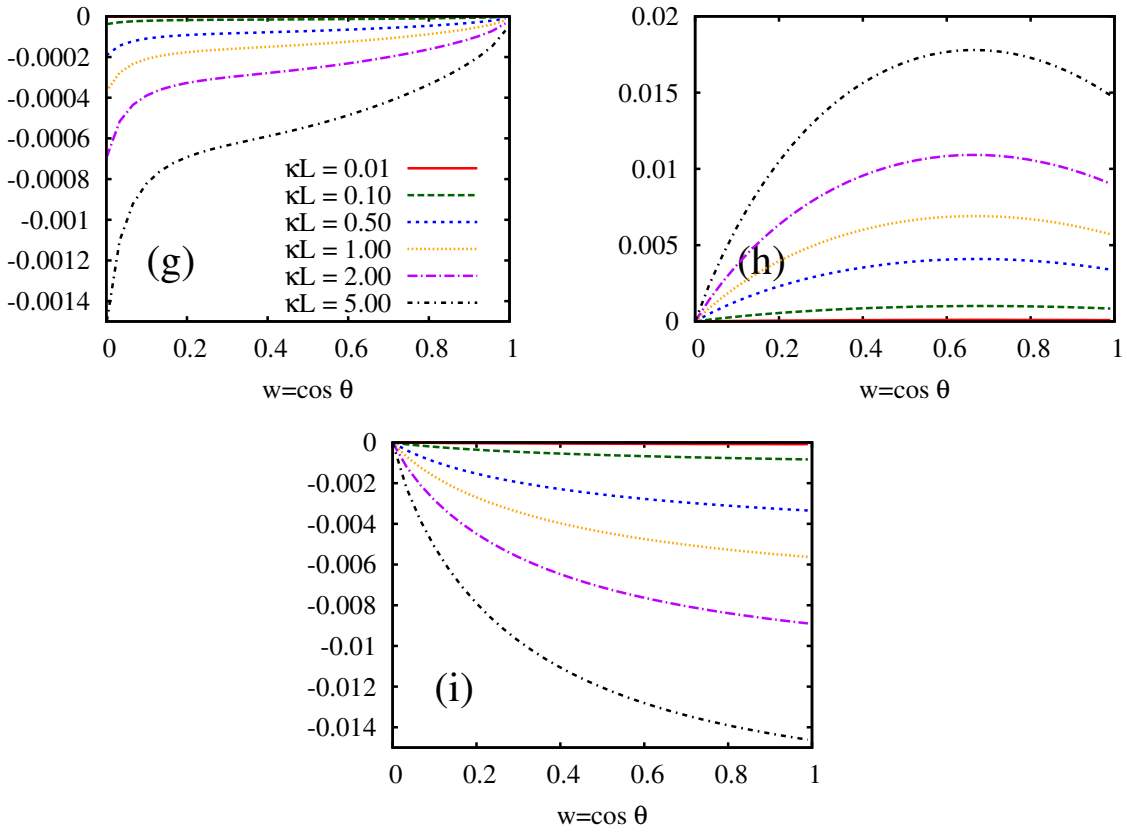

Figure 8.3: The κ-averaged coupling (tr) mobility coefficients normalised by the factor $\sqrt{\mu^t_\perp \mu^r_\perp}$ plotted as functions of the tilt angle $w = \cos\theta$ for relevant values of the penetration depth κL. (g) a_{tr}, (h) c_{tr}, (i) d_{tr}. Plots for a rod of aspect ratio $p = 5$.

It seems that even though the presence of the wall induces a translation-rotation coupling effect, its magnitude is in most cases negligibly small, as shown in Fig. 8.3. Although the importance of this contribution increases rapidly with κL, for practical reasons it may be neglected, as we will demonstrate further on.

8.3.2 Slender body approximation

In Chapter 5, while analysing the structure of the mobility tensor correction due to the presence of a wall, we stated that for a very elongated body of length L and diameter d, staying at a distance H apart from the wall, the effect of hydrodynamic interactions with the wall vanishes in the slender body limit, that is for $d \to 0$, with L/H held fixed. Thus, for very long and thin particles, such as slender rods or flat discs, one may successfully approximate the mobility matrix needed for the calculation of the first cumulant by its bulk analogue, with only diagonal components present in the tt and rr parts, and with no tr coupling terms. With the hydrodynamic properties

remaining unchanged with respect to the bulk fluid, the only difference into the scattered light correlation functions is then brought in by the non-uniform illumination and scattering effects, which we analyse in the next Section. The resulting first cumulant is analysed in Sec. 8.5.1. In this limit, the bulk diffusion coefficients needed for the calculation of the first cumulant may be obtained e.g. using the HYDROMULTIPOLE bead model, or - if a more accurate shape representation is needed - the shell model results of Ortega and García de la Torre *et al.* [157], as mentioned in Chapter 5.

8.4 Scattering effects

The EWDLS correlation functions results from an interplay between two factors. On one hand, hydrodynamic interactions with the wall alter the particle mobility, introducing an additional degree of anisotropy. On the other hand, the character of the measured correlation function is to a large extent determined by the evanescent illumination, characterised by the parameter κL. In this Section, we look upon the impact of this parameter on the scattering properties of the particle.

8.4.1 Evanescent scattering amplitude

As outlined in Chapter 3, the evanescent scattering amplitude is a natural extension of the bulk formula (6.26) to non-zero values of κL. In consequence, B depends now not only on the scattering vector $\mathbf{q}$ but also on the alignment of the particle with respect to the wall, quantified by the inclination angle θ. Since the electric field strength varies only in the z-direction, we expect that the effects of its decrease will be most pronounced in the configurations close to $\theta = 0$ (particle perpendicular to the wall), and will be absent for $\theta = \pi/2$ when the particle is aligned along the wall.

It is convenient to introduce the complex vector $\mathbf{Q} = \mathbf{q} + i\frac{\kappa}{2}\hat{\mathbf{e}}_z$ to rewrite the definition of the evanescent scattering amplitude as

$$B = \frac{1}{V}\int_V \mathrm{d}\mathbf{r}' \, \exp(i\mathbf{Q}\cdot\mathbf{r}'), \tag{8.36}$$

which resembles the bulk form, but now the scattering vector has a complex component. To examine the limiting forms of this variable, we note that since the decay of the electric field occurs on the characteristic length scales of κ^{-1}, and the effect of oscillatory spatial variation of the field in the z-direction is controlled by $q_\perp^{-1}$, we expect the dimensionless parameter $q_\perp\kappa^{-1}$ to control the importance of these two effects. Taking an example of a thin rod and a flat disc, we shall discuss these effects in more detail below.

Slender Rod Direct integration of the evanescent scattering amplitude (8.36) leads to the following relation for an infinitely thin rod of length L,

$$B = \frac{1}{L}\int_{L/2}^{-L/2} \mathrm{d}x \, \exp(x\mathbf{Q}\cdot\hat{\mathbf{u}}) = \frac{\sin Y}{Y}, \tag{8.37}$$

where $Y = \frac{1}{2}\mathbf{Q}L \cdot \hat{\mathbf{u}} = \frac{1}{2}\left(\mathbf{q}L + i\frac{\kappa L}{2}\hat{\boldsymbol{e}}_z\right) \cdot \hat{\mathbf{u}}$. In the limit of low penetration depth, i.e. $q\kappa^{-1} \gg 1$, the form factor reduces to the form known from bulk scattering,

$$B = 2\frac{\sin\frac{1}{2}qL}{qL}. \tag{8.38}$$

The second limiting case, $q\kappa^{-1} \ll 1$, refers to a strongly non-uniform illuminating field, so that no effect of q can be observed, since the field decays almost completely over only a part of the particle. Then, the scattering amplitude reads simply

$$B = \frac{\sinh\gamma w}{\gamma w}, \tag{8.39}$$

where $\gamma = \kappa L/4$.

Thin disc We consider now a disc of diameter L, or radius R, with its surface perpendicular to the orientation vector $\hat{\mathbf{u}}$. The scattering amplitude may be expressed as

$$B = \frac{1}{\pi R^2}\int_0^{2\pi} \mathrm{d}\psi \int_0^R \mathrm{d}\rho\, \rho \exp\left[i\mathbf{Q}\cdot\boldsymbol{\rho}\right], \tag{8.40}$$

with $\boldsymbol{\rho} = \rho\cos\psi\hat{\mathbf{u}}_{1\perp} + \rho\sin\psi\hat{\mathbf{u}}_{2\perp}$ lying in the plane of the disk, perpendicularly to $\hat{\mathbf{u}}$. Using the fact that

$$\int_0^{2\pi} \mathrm{d}\psi\ \exp[i(a\cos\psi + b\sin\psi)] = 2\pi J_0(\sqrt{a^2+b^2}), \tag{8.41}$$

where J_0 is the Bessel function of the first kind, we arrive at the result similar to the bulk case

$$B = 2\frac{J_1(Z)}{Z}, \tag{8.42}$$

with a rather complicated argument

$$Z = R\left[(\mathbf{Q}\cdot\hat{\mathbf{u}}_{1\perp})^2 + (\mathbf{Q}\cdot\hat{\mathbf{u}}_{2\perp})^2\right]^{1/2}. \tag{8.43}$$

In the case when $q\kappa^{-1} \gg 1$, the scattering amplitude simplifies to its bulk form

$$B = 2\frac{J_1(Z)}{Z}, \qquad Z = qR\sqrt{1-(\hat{\mathbf{q}}\cdot\hat{\mathbf{u}})^2}. \tag{8.44}$$

In the opposite case, $q\kappa^{-1} \ll 1$, we the scattering amplitude depends only on κR, and reads

$$B = 2\frac{I_1(Z)}{Z}, \qquad Z = \frac{\kappa}{2}\sin\theta, \tag{8.45}$$

with I_1 denoting the modified Bessel function.

The form of B at $q = 0$, being a function of κ only, given by Eqs. (8.39) and (8.45) for rods and discs, respectively, will prove useful in approximate calculations of the first cumulant, as we demonstrate in the following Section.

8.5 Analytical and numerical results

The analysis presented in the preceding sections is quite general, and covers all possible experimental arrangements. In order to be able to predict the values of the first cumulant in a given situation, we have developed Fortran numerical routines, which rely on numerical integration of the exact expressions for the first cumulant given above. Predictions from these codes may be directly compared to experiments, and are expected to hold over the whole range of analysed κ and $\mathbf{q}$. The main features of the software may be summed up in the following points:

1. Our software allows for the calculation of the first cumulant for an arbitrary axisymmetric particle. The input parameters are the values of experimental quantities, i.e.

$$\kappa,\ q_{\parallel},\ q_{\perp},\ \hat{\mathbf{n}}_0,\ \hat{\mathbf{n}}_s$$

   In this study, we decide to restrict to two situations: VH scattering from optically anisotropic particles and depolarised in the case when the optical anisotropy is small. Importantly, in the calculations, a general potential Φ of wall-particle interactions may be included.

2. For the evaluation of the hydrodynamic properties of the particle, we use three basic models:

   (a) EWDLS-Hydro code, which includes full wall-particle hydrodynamic interactions. In this model, the mobility depends on the particle distance to the wall and its orientation. The particle is represented by its corresponding bead model constructed out of spherical subunits glued together in a fixed configuration. The hydrodynamic mobility is calculated using the Hydromultipole Fortran codes [118]. The numerical predictions are valid for all wall-particle distances, including the lubrication regime. They allow for a convenient calculation of the averaged mobility coefficients for particles consisting of several beads, typically not more than 20, although calculations for a larger number of subunits are straightforward. For a given value of κL, the averaged coefficients are pre-calculated and then used in the calculation of the first cumulant for a range of scattering vectors q. This model, although the costliest of all, is also the most accurate, and will serve as reference for the two simplified schemes below.

   (a) EWDLS-Slender code, in which bulk mobility tensors are used as input. In this model, hydrodynamic interactions with the wall are neglected, and thus purely evanescent wave scattering and restricted volume effects are taken into account. As argued before, we expect this model hold for very elongated or flattened particles, since in the slender-body limit hydrodynamic interactions with the wall vanish. We also estimate the model to be accurate for low values of κL, where distance far apart from the wall are investigated. The mobility values are calculated using the bulk Hydromultipole codes for bead models of the particles.

   (c) EWDLS-Correction code, which includes the leading order correction term in the near-wall translational mobility tensor, derived in Sec. 5.5.3. The correction, which scales as inverse wall-particle distance from the wall, is expected to improve the bulk hydrodynamics model for moderate values of κL. Since the correction to the

rr and tr, rt parts is much less pronounced, we neglect it and use the bulk values for these components, i.e. constant rr mobility and no tr or rt contribution. It has to be noted, though, that the correction represents only the far-field wall effect, and cannot be used to estimate the mobility close to the boundary. To this end, a combined analytical scheme would be desirable, joining our asymptotic results with the lubrication regime solutions. Alas, no such approximation has been derived up to date. We will use this scheme comparing with EWDLS-Hydro to see in what range of the parameters it accurately reproduces the first cumulant.

3. The scattering amplitude is calculated either as a sum over the beads, or in the continuous limit of a thin particle using the expressions developed in Sec. 8.4.

4. Numerical integration over the angular degrees of freedom is performed using Gaussian quadratures [183].

The above-outlined numerical scheme, with different models for hydrodynamic interactions, are versatile and applicable to any experimentally relevant situation. However, due to an abundance of externally controlled independent parameters, for the presentation of results in this work we specify to a particular arrangement.

We choose to evaluate the first cumulant in an EWDLS set-up with the angle $\theta_r = 0$. All the relevant experimental conditions follow then from the general formulae given in Chapter 3. Remarkably, the same alignment has been used to explore the rotational dynamics of optically anisotropic spherical particles in Sec. 7.5.2. The scattering vector in the LAB frame for $\theta_r = 0$ may be written as $\mathbf{q} = q_{\parallel}\hat{\mathbf{e}}_y + q_{\perp}\hat{\mathbf{e}}_z$. The polarisation of the incident light reads then $\hat{\mathbf{n}}_0 = \hat{\mathbf{e}}_x$. By tuning the angle α of the polariser at the detector, different scattering geometries are recovered. It should be noted that the components of the scattered light polarisation vector are also related to the scattering vector, since both depend on the angle α_r. However, in model calculations below, we deliberately violate this rule, i.e. we change the scattering vector with the polarisation direction kept fixed, since it is our aim to pinpoint the effects purely due to changes in κ and q.

We restrict our considerations to two types of scattering: VH and depolarised. We plot the coefficients of the first cumulant as functions of two parameters - the scattering vector $\mathbf{q}$ and the penetration depth κ. Moreover, we assume hard-core type interactions of the particle and the wall. Thus, the allowed configurations of the particle are restricted geometrically by the boundary. General formulae valid for an arbitrary potential may be derived directly from the general formulae for the first cumulant, given in Sec. 8.2.

For the presentation of results we choose to divide the first cumulant by the corresponding bulk diffusion coefficients, calculated for each particle using the Hydromultipole package. For the purpose of direct comparison to bulk results, we choose to perform a scan of the $\mathbf{q}$-space, letting $q_{\parallel} = q_{\perp} = q_0$, so that $q = q_0\sqrt{2}$. We also simplify the notation by writing the bulk diffusion coefficients as

$$\bar{D}^t \equiv D^t, \qquad D^r_{\perp} \equiv D^r. \tag{8.46}$$

The first cumulant may now be written in the form

$$\Gamma^t = D^t \left(q^2 C^t(\kappa, \mathbf{q}) + \frac{\kappa^2}{4} C^t_\perp(\kappa, \mathbf{q}) \right), \tag{8.47}$$

$$\Gamma^r = D^r C^r(\kappa, \mathbf{q}), \tag{8.48}$$

$$(\Gamma^{tr} + \Gamma^{rt}) = D^r \left(-\frac{\kappa}{2} C^{tr}_\kappa(\kappa, \mathbf{q}) + q C^{tr}_q(\kappa, \mathbf{q}) \right), \tag{8.49}$$

with $C^t_\perp(\kappa, \mathbf{q}) = A^t_\perp(\kappa, \mathbf{q})/D^t$, $C^r(\kappa, \mathbf{q}) = A^r(\kappa, \mathbf{q})/D^r$, $C^{tr}_\kappa(\kappa, \mathbf{q}) = A^{tr}_\kappa(\kappa, \mathbf{q})/D^r$, and

$$C^t(\kappa, \mathbf{q}) = \frac{1}{2D^t} \left(A^t_\perp(\kappa, \mathbf{q}) + A^t_\parallel(\kappa, \mathbf{q}) + A^t_{\parallel\perp}(\kappa, \mathbf{q}) \right), \tag{8.50}$$

$$C^{tr}_q(\kappa, \mathbf{q}) = \frac{1}{\sqrt{2} D^r} \left(A^{tr}_\perp(\kappa, \mathbf{q}) + A^{tr}_\parallel(\kappa, \mathbf{q}) \right). \tag{8.51}$$

The coefficients C are evaluated using our software. In the following, we present the results for the two scattering geometries obtained using different models of hydrodynamic interactions.

8.5.1 Slender or thin particles

An approximate method for the determination of the first cumulant is to use a bulk-like model for its near-wall hydrodynamics. As we argued, this model should hold sway in the case of slender (thin) particles, such as elongated rods or flat discs. In this simple approximation, we note that for such particles the effect of hydrodynamic interactions may be neglected, and therefore the hydrodynamic diffusion tensors attain the simple bulk form, as given in Chapter 6. We will confine our attention to such thin rod and flat disc particles, which we previously discussed in the context of bulk DLS. However, the bulk hydrodynamics model is expected to hold sway generally for large penetration depth (low κL), where the results converge towards their bulk limit for $\kappa \to 0$.

Inserting the bulk diffusion tensors $\mathbf{D}^{tt}$ and $\mathbf{D}^{rr}$, as in Eqs. (6.14)-(6.16), into the general expressions from Sec. 8.2, we find that the first cumulant has only two contributions from translational and rotational motion, which we may explicitly evaluate using the bulk diffusion coefficients D^t, D^r, and the bulk translational diffusivity anisotropy ΔD^t.

In the particular case of hard-core interactions with the wall, the average over the z-coordinate may be performed, and the resulting expressions contain only the angular averages. The expression $\exp(-\kappa z_0)$ also simplifies in the limit of infinite aspect ratio, which for a rod-like particle of length L reads $\exp(-\gamma|w|)$, with $\gamma = \kappa L/2$. The simplified formulae valid for a general axisymmetric particle follow from Eqs. (8.47)-(8.48) and read

$$S = \left\langle e^{-\gamma|w|} |\mathcal{E}|^2 |B|^2 \right\rangle_{\hat{\mathbf{u}}}, \tag{8.52}$$

$$C^t_\perp = 1 + \frac{\Delta D^t}{D^t} \frac{1}{S} \left\langle e^{-\gamma|w|} |\mathcal{E}|^2 |B|^2 \left(u_z^2 - \tfrac{1}{3} \right) \right\rangle_{\hat{\mathbf{u}}}, \tag{8.53}$$

$$C^t_\parallel = 1 + \frac{\Delta D^t}{D^t} \frac{1}{S} \left\langle e^{-\gamma|w|} |\mathcal{E}|^2 |B|^2 \left(u_y^2 - \tfrac{1}{3} \right) \right\rangle_{\hat{\mathbf{u}}}, \tag{8.54}$$

$$C^t_{\parallel\perp} = \frac{\Delta D^t}{D^t} \frac{2}{S} \left\langle e^{-\gamma|w|} |\mathcal{E}|^2 |B|^2 u_y u_z \right\rangle_{\hat{\mathbf{u}}}, \tag{8.55}$$

$$C^r = \frac{1}{S} \left\langle e^{-\gamma|w|} \left\{ |\mathcal{E}|^2 |\mathbf{L}B|^2 + |B|^2 |\mathbf{L}\mathcal{E}|^2 + 2\mathrm{Re}\left[(B^* \mathbf{L} B) \cdot (\mathcal{E} \mathbf{L} \mathcal{E}^*) \right] \right\} \right\rangle_{\hat{\mathbf{u}}}. \tag{8.56}$$

The tr coefficients are absent, since in bulk $\mathbf{D}^{tr} = \mathbf{D}^{rt} = 0$. The remaining coefficients are easy to evaluate numerically without the need to address the problem of hydrodynamics. In the case of a flat disc, the exponential factor should be replaced by $\exp(-\kappa R \sin\theta)$, with R being now the disc radius. The essential role of this factor is the restriction of the scattering volume. In this simple case, one only needs to perform angular integration of the above equations to arrive at numerical predictions for the first cumulant and its behaviour with the changing scattering vector.

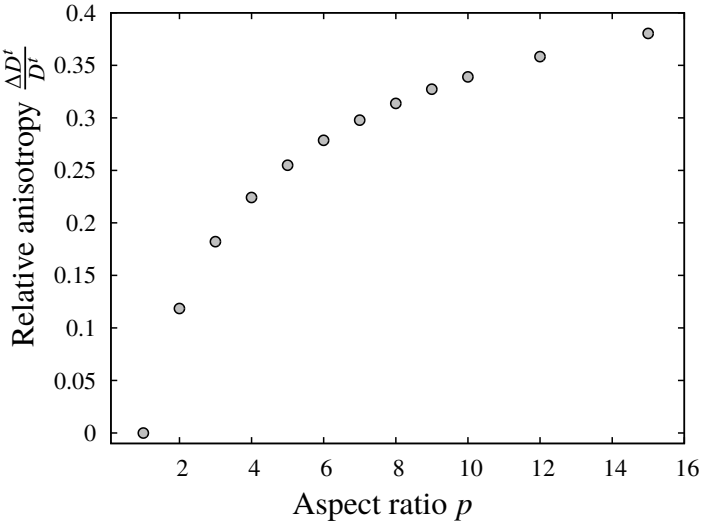

Figure 8.4: The relative bulk translational diffusivity anisotropy, $\Delta D^t / D^t$, controls the magnitude of the correction introduced by the functions C_1 and C_2 in the translational first cumulant (8.57). It is naturally more pronounced for elongated particles, tending to the theoretical limit of 0.75 for $p \to \infty$, in accord with the slender body results of Eqs. (5.54).

For the chosen q-scan, the first cumulant can be written as

$$\Gamma^t = D^t \left[q^2 \left(1 + \frac{\Delta D^t}{D^t} C_1(\kappa, \mathbf{q}) \right) + \frac{\kappa^2}{4} \left(1 + \frac{\Delta D^t}{D^t} C_2(\kappa, \mathbf{q}) \right) \right], \tag{8.57}$$

$$\Gamma^r = D^r C^r(\kappa, \mathbf{q}), \tag{8.58}$$

with the functions C_1 and C^r defined as generalisation of the bulk DLS results from Chapter 6. These translational functions $C_{1,2}$ are given by the relations:

$$C^t(\kappa, \mathbf{q}) = 1 + \frac{\Delta D^t}{D^t} C_1(\kappa, \mathbf{q}), \qquad C^t_\perp = 1 + \frac{\Delta D^t}{D^t} C_2(\kappa, \mathbf{q}). \tag{8.59}$$

For brevity, hereafter we drop the dependence on arguments $(\kappa, \mathbf{q})$. The magnitude of the terms C_1 and $C^t_\perp$ is controlled by the ratio of the bulk diffusivity anisotropy to the mean diffusion coefficient. These may be evaluated using the bulk HYDROMULTIPOLE routines to estimate the importance of this correction. In Fig 8.4, we plot the coefficient $\Delta D^t / D^t$ and demonstrate its increase with increasing particle aspect ratio.

The results of EWDLS-SLENDER for two scattering geometries are presented in Fig. 8.5 for rod-like particles, and in Fig. 8.6 for disc-like particles. In the limit $\kappa L \to 0$ (or $\kappa R \to 0$) the first cumulant converges towards its bulk form analysed in Chapter 2. It is evident that, apart from the shift of the initial value at intercept for $q = 0$, the shape of the functions C is not very

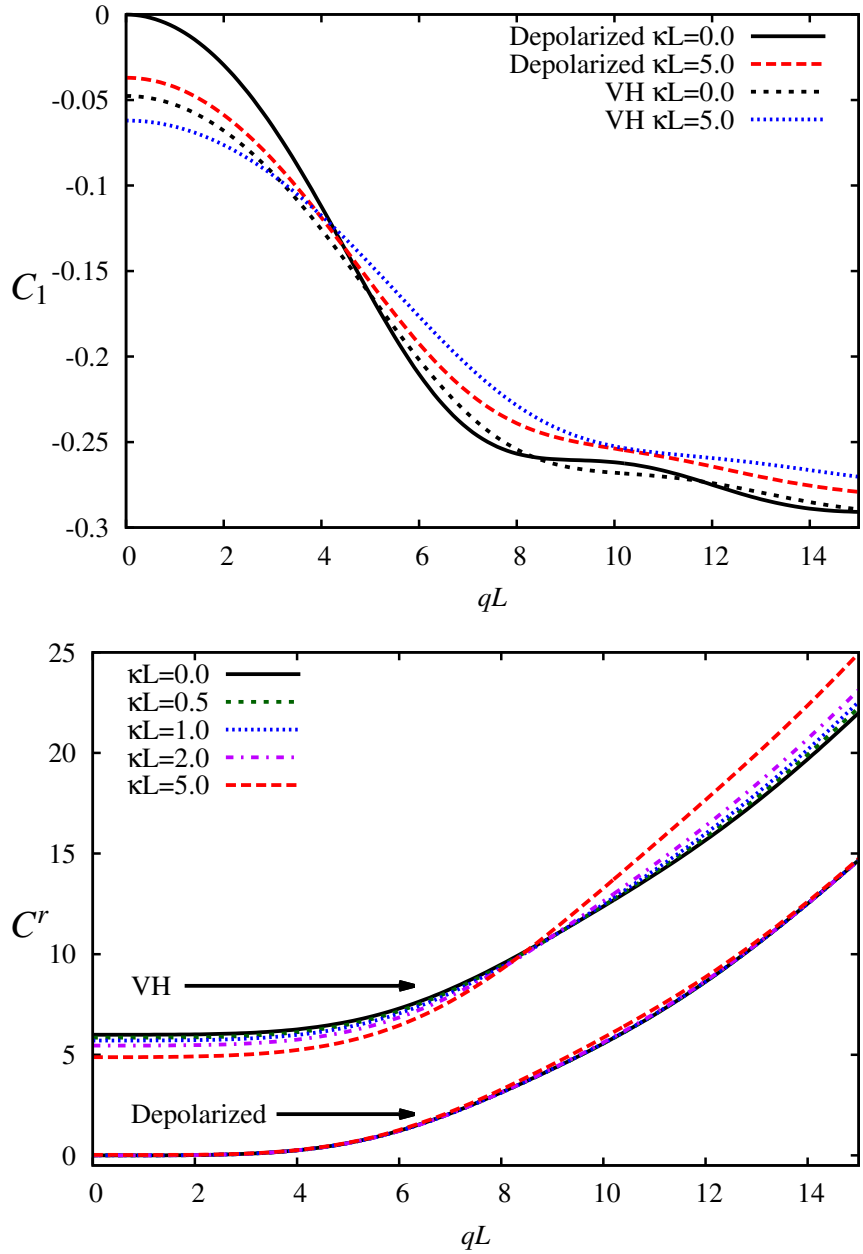

Figure 8.5: Components of the first cumulant for a slender rod in the evanescent field. Top: translational contribution C_1, as defined in Eq. (8.59). Bottom: Rotational contribution C^r. Both depolarised and VH scattering results are presented for several values of the penetration depth. There is only a slight change with increasing κL in these functions.

sensitive to changes in κL (κR), especially in the large penetration depth regime in which we expect the slender-body type approximation to hold. With reasonable accuracy, one may then disregard the dependence of the functions C_1 and C^r on κ. It is important to stress, however, that the first cumulant does depend on κ strongly via the term $\frac{\kappa^2}{4}(\bar{D}^t + \Delta D^t C_2)$. This term contributes to the non-zero value of Γ at $q = 0$, even in the case of depolarised scattering. The function C_2 is plotted in Fig. 8.7 in the case of a rod in depolarised and VH scattering. Other cases (depolarised and VH scattering for platelets) are not plotted in this work but they show a similar behaviour, with only a slight dependence on q.

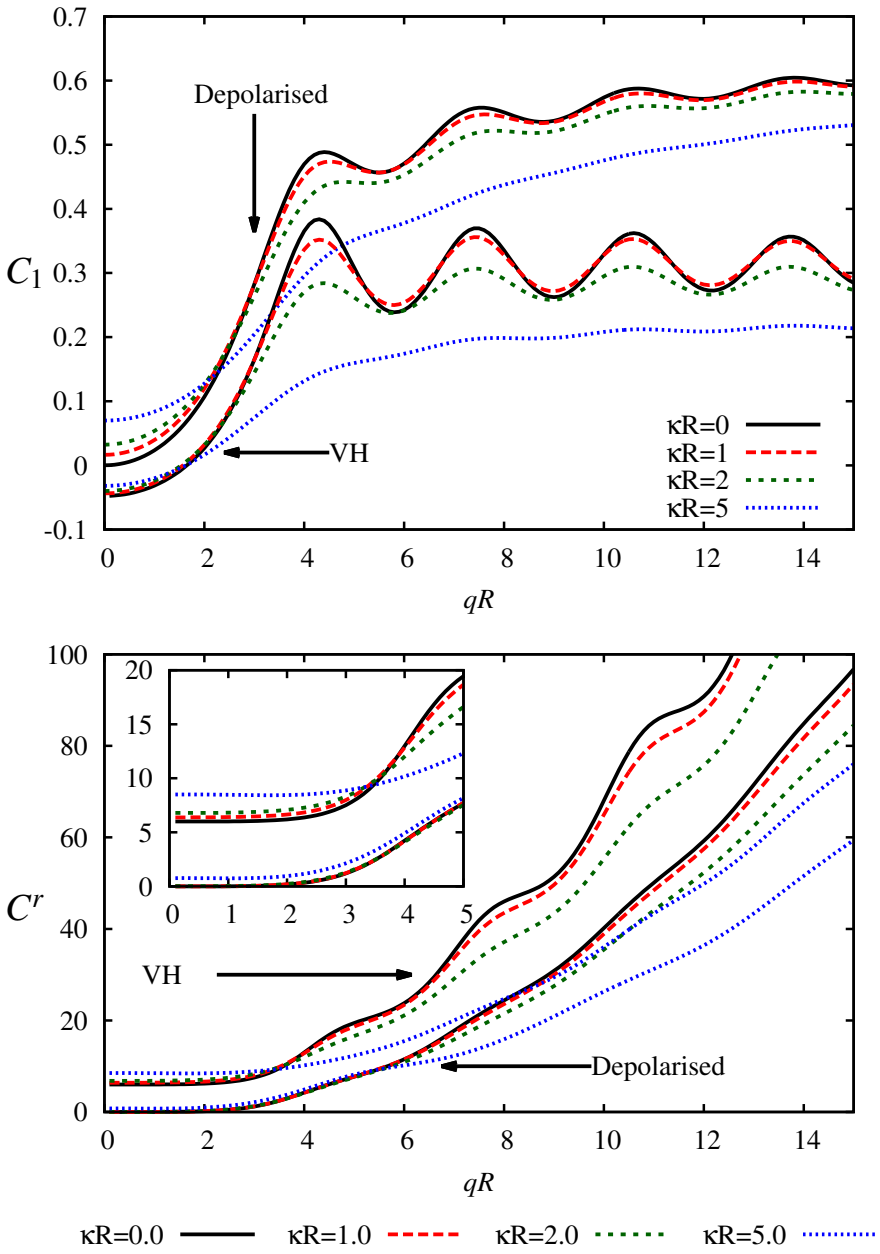

Figure 8.6: Components of the first cumulant for a slender disc in the evanescent field. Top: translational contribution C_1, as defined in Eq. (8.59). Bottom: Rotational contribution C^r. Both depolarised and VH scattering results are presented for several values of the penetration depth. The inset in the lower figure presents the low-q behaviour in more detail.

It seems that in the absence of hydrodynamic interactions the inherent features of EWDLS experiments, including the restricted scattering volume, change the character of relaxation of the measured correlation functions, especially in the low qL range. This may either lead to a slowdown of (mostly rotational) relaxation (for rod-like particles), or a significant enhancement (for slender discs). To elucidate the character of relaxation in a wall-bounded system, one needs to take into account the effect of hydrodynamic slowdown due to the presence of the wall, which is discussed in the next section.

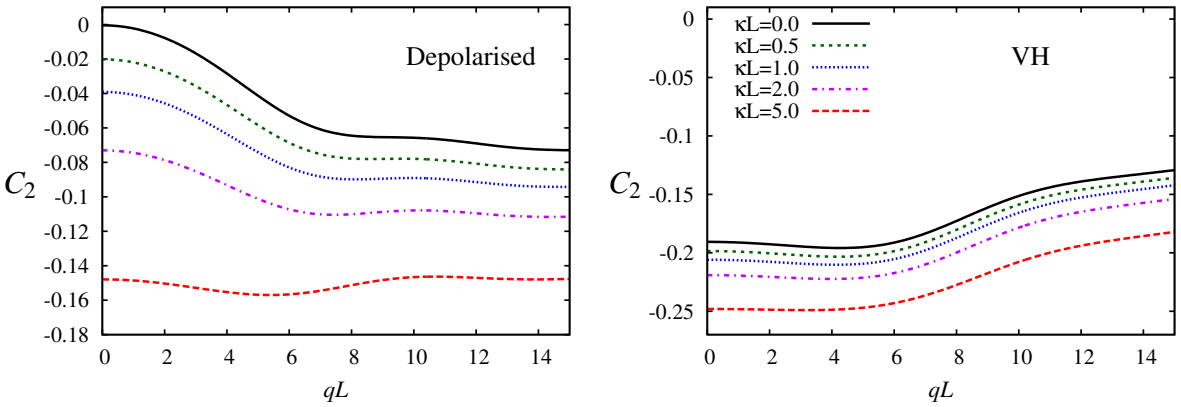

Figure 8.7: The term C_2 in the first cumulant for rod like particles is typically small and weakly dependent on q but should be taken into account for the calculation of the first cumulant at low scattering vector. The intercept of Γ^t with $q = 0$ is determined by $\frac{\kappa^2}{4}(D^t + \Delta D^t C_2)$, and is slightly more pronounced in VH scattering.

8.5.2 Wall-particle hydrodynamic interactions

The model which incorporates hydrodynamic interactions between the wall and the particle is crucial for the analysis of the experimental EACFs, since it encompasses both effects which determine the dynamics of the EACF: the non-uniform illumination and increased near-wall friction.

Modelling of the particles In the present work, we restrict our attention to two types of particles – rods and platelets. The particle bead models are sketched below:

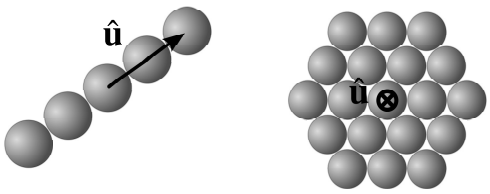

We model the rod-shaped particles as straight strings of identical spherical beads. We have used rods with aspect ratio $p = 5$ and $p = 9$ for the needs of this work, but the scheme is general. If the rod is located at $\mathbf{r}_0$, and has the orientation $\hat{\mathbf{u}}$, the positions of the beads may be conveniently expressed as

$$\mathbf{r}_m = \mathbf{r}_0 + m\sigma\hat{\mathbf{u}}, \quad m = -\tfrac{1}{2}(p-1), \ldots, \tfrac{1}{2}(p-1), \tag{8.60}$$

with σ being the bead diameter.

To model a disc-like particle, we choose to compose it of spherical beads arranged in a hexagonal lattice. To construct a hexagonal platelet with P particles on its side, one needs $N = 3P(P-1)+1$ beads. The number of beads in such consecutive hexagons (1,7,19, etc.) is called a centred hexagonal number. Due to a rapidly increasing number of beads, we restrict here to the case of $P = 2$. It is important to stress, however, that calculations for a larger number of beads are also possible. We also note that although the hexagonal conglomerate has no exact rotational

symmetry about the axis $\hat{\mathbf{u}}$, the hydrodynamic mobility matrix of a disc-like particle is obtained in our calculations by rotating the particle about its symmetry axis and averaging the obtained mobility.

In the following, we analyse specifically results for colloidal rods and discs, pointing out the differences to bulk scattering. The general distinguishing feature here is again the presence of the term $\frac{\kappa^2}{4} D^t$ in the first cumulant. This term plays an important role especially in the low-q region, where the other components proportional to q^2 decrease to zero. As we will demonstrate, the coefficients C of the first cumulant do not depend significantly on the scattering vector independently of the scattering geometry. Thus the dominant behaviour of the first cumulant except for the κ^2-terms is linear in q^2, similarly to the bulk case.

Due to an abundance of available numerical results, and the large number of the functions A (or C) in the expressions for the first cumulant, it would be rather cumbersome to present all of them here. Instead, we include a selection of results corresponding to the tt, rr and tr contributions in the two chosen scattering models.

Rod-shaped particles

The rotational contribution, plotted in Fig. 8.9, shows a dependence on the scattering vector similar to that observed in a bulk fluid. For large values of the scattering vector q, the function C^r becomes proportional to q^2, with the slope approximately independent of the penetration depth. The value of κL influences mostly the initial value (the intercept at $q = 0$). The decrease of this intercept is larger than in the case of a slender-body type approximation, owing to the decrease of rotational mobility close to a wall. This effect is, however, not much pronounced, since the rotational degrees of freedom are generally less hindered in the vicinity of the wall than the translational ones.

The last contribution comes from the off-diagonal mobility matrix components which describe coupling between the translational and rotational motion. To demonstrate its magnitude, we have chosen to present the results only for rod-like particles in the depolarised scattering regime. These are plotted in Fig. 8.10. It has been verified that the magnitude of these terms is not significantly different in VH geometry, and in both cases for disc-like particles. Although their shapes differ slightly, the numerical values are of the same order of magnitude. The term C_κ^{tr} is small even for large values of κL. The term C_q^{tr} for large scattering vectors becomes proportional to q, so that $qC_q^{tr} \sim q^2$, and therefore we decided to plot the function $q^{-1}C_q^{tr}$ instead. It is clear from the Figure that this contribution may now also be approximated by a constant function with a negligibly small numerical value. This leads us to an important simplification: In practical situations, the $tr + rt$ terms in the first cumulant may be disregarded. This is equivalent to the neglect of the tr and rt hydrodynamic mobility tensors in the full mobility matrix $\boldsymbol{\mu}$.

Disc-shaped particles

The case of disc-like colloids, is slightly more expensive computationally, since for a disc of aspect ratio $p \approx 1/2P$ one needs $N = 3P(P-1) + 1$ beads, so that the number of beads grows quadratically with P corresponding to the aspect ratio, differently from the linear dependence

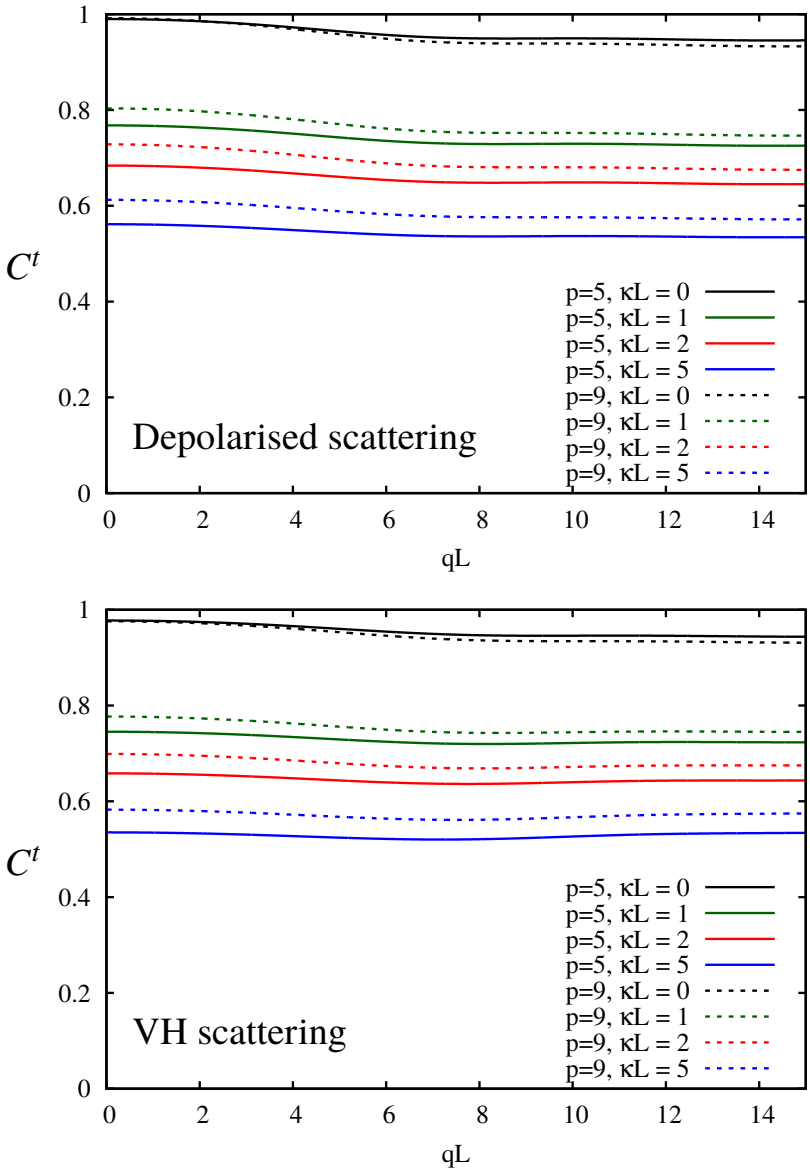

Figure 8.8: Translational contribution to the first cumulant C^t for rod-like particles in the depolarised scattering (top) and VH scattering mode (bottom), presented for two values of rod aspect ratio $p = 5, 9$. There is virtually no dependence on the scattering vector. The amplitude of the function C^t decreases with increasing κL due to hydrodynamic interactions.

for a rod. We have therefore decided to present results for $P = 2$, i.e. for a hexagonal disc made of $N = 7$ beads.

The translational contribution is presented in Fig. 8.11 in both scattering geometries. The functions have an oscillatory character which is not clearly visible in the graphs due to a very small amplitude. The magnitude of the coefficients changes with κL significantly but the dependence on the scattering vector may be neglected.

The rotational part retains the dependence on q, similarly to the bulk case, and the amplitude is shifted downwards, as seen in Fig. 8.12. Interestingly, in the low-q regime, there is again no dependence on q, so in most experimentally relevant configurations this contribution will

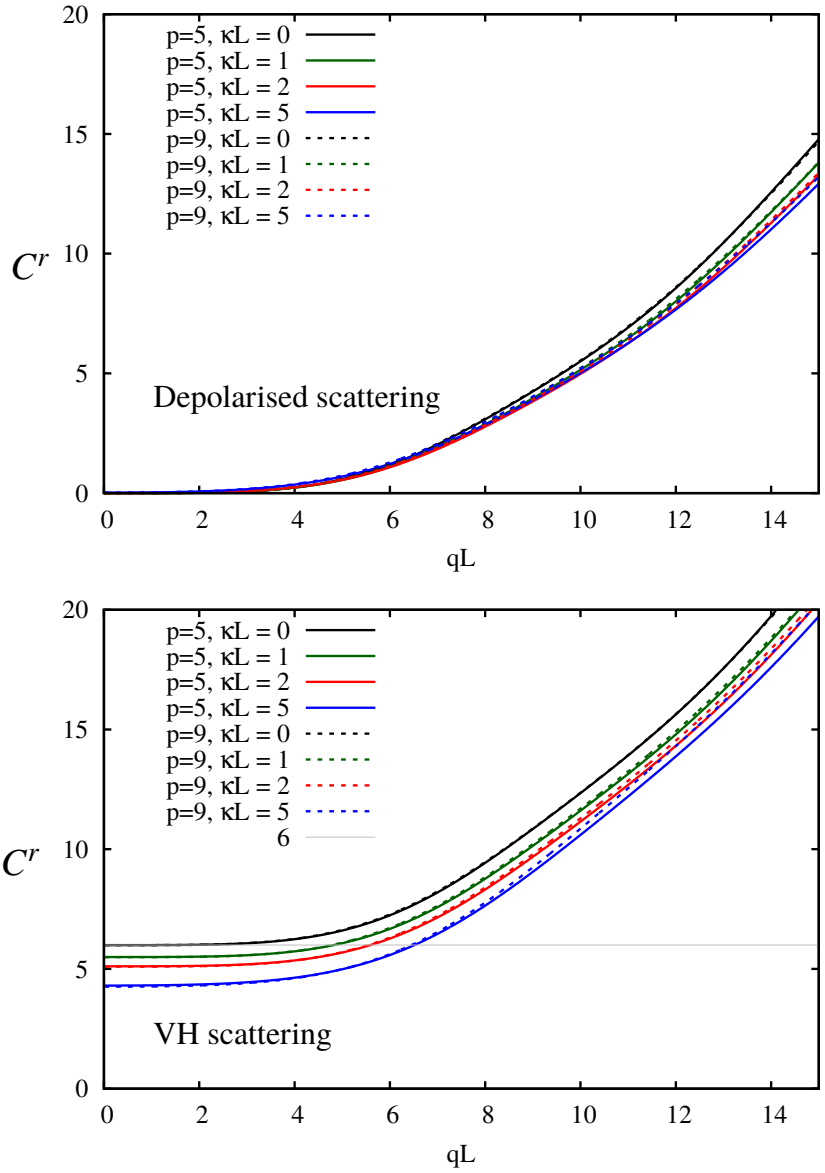

Figure 8.9: Rotational contribution to the first cumulant C^r for rod-like particles in the depolarised scattering (top) and VH scattering mode (bottom), presented for two values of rod aspect ratio $p = 5, 9$. This contribution depends strongly on the scattering vector, although the slope seems to be independent of the penetration depth. The effect of hydrodynamic interaction is the downwards shift of the intercept at $q = 0$. The rotational contribution seems also to depend on the rod aspect ratio only through the value of the free bulk diffusion coefficient $D^r_\perp$. The grey grid line indicates the bulk value at $q = 0$ (i.e. 6).

be constant with the amplitude shift for a given κR resulting from the hindrance of rotational motion close to a wall.

We refrain here from plotting the $tr + rt$ parts, as these have been shown before to be negligible, and are of magnitude similar to the case of rod-like colloids.

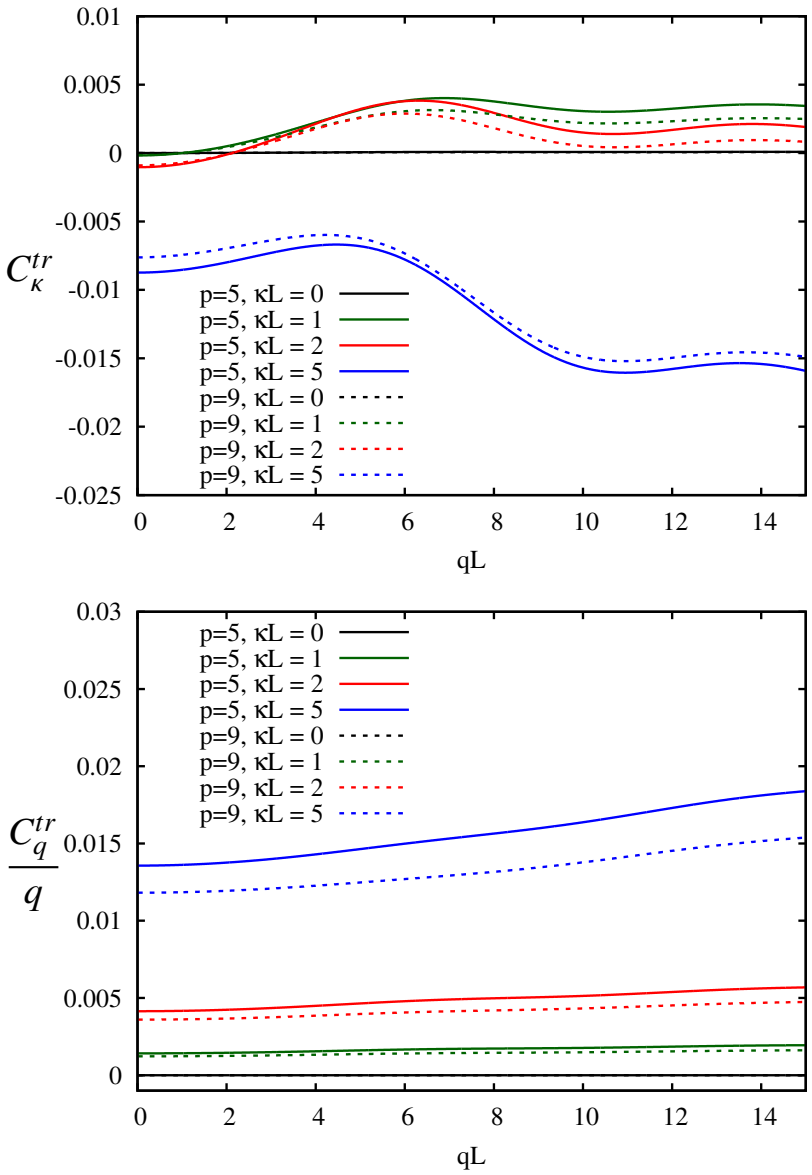

Figure 8.10: Coupling $(tr + rt)$ contribution to the first cumulant for rod-like particles in the depolarised scattering mode for two values of rod aspect ratio. Top: the term C_κ^{tr}. Bottom: the term (C_q^{tr}/q), demonstrating no significant change with q.

8.5.3 Approximations to the first cumulant

We have presented a toolbox which allows for convenient calculation of the components of the first cumulant for various particle shapes in two essential models: with the neglect of hydrodynamic interactions, and with full hydrodynamic interactions included. A question arises now: in which cases one may use the simplified model with bulk hydrodynamics which does not require advanced modelling tools to account for the wall drag effects? Below, we shall focus on the first cumulant and identify its dominant behaviour with the scattering vector qL and its changes with increasing κL. The results presented in the preceding Section allow us to conclude the analytical and numerical analysis by formulating a handful of approximations which may be used in practical situations for the interpretation of EWDLS experimental results. Although

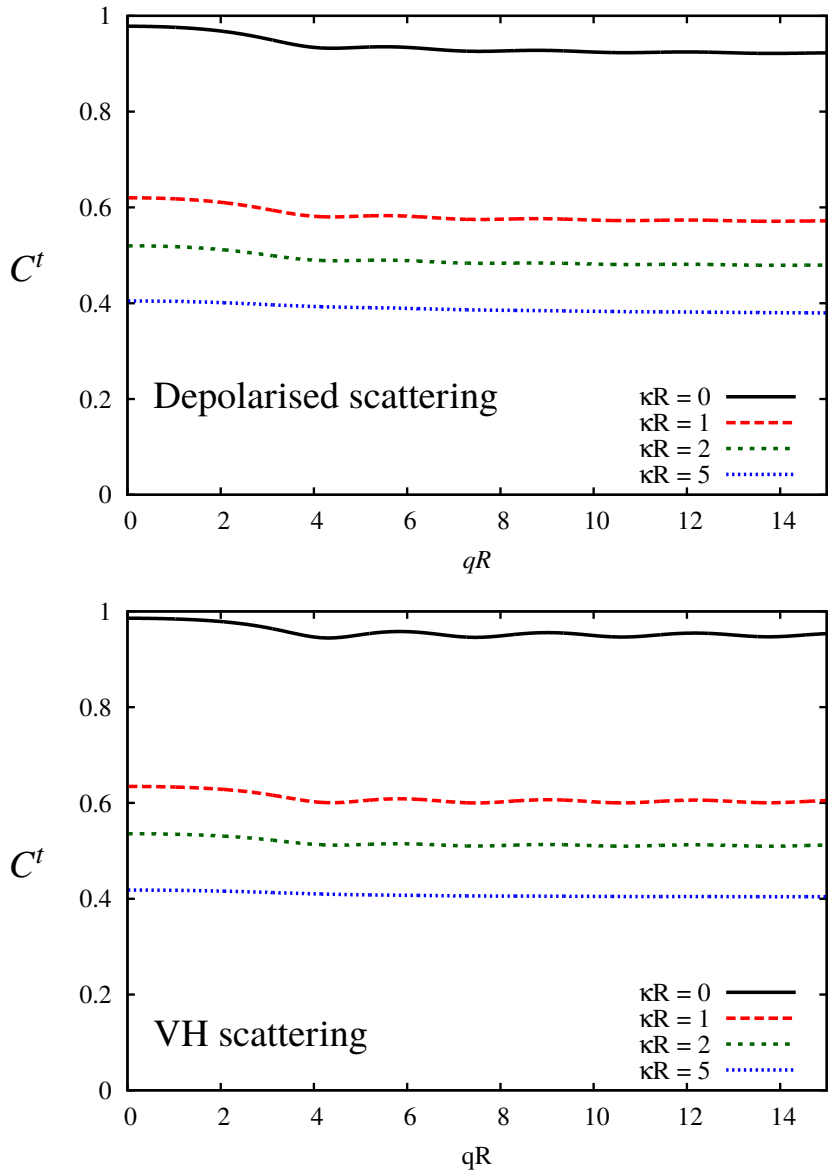

Figure 8.11: Translational contribution to the first cumulant C^t for planar hexagonal particles (discs) in the depolarised scattering (top) and VH scattering mode (bottom), for hexagons made of $N = 7$ beads. In both cases the results are very similar. The amplitude of the function C^t decreases again with increasing κL due to hydrodynamic interactions but no essential effect of the scattering vector is visible.

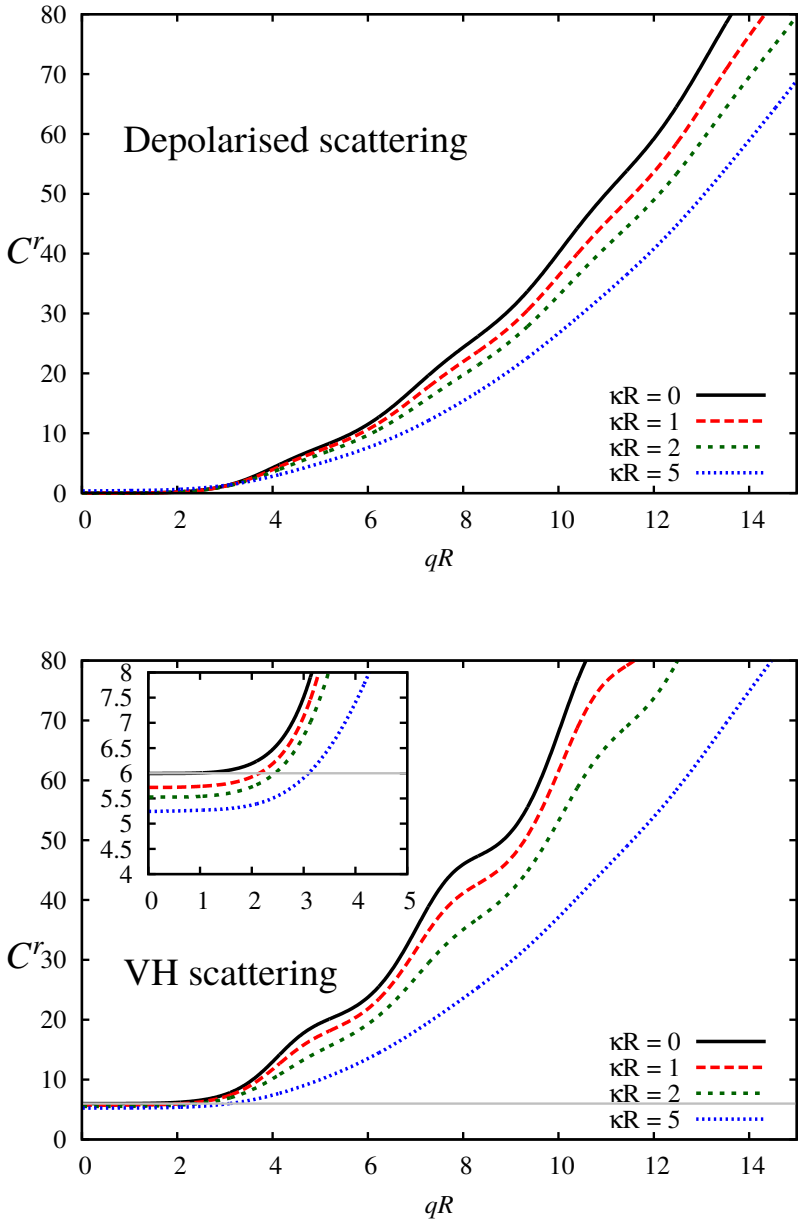

Figure 8.12: Rotational contribution to the first cumulant C^r for disc-shaped particles in the depolarised scattering (top) and VH scattering mode (bottom), presented for hexagonal platelets made of $N = 7$ beads. There is a typical dependence on the scattering vector, again with the effect of hydrodynamic interactions visible in the shift of the intercept at $q = 0$, magnified in the inset.

the software created for the calculations performed above is quite general, and virtually all the relevant parameters may be varied depending on the actual system of interest, it is valuable to have a simple approximate scheme illustrating the general structure of the result. We restrict here again to a rod-like particle of aspect ratio $p = 9$.

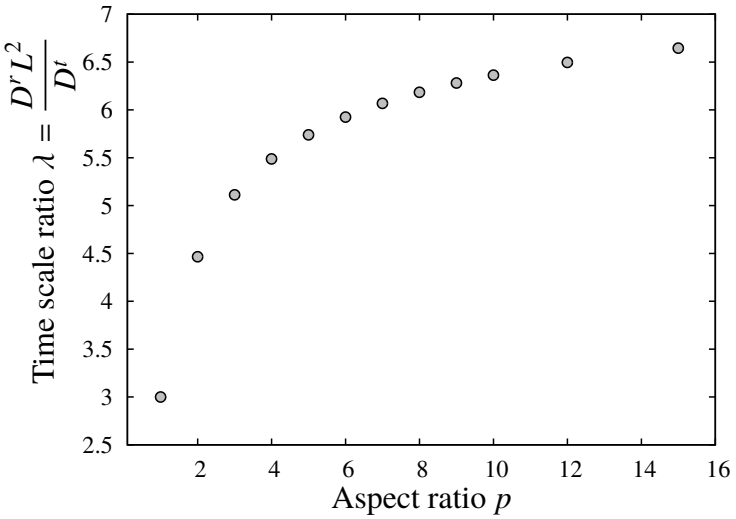

Figure 8.13: The ratio of time scales of translational to rotational relaxation for a bead model of a rod-like particle. Numerical results have been obtained using the HYDROMULTIPOLE routines. For elongated particles, the time scale of translational motion becomes longer, and thus rotational relaxation becomes more pronounced in the first cumulant (8.62). In the limit of $p \to \infty$, the ratio tends to $\lambda = 9$.

Time scales With the tr and rt parts neglected, as discussed before, we may distinguish in the first cumulant two contributions

$$\Gamma = \Gamma^t + \Gamma^r, \tag{8.61}$$

stemming from translational and rotational relaxation, respectively. The natural time scale of translational relaxation is the structural relaxation time $\tau_t = L^2/D^t$. The characteristic rotational relaxation time is given by $\tau_r = 1/D^r$, and thus we presented the translational part as $\Gamma^t\tau_t$ and the rotational part as $\Gamma^r\tau_r$. In the total dimensionless first cumulant taking τ_t as the base time scale, we have

$$\frac{\Gamma L^2}{D^t} = (\Gamma^t + \Gamma^r)\tau_t = \Gamma^t\tau_t + \lambda C^r, \tag{8.62}$$

where $\lambda = \tau_r/\tau_t = \frac{D^r L^2}{D^t}$ is the ratio of time scales, and the function C^r is defined in Eqn. (8.58). This ratio depends on the aspect ratio of the particle via the bulk diffusivity coefficients, as discussed in Chapter 5. Since λ increases from 3 for spheres ($p = 1$) to 9 for very elongated (slender) particles, as shown in Fig. 8.13, we expect the rotational relaxation to play an increasingly important role in the first cumulant.

Analysis of the first cumulant In the general structure of the first cumulant, we noticed that the coefficients appearing in the expressions are weakly dependent on the scattering vector. Hence the first cumulant for axisymmetric particles retains the structure quadratic in the scattering vector, possessing contributions proportional to $q_\parallel^2$ and $q_\perp^2$. An important difference to bulk scattering is the presence of an additional term proportional to κ^2, which plays an important role especially in the regime of small qL. The coefficients accompanying these quadratic quantities have to be evaluated numerically or semi-analytically, for which we have developed a set of practical numerical codes, EWDLS-SLENDER for the case when hydrodynamic interactions may be neglected, and EWDLS-HYDRO where both scattering effects and wall-particle hydrodynamic interactions are included. Below, we suggest a couple of simplifications allowing for a crude

estimation of the form of the first cumulant in these cases. Importantly, these simplifications are valid in the range of experimentally relevant values of the penetration depth and scattering vector.

We propose to characterize the translational part of the first cumulant solely by its intercept with the $q = 0$ axis, and its slope, encoded in the so-called effective diffusion coefficient, viz.

$$\Gamma^t = \gamma^t + q^2 D^t_{\text{eff}}, \tag{8.63}$$

with the intercept defined as $\gamma^t = \frac{\kappa^2}{4} D^t C^t_\perp(\kappa, q = 0)$, and the effective diffusion coefficient $D^t_{\text{eff}} = D^t C^t$, both defined in Eq. (8.47), and depending on the penetration depth. Importantly, we see no significant difference for VH and depolarised scattering: the results do not differ by more that 10%. We therefore treat the translational part as polarisation-independent. For the rotational part, we propose to approximate it by a constant factor for low q's, say $qL < 5$, while for larger scattering vector, say $qL > 8$, we expect this contribution to increase quadratically in q, similarly to the translational part. We therefore have

$$\Gamma^r \approx \begin{cases} \gamma^r & \text{for } qL \leqslant 5 \\ q^2 D^r_{\text{eff}} + \text{const.} & \text{for } qL \geqslant 8 \end{cases}, \tag{8.64}$$

with $\gamma^r = D^r C^r(\kappa, q = 0)$, in accord with Eq. (8.48). For intermediate q's we observe a crossover between the two regimes. The results for rotational cumulant strongly depend on the scattering geometry. In the following, we focus on the experimentally interesting range of $qL < 8$, when the rotational contribution may be treated as constant. We shall refrain here from discussing also the slope and shift of the translational cumulant for large q, although it is generally straightforward and can be likewise calculated using our software.

In Fig 8.14, we plot the intercept γ^t of the translational first cumulant Γ^t with the $q = 0$ axis. The results were obtained using the three aforementioned models of hydrodynamic interactions (HI). We see that in the model of bulk mobility of the particle, the intercept shifts upwards proportionally to $(\kappa L)^2$. This effect is hampered by the presence of HI with the wall. It turns out, however, that for moderate values of the penetration depth (up to ca. $\kappa L \sim 2$), including the leading order correction to the translational mobility, for which we have derived a closed analytical form in Chapter 5, correctly reproduces the intercept of the first cumulant. We also note that since the correction term underestimates the mobility for close wall-particle distances, predictions using the *tt* correction overestimate the near-wall slowdown of the dynamics. For higher values of κL, one has to use more precise numerical tools, such as the HYDROMULTIPOLE codes.

The normalised slope of the translational cumulant, D_{eff}/D^t, may likewise be determined using the aforementioned models. The result is plotted in Fig. 8.15. With the neglect of wall-particle HI, the slope only slightly depends on κL due to scattering effects. Including HI leads to a significant change in the measured dynamics, since the increased friction slows down the decay of the EACF. Again we observe that an approximate scheme including only the leading order correction to bulk mobility due to the presence of the wall suffices to reproduce the observed behaviour for low to moderate values of $\kappa L \leq 2$. For smaller penetration depth (larger κL), it is necessary to use the full HI scheme.

The normalised rotational shift γ^r/D^r is calculated in two scattering geometries, VH and depolarised, and presented in Fig. 8.16. It is evident that the rotational contribution in the

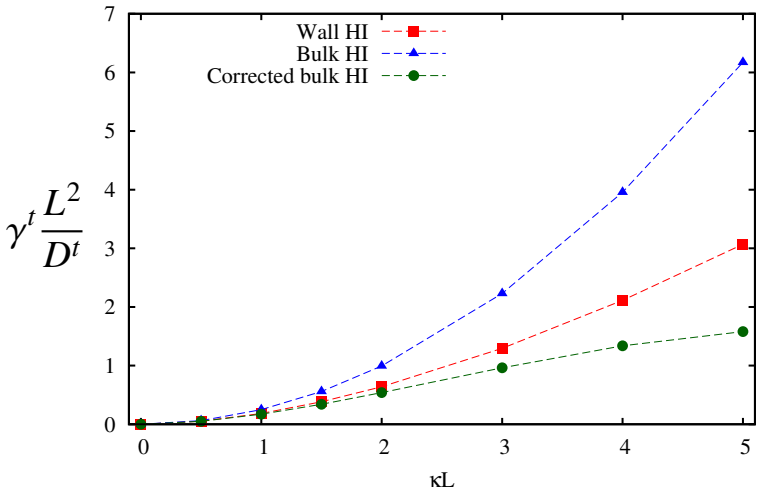

Figure 8.14: The intercept γ^t of the translational cumulant at $q = 0$, calculated for a range of penetration depths using three different models for hydrodynamic interactions (HI). Assuming the bulk mobility, i.e. no HI with the wall (blue triangles), leads to a shift linear in κ^2. Including the full wall-particle HI (red squares) is most costly numerically, but also the most precise. In order to correct the bulk mobility for wall-HI in leading order, we employed the analytical *tt* correction (green circles). It seems that the correction can be effectively used to account for the effect of HI up to ca. $\kappa L \sim 2$.

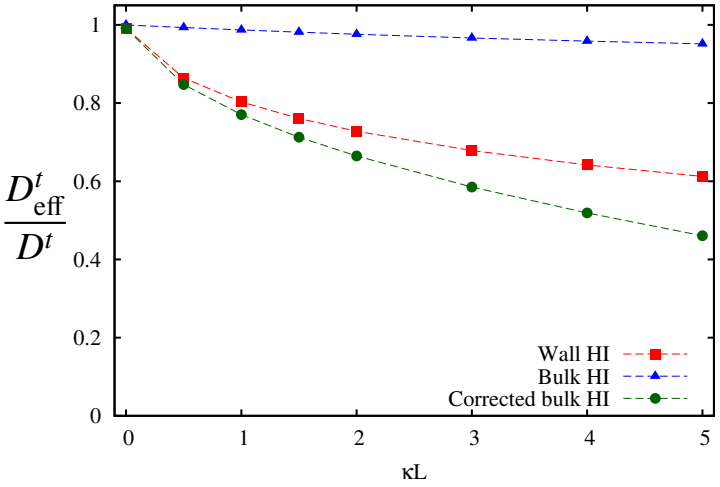

Figure 8.15: The normalised slope of the translational cumulant, D^t_{eff}/D^t is calculated using three hydrodynamic interactions (HI) models: bulk mobility (blue triangles), full wall-particle HI (red squares), and leading order *tt* correction to bulk mobility due to a wall (green circles). It is evident that the presence of HI has a pronounced effects on the dynamics, even for low values of κ. For the values of penetration depth not too large, say $\kappa L \leq 2$, it is enough to include the analytical correction term instead of full HI scheme to correctly reproduce the slope. However, for larger values of κL, full numerical scheme has to be used.

depolarised regime may be disregarded compared to VH scattering. In the latter, the intercept is weakly dependent on κ but drops by ca. 20% over the range of κL from 0 to 5 due to scattering effects. The inclusion of hydrodynamic interactions increases the downwards shift. However, even for $\kappa L = 3$, the relative decrease of γ^r with respect to bulk-HI is by only 10%.

This suggests that for a crude estimation of the effect it is sufficient to use the bulk mobility model, which is much faster in calculations. For larger scattering vectors, when Γ^r depends quadratically on q, the effect of hydrodynamic interactions is slightly more pronounced and full wall-HI scheme should be used in calculations. However, such values of qL are not practical in EWDLS experiments, and therefore we refrain from a further discussion.

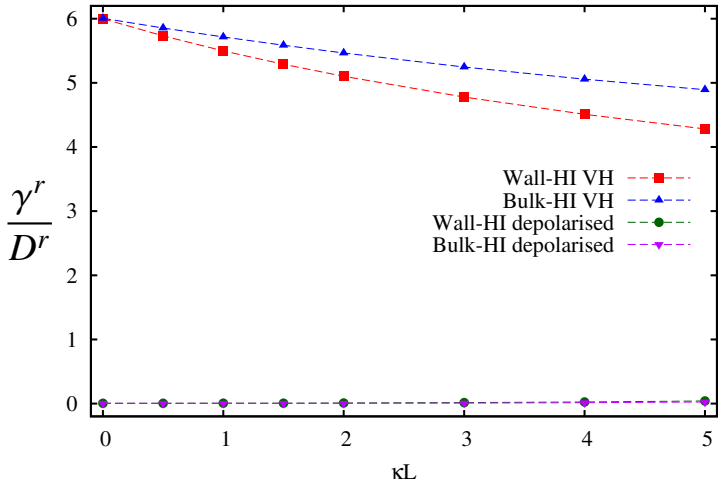

Figure 8.16: The normalised intercept of the rotational cumulant at $q = 0$, γ^r/D^r, is calculated for two scattering geometries, assuming either bulk mobility of the particle with the neglect of particle-wall HI (blue triangles for VH), or by evaluating the effect of HI numerically with high precision (red squares for VH). The constant value of the rotational cumulant is approximately valid in the whole experimentally interesting range of $qL < 8$. In depolarised scattering, we observe no effect of rotations in the first cumulant. In the VH geometry, the intercept is shifted downwards due to scattering effects even in the case of bulk mobility. The effect is enhanced by the inclusion of HI. However, since the rotational motion is less affected by the wall compared to translational one, it seems reasonable to use the bulk mobility predictions even for $\kappa L = 3$, where they differ by ca. 10%.

Including the leading order correction to bulk hydrodynamics seems to be an efficient scheme to reproduce the characteristics of the first cumulant for low values of κL. However, for larger κL, when the region close to the wall is probed, the correction leads to erroneous results, since it may lead to negative mobility close to the surface. For an accurate simplified scheme, one would have to include the near-wall lubrication behaviour and combine it with the far-field correction.

It is important to mention that the aspect ratio of the particle plays an important role in our considerations. In Chapter 5 and in Sec. 8.3.2, we discussed the hydrodynamic effects for elongated particles and concluded that in the limit of a slender particle, such as a needle-like rod, or a flat disc, the effect of hydrodynamic interactions with the wall vanishes, and thus the bulk mobility model shall represent their EWDLS properties correctly. As an example of this tendency, we consider a rod-like particle of a larger aspect ratio $p = 19$, and compare the results for the translational cumulant with the previously analysed $p = 9$ case. In Fig. 8.17, we plot the intercept γ^t and the slope D^t_{eff} of the translational cumulant for the two particles. It is clear from the Figure that with all other parameters (qL, κL) kept fixed, increasing the particle aspect ratio diminishes the hindering effect of HI, thus decreasing the deviation from the bulk hydrodynamics model. Importantly, the bulk hydrodynamics model results are very similar for

$p = 9$ and $p = 19$. This is due to the fact that for given qL and κL the only difference between the two lies in the relative diffusivity anisotropy, $\Delta D^t / D^t$, which is similar for both aspect ratios. We note that the decrease of the role of HI is very slow with increasing p, since it is linear in the slenderness parameter $\epsilon = 1/\log p$. We expect that for very slender particles there is no need to include the wall-particle HI to correctly estimate the first cumulant. On the other hand, this implies that the effect of HI is most pronounced for a spherical particle. In such a limit the hydrodynamic effects will determine the dynamics, as we investigated closely in the previous Chapter 7.

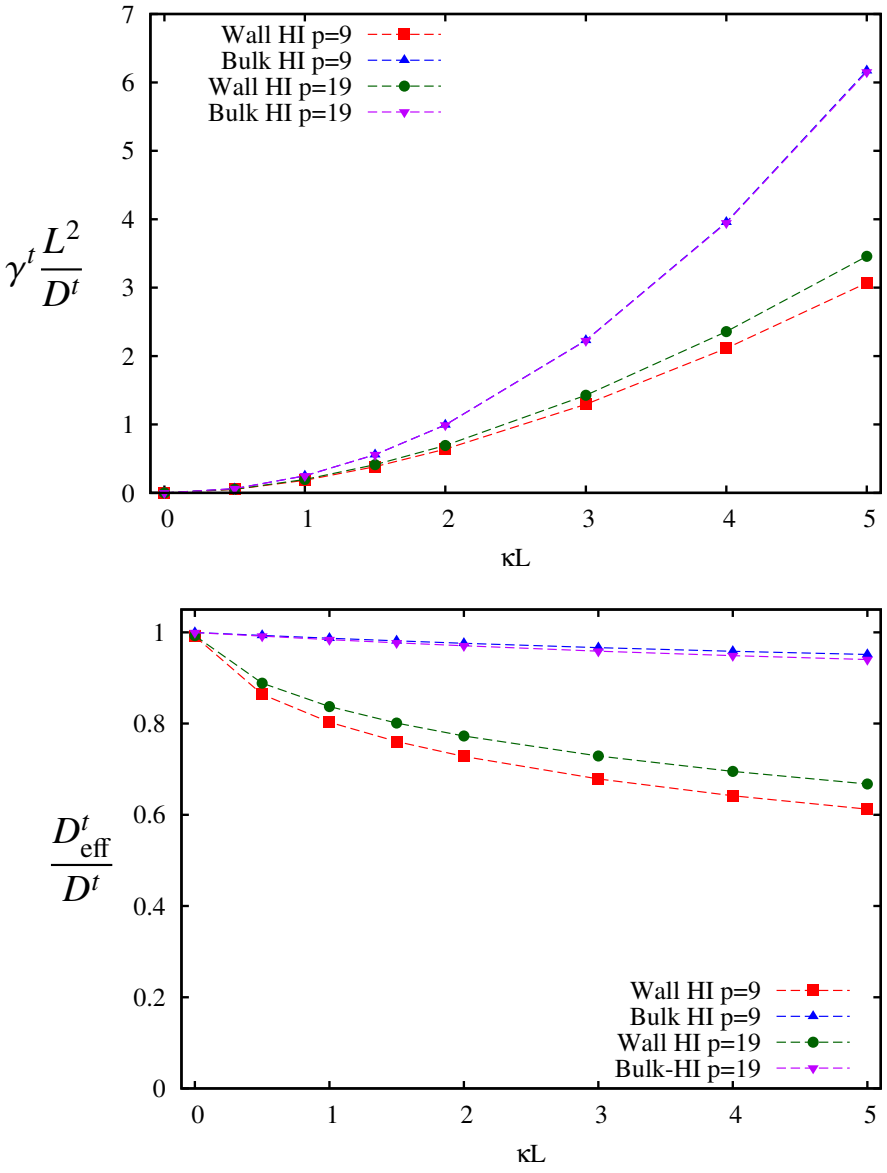

Figure 8.17: The intercept and slope of the translational cumulant for two chosen aspect ratios of the particle, $p = 9$, and a more elongated one with $p = 19$. With all other parameters kept fixed, we find that the more slender the particles are, the weaker is the effect of HI, in agreement with our earlier considerations on slender bodies dynamics. Thus we expect the bulk hydrodynamics model to be applicable for very thin particles. The bulk hydrodynamics results for both aspect ratios differ only slightly, because of their similar relative hydrodynamic anisotropy.

9 Conclusions and final remarks

The main purpose of this Thesis was to develop an appropriate theoretical description, which is necessary to interpret the results of evanescent wave dynamic light scattering (EWDLS) experiments. The interplay between near-wall hydrodynamic interactions, and the non-uniform illumination of the sample by an evanescent wave, render the understanding of experimentally measured quantities very involved. The time autocorrelation function of the scattered electric field (EACF) measured in experiments contains an averaged effect of the illumination and diffusive dynamics of the suspension. It is usually analysed in the short-time regime by means of its initial decay rate, called the first cumulant.

Our approach, basing on the generalised Smoluchowski equation, allowed us to construct general and explicit expressions for the first cumulant in terms of the form of the scattered electric field. The resulting expressions involve also the averaged hydrodynamic mobility tensors of the suspended particles. In a dilute regime, which is in focus of this work, the system is fully characterised by single-particle quantities only, and therefore the EACF contains information about the properties of an isolated particle and its Brownian motion in the presence of a boundary.

The aim of this research was to explore the effects of optical anisotropy of the particles in EWDLS measurements, in order to derive theoretical predictions for the short-time decay of EACF in given experimental conditions. The anisotropy may have two independent sources. Firstly, it may stem from an intrinsic birefringence of the particle and its internal composition, resulting in anisotropic polarisability of the particle. Secondly, it may result from the anisotropic shape of the particle which manifests itself both in its shape-dependent scattering properties, and in anisotropic hydrodynamic properties described by the particle mobility tensor. The combination of these two effects has been investigated in a number of light scattering studies in a bulk fluid, resulting in a general understanding of the DLS correlation functions for a variety of systems. The important difference brought by the EWDLS experiments is the use of a non-uniform illumination profile to explore only the near-wall effects in the dynamics of such particles. Moreover, the presence of a no-slip boundary dramatically influences the suspension hydrodynamics by hindering the motion of particles as they stay closer to the surface. The wall introduces also an additional anisotropy in the directions of motion along and perpendicular to the wall.

The first part of the work has been devoted to spherical colloids. In collaboration with an experimental group from Forschungszentrum Jülich in Germany, we have performed a combined theoretical and experimental EWDLS study of the dynamics of a suspension of spherical particles. In our works, we have proved the EWDLS technique to be capable of resolving the anisotropic translational, and rotational diffusion of spherical colloids confined by a planar hard

wall. For the investigation of the latter phenomenon, we have used optically anisotropic spherical particles characterised by an axisymmetric polarisability distribution. In result, we have derived and verified exact theoretical expressions for the first cumulant in both cases, and we were able to extract from the experiments the average translational and rotational diffusion coefficients in the directions parallel and perpendicular to the wall, as summarised in Chapter 7. The results of our investigations have been published in three research papers [88–90]. These works are results of a close collaboration between the group of J. Dhont at FZ Jülich, and the Author working with B. Cichocki at the University of Warsaw in Poland. The joint research papers comprise of theoretical predictions, juxtaposed tu numerical simulations, and an experimental verification. The measurements have been conducted and analysed by P. Lang, S. Rogers and J. Dhont, while the theoretical description and the numerical models have been developed by the Author under the kind supervision of B. Cichocki.

The second part of the Thesis contains a number of theoretical results concerning yet a more complex suspension of axisymmetric particles. This includes a broad range of model soft matter systems, elements of which possess a rod-like or a disc-like shape. The major difference to the previous case of spheres is the fact that the anisotropic (strictly: axisymmetric) hydrodynamic properties of the particle are now coupled to another anisotropy, brought in by the wall. In addition, the elongated shape introduces the shape effects to the scattered electric field, which are irrelevant for a highly symmetric spherical particle. To understand the structure of the measured EACF, we have analysed the aforementioned factors separately. We finally combined them in Chapter 8 by developing general expressions for the first cumulant for particles of prescribed axially symmetric shape and polarisability. The expressions have been analysed in the relevant limiting cases in terms of the difference to classic DLS experiments. In result of our work, we have devised numerical routines which allow for an easy and fast calculation of the first cumulant for given experimental conditions. The software accounts for the effects of shape by using the hydrodynamic multipole expansion method to calculate the mobility of bead-modelled particles close to a wall. Encoded are also the effects of shape on the scattered electric field. For a given set of experimental parameters, including the components of the scattering vector $q_{\parallel}$ and $q_{\perp}$, the penetration depth κ, the directions of polarisation of the incident and scattered beam, and the alignment of the set-up, our codes produce the values of the first cumulant which may be directly compared to experiments. The results of this investigations, apart from a convenient numerical toolbox for the calculation of Γ, is a set of practical approximations, which may be used to crudely estimate the expected outcome of the experiments. It follows from our observations, that the first cumulant may be considered to have only the translational and rotational contribution. In the investigated range of q and κ, it seems justified to approximate the translational part by a linear function of q^2, with the slope and intercept which may be reproduced using our software. In the range of low κ, simplified models of hydrodynamic interactions may be used for calculations. The rotational part was shown to be well represented in the experimentally relevant range of κ and q by a constant function, thus independent of the scattering vector. The value of this function may again be easily calculated in the VH geometry. In the case of depolarised scattering it may be neglected, so that the first cumulant will have only the translational part. A summary of our investigations will soon be sent for publication. It is to be hoped that relevant experiments will be performed in close future, thus allowing for an experimental verification. A successful comparison would open the way to explore the dynamics of more complex systems in geometric confinement by means of EWDLS.

An additional important result derived in the course of this work concerns the mobility of

axisymmetric particles in the presence of the wall. Analysing the influence of the wall on the dynamics of a single particle, in Chapter 5 we have derived analytic expressions for the asymptotic correction to the single-particle mobility tensor due to the presence of a nearby wall. For an axisymmetric particle of characteristic size L, staying at a distance H apart from the wall, we have developed a scattering series expansion which allowed us to find the correction terms to the bulk mobility tensor for its translational (tt), rotational (rr), and coupling components (tr and rt), valid up to the order $(L/H)^3$. By comparing with precise numerical results for rod-like particles, we have then demonstrated that even the dominant terms, which decay as L/H in the tt case, and as $(L/H)^3$ in the rr case, constitute a valid approximation for the particle mobility near a wall even up to $L \sim H$. Moreover, our results allowed us to extract the angular dependence of the correction to the bulk mobility tensor on the particle orientation (inclination) with respect to the wall. The approximate scheme using this correction has been shown to correctly reproduce the effect of hydrodynamic interactions for EWDLS predictions with a large penetration depth. However, using this scheme for close wall-particle distances may lead to unphysical results of negative near-wall mobility. Thus, in order to develop a full approximate scheme, the far-field correction has to be combined with the correct near-field lubrication behaviour of the mobility matrix elements. Construction of such a scheme requires a further analysis and is the topic of our current research.

A Friction tensor for a conglomerate of spheres

In Section 5.2.1, we stated that the single-particle friction (and thus mobility) matrix may be obtained from the general friction tensor $\boldsymbol{\zeta}_N$ for N spherical particles by an appropriate inclusion of the rigid body motion constraints [96, 184]. We shall now outline a procedure which allows to construct these quantities. Consider a complex particle represented by its bead model, i.e. a group of N spherical beads of radii a staying in a fixed relative configuration and thus mimicking the shape of the original particle of interest. The position of the conglomerate is defined by an arbitrary body-fixed reference point $\mathbf{R}_0$. Assume the particle to be in a general linear ambient flow $\mathbf{V}_0 + \boldsymbol{\Omega}_0 \times \mathbf{r} + \mathbf{E}_0 \cdot \mathbf{r}$. In result, force densities are induced on the spheres. The force moments from the individual beads sum up to the total force $\mathbf{F}_0$, torque $\mathbf{T}_0$, and symmetric dipole moment $\mathbf{S}_0$ via

$$\mathbf{F}_0 = \sum_i \mathbf{F}_i, \tag{A.1}$$

$$\mathbf{T}_0 = \sum_i \mathbf{T}_i + \sum_i \mathbf{R}_i \times \mathbf{F}_i, \tag{A.2}$$

$$\mathbf{S}_0 = \sum_i \mathbf{S}_i + \sum_i \overline{\mathbf{R}_i \mathbf{F}_i}, \tag{A.3}$$

where $\mathbf{R}_i$ denotes the position of the bead i with respect to the centre $\mathbf{R}_0$, and the bar denotes the symmetric and traceless part. This relation may be conveniently written down introducing the symmetric and antisymmetric tensors which act on an arbitrary vector $\mathbf{F}$ in the following way

$$\mathbf{L}_A(i) \cdot \mathbf{F} = \mathbf{R}_i \times \mathbf{F}, \tag{A.4}$$

$$\mathbf{L}_S(i) \cdot \mathbf{F} = \overline{\mathbf{R}_i \mathbf{F}}, \tag{A.5}$$

from which their matrix elements are read out as

$$L_A(i)_{\alpha\beta} = \epsilon_{\alpha\gamma\beta} R_{i,\gamma}, \tag{A.6}$$

$$L_S(i)_{\alpha\beta\gamma} = \frac{1}{2}(R_{i,\alpha}\delta_{\beta\gamma} + R_{i,\beta}\delta_{\alpha\gamma}) - \frac{1}{3} R_{i,\gamma}\delta_{\alpha\beta}. \tag{A.7}$$

We may now write the relations (A.1) in the form

$$\begin{pmatrix} \mathbf{F}_0 \\ \mathbf{T}_0 \\ \mathbf{S}_0 \end{pmatrix} = \mathbf{K} \cdot \begin{pmatrix} \boldsymbol{\mathcal{F}} \\ \boldsymbol{\mathcal{T}} \\ \boldsymbol{\mathcal{S}} \end{pmatrix}, \tag{A.8}$$

$\mathcal{F} = (\mathbf{F}_1, \ldots, \mathbf{F}_N)$, and $\mathcal{T} = (\mathbf{T}_1, \ldots, \mathbf{T}_N)$, $\mathcal{S} = ((\mathbf{R}_1\mathbf{F}_1)^S, \ldots, (\mathbf{R}_N\mathbf{F}_N)^S)$, and the $6N \times 6$ rectangular matrix $\mathbf{K}$ is read out explicitly from Eq. (A.1) as

$$\mathbf{K} = \begin{pmatrix} \mathbf{1} & \ldots & \mathbf{1} & \mathbf{0} & \ldots & \mathbf{0} & \mathbf{0} & \ldots & \mathbf{0} \\ \mathbf{L}_A(1) & \ldots & \mathbf{L}_A(N) & \mathbf{1} & \ldots & \mathbf{1} & \mathbf{0} & \ldots & \mathbf{0} \\ \mathbf{L}_S(1) & \ldots & \mathbf{L}_S(N) & \mathbf{0} & \ldots & \mathbf{0} & \mathbf{1} & \ldots & \mathbf{1} \end{pmatrix}. \tag{A.9}$$

Turning to the particle kinematics, the flow incident on the sphere i reads

$$\mathbf{V}_i = \mathbf{V}_0 + \boldsymbol{\Omega}_0 \times \mathbf{R}_i, \tag{A.10}$$

$$\boldsymbol{\Omega}_i = \boldsymbol{\Omega}_0, \tag{A.11}$$

$$\mathbf{E}_i = \mathbf{E}_0. \tag{A.12}$$

Taking into account that $\boldsymbol{\Omega}_0 \times \mathbf{R}_i = \mathbf{L}_A^{\mathrm{T}}(i)$ and $\mathbf{E}_0 \cdot \mathbf{R}_i = \mathbf{L}_S^{\mathrm{T}} : \mathbf{E}_0$, the relations between the total and individual velocities are also conveniently written as

$$\begin{pmatrix} \mathbf{V}^s \\ \boldsymbol{\Omega}^s \\ \mathbf{E}^s \end{pmatrix} = \mathbf{K}^{\mathrm{T}} \cdot \begin{pmatrix} \mathbf{V} \\ \boldsymbol{\Omega} \\ \mathbf{E} \end{pmatrix}, \tag{A.13}$$

where $\mathbf{V}^s = (\mathbf{V}_1, \ldots, \mathbf{V}_N)$, and $\boldsymbol{\Omega}^s = (\boldsymbol{\Omega}_1, \ldots, \boldsymbol{\Omega}_N)$, $\mathbf{E}^s = (\mathbf{E}_1, \ldots, \mathbf{E}_N)$. Combining Eqs. (A.8) and (A.13), we find that the friction matrix $\boldsymbol{\zeta}$ for the conglomerate moving like a rigid-body is given in terms of the many-particle friction tensor by

$$\boldsymbol{\zeta} = \mathbf{K} \cdot \boldsymbol{\zeta}_N \cdot \mathbf{K}^{\mathrm{T}}, \tag{A.14}$$

The mobility tensor of the conglomerate is then calculated by inverting the friction tensor $\boldsymbol{\zeta}$ in the t, r subspace.

In particular, for the 3×3 translational friction matrix, Eq. (5.21) yields

$$\boldsymbol{\zeta}_0^{tt} = \sum_{i,j=1}^{N} \boldsymbol{\zeta}_{ij}^{tt}. \tag{A.15}$$

B The wall correction to mobility: asymptotic results

In Chapter 5, we have presented the final expressions for the wall-corrected mobility matrix of an axisymmetric particle. Here we examine the derivation in more detail, emphasizing the technical side of the calculations. Instead of repeating the definitions of important quantitites, we stick to the notation from the preceding chapters.

In order to derive the correction, we proceed as follows. First, we look upon the scattering expansion of the grand resistance matrix for an arbitrarily-shaped particle. This leads to the approximate multipole form of the correction which involves the wall-particle propagator $\mathbf{G}_w$ and the bulk grand resistance matrix of the particle $\mathbf{Z}_b$. We then derive explicit expressions for the correction to all the parts of the friction matrix (tt, tr, rt, and rr) and examine their dependence on the wall-particle distance H. We then invert the corrected friction matrix to arrive at the corrected mobility matrix.

B.1 The scattering series

As stated in Chapter 5, and using the notation therein, the grand resistance matrix in Eq. (5.46) may be written as

$$\mathbf{Z} = \mathbf{Z}_0(\mathbf{1} + \mathbf{G}_0\mathbf{Z}_0 + \mathbf{G}_w\mathbf{Z}_0)^{-1}, \tag{B.1}$$

We wish to look for the asymptotic form of this matrix when the wall-particle distance is considerably larger than the particle itself, so we expect the wall contribution $\mathbf{G}_w\mathbf{Z}_0$ to be a small correction to $\mathbf{G}_0\mathbf{Z}_0$. Using the matrix identity

$$(\mathbf{1} + \mathbf{A})^{-1} - (\mathbf{1} + \mathbf{B})^{-1} = (\mathbf{1} + \mathbf{A})^{-1}(\mathbf{B} - \mathbf{A})(\mathbf{1} + \mathbf{B})^{-1}, \tag{B.2}$$

with $\mathbf{A} = \mathbf{G}_0\mathbf{Z}_0 + \mathbf{G}_w\mathbf{Z}_0$, and $\mathbf{B} = \mathbf{G}_0\mathbf{Z}_0$, we find the following exact relation

$$\mathbf{Z} = \mathbf{Z}_0\frac{1}{\mathbf{1} + \mathbf{G}_0\mathbf{Z}_0} - \mathbf{Z}_0\frac{1}{\mathbf{1} + \mathbf{G}_0\mathbf{Z}_0 + \mathbf{G}_w\mathbf{Z}_0}\mathbf{G}_w\mathbf{Z}_0\frac{1}{\mathbf{1} + \mathbf{G}_0\mathbf{Z}_0}. \tag{B.3}$$

In the case of large wall-particle distances, it is justified to expand fraction containing the wall contribution in the denominator of the latter expression, which yields the form of the correction to the bulk resistance matrix

$$\mathbf{\Delta} = \mathbf{Z} - \mathbf{Z}_b = -\mathbf{Z}_b\mathbf{G}_w\mathbf{Z}_b + \mathbf{Z}_b\mathbf{G}_w\mathbf{Z}_b\mathbf{G}_w\mathbf{Z}_b - \dots \tag{B.4}$$

with $\mathbf{Z}_b$ being short for the bulk resistance matrix $\mathbf{Z}_0(1 + \mathbf{G}_0\mathbf{Z}_0)^{-1}$. Thus we may express the leading-order correction to the bulk friction matrix of a particle in terms of the friction matrix itself and the propagator $\mathbf{G}_w = \mathbf{G}' \cdot \mathcal{R}$, which in this case describes the hydrodynamic interactions between pairs of spheres belonging to different conglomerates - the particle and its mirror image, as discussed in Chapter 5.

The dominant term in the correction is thus given by $\mathbf{\Delta} \approx -\mathbf{Z}_b\mathbf{G}_w\mathbf{Z}_b$. Further on, we evaluate this term for all the elements of the mobility matrix in the t, r subspace.

B.2 The derivation of the explicit form of the correction

For simplicity, we shall consider here only one submatrix of the friction matrix, say, tt. The procedure is analogous for all the other components. Having the multipole form of the correction $\mathbf{\Delta}$, we find the tt part of the friction matrix by projecting onto the tt (that is $l = 1, \sigma = 0$) subspace,

$$\mathbf{\Delta}^{tt} = \mathcal{P}^t \mathbf{\Delta} \mathcal{P}^t \tag{B.5}$$

where $\mathcal{P}^t$ is the relevant projection operator. Since now the single-particle friction matrix may be constructed from the many-particle matrix elements $\mathbf{\Delta}_{ij}$, as sketched in Sec. 5.2.4, we need to find the multipole elements of the correction matrix between the particles i and j, denoted by $\mathbf{\Delta}^{tt}_{ij} = \mathbf{\Delta}(i1m0, j1m'0)$. Using the Einstein's summation convention and Eq. (B.4), we may write

$$\mathbf{\Delta}^{tt}_{ij} \approx -Z_b(i1m0, pl_1m_1\sigma_1)G_w(pl_1m_1\sigma_1, ql_2m_2\sigma_2)Z_b(ql_2m_2\sigma_2, j1m'0). \tag{B.6}$$

The propagator of interactions between the particle p and the image of particle q (denoted by q^*) explicitly depends on the distance between the two, $\mathbf{R}_{pq^*}$. We now turn to the wall-particle propagator $\mathbf{G}_w = \mathbf{G}' \cdot \mathcal{R}$. Its multipole matrix elements for interacting particles p and q read

$$G_w(plm\sigma, ql'm'\sigma') = G'(\mathbf{R}_{ps^*}; plm\sigma, sl_1m_1\sigma_1)\mathcal{R}(h_q; sl_1m_1\sigma_1, ql'm'\sigma'), \tag{B.7}$$

where $h_q = \hat{\mathbf{e}}_z \cdot \mathbf{R}_q$, and the two factors on the right-hand-side have the explicit form

$$G'(\mathbf{R}_{ps^*}; plm\sigma, sl_1m_1\sigma_1) = \frac{n_{lm}}{\eta n_{l_1m_1}} S^{+-}(\mathbf{R}_p - \mathbf{R}^*_s; lm\sigma, l_1m_1\sigma_1), \tag{B.8}$$

$$\mathcal{R}(h_q; sl_1m_1\sigma_1, ql'm'\sigma') = \delta_{sq}\tilde{\mathcal{R}}(h_q; l_1m_1\sigma_1, l'm'\sigma'). \tag{B.9}$$

The asterisk here denotes again the mirror image of the particle in question, e.g. $\mathbf{R}^*_s$ is the position of the mirror image of particle s. The function S^{+-}, defined in Ref. [185], decays with the distance $R = |\mathbf{R}_p - \mathbf{R}^*_s|$ as $1/R^{l+l_1+\sigma+\sigma_1-1}$. The operator $\tilde{\mathcal{R}}$ accounts for the change of the flow multipolar character due to a reflection off the wall. It is diagonal in m, m' and has non-vanishing terms only for $l_1 - 2 \leq l' \leq l_1 + 2$. Moreover, it depends on the distance of particle q from the wall, $h = \mathbf{R}_q \cdot \hat{\mathbf{e}}_z$. Explicit expressions the matrix elements of $\mathcal{R}$ are given in Refs. [118, 186], together with the normalisation factors n_{lm}.

By a careful analysis of the wall-distance dependence of $\mathbf{G}'$ we were able to identify the slowest decaying terms, which die out asymptotically as $1/R$, with $R = |\mathbf{R}_p - \mathbf{R}^*_q|$. All these terms are incorporated in $G_w(p1m0, q1m'0)$, which means that in leading order (for the tt contribution) one may analyse the correction in the form

$$\mathbf{\Delta}^{tt}(i1m0, j1m'0) \approx -Z_b(i1m0, p1m_10)G_w(p1m_10, q1m_20)Z_b(q1m_20, j1m'0). \tag{B.10}$$

Now, the positions of the particles within the conglomerate may be written as $\mathbf{R}_i = \mathbf{R}_0 + \mathbf{r}_i$, $i = 1, \ldots, N$ and analogously for the mirror image conglomerate. Moreover, the conglomerate is at a distance $H = \mathbf{R}_0 \cdot \hat{\mathbf{e}}_z$ from the wall. As we argued in Sec. 5.5.3, and shown in Fig. 5.3, we may expand this distance between two particles belonging to different conglomerates around the vertical vector connecting the centre of the particle with the centre of its image.

In the leading order, having in mind that the particles p and q within the conglomerate are close together compared to p and p^*, that is $|\mathbf{r}_p - \mathbf{r}_q| \ll H$, the interparticle distances R and h in Eq. (B.8) are approximately given by:

$$\mathbf{R}_{pq^*} \approx 2H\hat{\mathbf{n}}, \qquad h = \hat{\mathbf{e}}_z \cdot \mathbf{R}_p \approx H, \tag{B.11}$$

for every pair of particles (see Fig. 5.3). Thus, in leading order we have the propagator $\mathbf{G}_w(\mathbf{R} = 2H\hat{\mathbf{n}})$. We may then recast Eq. (B.10) writing the sum over particle labels explicitly as

$$\mathbf{\Delta}(i1m0, j1m'0) \approx -\sum_{p,q} Z_b(i1m0, p1m_10) G_w(1m_10, 1m_20) Z_b(q1m_20, j1m'0), \tag{B.12}$$

with the propagator matrix elements calculated between the centres of the particle and its mirror image. The correction $\mathbf{\Delta}^{tt} = \mathbf{\Delta}(1m0, 1m'0) = \sum_{i,j} \mathbf{\Delta}(i1m0, j1m'0)$ may now be expressed using the grand friction matrices of the conglomerate $Z_b(lm\sigma, l'm'\sigma') = \sum_{i,p} Z_b(ilm\sigma, pl'm'\sigma')$ as

$$\mathbf{\Delta}(1m0, 1m'0) = -Z_b(1m0, 1m_10) G_w(1m_10, 1m_20) Z_b(1m_20, 1m'0). \tag{B.13}$$

Moreover, the matrix elements $Z_b(1m_20, 1m'0)$ correspond to components of the bulk friction matrix $\boldsymbol{\zeta}^{tt}(m, m')$ for a bead-model of a particle. Denoting $[G_w^{tt}]_{m,m'} = G_w(1m0, 1m'0)$, as we will justify below, we have a simple matrix relation for the correction

$$\mathbf{\Delta} = -\boldsymbol{\zeta}^{tt} \cdot \mathbf{G}_w^{tt} \cdot \boldsymbol{\zeta}^{tt}. \tag{B.14}$$

In this way, explicit expressions for the correction may be obtained for other low multipoles (t, r, d).

B.3 The propagator

It should be noted here that in the above derivation the propagator $\mathbf{G}_w$ is calculated between the position of the conglomerate center $\mathbf{R}_0$ and its mirror image at $\mathbf{R}_0^*$. These two points may be connected by the vector $2H\hat{\mathbf{n}}$, so they lie at the axis normal to the wall. This fact has important implications for the symmetry of the propagator $\mathbf{G}_w(\mathbf{R} = 2H\hat{\mathbf{n}})$, which in this case becomes axisymmetric.

For the needs of further calculations, we will need all the propagators connecting the lowest-order multipoles. Since the propagators have axial symmetry around $\hat{\mathbf{n}} = \hat{\mathbf{e}}_z$, they have the form analogous to the bulk mobility matrix from Eq. (5.48) [9, 116], with a different axial vector.

Using the technique described in the preceding Section, we were able to find the propagator multipole matrix elements $(lm\sigma|\, \widehat{G}(\mathbf{R} = 2H\hat{\mathbf{n}})\, |l'm'\sigma')$ in this particular case as functions of the wall-particle distance H

$$\mathbf{G}_w^{ab} = \frac{1}{8\pi\eta} \left(\frac{1}{2H}\right)^{l+l'+\sigma+\sigma'-1} \mathbf{g}^{ab}, \tag{B.15}$$

with a being short for $(lm\sigma)$ and b standing for $(l'm'\sigma')$, and the directional tensors $\mathbf{g} = \mathbf{g}(\hat{\mathbf{n}})$ depending only on the direction normal to the wall. For lowest-order multipoles, $a, b \in \{t, r, d\}$, as we introduced in Eq. (5.47). For example, we have

$$\mathbf{G}_w^{td} = \frac{1}{8\pi\eta}\frac{1}{(2H)^2}\mathbf{g}^{td}. \tag{B.16}$$

The directional tensors are given by

$$\begin{aligned}
g^{tt}_{\alpha\beta} &= -\frac{3}{2}n_\alpha n_\beta - \frac{3}{4}(\delta_{\alpha\beta} - n_\alpha n_\beta), \\
g^{rr}_{\alpha\beta} &= -n_\alpha n_\beta - \frac{5}{2}(\delta_{\alpha\beta} - n_\alpha n_\beta), \\
g^{tr}_{\alpha\beta} &= g^{rt}_{\alpha\beta} = 0, \\
g^{td}_{\alpha\beta\gamma} &= \frac{9}{2}n_\alpha \overline{n_\beta n_\gamma}^{(\beta\gamma)} + 3\overline{(\delta_{\alpha\beta} - n_\alpha n_\beta)n_\gamma}^{(\beta\gamma)}, \\
g^{rd}_{\alpha\beta\gamma} &= -3n_\sigma \overline{\epsilon_{\sigma\alpha\beta}n_\gamma}^{(\beta\gamma)}, \\
g^{dt}_{\alpha\beta\gamma} &= g^{td}_{\gamma\alpha\beta} = \frac{9}{2}\overline{n_\alpha n_\beta}^{(\alpha\beta)} n_\gamma + 3\overline{n_\alpha(\delta_{\beta\gamma} - n_\beta n_\gamma)}^{(\alpha\beta)}, \\
g^{dr}_{\alpha\beta\gamma} &= -g^{rd}_{\gamma\beta\alpha} = 3\overline{n_\alpha \epsilon_{\beta\gamma\sigma}}^{(\alpha\beta)} n_\sigma, \\
g^{dd}_{\alpha\beta\gamma\nu} &= -18\overline{n_\alpha n_\beta}^{(\alpha\beta)}\overline{n_\gamma n_\nu}^{(\gamma\nu)} - 18\left[\overline{\delta_{\alpha\gamma}n_\beta n_\nu}^{(\alpha\beta)(\gamma\nu)} - \overline{n_\alpha n_\beta}^{(\alpha\beta)}\overline{n_\gamma n_\nu}^{(\gamma\nu)}\right] \\
&\quad -3\left[\overline{\delta_{\alpha\gamma}\delta_{\beta\nu}}^{(\alpha\beta)(\gamma\nu)} - 2\overline{\delta_{\alpha\gamma}n_\beta n_\nu}^{(\alpha\beta)(\gamma\nu)} + \frac{1}{2}\overline{n_\alpha n_\beta}^{(\alpha\beta)}\overline{n_\gamma n_\nu}^{(\gamma\nu)}\right].
\end{aligned} \tag{B.17}$$

The appropriate reductions were already defined in Sec. 5.4. For this calculation, the expressions (B.8) and (B.9), given in full in Ref. [118] have been evaluated in MATHEMATICA using the explicit form of the multipole functions S^{+-} from Ref. [185]. The result has then been converted from the complex spherical basis of Ref. [116] to the Cartesian basis using the technique described in Refs. [96, 187].

B.3.1 The wall-corrected friction tensor

It follows from symmetry properties that the bulk friction matrix of a general axisymmetric particle has the form analogous to that in Eq. (5.52), explicitly

$$\zeta = \begin{pmatrix} \zeta^{tt} & 0 & \zeta^{td} \\ 0 & \zeta^{rr} & \zeta^{rd} \\ \zeta^{dt} & \zeta^{dr} & \zeta^{dd} \end{pmatrix} \tag{B.18}$$

with no tr elements. In the presence of a wall, the friction matrix reads $\boldsymbol{\zeta}_w = \boldsymbol{\zeta} + \boldsymbol{\Delta\zeta}_w$. The t, r elements of the correction are given by

$$\boldsymbol{\Delta\zeta}_w^{tt} = -\frac{1}{8\pi\eta}\frac{1}{2H}\boldsymbol{\zeta}^{tt}\mathbf{g}^{tt}\boldsymbol{\zeta}^{tt} + O(H^{-2}), \tag{B.19}$$

$$\boldsymbol{\Delta\zeta}_w^{tr} = -\frac{1}{8\pi\eta}\frac{1}{(2H)^2}(\boldsymbol{\zeta}^{tt}\mathbf{g}^{tr}\boldsymbol{\zeta}^{rr} + \boldsymbol{\zeta}^{tt}\mathbf{g}^{td}\boldsymbol{\zeta}^{dr}) + O(H^{-3}), \tag{B.20}$$

$$\boldsymbol{\Delta\zeta}_w^{rt} = -\frac{1}{8\pi\eta}\frac{1}{(2H)^2}(\boldsymbol{\zeta}^{rr}\mathbf{g}^{rt}\boldsymbol{\zeta}^{tt} + \boldsymbol{\zeta}^{rd}\mathbf{g}^{dt}\boldsymbol{\zeta}^{tt}) + O(H^{-3}), \tag{B.21}$$

$$\boldsymbol{\Delta\zeta}_w^{rr} = -\frac{1}{8\pi\eta}\frac{1}{(2H)^3}(\boldsymbol{\zeta}^{rr}\mathbf{g}^{rr}\boldsymbol{\zeta}^{rr} + \boldsymbol{\zeta}^{rr}\mathbf{g}^{rd}\boldsymbol{\zeta}^{dr} + \boldsymbol{\zeta}^{rd}\mathbf{g}^{dr}\boldsymbol{\zeta}^{rr} + \boldsymbol{\zeta}^{rd}\mathbf{g}^{dd}\boldsymbol{\zeta}^{dr}) + O(H^{-4}), \tag{B.22}$$

Using the relations (B.19)-(B.22), together with Eqs. (5.12) and (5.13), we finally find the leading-order terms in the mobility tensors $\boldsymbol{\mu}_w = \boldsymbol{\mu} + \boldsymbol{\Delta\mu}_w$ with the correction

$$\boldsymbol{\Delta\mu}_w^{tt} = \frac{1}{8\pi\eta}\frac{1}{2H}\mathbf{g}^{tt} + O(H^{-2}), \tag{B.23}$$

$$\boldsymbol{\Delta\mu}_w^{tr} = -\frac{1}{8\pi\eta}\frac{1}{(2H)^2}\mathbf{g}^{td}\boldsymbol{\mu}^{dr} + O(H^{-3}), \tag{B.24}$$

$$\boldsymbol{\Delta\mu}_w^{rt} = [\boldsymbol{\Delta\mu}^{tr}]^T = \frac{1}{8\pi\eta}\frac{1}{(2H)^2}\boldsymbol{\mu}^{rd}\mathbf{g}^{dt} + O(H^{-3}), \tag{B.25}$$

$$\boldsymbol{\Delta\mu}_w^{rr} = \frac{1}{8\pi\eta}\frac{1}{(2H)^3}(\mathbf{g}^{rr} - \mathbf{g}^{rd}\boldsymbol{\mu}^{dr} + \boldsymbol{\mu}^{rd}\mathbf{g}^{dr} - \boldsymbol{\mu}^{rd}\mathbf{g}^{dd}\boldsymbol{\mu}^{dr} + O(H^{-4}). \tag{B.26}$$

For the evaluation of the explicit form of the correction, we exploit the axial symmetry of the mobility tensor of the particle about the direction of $\hat{\mathbf{u}}$, and the axial symmetry of the propagator about $\hat{\mathbf{e}}_z$. The corresponding expressions in leading order read in the RW (body-fixed) frame are given in Eqs. (5.77) for the tt part, and (5.78) for the rr part. The remaining tr contribution, although very small, may be written for completeness as

$$\boldsymbol{\Delta\mu}^{tr} = -\frac{1}{8\pi\eta}\frac{1}{(2H)^2}\frac{3\mu^{dr}}{2}\begin{pmatrix} 0 & (1+\cos^2\theta)\sin\theta & 0 \\ 0 & 0 & \cos\theta \\ 0 & -(1+\sin^2\theta)\cos\theta & 0 \end{pmatrix}, \tag{B.27}$$

$$\boldsymbol{\Delta\mu}^{rt} = \left[\boldsymbol{\Delta\mu}^{tr}\right]^T. \tag{B.28}$$

We note that the wall-corrected mobility matrix constructed as $\boldsymbol{\mu} + \boldsymbol{\Delta\mu}_w$ possesses all the required symmetries outlined in Sec. 5.2.2.

Bibliography

[1] P. G. de Gennes, Soft Matter **1**, 16 (2005).

[2] M. Doi, *Soft Matter Physics*, Oxford Univ. Press, 2013.

[3] M. Smoluchowski, Ann. Phys. **21**, 755 (1906).

[4] A. Einstein, Ann. Phys. **17**, 549 (1905).

[5] A. Einstein, Ann. Phys. **19**, 371 (1905).

[6] R. Mazo, *Brownian Motion: Fluctuations, Dynamics, and Applications*, Oxford Univ. Press, 2002.

[7] P. N. Pusey, Colloidal Suspensions, in *Liquids, Freezing and Glass Transition*, edited by J. P. Hansen, D. Levesque, and J. Zinn-Justin, page 763, Elsevier, Amsterdam, 1991.

[8] R. B. Jones and P. N. Pusey, Annu. Rev. Phys. Chem. **42**, 137 (1991).

[9] S. Kim and S. J. Karrila, *Microhydrodynamics: Principles and Selected Applications*, Butterworth-Heinemann, Boston, 1991.

[10] J. K. G. Dhont, *An Introduction to Dynamics of Colloids*, Studies in Interface Science, Elsevier, 1996.

[11] R. G. Larson and J. J. Magda, Macromolecules **22**, 3004 (1989).

[12] O. B. Usta, J. E. Butler, and A. J. C. Ladd, Phys. Fluids **18**, 031703 (2006).

[13] H. Tanaka, J. Phys. Condens. Matter **13**, 4637 (2001).

[14] P. Wojtaszczyk and J. B. Avalos, Phys. Rev. Lett. **80**, 754 (1998).

[15] P. Szymczak and M. Cieplak, J. Physics. Condens. Matter. **23**, 033102 (2011).

[16] E. S. G. Shaqfeh, J. Nonnewton. Fluid Mech. **130**, 1 (2005).

[17] G. Nägele, Phys. Rep. **272**, 215 (1996).

[18] G. G. Stokes, Trans. Cambridge Philos. Soc. **9**, 8 (1851).

[19] Z. Adamczyk, *Particles at Interfaces, Interactions, Deposition, Structure*, Academic Press, 1998.

[20] K. C. Khilar and H. S. Fogler, *Migration of Fines in Porous Media*, Kluwer Academic Publishers, 2006.

[21] W. Norde and J. Lyklema, Colloids and Surfaces **38**, 1 (1989), 6th International Conference on Surface and Colloid Science.

[22] J. W. Costerton, Z. Lewandowski, D. E. Caldwell, D. R. Korber, and H. M. Lappin-Scott, Ann. Rev. Microbiol. **49**, 711 (1995), PMID: 8561477.

[23] I. H. Riedel, K. Kruse, and J. Howard, Science **309**, 300 (2005).

[24] E. Lauga and T. R. Powers, Rep. Prog. Phys. **72**, 096601 (2009).

[25] C. W. J. Beenakker and P. Mazur, Phys. Fluids **28**, 767 (1985).

[26] D. Leighton and A. Acrivos, Chem. Eng. Sci **41**, 1377 (1986).

[27] D. Leighton and A. Acrivos, J. Fluid Mech. **177**, 109 (1987).

[28] D. Leighton and A. Acrivos, J. Fluid Mech. **181**, 415 (1987).

[29] T. M. Squires and S. Quake, Rev. Mod. Phys. **77**, 977 (2005).

[30] C. Rice and R. Whitehead, J. Phys. Chem. **69**, 4017 (1965).

[31] D. Psaltis, S. R. Quake, and C. Yang, Nature **442**, 381 (2006).

[32] T. Sawetzki, S. Rahmouni, C. Bechinger, and D. W. M. Marr, Proc. Natl. Acad. Sci. USA **105**, 20141 (2008).

[33] C. Effenhauser, G. Bruin, and A. Paulus, Electrophoresis **18**, 2203 (1997).

[34] R. Carlson, C. Gabel, S. Chan, and R. Austin, Biomed. Microdevices **1**, 39 (1998).

[35] N. G. Van Kampen, *Stochastic Processes in Physics and Chemistry*, Elsevier, 3rd edition, 2001.

[36] H. A. Lorentz, *Abhandlung über Theoretische Physik*, B. G. Teubner, Leipzig und Berlin, 1907.

[37] H. Faxén, Ark. Mat. Astron. Fys. **17**, 1 (1923).

[38] J. Happel and H. Brenner, *Low Reynolds Numbers Hydrodynamics*, Kluwer, Dordrecht, 1991.

[39] H. Brenner, Chem. Eng. Sci. **16**, 242 (1961).

[40] A. J. Goldman, R. G. Cox, and H. Brenner, Chem. Eng. Sci. **22**, 637 (1967).

[41] A. J. Goldman, R. G. Cox, and H. Brenner, Chem. Eng. Sci. **22**, 653 (1967).

[42] W. Dean and M. O'Neill, Mathematika **10**, 13 (1963).

[43] W. Dean and M. O'Neill, Mathematika **11**, 67 (1964).

[44] G. S. Perkins and R. B. Jones, Physica A **171**, 575 (1991).

[45] G. S. Perkins and R. B. Jones, Physica A **189**, 447 (1992).

[46] B. Cichocki and R. B. Jones, Physica A **258**, 273 (1998).

[47] A. Banerjee and K. Kihm, Phys. Rev. E **72**, 042101 (2005).

[48] K. D. Kihm, A. Banerjee, C. K. Choi, and T. Takagi, Exp. Fluids **37**, 811 (2004).

[49] D. C. Prieve, F. Lanni, and F. Luo, Faraday Discuss. Chem. Soc. **83**, 297 (1987).

[50] D. C. Prieve, Adv. Coll. Interf. Sci. **82**, 93 (1999).

[51] J. Y. Walz and L. Suresh, J. Chem. Phys. **103** (1995).

[52] B. Lin, J. Yu, and S. Rice, Phys. Rev. E **62**, 3909 (2000).

[53] L. Joly, C. Ybert, and L. Bocquet, Phys. Rev. Lett. **96**, 046101 (2006).

[54] M. D. Carbajal-Tinoco, R. Lopez-Fernandez, and J. L. Arauz-Lara, Phys. Rev. Lett. **99**, 138303 (2007).

[55] P. P. Lele, J. W. Swan, J. F. Brady, N. J. Wagner, and E. M. Furst, Soft Matter **7**, 6844 (2011).

[56] R. Sadr, C. Hohenegger, H. Li, P. J. Mucha, and M. Yoda, J. Fluid Mech. **577**, 443 (2007).

[57] P. Huang and K. Breuer, Phys. Rev. E **76**, 046307 (2007).

[58] L. Lobry and N. Ostrowsky, Phys. Rev. B **53**, 12050 (1996).

[59] K. Ishii, T. Iwai, and H. Xia, Opt. Express **18**, 7390 (2010).

[60] M. A. Plum, W. Steffen, G. Fytas, W. Knoll, and B. Menges, Opt. Express **17**, 10364 (2009).

[61] M. A. Plum, J. Rička, H.-J. Butt, and W. Steffen, New J. Phys. **12**, 103022 (2010).

[62] M. Haghighi, M. N. Tahir, W. Tremel, H.-J. Butt, and W. Steffen, J. Chem. Phys. **139**, 064710 (2013).

[63] P. Holmqvist, J. K. G. Dhont, and P. R. Lang, Phys. Rev. E **74**, 021402 (2006).

[64] P. Holmqvist, J. K. G. Dhont, and P. R. Lang, J. Chem. Phys. **126**, 044707 (2007).

[65] R. Sigel, Curr. Op. Coll. Interf. Sci. **14**, 426 (2009).

[66] K. H. Lan, N. Ostrowsky, and D. Sornette, Phys. Rev. Lett. **57**, 17 (1986).

[67] N. Garnier and N. Ostrowsky, J. Phys. II France **1**, 1221 (1991).

[68] N. Ostrowsky and N. Garnier, Progr. Colloid Polym. Sci. **84**, 371 (1991).

[69] N. Ostrowsky and L. Lobry, Il Nuovo Cimento D **16**, 1111 (1994).

[70] M. I. M. Feitosa and O. N. Mesquita, Phys. Rev. A **44**, 6677 (1991).

[71] H. Matsuoka et al., J. Colloid Polym. Sci. **276**, 349 (1998).

[72] B. Cichocki, E. Wajnryb, J. Bławzdziewicz, J. K. G. Dhont, and P. R. Lang, J. Chem. Phys. **132**, 074704 (2010).

[73] J. W. Swan and J. F. Brady, J. Chem. Phys. **135**, 014701 (2011).

[74] V. N. Michailidou, G. Petekidis, J. W. Swan, and J. F. Brady, Phys. Rev. Lett. **102**, 068302 (2009).

[75] V. N. Michailidou, J. W. Swan, J. F. Brady, and G. Petekidis, J. Chem. Phys. **139**, 164905 (2013).

[76] B. Loppinet, J. K. G. Dhont, and P. R. Lang, Eur. Phys. J. E **35**, 62 (2012).

[77] Z. Li et al., J. Fluid Mech. **766**, 147 (2015).

[78] B. Loppinet, G. Petekidis, and G. Fytas, Langmuir **14**, 4958 (1998).

[79] G. Fytas et al., Science **274**, 2041 (1998).

[80] G. E. Yakubov et al., Phys. Rev. Lett. **92**, 115501 (2004).

[81] P. Holmqvist, D. Kleshchanok, and P. R. Lang, Langmuir **23**, 12010 (2007).

[82] Z. Cheng and T. G. Mason, Phys. Rev. Lett. **90**, 018304 (2003).

[83] R. Cherry, A. Bürkli, M. Busslinger, and G. Schneider, Nature **263**, 389 (1976).

[84] R. A. Cone, Nat. New Biol. **236**, 39 (1972).

[85] M. Eigen and G. G. Hammes, in *Advances in Enzymology and Related Subjects of Biochemistry*, edited by F. F. Ford, page 1, John Wiley & Sons, Hoboken, NJ, Vol. 25, 1963.

[86] K. Solc and W. H. Stockmayer, J. Chem. Phys. **54**, 2981 (1971).

[87] R. J. Hall and D. A. Greenhalgh, Opt. Commun. **40**, 417 (1982).

[88] M. Lisicki, B. Cichocki, J. K. G. Dhont, and P. R. Lang, J. Chem. Phys. **136**, 204704 (2012).

[89] S. A. Rogers, M. Lisicki, B. Cichocki, J. K. G. Dhont, and P. R. Lang, Phys. Rev. Lett. **109**, 098305 (2012).

[90] M. Lisicki, B. Cichocki, S. Rogers, J. K. G. Dhont, and P. R. Lang, Soft Matter **10**, 4312 (2014).

[91] R. B. Jones and R. Schmitz, Physica A **149**, 373 (1988).

[92] V. Degiorgio, R. Piazza, and T. Bellini, Adv. Colloid Interface Sci. **48**, 61 (1994).

[93] R. Piazza et al., Prog. Colloid Polym. Sci. **81**, 89 (1990).

[94] V. Degiorgio, R. Piazza, and R. B. Jones, Phys. Rev. E **52**, 2707 (1995).

[95] R. B. Jones, J. Chem. Phys. **123**, 164705 (2005).

[96] M. L. Ekiel-Jeżewska and E. Wajnryb, Precise Multipole Method for Calculating Hydrodynamic Interactions Between Spherical Particles in the Stokes Flow, in *Theoretical Methods for Micro Scale Viscous Flows*, edited by F. Feuillebois and A. Sellier, pages 127–172, 2009.

[97] M. De Corato, F. Greco, G. D'Avino, and P. L. Maffettone, J. Chem. Phys. **142**, 194901 (2015).

[98] J. T. Padding and W. J. Briels, J. Chem. Phys. **132**, 054511 (2010).

[99] W. B. Russel, E. J. Hinch, L. G. Leal, and G. Tieffenbruck, J. Fluid Mech. **83**, 273 (1977).

[100] N. J. De Mestre and W. B. Russel, J. Eng. Math. **9**, 81 (1975).

[101] B. J. Berne and R. Pecora, *Dynamic Light Scattering: With Applications to Chemistry, Biology, and Physics*, Dover Books on Physics Series, Dover Publications, 2000.

[102] H. van de Hulst, *Light Scattering by Small Particles*, Dover Books on Physics Series, Dover Publications, 1957.

[103] J. D. Jackson, *Classical electrodynamics*, Wiley, New York, NY, 3rd edition, 1999.

[104] L. D. Landau and E. M. Lifshitz, *Electrodynamics of Continuous Media*, Course of Theoretical Physics, Pergamon Press, 1987.

[105] J. Venermo and A. Sihvola, J. Electrostat. **63**, 101 (2005).

[106] A. Sihvola, J. Nanomater. **2007**, 1 (2007).

[107] B. Cichocki and B. U. Felderhof, J. Chem. Phys. **90**, 4960 (1989).

[108] H.-Y. Kim, J. Sofo, D. Velegol, M. Cole, and G. Mukhopadhyay, Phys. Rev. A **72**, 053201 (2005).

[109] B. W. Kwaadgras, M. Verdult, M. Dijkstra, and R. van Roij, J. Chem. Phys. **135**, 134105 (2011).

[110] B. W. Kwaadgras, M. Dijkstra, and R. van Roij, J. Chem. Phys. **136**, 131102 (2012).

[111] K. H. Lan, N. Ostrowsky, and D. Sornette, New Trends Colloid Sci. **185** (1987).

[112] M. Abramowitz and I. A. Stegun, *Handbook of mathematical functions*, Dover, 1972.

[113] G. Nägele, Colloidal hydrodynamics, in *Proceedings of the International School of Physics 'Enrico Fermi'*, edited by C. Bechinger, F. Sciortino, and P. Ziherl, IOS, Amsterdam; SIF, Bologna., 2013.

[114] R. Kubo, Rep. Prog. Phys. **29**, 255 (1966).

[115] B. U. Felderhof, Physica A **151**, 1 (1988).

[116] B. Cichocki, B. U. Felderhof, and R. Schmitz, Physicochem. Hydrodyn. **10**, 383 (1988).

[117] B. Cichocki, B. U. Felderhof, K. Hinsen, E. Wajnryb, and J. Bławzdziewicz, J. Chem. Phys. **100**, 3780 (1994).

[118] B. Cichocki, R. B. Jones, R. Kutteh, and E. Wajnryb, J. Chem. Phys. **112**, 2548 (2000).

[119] G. K. Batchelor, *An Introduction to Fluid Dynamics*, Cambridge Mathematical Library, Cambridge University Press, 2000.

[120] E. M. Purcell, Am. J. Phys. **45**, 3 (1977).

[121] J. F. Brady and G. Bossis, Annu. Rev. Fluid Mech. **20**, 111 (1988).

[122] D. L. Ermak and J. A. McCammon, J. Chem. Phys. **69**, 1352 (1978).

[123] G. Nägele, Brownian Dynamics simulations, in *Computational Condensed Matter Physics*, volume 32, Forschungszentrum Jülich Publishing, 37th IFF Spring School edition, 2006.

[124] B. Cichocki, M. L. Ekiel-Jeżewska, and E. Wajnryb, J. Chem. Phys. **140**, 164902 (2014).

[125] B. Cichocki, M. L. Ekiel-Jeżewska, and E. Wajnryb, J. Chem. Phys. **136**, 071102 (2012).

[126] M. Makino and M. Doi, J. Phys. Soc. Japan **73**, 2739 (2004).

[127] M. L. Ekiel-Jeżewska and E. Wajnryb, Phys. Rev. E **83**, 067301 (2011).

[128] D. Bedeaux and P. Mazur, Physica A **78**, 505 (1974).

[129] R. Jones and R. Schmitz, Physica A **149**, 373 (1988).

[130] M. Lisicki, ArXiv: 1312.6231 (2013).

[131] J. R. Blake, Proc. Camb. Phil. Soc. **70**, 303 (1971).

[132] D. Lopez and E. Lauga, Phys. Fluids **26**, 071902 (2014).

[133] R. Schmitz and B. U. Felderhof, Physica A **92**, 423 (1978).

[134] H. Lamb, *Hydrodynamics*, Cambridge Univ. Press, 1916.

[135] R. Schmitz and B. U. Felderhof, Physica A **113**, 90 (1982).

[136] R. Schmitz and B. U. Felderhof, Physica A **113**, 103 (1982).

[137] V. Devanathan, *Angular Momentum Techniques in Quantum Mechanics*, Kluwer, 2002.

[138] B. Cichocki, M. L. Ekiel-Jeżewska, and E. Wajnryb, J. Chem. Phys. **111**, 3265 (1999).

[139] L. Durlofsky, J. F. Brady, and G. Bossis, J. Fluid Mech. **180**, 21 (1987).

[140] J. Rotne and S. Prager, J. Chem. Phys. **50**, 4831 (1969).

[141] G. Bossis, A. Meunier, and J. D. Sherwood, Phys. Fluids **3** (1991).

[142] R. M. Jendrejack, D. C. Schwartz, J. J. de Pablo, and M. D. Graham, J. Chem. Phys. **120** (2004).

[143] J. W. Swan and J. F. Brady, Phys. Fluids **19**, 113306 (2007).

[144] E. Wajnryb and J. S. Dahler, The Newtonian viscosity of a moderately dense suspension, in *Advances in Chemical Physics*, edited by I. Prigogine and S. A. Rice, volume 102, pages 193–313, J Wiley & Sons, 1997.

[145] G. K. Batchelor, J. Fluid Mech. **44**, 419 (1970).

[146] J. B. Keller and S. I. Rubinow, J. Fluid Mech. **75**, 705 (1976).

[147] R. E. Johnson, J. Fluid Mech. **99**, 411 (1980).

[148] W. H. Mitchell and S. E. Spagnolie, J. Fluid. Mech. **772**, 600 (2015).

[149] J. Riseman and J. G. Kirkwood, J. Chem. Phys. **18**, 512 (1950).

[150] J. Antosiewicz and D. Porschke, J. Phys. Chem. **93**, 5301 (1989).

[151] E. Banachowicz, J. Gapiński, and A. Patkowski, Biophys. J. **78**, 70 (2000).

[152] Z. Adamczyk, K. Sadlej, E. Wajnryb, M. L. Ekiel-Jeżewska, and P. Warszyński, J. Colloid Interf. Sci. **347**, 192 (2010).

[153] Z. Adamczyk et al., J. Colloid Interf. Sci. **385**, 244 (2012).

[154] J. García de la Torre and B. Carrasco, Biopolymers **63**, 163 (2002).

[155] B. Carrasco and J. García de la Torre, Biophys. J. **76**, 3044 (1999).

[156] H. Yamakawa, J. Chem. Phys. **53**, 436 (1970).

[157] A. Ortega and J. García de la Torre, J. Chem. Phys. **119**, 9914 (2003).

[158] J. García de la Torre and V. A. Bloomfield, Q. Rev. Biophys. **14**, 81 (1981).

[159] M. M. Tirado, C. L. Martínez, and J. García de la Torre, J. Chem. Phys. **81**, 2047 (1984).

[160] D. J. Acheson, *Elementary Fluid Dynamics*, Oxford Univ. Press, 1990.

[161] R. Piazza, V. Degiorgio, M. Corti, and J. Stavans, Phys. Rev. B **42**, 4885 (1990).

[162] R. Piazza and V. Degiorgio, Physica A **182**, 576 (1992).

[163] R. Piazza and V. Degiorgio, J. Phys. Condens. Matter **5**, 173 (1993).

[164] R. Piazza and V. Degiorgio, J. Phys. Condens. Matter **8**, 9497 (1996).

[165] V. Degiorgio, R. Piazza, M. Corti, and J. Stavans, J. Chem. Soc. Faraday Trans. **87**, 431 (1991).

[166] T. Maeda and S. Fujime, Macromolecules **1167**, 1157 (1984).

[167] S. Fujime and K. Kubota, Biophys. Chem. **23**, 1 (1985).

[168] D. Kleshchanok, M. Heinen, G. Nägele, and P. Holmqvist, Soft Matter **8**, 1584 (2012).

[169] B. Cichocki, E. Wajnryb, J. Bławzdziewicz, J. K. G. Dhont, and P. R. Lang, J. Chem. Phys. **132**, 074704 (2010).

[170] V. N. Michailidou, G. Petekidis, J. Swan, and J. F. Brady, Phys. Rev. Lett. **102**, 068302 (2009).

[171] C. Korn and U. S. Schwarz, Phys. Rev. Lett. **97**, 138103 (2006).

[172] C. B. Korn and U. S. Schwarz, J. Chem. Phys. **126**, 095103 (2007).

[173] D. Frenkel and B. Smit, *Understanding Molecular Simulation: From Algorithms to Applications*, Computational science series, Elsevier Science, 2001.

[174] T. J. Murphy and J. Aguirre, J. Chem. Phys. **57**, 2098 (1972).

[175] E. Dickinson, S. A. Allison, and J. A. McCammon, J. Chem. Soc. Faraday Trans. 2 **81**, 591 (1985).

[176] R. B. Jones and F. N. Alavi, Physica A **187**, 436 (1992).

[177] J. N. Israelachvili, *Intermolecular And Surface Forces: With Applications To Colloidal And Biological Systems*, Academic Press, 1992.

[178] W. Steffen, *Private communication*.

[179] P. Holmqvist, D. Kleshchanok, and P. R. Lang, Eur. Phys. J. E **26**, 177 (2008).

[180] L. Helden, G. Koenderink, P. Leiderer, and C. Bechinger, Langmuir **20**, 5662 (2004).

[181] J. Buitenhuis, *Colloidal Dispersions of Sterically Stabilized Boehmite Rods: Particle Clustering, Light Scattering, Phase Separation and Sedimentation*, Universiteit Utrecht, Faculteit Scheikunde, 1994.

[182] J. Rodríguez-Fernández, J. Perez-Juste, L. M. Liz-Marzan, and P. R. Lang, J. Phys. Chem. C **111**, 5020 (2007).

[183] W. H. Press, S. A. Teukolsky, W. T. Vetterling, and B. P. Flannery, *Numerical Recipes in FORTRAN 90*, Cambridge Univ. Press, 1996.

[184] B. Cichocki and K. Hinsen, Phys. Fluids **7**, 285 (1995).

[185] B. U. Felderhof and R. B. Jones, J. Math. Phys. **30**, 339 (1989).

[186] B. Cichocki and R. B. Jones, Physica A **258**, 273 (1998).

[187] E. Wajnryb, *Geometrical properties of electrostatic fields and Navier-Stokes flows*, Unpublished.